



Graduate School in Civil Engineering and Architecture

University of Pavia, Italy

DICAr - Department of Civil Engineering and Architecture

**DISCRETE ELEMENT MODELS
FOR THE SEISMIC ASSESSMENT
OF UNREINFORCED MASONRY STRUCTURES**

A Thesis Submitted in Partial Fulfilment of the Requirements
for the Degree of Doctor of Philosophy in

CIVIL ENGINEERING AND ARCHITECTURE

Candidate:

Daniele Malomo

Supervisors:

Prof. Andrea Penna – University of Pavia, Italy

Prof. Rui Pinho – University of Pavia, Italy

Prof. Matthew J. DeJong – University of California, Berkeley, United States

September, 2018

Signature of author
University of Pavia, Italy
Department of Civil Engineering and Architecture, DICAr
September, 2018

Certified by.....
Andrea Penna
Associate Professor of Structural Engineering
Thesis Supervisor

Accepted by.....
Ferdinando Auricchio
Full Professor of Mechanics of Solids
Coordinator of the Doctoral School, DICAr

Thesis Supervisors

.....
Andrea Penna
Associate Professor of Structural Engineering
Department of Civil Engineering and Architecture, DICAr
University of Pavia, Italy

.....
Rui Pinho
Associate Professor of Structural Engineering
Department of Civil Engineering and Architecture, DICAr
University of Pavia, Italy

.....
Matthew J. DeJong
Assistant Professor of Structural Engineering, Mechanics and Materials
Department of Civil and Environmental Engineering
University of California, Berkeley, United States

DISCRETE ELEMENT MODELS FOR THE SEISMIC ASSESSMENT OF UNREINFORCED MASONRY STRUCTURES

by

Daniele Malomo

Submitted to the Department of Civil Engineering and Architecture on September 28, 2018
in partial fulfilment of the requirements for the degree of
Doctor of Philosophy in Civil Engineering and Architecture

Abstract

Numerical modelling of unreinforced masonry (URM) structures subjected to earthquake loading is still an open challenge. Their dynamic response, as witnessed by experimental evidence, may vary considerably depending on several internal and external factors, making it extremely hard to predict damage initiation and propagation, strength and displacement capacity. In this context, discontinuum-based approaches, which explicitly account for the discrete nature of masonry assemblies, are steadily gaining popularity, being naturally suitable for simulating contact, sliding and large displacements among distinct blocks. However, due to the high computational cost usually required, their use is mostly confined to the analysis of local mechanisms. Moreover, having been originally conceived for solving other types of mechanical problems, their employment often calls for the elaboration of peculiar modelling strategies for achieving accurate results within a reasonable timeframe. This dissertation aims at improving and developing effective numerical methodologies for the seismic assessment of URM structures, ranging from the representation of local damage at the joint level to global collapse of complete buildings, in the framework of discontinuum-based micro-models. First, the applicability of a relatively new addition to the discrete element family, the Applied Element Method, whose use was mainly devoted to the progressive collapse analysis of large-scale concrete and steel systems, is scrutinised and consequently verified through comparison with a wide range of experimental results. Both quasi-static and dynamic in-plane and out-of-plane tests on full-scale calcium silicate and clay brick masonry components are reproduced, and particular emphasis is given to the optimisation of calibration processes, as well as to the derivation of equivalent material properties of both unit and mortar when experimental outcomes are not available. For the first time, the out-of-plane two-way bending dynamic behaviour of cavity-walls, subjected to shake-table test, is accounted for numerically until full collapse, readily enabling the estimation of produced debris areas. Given the encouraging results obtained, the employed methodology is extended to the assessment of various full-scale URM building prototypes with both flexible and rigid diaphragms, tested dynamically up to collapse or near-collapse conditions. Use was made of analytical and simplified procedures, directly implemented in the code, thereby balancing accuracy and computational expense. Second, the features of a typically-employed discrete approach, the Distinct Element Method, are enhanced through the introduction of a simplified criterion for modelling masonry crushing phenomena, originally not included in the standard formulation. Subsequently, a specific methodology for reproducing effectively the cyclic behaviour of mortared joint URM panels, presently not available in literature, is proposed and validated against experimental outcomes. Similarly, the influence of the masonry textures on the monotonic response of laterally-loaded URM piers is pointed out by comparing stiffness, shear and displacement capacity of the most widespread periodic and quasi-periodic brickworks with those of the standard running bond walls, resulting in the development of several analytical expressions for promptly quantifying the observed dissimilarities. Finally, aimed at combining the efficiency of simplified numerical strategies and the advantages of homogenisation techniques with the accuracy of discrete models, a new Finite-Distinct macroelement approach is validated against laboratory tests on full-scale piers under in-plane cyclic loading.

Acknowledgements (in Italian)

Desidero innanzitutto ringraziare i Professori Andrea Penna e Rui Pinho, relatori di questa tesi, per la loro guida e costante ispirazione. Questo lavoro ha notevolmente beneficiato della loro esperienza, così come dei loro preziosi commenti e consigli.

Ringrazio il Professor Matthew DeJong, ora all'Università di Berkeley, California, per tutto l'interesse e l'energia che ha messo nel lavoro che ho avuto il piacere di svolgere sotto la sua supervisione all'Università di Cambridge, e per tutte gli stimolanti confronti che abbiamo avuto durante e dopo il mio soggiorno.

Ricordo con piacere anche tutti i ragazzi del Department of Engineering a Cambridge, con cui ho condiviso più di una nottata di lavoro in laboratorio. In particolare, sono in debito con Anjali, per essersi dimostrata una grandissima amica, oltre che una brillante ricercatrice.

Non sarebbe stato possibile realizzare questo lavoro senza il supporto di tutto il gruppo di ricerca sulle murature (Eucentre, IUSS e Università di Pavia), da cui ho imparato molto. Le analisi numeriche svolte in questa tesi hanno beneficiato della qualità del lavoro sperimentale svolto, tra gli altri, da Chicco, Umberto, Stelios, Satya e Luca, che ringrazio sentitamente. Un grazie anche a Simone, Claudio ed Edoardo (Università di Pavia) per aver reso la stesura di questa tesi una piacevole avventura, nonostante il caldo di Luglio-Agosto.

Ai ragazzi dell'UPOL, e in particolare a Riccardo, anche amico e collega, va un enorme grazie per avermi fatto subito sentire a casa a Pavia e per tutte le avventure passate insieme.

Inoltre, non posso che ringraziare tutti i miei amici storici, in particolare Gianluca, Francesco, Nicola, Armando, Michele, Redon, Christopher, Gianmarco e Angelo. Spero di poter ricambiare un giorno tutto quello che mi hanno dato.

Ringrazio la mia famiglia, per il costante supporto e per l'incoraggiamento che non mi ha mai fatto mancare. Ringrazio mio fratello Alessandro, con cui ho condiviso parte del mio primo anno a Pavia, perché, pur essendo così diversi, è sempre stato lì per me. A Lucia e Nicola, che sicuramente avrebbe trovato il modo di scherzarci su, un grande grazie per avermi sempre dimostrato il loro affetto.

Dedico questo lavoro a mia moglie Roberta, che ha avuto la pazienza di starmi vicino anche lungo tanti altri percorsi, tutti fatti di alti e bassi, senza mai esitare. Il suo supporto, la sua positività e il suo entusiasmo per la vita hanno reso possibile tutto questo.

Contents

CHAPTER 1	INTRODUCTION	2
1.1	PROBLEM OVERVIEW.....	2
1.2	RESEARCH MOTIVATION AND OBJECTIVES.....	5
1.3	OUTLINE OF CONTENTS.....	7
	REFERENCES	9
CHAPTER 2	IN-PLANE CYCLIC RESPONSE OF URM WALLS SUBJECTED TO SHEAR-COMPRESSION QUASI-STATIC LOADING	14
2.1	INTRODUCTION.....	14
2.2	THE APPLIED ELEMENT METHOD AND THE IN-PLANE MODELLING OF MASONRY STRUCTURES..	17
2.2.1	<i>Masonry material model and in-plane failure criteria</i>	<i>18</i>
2.3	PROPOSED MODEL CALIBRATION PROCESS FOR CALCIUM SILICATE AND CLAY BRICK MASONRY ELEMENTS.....	21
2.4	URM WALLS SUBJECTED TO IN-PLANE CYCLIC LOADING.....	23
2.5	SIMULATION OF TESTS ON BOTH CALCIUM SILICATE AND BRICK MASONRY PANELS.....	26
2.5.1	<i>Preliminary results obtained with uncalibrated mechanical properties.....</i>	<i>27</i>
2.5.2	<i>Results obtained with calibrated mechanical properties</i>	<i>27</i>
2.6	CONCLUSIONS	32
	ACKNOWLEDGEMENTS.....	32
	REFERENCES	33
CHAPTER 3	OUT-OF-PLANE DYNAMIC BEHAVIOUR OF URM ASSEMBLIES IN BOTH ONE WAY AND TWO-WAY BENDING CONDITIONS	38
3.1	INTRODUCTION.....	38
3.2	OVERVIEW OF TYPICALLY-EMPLOYED URM MODELLING APPROACHES.....	39
3.3	THE APPLIED ELEMENT METHOD FOR MASONRY STRUCTURES.....	41
3.3.1	<i>Simulation of out-of-plane mechanisms</i>	<i>44</i>
3.3.2	<i>First verification of AEM with material characterisation tests.....</i>	<i>45</i>
3.4	OVERVIEW OF OUT-OF-PLANE SHAKE-TABLE TESTS CONSIDERED IN THIS STUDY.....	46
3.4.1	<i>One-way bending tests</i>	<i>46</i>
3.4.2	<i>One-way bending tests.....</i>	<i>48</i>
3.4.3	<i>Estimation of debris area from the collapse of the specimens.....</i>	<i>49</i>
3.5	NUMERICAL SIMULATION OF THE SHAKE-TABLE OUT-OF-PLANE TESTS	50
3.5.1	<i>One-way bending tests.....</i>	<i>52</i>
3.5.2	<i>Two-way bending tests</i>	<i>55</i>
3.6	CONCLUSIONS	60
	ACKNOWLEDGEMENTS.....	61
	REFERENCES	61
CHAPTER 4	SHAKE-TABLE TESTS ON URM CAVITY-WALL BUILDING PROTOTYPES	69
4.1	INTRODUCTION.....	69
4.2	MODELLING THE SHAKE-TABLE RESPONSE OF URM BUILDING SPECIMENS.....	70

4.3	THE APPLIED ELEMENT METHOD FOR MASONRY STRUCTURES.....	71
4.4	NUMERICAL REPRESENTATION OF BUILDING DETAILS AND COMPONENTS.....	73
4.4.1	<i>Idealisation of some construction details of terraced house test specimen.....</i>	73
4.4.2	<i>Simulation of in-plane and out-of-plane tests on URM components.....</i>	75
4.4.3	<i>Modelling the in-plane cyclic performances of a timber roof sub-structure.....</i>	76
4.5	SIMULATION OF SHAKE-TABLE TESTS ON URM BUILDING SPECIMENS.....	78
4.5.1	<i>LNEC-BUILD2: attic-roof substructure.....</i>	79
4.5.2	<i>LNEC-BUILD1: 2nd floor-roof substructure.....</i>	81
4.5.3	<i>EUC-BUILD1: complete structure.....</i>	84
4.6	CONCLUSIONS.....	88
	ACKNOWLEDGEMENTS.....	88
	REFERENCES.....	88

CHAPTER 5 SHAKE-TABLE RESPONSE OF A DOUBLE-LEAF UNREINFORCED CLAY BRICK MASONRY HOUSE SPECIMEN93

5.1	INTRODUCTION.....	93
5.2	THE APPLIED ELEMENT METHOD AND THE MODELLING OF URM STRUCTURES.....	96
5.3	MODELLING OF CONSTRUCTIVE DETAILS AND SUB-COMPONENTS OF TYPICAL CLAY BRICK MASONRY DUTCH DETACHED HOUSES.....	98
5.3.1	<i>Idealisation of constructive details.....</i>	98
5.3.2	<i>Numerical representation of timber diaphragms.....</i>	99
5.3.3	<i>Simulating in-plane and out-of-plane failure modes of URM elements.....</i>	101
5.4	SIMULATING THE SHAKE-TABLE PERFORMANCES OF EUC-BUILD2.....	104
5.4.1	<i>Brief overview of the specimen response.....</i>	104
5.4.2	<i>Comparison between experimental and numerical results.....</i>	105
5.5	CONCLUSIONS.....	109
5.6	ACKNOWLEDGEMENTS.....	110
	REFERENCES.....	110

CHAPTER 6 IN-PLANE CYCLIC PERFORMANCES OF URM WALLS SUBJECTED TO SHEAR-COMPRESSION118

6.1	INTRODUCTION.....	118
6.2	THE DISTINCT ELEMENT METHOD FOR MASONRY STRUCTURES.....	120
6.2.1	<i>Simulation of in-plane failure mechanisms.....</i>	122
6.2.2	<i>Modelling quasi-static phenomena using explicit time-integration schemes.....</i>	125
6.2.3	<i>First verification of DEM with material characterisation tests.....</i>	127
6.3	URM WALLS SUBJECTED TO IN-PLANE CYCLIC LOADING.....	128
6.4	SIMULATION OF THE IN-PLANE RESPONSE OF FULL-SCALE URM SPECIMENS.....	130
6.4.1	<i>Hysteretic response and bilinear idealisation.....</i>	132
6.4.2	<i>Joint crack pattern and failure through units.....</i>	138
6.4.3	<i>Effect of cyclic loading.....</i>	140
6.4.4	<i>Adequacy of numerical results.....</i>	142
6.5	CONCLUSIONS.....	144
	ACKNOWLEDGEMENTS.....	145
	REFERENCES.....	145

CHAPTER 7 INFLUENCE OF BOND PATTERN ON THE IN-PLANE BEHAVIOUR OF URM PIERS 151

7.1	INTRODUCTION.....	151
7.2	OVERVIEW OF TYPICALLY EMPLOYED URM MODELLING APPROACHES	152
7.3	SIMULATING THE IN-PLANE RESPONSE OF URM ASSEMBLIES USING THE DEM	155
7.4	MODELLING STRATEGY AND FIRST VERIFICATION AGAINST EXPERIMENTAL RESULTS	158
7.4.1	<i>Using explicit time-integration schemes for solving quasi-static problems</i>	<i>158</i>
7.4.2	<i>Evaluation of cyclic force-displacement envelopes using monotonic analysis.....</i>	<i>159</i>
7.4.3	<i>First verification with experimental tests</i>	<i>160</i>
7.5	PARAMETRIC ANALYSIS.....	163
7.5.1	<i>Methodology and definition of key-parameters.....</i>	<i>164</i>
7.5.2	<i>Lateral stiffness.....</i>	<i>165</i>
7.5.3	<i>In-plane strength.....</i>	<i>167</i>
7.5.4	<i>Failure mode and displacement capacity.....</i>	<i>170</i>
7.6	CONCLUSIONS	175
	REFERENCES	177

CHAPTER 8 A HOMOGENISED DISTINCT MACRO-BLOCK FOR SIMULATING THE IN-PLANE CYCLIC RESPONSE OF URM WALLS 184

8.1	INTRODUCTION.....	184
8.2	HOMOGENISED DISTINCT MACRO-BLOCK (HDM) REPRESENTATIVE OF A MASONRY PANEL... 186	
8.2.1	<i>Interface springs.....</i>	<i>187</i>
8.2.2	<i>Homogenised FE macro-block</i>	<i>189</i>
8.3	MODELLING THE IN-PLANE CYCLIC BEHAVIOUR OF URM PIERS.....	192
8.4	SIMULATION OF THE CYCLIC LATERAL RESPONSE OF A URM FAÇADE AND COMPARISON WITH MICRO-MODELLING APPROACH.....	195
8.5	CONCLUSIONS	198
	ACKNOWLEDGEMENTS.....	199
	REFERENCES	200

CHAPTER 9 CLOSING REMARKS AND FUTURE RESEARCH 204

9.1	SUMMARY OF MAIN FINDINGS AND PRIMARY CONTRIBUTIONS	204
9.2	FUTURE DEVELOPMENTS.....	206

APPENDIX I DERIVATION AND ASSEMBLAGE OF STIFFNESS MATRICES IN THE FRAMEWORK OF THE APPLIED ELEMENT METHOD (2D)..... 210

No great achievement is possible
without persistent work

-Bertrand Russell

CHAPTER 1

Introduction

CHAPTER 1 Introduction

In this Chapter, a brief overview on the state-of-art in numerical modelling of masonry structures is proposed. More detailed literature reviews, specifically tailored to the various subjects under study, are reported at the beginning of each Chapter. In what follows, major importance will be given to advantages and main drawbacks of the typically-employed computational strategies, ranging from the first pioneering applications to the latest advancements and open challenges. The aim is to set the context for the contributions made in this dissertation. Consequently, scopes and objectives of the latter are presented and discussed. Finally, the organisation of the Thesis and an outline of contents is summarised.

1.1 Problem overview

Unreinforced masonry (URM) structures are largely widespread all over the world. Despite their intrinsic vulnerability towards horizontal actions, they often represent the majority of the building stock in both historically earthquake-prone regions and countries now exposed to induced seismicity due to human activities, which in recent years substantially increased the number of URM constructions subjected to ground shaking (Foulger et al. 2018). Their dynamic behaviour typically entails the activation of complex and sometimes conflicting aspects of response, depending on masonry and diaphragm type, interaction between in-plane and out-of-plane actions, as well as on the degree of elevation and plan irregularity. Experimental testing of complete structural systems, rather than on isolated components, constitutes an invaluable source of information for the understanding of the abovementioned phenomena, as noted by Calvi et al. (1996). However, when comparing the inventory and inherent diversity of URM assemblies with the relatively limited number of tests on building prototypes conducted so far, it is clear that alternative solutions should be also considered, because of understandable practical and economic reasons.

In this context, the employment of appropriate numerical methods, accurately calibrated on experimental outcomes, might contribute significantly towards the investigation of both causes and effects of damage induced by seismic events. However, the modelling of masonry material still poses several significant difficulties, which might be attributable to a wide range of both internal (e.g. anisotropy, unit geometry and arrangement, mortar bond thickness, mechanical properties of components) and external (e.g. loading rate, boundary conditions, vertical compression) factors, as further explained by de Felice et al. (2017).

Whilst the use of simplified approaches, including geometrical and equilibrium-based procedures (e.g. Block et al. 2006; Heyman 1966; Livesley 1978; Roca 2006), as well as equivalent frame (e.g. Addessi et al. 2015; Belmouden and Lestuzzi 2009; Roca et al. 2005), storey mechanism (e.g. Braga and Dolce 1982; Tomažević 1987) and macroelement (e.g. Chen et al. 2008; Penna et al. 2014; Raka et al. 2015) models, presents many advantages given the reduced computational cost usually required, in the case of irregular structural systems and out-of-plane governed responses, which are typically neglected, it

might lead to inadequate results, as broadly discussed in e.g. Quagliarini et al. (2017). Similarly, albeit continuum-based methods (e.g. De Buhan and de Felice 1997; Lourenco et al. 1998; Saloustros et al. 2018), commonly implemented in the Finite Element (FE) framework, can be probably be deemed as one of the most frequently employed computational strategies for the large-scale analysis of masonry structures (Lourenço and Milani 2014), the level of accuracy associated to the development of effective homogenisation procedures is unavoidably dependent on the degree of morphological and mechanical heterogeneity of the masonry material under study.

Micro-models, ranging from the first pioneering proposals (e.g. Moreau 1988; Shi and Goodman 1988) to more recent developments (e.g. Chetouane et al. 2005; D’Altri et al. 2018; Sarhosis and Lemos 2018), instead, are naturally suitable for representing the mutual interaction among discrete blocks and damage propagation, accounting explicitly for the system discontinuity. Regardless, since achieving accurate results in a reasonable timeframe might be extremely challenging, their employment is presently confined to the analysis of local mechanisms (e.g. Andreotti et al. 2018; de Felice 2011).

Amongst others, the Distinct Element Method (DEM), initially proposed by Cundall (1971) for solving rock mechanics problems, presents unique features, including the possibility of describing automatically contact and re-contact between adjacent elements and making units deformable by superimposing an internal FE mesh. Moreover, having been implemented within an explicit time integration computational platform, it is particularly convenient in the case of impulsive and dynamic loading. Nevertheless, since crushing phenomena are neglected, its use is often limited to the simulation of dry-joint assemblies, in which blocks are idealised as fully rigid. Aimed at overcoming this issue, an attempt was made in this endeavour to include in the standard DEM formulation a simplified compressive failure criterion, whose full details are given in the dedicated Chapter. The Rigid Body and Spring Models (RBSM), originally conceived by Kawai (1978), are steadily gaining popularity, representing an acceptable compromise between accuracy and computational expense. However, notwithstanding a few remarkable applications (e.g. Casolo and Peña 2007; Casolo and Uva 2013), there is still some lacking consistency in literature regarding the RBSM simulation of experimentally-tested dynamic responses of complex URM building specimens. Recently, upgrades of these initial schemes have been proposed or adapted to the analysis of the global response of masonry structures by several researchers. Amongst others, the work of Pantò et al. (2017) substantially extended the capabilities of a plane discrete-macro-model (Caliò et al. 2012) to the 3D representation of out-of-plane failures, achieving convincing results (e.g. Cannizzaro and Lourenço 2017), also supported by experimental evidence (i.e. shake-table test on reduced-scale U-shaped URM specimens), with an acceptable computational burden. Thus, its application to more complex URM constructions seems to be promising, although not fully explored.

Similarly, the numerical outcomes lately obtained on large-scale URM buildings (e.g. Garofano and Lestuzzi 2016; Karbassi and Lestuzzi 2012) using a relative new discrete element approach, the Applied Element Method (AEM), mostly employed for the simulation of the effects of impact and blast loading on both concrete and steel-framed structures (e.g. Elshaer et al. 2017; Salem et al. 2016), appear encouraging, given also the possibility of representing explicitly collapse modes and associated debris areas within an appropriate timeframe. However, in most of the abovementioned cases, experimental

counterparts were not provided. Indeed, verification against complete URM structural systems tested dynamically, presently not available in literature, is still certainly needed. To this end, as broadly discussed in the body of this dissertation, a comprehensive validation process is herein proposed.

With reference to the general framework, as noted by Lemos (2007), recent computational developments are progressively allowing the discontinuum-based techniques to be applied more broadly in both research and engineering practice. A significant change is taking place in terms of what is expected of numerical analysis, especially in the field of masonry structures, where an increasingly high level of accuracy on a global scale is often required, as witnessed by both the rising number of applications of micro-modelling strategies and the recent trends of seismic design codes, which are encouraging the use of advanced computational procedures. However, despite the latter aspects and in addition to the analysis time, further improvements should be pursued in the future. Amongst others, it is worth mentioning that since most of the abovementioned discrete numerical methods were not originally conceived for simulating the behaviour of URM systems, their employment frequently calls for the elaboration of *ad-hoc* computational strategies, not readily applicable to the general case.

Finally, drawing on the experience gained by the author with advanced numerical models, a more profitable interaction between simplified and refined approaches, which should not be an aim in themselves, is absolutely necessary. Indeed, they should be regarded as complementary, giving the fact that they can consistently enhance each other. This probably represents the easiest and advantageous way to investigate numerically the global dynamic performances of URM structures. This dissertation, whose findings are widely discussed in the following Chapters and already employed for calibrating simplified procedures (e.g. Crowley and Pinho 2017), aims at enhancing and developing reliable experimentally-calibrated discrete element micro-models for the numerical assessment of complex URM systems subjected to earthquake loading. To this end, the capabilities of the selected modelling techniques (i.e. AEM, DEM) were verified against a wide range of laboratory results, and their performances improved through the introduction of simplified assumptions based on both analytical formulations and experimental evidence. Moreover, a preliminary attempt to combine the efficiency of simplified numerical strategies with the accuracy of discontinuum-based methods is proposed, resulting in the definition of a hybrid model, as discussed in more detail in the next section.

1.2 Research motivation and objectives

As previously mentioned, the high vulnerability of blocky assemblies under earthquake loading, combined with their large presence in countries exposed to ground shaking, unavoidably make the assessment of URM constructions a global need. Despite the advantages of testing complete structural systems, only a relatively limited number of experiments, compared to the great variability of masonry types, can be performed. Thus, the development and the calibration of reliable numerical models, among which those founded on a discontinuum domain appear naturally suitable for describing the static/dynamic mechanisms among distinct units, might represent a practical and cost-effective option for enhancing the understanding of the behaviour of URM structures subjected to horizontal actions. This context, together with the observations reported in the previous section, provides the general motivation for this work:

- The interaction between in-plane and out-of-plane modes, as well as among local and global failure mechanisms, diaphragm type and masonry properties may have a not-negligible influence on the overall dynamic behaviour of URM constructions. However, since they cannot be investigated exclusively through direct testing, the selection of suitable numerical methods, able to account for the abovementioned aspects simultaneously, is certainly needed, albeit still represents an open challenge
- There is the need of properly adapting, calibrating and further validating the capabilities of the available discrete element models, originally developed for solving problems in different fields of mechanics, against laboratory tests
- The use of discontinuum-based computational procedures is mostly confined to the analysis of local mechanisms. The development of efficient modelling and optimisation strategies for enabling the discrete element simulation of large-scale URM structures subjected to static and dynamic loading is of crucial importance, and not yet fully explored
- Out-of-plane failure mechanisms of URM components are typically neglected by simplified approaches. They might produce large debris areas, both inside and outside the considered URM building. Given the importance of such aspect in practical applications of seismic risk and the potential offered by micro-models, this is something that should be undoubtedly addressed
- Of primary concern is the interaction between advanced and simplified methods, which should be intended as complementary. The possibility of calibrating the latter on the micro-modelling outcomes, as well as the introduction of simplified assumptions in the framework of advanced methods, should be investigated further

Based on the abovementioned aspects, this dissertation aims:

To improve and develop effective numerical methods, accurately calibrated against experimental results, for the seismic assessment of URM structures at both local and global scales, in the framework of discontinuum-based micro-models.

To meet this objective, two main micro-modelling approaches will be scrutinised, verified and improved, as briefly summarised in the next section. The computational platforms and the experimental campaigns to which this work is referred were selected carefully, allowing a wide-range exploration of available techniques, founded on different and sometimes opposite assumptions, as well as of numerical challenges of various levels of complexity.

From a numerical viewpoint, are herein investigated:

- implicit and explicit time integration schemes
- quasi-static and dynamic nonlinear analyses
- continuum and discontinuum domains
- large displacement and collapse modes
- micro and macro-models
- rigid and deformable blocks
- mesh-based and meshless approaches
- local and global responses

In terms of experimental tests, the following ones were selected and reproduced numerically. It is noted that the specimens under study were constituted by calcium silicate and both hollow and solid clay brick masonries, as specified case-by-case in each Chapter.

- characterisation tests on small-scale masonry samples
- in-plane and out-of-plane tests on full-scale single leaf, double wythe, and cavity-wall URM components subjected to both quasi-static and dynamic loading
- quasi-static cyclic test on a full-scale timber roof substructure
- shake-table test on a full-scale timber roof-URM gables assembly
- shake-table tests on one and two-storeys full-scale cavity-wall systems with both flexible and rigid diaphragms
- shake-table test on a double-wythe URM full-scale building prototype with flexible diaphragms

It is worth mentioning that the experimental work described in this dissertation was carried out within the framework of the research programme on hazard and risk of induced seismicity in the Groningen region (The Netherlands), sponsored by the Nederlandse Aardolie Maatschappij BV (NAM). Full credits to those whose were involved in the testing campaigns referred to this dissertation, and provided precious assistance in accessing the test data, will be given individually at the end of each Chapter.

In the subsequent section, an outline of the dissertation is proposed, pointing out the connection among the various aspects investigated and laying down the sequential organisation according to which are presented.

1.3 Outline of contents

In addition to *Chapter 1*, which includes this introduction, two main parts are comprised this dissertation, hereinafter referred to as *Part A* and *Part B* respectively.

The general organisation of this work is paper-based, meaning that each section is a conveniently adapted version of a research contribution published/submitted/to be submitted to either an international journal or a conference. All details are summarised at the beginning of each endeavour, before the abstract, including the name of the selected journals or conference proceedings.

Each section has its own literature review, as well as the related conclusions and findings, tailored on the specific subject under study. Consequently, the author is aware that some information regarding both modelling state-of-art and computational aspects discussed in the various sections may appear redundant, albeit an effort was made to adapt numerical formulations and strategies on a case-by-case basis.

In *Part A*, the applicability of the Applied Element Method (AEM) to the modelling of both local and global failure modes of masonry structures is scrutinised and its performances improved through the introduction of suitable calibration procedures and modelling strategies.

Chapter 2 and *Chapter 3* are focused on the AEM modelling of in-plane and out-of-plane local failure mechanisms respectively. Such validation process includes comparisons with in-plane quasi-static cyclic tests on full-scale URM piers subjected to shear-compression (i.e. *Chapter 2*) and out-of-plane shake-table tests of URM full-scale components under both one-way and two-way bending conditions (i.e. *Chapter 3*). In the latter case, which as far as the author is aware of is one of the first numerical attempts to characterise the dynamic two-way bending out-of-plane response of full-scale cavity-wall systems, the capabilities of the AEM model in adequately evaluating the experimentally-observed debris areas are also assessed.

Chapter 4 and *Chapter 5* extend the methodologies previously proposed and verified to the simulation of global failure mechanisms of full-scale URM building prototypes, tested dynamically up to collapse or near-collapse conditions. In particular, *Chapter 4* deals with predicting hysteretic behaviour, crack patterns and explicit collapse modes of three different specimens, built according to the cavity-wall construction technique, typically employed in Northern Europe, and characterised by the presence of both rigid and flexible diaphragms. A similar computational problem is addressed in *Chapter 5*, where the shake-table response of a double-wythe clay brick URM house specimen with timber diaphragms is replicated numerically. As in the previous case, although the test was stopped before full collapse, the model was pushed forward, imposing additional ground motions with a view to provide a reasonable estimation of the actual seismic resistance of these building typologies.

In *Part B*, the use of the Distinct Element Method (DEM) is investigated and enhanced, implementing several new features and optimising the simulation of quasi-static phenomena.

In *Chapter 6* and *Chapter 7* the DEM capabilities in satisfactory reproducing the in-plane local modes of URM piers under shear-compression biaxial stress states are explored and enlarged. *Chapter 6* entails the simulation of the quasi-static cyclic behaviour of URM panels with mortared joints, presently not available in literature. Its employment is optimised by introducing dynamic relaxation schemes and numerical workarounds, including mass, time and size scaling procedures. Both single leaf and double-wythe full-scale specimens were considered. A new methodology for representing explicitly masonry crushing phenomena is presented and verified. Special attention is devoted to the model adequacy, assessed through a statistical procedure. *Chapter 7*, inspired by the findings in the previous one, is focused on the numerical assessment of the influence of typically-employed periodic and quasi-periodic bond patterns on the response of laterally-loaded piers. Several combinations of masonry types, boundary conditions, aspect ratios and vertical compressions are considered, and the results obtained for each brickwork compared with the behaviour exhibited by standard running bond walls. With a view to calibrate simplified approaches accounting for the observed dissimilarities, numerically-inferred analytical expressions are proposed.

Chapter 8 deals the development of hybrid computational approaches. Indeed, aimed at combining the efficiency of the macroelement strategy and the advantages of homogenisation procedures with the accuracy of DEM-based methods, a new Finite-Distinct macro-block model for predicting the cyclic response of URM panels is preliminary validated against experimental outcomes.

In *Chapter 9* the main findings related to the work herein proposed, as well as the potential future developments are briefly summarised.

Finally, *Appendix I* focuses on the most relevant aspects concerning the theoretical formulation of the AEM. Particular importance is given to the stiffness matrices derivation and to their assembly for the simple case of two adjacent plane units which interact to each other. Contrarily, the DEM formulation was not included in this work, because it has been widely investigated throughout years by several authors (e.g. Cundall 1971; Lemos 2007), whose contributions the reader are referred. Regardless, it is noted that at the beginning of each “DEM Chapter”, the theoretical background and the formulation for masonry assemblies is briefly presented.

References

- Addressi, D., Mastrandrea, A., and Sacco, E. (2015). "A force-based equivalent frame element for push-over analysis of masonry structures." *Key Engineering Materials*, 624, 405–412.
- Andreotti, G., Graziotti, F., and Magenes, G. (2018). "Detailed micro-modelling of the direct shear tests of brick masonry specimens: The role of dilatancy." *Engineering Structures*, Elsevier, 168, 929–949.
- Belmouden, Y., and Lestuzzi, P. (2009). "An equivalent frame model for seismic analysis of masonry and reinforced concrete buildings." *Construction and Building Materials*.
- Block, P., Ciblac, T., and Ochsendorf, J. (2006). "Real-time limit analysis of vaulted masonry buildings." *Computers & Structures*, Elsevier, 84(29), 1841–1852.
- Braga, F., and Dolce, M. (1982). "A method for the analysis of antiseismic multi-storey masonry buildings (In Italian)." *Proceedings of the 6th International Brick Masonry Conference*, Rome, Italy, 1089–1099.
- De Buhan, P., and de Felice, G. (1997). "A homogenization approach to the ultimate strength of brick masonry." *Journal of the Mechanics and Physics of Solids*, Pergamon, 45(7), 1085–1104.
- Caliò, I., Marletta, M., and Pantò, B. (2012). "A new discrete element model for the evaluation of the seismic behaviour of unreinforced masonry buildings." *Engineering Structures*, Elsevier, 40, 327–338.
- Calvi, G. M., Kingsley, G. R., and Magenes, G. (1996). "Testing of masonry structures for seismic assessment." *Earthquake Spectra*, 12(1), 145–162.
- Cannizzaro, F., and Lourenço, P. B. (2017). "Simulation of Shake Table Tests on Out-of-Plane Masonry Buildings. Part (VI): Discrete Element Approach." *International Journal of Architectural Heritage*, Taylor & Francis, 11(1), 125–142.
- Casolo, S., and Peña, F. (2007). "Rigid element model for in-plane dynamics of masonry walls considering hysteretic behaviour and damage." *Earthquake Engineering and Structural Dynamics*, 36(8), 1029–1048.
- Casolo, S., and Uva, G. (2013). "Nonlinear analysis of out-of-plane masonry façades: Full dynamic versus pushover methods by rigid body and spring model." *Earthquake Engineering & Structural Dynamics*, Wiley-Blackwell, 42(4), 499–521.
- Chen, S.-Y., Moon, F. L., and Yi, T. (2008). "A macroelement for the nonlinear analysis of in-plane unreinforced masonry piers." *Engineering Structures*, Elsevier, 30(8), 2242–2252.
- Chetouane, B., Dubois, F., Vinches, M., and Bohatier, C. (2005). "NSCD discrete element method for modelling masonry structures." *International journal for numerical methods in engineering*, Wiley-Blackwell, 64(1), 65–94.
- Crowley, H., and Pinho, R. (2017). *Report on the v5 fragility and consequence models for the Groningen field. Report-Groningen Field Seismic Hazard and Risk Assessment Project*.
- Cundall, P. A. (1971). "A computer model for simulating progressive large scale movements in blocky rock systems." *Proc. Symp. Rock Fracture (ISRM)*, Nancy.
- D'Altri, A. M., de Miranda, S., Castellazzi, G., and Sarhosis, V. (2018). "A 3D detailed micro-model for the in-plane and out-of-plane numerical analysis of masonry panels." *Computers & Structures*, Pergamon, 206, 18–30.
- Elshaer, A., Mostafa, H., and Salem, H. (2017). "Progressive collapse assessment of

- multistory reinforced concrete structures subjected to seismic actions.” *KSCE Journal of Civil Engineering*, Korean Society of Civil Engineers, 21(1), 184–194.
- de Felice, G. (2011). “Out-of-plane seismic capacity of masonry depending on wall section morphology.” *International Journal of Architectural Heritage*, 5(4–5), 466–482.
- de Felice, G., De Santis, S., Lourenço, P. B., and Mendes, N. (2017). “Methods and Challenges for the Seismic Assessment of Historic Masonry Structures.” *International Journal of Architectural Heritage*, Taylor & Francis, 11(1), 143–160.
- Foulger, G. R., Wilson, M. P., Gluyas, J. G., Julian, B. R., and Davies, R. J. (2018). “Global review of human-induced earthquakes.” *Earth-Science Reviews*, Elsevier, 178, 438–514.
- Garofano, A., and Lestuzzi, P. (2016). “Seismic Assessment of a Historical Masonry Building in Switzerland: The ‘Ancien Hôpital De Sion.’” *International Journal of Architectural Heritage*, Taylor & Francis, 10(8), 975–992.
- Heyman, J. (1966). “The stone skeleton.” *International Journal of Solids and Structures*, Elsevier, 2(2), 249IN1257IN5265--256IN4264IN12279.
- Karbassi, A., and Lestuzzi, P. (2012). “Fragility Analysis of Existing Unreinforced Masonry Buildings through a Numerical-based Methodology.” *The Open Civil Engineering Journal*, 6(1), 121–130.
- Kawai, T. (1978). “New discrete models and their application to seismic response analysis of structures.” *Nuclear Engineering and Design*, Elsevier, 48(1), 207–229.
- Lemos, J. V. (2007). “Discrete element modeling of masonry structures.” *International Journal of Architectural Heritage*, Taylor & Francis, 1(2), 190–213.
- Livesley, R. K. (1978). “Limit analysis of structures formed from rigid blocks.” *International Journal for Numerical Methods in Engineering*, Wiley-Blackwell, 12(12), 1853–1871.
- Lourenço, P. B., and Milani, G. (2014). “Homogenization and Seismic Assessment: Review and Recent Trends.” *Mechanics of Masonry Structures SE - 7*, 293–341.
- Lourenço, P., Rots, J., and Blaauwendraad, J. (1998). “Continuum Model for Masonry: Parameter Estimation and Validation.” *Journal of Structural Engineering*, 124(6), 642–652.
- Moreau, J. J. (1988). “Unilateral contact and dry friction in finite freedom dynamics.” *Nonsmooth mechanics and Applications*, Springer, 1–82.
- Pantò, B., Cannizzaro, F., Caliò, I., and Lourenço, P. B. (2017). “Numerical and Experimental Validation of a 3D Macro-Model for the In-Plane and Out-Of-Plane Behavior of Unreinforced Masonry Walls.” *International Journal of Architectural Heritage*, 11(7), 946–964.
- Penna, A., Lagomarsino, S., and Galasco, A. (2014). “A nonlinear macroelement model for the seismic analysis of masonry buildings.” *Earthquake Engineering & Structural Dynamics*, Wiley-Blackwell, 43(2), 159–179.
- Quagliarini, E., Maracchini, G., and Clementi, F. (2017). “Uses and limits of the Equivalent Frame Model on existing unreinforced masonry buildings for assessing their seismic risk: A review.” *Journal of Building Engineering*, Elsevier, 10, 166–182.
- Raka, E., Spacone, E., Sepe, V., and Camata, G. (2015). “Advanced frame element for seismic analysis of masonry structures: model formulation and validation.” *Earthquake Engineering & Structural Dynamics*, Wiley-Blackwell, 44(14), 2489–2506.
- Roca, P. (2006). “Assessment of masonry shear-walls by simple equilibrium models.” *Construction and Building Materials*, 20(4), 229–238.

- Roca, P., Molins, C., and Marí, A. R. (2005). “Strength Capacity of Masonry Wall Structures by the Equivalent Frame Method.” *Journal of Structural Engineering*, 131(10), 1601–1610.
- Salem, H., Mohssen, S., Nishikiori, Y., and Hosoda, A. (2016). “Numerical Collapse Analysis of Tsuyagawa Bridge Damaged by Tohoku Tsunami.” *Journal of Performance of Constructed Facilities*, 30(6), 04016065.
- Saloustros, S., Pelà, L., Cervera, M., and Roca, P. (2018). “An Enhanced Finite Element Macro-Model for the Realistic Simulation of Localized Cracks in Masonry Structures: A Large-Scale Application.” *International Journal of Architectural Heritage*, Taylor & Francis, 12(3), 432–447.
- Sarhosis, V., and Lemos, J. V. (2018). “A detailed micro-modelling approach for the structural analysis of masonry assemblages.” *Computers and Structures*, Pergamon, 206, 66–81.
- Shi, G. H., and Goodman, R. E. (1988). “Discontinuous deformation analysis—a new method for computing stress, strain and sliding of block systems.” *The 29th US Symposium on Rock Mechanics (USRMS)*.
- Tomazėvič, M. (1987). “Dynamic modelling of masonry buildings: storey mechanism model as a simple alternative.” *Earthquake Engineering & Structural Dynamics*, Wiley-Blackwell, 15(6), 731–749.

PART A

Modelling local and global failure modes of
URM components and large-scale assemblies
using the Applied Element Method

CHAPTER 2

In-plane cyclic response of URM walls subjected to
shear-compression quasi-static loading

CHAPTER 2 In-plane cyclic response of URM walls subjected to shear-compression quasi-static loading

Malomo D., Pinho R., Penna A. (2018). “Using the Applied Element Method for modelling calcium silicate brick masonry subjected to in-plane cyclic loading.” *Earthquake Engineering & Structural Dynamics*, 47(7), 1610–1630.

Abstract. The response of both calcium-silicate and clay brick unreinforced masonry structures to horizontal cyclic loading has recently become the focus of experimental and numerical research, given its extensive use in some areas of the world that are now exposed to induced earthquakes (e.g. north of the Netherlands). In order to assess the seismic behaviour of such construction, a relatively wide range of modelling methodologies are available, amongst which the discrete elements approach, which takes into account the intrinsic heterogeneity of a brick-mortar assembly, can probably be deemed as the most appropriate computational procedure. On the other hand, however, since discrete elements numerical methods are based on a discontinuum domain, often they are not able to model every stage of the structural response adequately, and because of the high computational burden required, the analysis scale should be chosen carefully. The Applied Element Method (AEM) is a relatively recent addition to the discrete elements family, with a high potential for overcoming the aforementioned limitations or difficulties. Initially conceived to model blast events and concrete structures, its use in the earthquake engineering field is, of late, increasing noticeably. In this paper, the employment of the AEM to model the in-plane cyclic response of both calcium-silicate and clay brick masonry panels is discussed and scrutinised, also through the comparison with experimental results of in-plane cyclic shear-compression tests on unreinforced masonry wall specimens.

Keywords: applied element method; numerical modelling; in-plane; unreinforced masonry

2.1 Introduction

The Groningen region, in the north of the Netherlands, historically not prone to tectonic earthquakes, has in recent years been subjected to seismic events induced by reservoir depletion due to gas extraction (van Elk et al. 2018). Construction in this region is dominated by the presence of unreinforced masonry (URM) structures, featuring calcium-silicate (CS) and clay (CL) bearing walls, both of which have thus now become the focus of experimental research endeavours aimed at assessing their response to horizontal seismic loading (e.g. Graziotti et al. 2015, 2016c). The work described in this paper concerns thus the examination and verification, through comparison with experimental data, of a possible modelling strategy for the assessment of the in-plane response of the aforementioned URM walls. Use was made of the Applied Element Method (Meguro and Tagel-Din 2000, 2001, 2002), with a view to assess how this relatively recent addition to the discrete elements

methods family may or may not feature the capability of producing a reliable estimation of the seismic response of this type of structural elements.

Since the lateral capacity of masonry elements may vary considerably depending on several factors, including masonry type and boundary conditions, four CL brick and three CS masonry piers subjected to in-plane cyclic shear-compression, with different aspect ratios and tested according to various experimental configurations, were considered. The structural analysis software tool Extreme Loading for Structures (ELS) (ASI, 2018), was employed to carry out the AEM modelling of this study.

Several modelling techniques of different levels of complexity and computational burden are available for reproducing analytically the behaviour of masonry structures. Simplified methods ranging from the application of Limit Analysis (Block et al. 2006; D’Ayala and Speranza 2003; Heyman 1966) to storey mechanism models (Braga and Dolce 1982; Tomažević 1987) have been employed over the years to study the seismic behaviour of masonry elements and buildings. Among these simplified procedures, Graziotti et al. (2016a) proposed an equivalent SDOF model for the evaluation of the global response of URM buildings using nonlinear dynamic analyses (Costa et al. 2015; DeJong and Dimitrakopoulos 2014). Within a macro-modelling methodology, instead, homogenised finite masonry portions are assembled obtaining a global model with the aim to reduce computational efforts. Amongst other numerical approaches, the macroelement modelling strategy, typically implemented in equivalent-frame models, represents an acceptable compromise between accuracy and computational burden. In this regard, a wide range of contributions have been proposed (Addessi et al. 2015; Chen et al. 2008; Lagomarsino et al. 2013; Penna et al. 2014; Raka et al. 2015). In order to decrease the approximation level, more refined numerical procedures, such as the Finite Element Method (FEM), have been adapted and applied to masonry structures, implementing nonlinear constitutive laws and by means of a material homogenisation process. Two main numerical approaches are thus distinguished: the first one, based on a continuum idealisation, or macro-modelling, and the second one, which partially takes into account the system discontinuity, or micro-modelling. A comprehensive review of these methods can be found in Roca et al. (2010). Nowadays, even though FEM is probably the most employed numerical tool, and extended or hybrid methods have been additionally implemented, phenomena such as block separation, rotation or frictional sliding are still complex to model.

Approaches that intrinsically account for the discrete nature of masonry, have been also formalised since the early seventies (Cundall 1971). According to the Discrete Element Method (DEM), the units, depending on the problem peculiarities, can be modelled as rigid (only interaction constitutive law is needed), pseudo-rigid, or deformable (continuum constitutive law must be included), replacing the real masonry arrangement without any meshing process (Bakeer 2009; Lemos 2007). The classical formulation of the DEM by Cundall and Hart (1992) provides two main hypotheses, i.e. finite displacements and rotations modelling and an automatic detection of element contact/collision. However, it is noted that sometimes the borderline between FEM and DEM appears blended in light of other recent advancements (MDEM, EDEM, DEM/FEM), as accurately reported in Lourenço (2002). The DEM procedure is naturally well suited for collapse simulation, and thanks to this important feature a wide range of DEM versions have been developed, as discussed in what follows. Examples of successful applications to the seismic analysis of

masonry structures can be found e.g. in De Lorenzis et al. (2007) and in Tondelli et al. (2016). In order to improve contact and impact modelling, the Discontinuous Deformation Analysis (DDA) was initially proposed by Shi Gen-hua and Goodman (1988) with the aim of solving geotechnical problems, anticipating the formulation of the Non-Smooth Contact Dynamics (NSCD), founded on similar principles and initially elaborated by Jean (1999). It involves an implicit time-stepping scheme in which blocks can be either rigid or deformable. Coulomb frictional phenomena between blocks are based on the work of Moreau (1988), assuming unilateral contact. The NSCD method has been recently used to model the dynamic response of masonry structures, including numerical investigations on the in-plane behaviour of masonry walls (Chetouane et al. 2005; Portioli and Cascini 2016), arches (Rafiee et al. 2008a) and analyses of historical masonry structures (Rafiee et al. 2008b).

Notwithstanding the good results reported by the aforementioned researchers and the great potential of these discrete elements methods, their empirical formulation (e.g. the relationships between micro and macroscopic parameters), and the amount of data required to build a model often make them difficult to apply efficiently, even when dealing with simple structures. Furthermore, since most of the current available DEM codes are based on explicit numerical methods, the modelling of static or quasi-static phenomena is often computationally inefficient, requiring dynamic relaxation schemes and a proper calibration of the damping factors. A different computational methodology, which partially overcomes these issues, characterises the rigid body spring model (RBSM), (Kawai 1978). According to the latter, a masonry assembly is assumed to be composed of rigid blocks connected by discrete deformable interfaces with distributed normal and tangential nonlinear springs. The global response is obtained considering spring elongation and failures, which allows representing the final configuration of rigid block assembly. Although this approach was originally elaborated for handling static problems, some applications (Casolo 2000) have shown that, under several assumptions and considering relatively small structures, adequate results can be obtained even in the dynamic range.

Meguro and Tagel-Din (2000, 2001, 2002) proposed an analogous but more efficient approach, the Applied Element Method (AEM), in which rigid units interact with each other through linear or nonlinear springs that represent the material properties. Whilst the RBSM often considers an additional spring at the joint level aimed at modelling the local rotational effects, in the AEM this contribution is accounted automatically assigning a different shear stiffness to the interface springs (thus decreasing the matrices dimensions). Another difference between these two similar methods is that, contrary to AEM, in most of the applications to masonry structures the RBSM element discretisation is based on an equivalent mesh, considering the influence of the unit arrangement by means of energy relations between the discrete (real) model and a representative homogenised macroscopic segment (Casolo 2009). As demonstrated by Tagel-Din and Meguro (1998), the Poisson effect is accounted intrinsically by the AEM, whereas the RBSM formulation requires additional degrees of freedom (DOFs) or the spring stiffness manipulation (Furukawa et al. 2012). Finally, unlike the AEM (Karbassi and Nolle 2013), analysis up to complete collapse of a structure using RBSM is unattainable, since the latter does not consider the re-contact between neighbouring elements (if different from the ones initially set). In this work, the employment of the AEM in the modelling of both CS and CL brick masonry walls is further discussed and verified.

2.2 The Applied Element Method and the in-plane modelling of masonry structures

In this section, an overview of the AEM formulation of masonry structures is proposed. More specifically, given the nature of the mechanical phenomena being investigated in this contribution (i.e. in-plane actions), only the 2D case was considered. Within this framework, an arbitrary masonry segment is composed of brick elements connected to each other by equivalent springs, in which the mechanical properties of brick-mortar interfaces (Figure 1) are lumped (i.e. no additional DOFs are assigned to mortar layers). A given brick can be modelled as a rigid block or as an assembly of units; if it is desired to model potential splitting or crushing of bricks, then the latter need necessarily to be discretised).

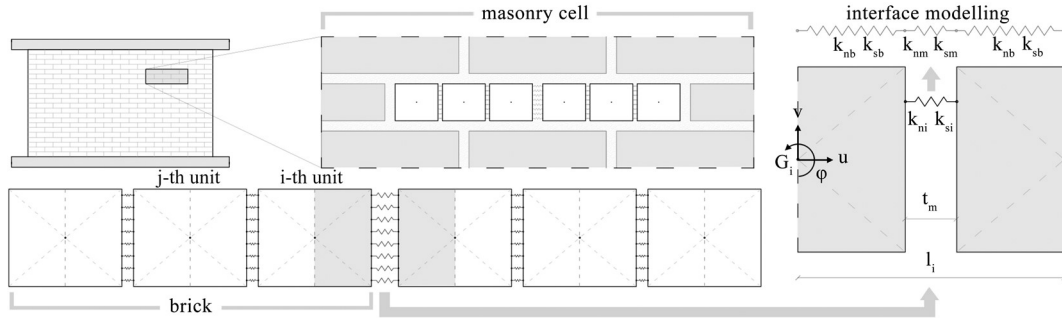


Figure 1 AEM discretisation of a masonry segment (adapted from Malomo et al. 2018)

From a computational viewpoint, two different stiffness matrices are needed here: for the brick elements assembly, since the springs connect elements of identical material, $[K_{bg}]$ is composed of the brick stiffnesses k_{nb} and k_{sb} only, whereas for the interfaces, $[K_{ig}]$ is made up inferring the equivalent stiffnesses k_{ni} and k_{si} (which, as indicated in Figure 1, are obtained assuming the brick and mortar springs arranged in series).

$$k_{nb} = \left(\frac{E d t_j}{l_j} \right), \quad k_{sb} = \left(\frac{G d t_j}{l_j} \right) \quad (1)$$

$$\frac{1}{k_{ni}} = \left(\frac{l_i - t_m}{E_b d t_i} + \frac{t_m}{E_m d t_i} \right), \quad \frac{1}{k_{si}} = \left(\frac{l_i - t_m}{G_b d t_i} + \frac{t_m}{G_m d t_i} \right) \quad (2)$$

These parameters, representing the brick-mortar interaction, take into account both the brick and the mortar elastic properties, as shown below. In Eq. (3), the upper left quarter components $[K_{ig/4}]$ of an interface global stiffness matrix $[K_{ig}]$ is reported, where $\Delta\bar{x}_i, \Delta\bar{y}_i$ are the horizontal and vertical relative displacement at the joint level respectively (with reference to the unit centroid), $c = \cos(\varphi)$, and $s = \sin(\varphi)$.

$$\begin{bmatrix} k_{ni}(c\varphi)^2 + k_{si}(s\varphi)^2 & (k_{ni} - k_{si})(c\varphi)(s\varphi) & -k_{ni}(c\varphi)(\Delta\bar{y}_i) - k_{si}(s\varphi)(\Delta\bar{x}_i) \\ (k_{ni} - k_{si})(c\varphi)(s\varphi) & k_{si} & -k_{ni}(c\varphi)(\Delta\bar{y}_i) + k_{si}(s\varphi)(\Delta\bar{x}_i) \\ -k_{ni}(c\varphi)(\Delta\bar{y}_i) - k_{si}(s\varphi)(\Delta\bar{x}_i) & -k_{ni}(c\varphi)(\Delta\bar{y}_i) + k_{si}(s\varphi)(\Delta\bar{x}_i) & k_{ni}(\Delta\bar{y}_i)^2 + k_{si}(\Delta\bar{x}_i)^2 \end{bmatrix} \quad (3)$$

In a post-cracked response stage, the elastic parameters implemented in Eq. (3) should be modified according to the material constitutive laws. The AEM employs these criteria

changing the stiffness values at each loading step, taking into account the damage evolution; when a given amount of springs has failed and their stiffness is set to zero, contact between units is lost.

2.2.1 Masonry material model and in-plane failure criteria

The material models commonly adopted for URM simplified micro-modelling, as well as the failure criteria considered, are herein described, with particular emphasis on the ones implemented in ELS. In this framework, the behaviour of URM structures in the framework of plasticity is modelled considering five different types of allowed failure modes, depicted in Figure 2: (1) cracking of the joints, (2) sliding along the bed or head joints, (3) cracking of units in direct tension, (4) diagonal tension cracking of the bricks due to shear-compression and (5) splitting of bricks, (Lourenço et al. 1995).

Under these assumptions, it is clear that the first two modes, (1) and (2), should be taken into account by the interface springs, mode (3) should be described by brick springs, and (4) is combined mechanisms involving both interface and brick springs. Failure modes (5) involves both mortar and units. Since the mortar interface is modelled as a zero-thickness interface, and thus the Poisson's effect cannot be included explicitly (Asteris et al. 2015), a compressive cap can be implemented to limit the compression stresses in the masonry, according to the behaviour observed under uniaxial testing. The masonry constitutive model typically implemented in AEM codes, for failure modes that come from the joint participation of unit and mortar in high compressive stress, is a linearised version of the "composite interface cap model" proposed by Lourenço et al. (1995) for simplified micro-modelling approaches (see Figure 3).

The main objective is to establish an elastic bound, introducing numerical operators able to define mathematically each failure mode, i.e. the yield functions. Each failure mode is associated with a pre-defined failure surface. Yielding can only occur if the stresses σ satisfy the general yield criterion $f_i(\sigma, \bar{\sigma}_i(\kappa_i)) = 0$, where the yield stress value $\bar{\sigma}_i$ is a function of a scalar κ_i , which is introduced as a measure for the amount of hardening/softening of i -th yield surface (i.e. plastic deformations) The cap model implemented in the employed AEM code consists of a simplified composite yield criterion with a tension cut-off $f_1(\sigma, \kappa_1) = (\sigma - \bar{\sigma}_1)$, a Coulomb friction model $f_2(\sigma, \kappa_2) = [|\tau| - (\tan(\phi_1)\sigma + \bar{\sigma}_2)]$ and a compressive cap $f_3(\sigma, \kappa_3) = [|\tau| + \tan(\phi_2)(\bar{\sigma}_3 - \sigma)]$.

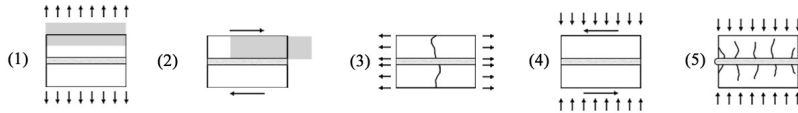


Figure 2 Typical brick-mortar failure mechanisms (adapted from Lourenço et al. 1995)

The yield values are given by Eq. (4) and (5), where f_{tm} is the bond strength, $\kappa_{1,2,3}$ are the hardening/softening parameters, G_f^I and G_f^{II} the fracture energy of first and second mode, and c is cohesion. Furthermore, ϕ is the interface friction angle, σ_s , σ_p , σ_m , σ_r , κ_m , and κ_p are factors which can be obtained from uniaxial compression tests (Khoo and Hendry 1973). Associate and non-associate flow rules are adopted for f_{1-3} and f_2 respectively.

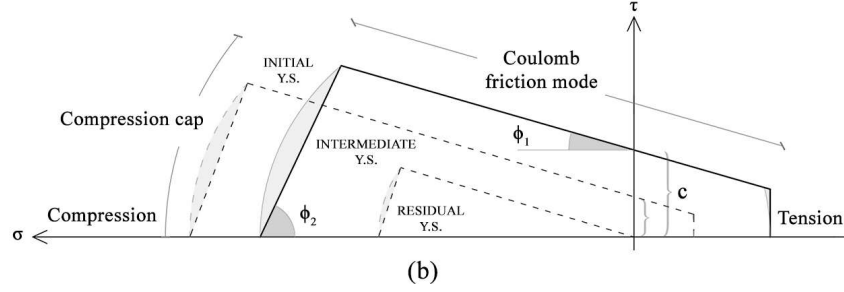


Figure 3 Linearised composite interface cap model (adapted from Lourenço et al. 1995)

$$\bar{\sigma}_1 = \begin{cases} ft_m \left(1 - \frac{(ft_m)(\kappa_1)}{G_f^I} \right), & \kappa_1 \leq \left(\frac{2G_f^I}{ft_m} \right) \\ 0 & , \quad \kappa_1 > \left(\frac{2G_f^I}{ft_m} \right) \end{cases} \quad (4)$$

$$\bar{\sigma}_2 = \begin{cases} c \left(1 - \frac{(c)(\kappa_2)}{G_f^{II}} \right), & \kappa_2 \leq \left(\frac{2G_f^{II}}{c} \right) \\ 0 & , \quad \kappa_2 > \left(\frac{2G_f^{II}}{c} \right) \end{cases} \quad (5)$$

$$\bar{\sigma}_3 = \begin{cases} \bar{\sigma}_a(\kappa_3) = \bar{\sigma}_i + (\bar{\sigma}_p - \bar{\sigma}_i) \left(\frac{2\kappa_3}{\kappa_p} - \frac{\kappa_3^2}{\kappa_p^2} \right)^{-0.5}, & \kappa_3 \leq \kappa_p \\ \bar{\sigma}_b(\kappa_3) = \bar{\sigma}_p + (\bar{\sigma}_m - \bar{\sigma}_p) \left(\frac{\kappa_3}{\kappa_m} - \frac{\kappa_p}{\kappa_p} \right)^2, & \kappa_p < \kappa_3 \leq \kappa_m \\ \bar{\sigma}_c(\kappa_3) = \bar{\sigma}_r + (\bar{\sigma}_m - \bar{\sigma}_r) \left(m \frac{\kappa_3 - \kappa_m}{\bar{\sigma}_m - \bar{\sigma}_r} \right), & \kappa_m < \kappa_3 \end{cases} \quad \text{with } m = 2 \left(\frac{\bar{\sigma}_m - \bar{\sigma}_p}{\kappa_m - \kappa_p} \right) \quad (6)$$

The masonry compressive strength (fc_m) of the cap model follows the nonlinear law depicted in Figure 4(a) (Pandey and Meguro 2004). Nevertheless, since each component of masonry is modelled individually (i.e. no homogenised masonry properties like fc_m are considered), an equivalent mortar and brick compressive strength might be introduced (otherwise an early compressive failure of the weakest component might occur) in order to reproduce the masonry compressive response adequately. In this endeavour, rather than altering both the component properties, the mortar compressive strength has been set equal to the one of the brick material. This simplified procedure, which may overestimate the increase of mortar compressive strength due to the confinement effect, has proved to be effective in this specific case, leading to reasonable results. The brick material failure envelope (see Figure 4(b)), instead, is given by the Khoo-Hendry biaxial compressive failure criterion introduced in Eq. (7), where fc_b is the brick compressive strength, fc_b' and ft_b' are the compressive and lateral tensile uniaxial strength of bricks, respectively.

$$\frac{fc_b}{fc_b'} + \left(\frac{ft_b}{ft_b'} \right) \geq 0 \quad (7)$$

$$c = c_0 \left(\frac{c_0}{\sigma_r^{II}} \right)^{(\Delta_{pl})} \quad (8)$$

$$ft_m = ft_m \left(\frac{ft_m}{\sigma_r^I} \right)^{(\Delta_{pl})} \quad (9)$$

In the Mohr-Coulomb failure criterion implemented in the AEM code initially developed by Meguro and employed in some of the first numerical applications (e.g. Guragain et al. 2006), the cohesion value is assumed constant until the applied

strain exceeds the associated yield point, after which it asymptotically decreases. This kind of behaviour is described mathematically by Eq. (8), where c_0 is the initial cohesion and Δ_{pl} is plastic displacement, which mainly depends on the value assigned to the associated fracture energy, G_f^{II} . The expression proposed in Eq. (8) describes analytically the experimental response observed in several shear tests, as reported in Van Zijl (1996).

However, the AEM code employed in this endeavour further simplified this phenomenon by setting the cohesion to zero or eventually assigning a residual cohesion right after the exceedance of the yield point γ_y . Similarly, the bond tensile behaviour presented in Pandey and Meguro (2004) shows a post-peak exponential softening branch, after an initial linear trend, as is clearly shown through Eq. (9) and widely supported by laboratory results. The tensile response of the mortared joint considered for the numerical models proposed in what follows, instead, does not make use of the softening branch. Indeed, once the actual tensile stress exceeds the limit value of f_y , the tensile strength immediately decreases to zero (or to its residual constant value, if specified). In Figure 4 below the abovementioned simplified laws are illustrated, highlighting (dark grey envelopes) the small variations implemented in the current version of the employed AEM code with respect to the original formulation.

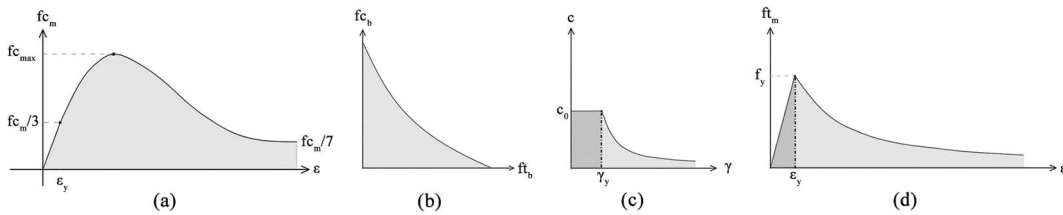


Figure 4 Compressive hardening/softening (a), Khoo-Hendry strength envelope (b), cohesion (c) and bond degradation (d) (adapted from Malomo et al. 2018)

Mortared joints, if subjected to shear-compression loading, might exhibit residual shear strength due to the mechanical interaction between mortar and units (i.e. because of the asperity, or roughness, of both the surfaces). This evidence was observed and reported by several authors (Van der Pluijm 1993), while no residual cohesion was detected for dry masonry joints during cyclic couplet tests (Lourenço and Ramos 2004). Numerical applications can be also found in Milosevic et al. (2012) and Parisi and Augenti (2012). The concept of the roughness factor may be mathematically described as the ratio between an actual surface (including material coarseness) and its projection (projected area), as depicted in Figure 5 below:

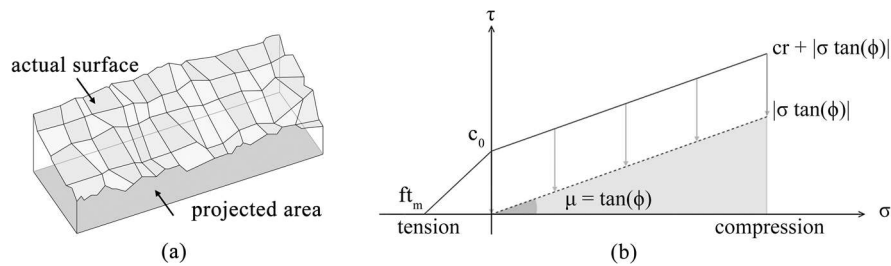


Figure 5 Representation of the roughness mathematical concept (a) and its influence on the Mohr-Coulomb criterion (b) (adapted from Malomo et al. 2018)

This parameter, mostly used in other fields of mechanics, can be determined empirically by means of the Gauckler–Manning–Strickler formulae. At the joint level, it controls the ability of closed cracks to carry shear stress, influencing only the post-cracking behaviour (i.e. when applied stress > shear stress limit). When sliding occurs ($c = 0$), r activates residual frictional resistance by imposing $c \neq 0$ (depending on the level of interface coarseness), as reported in Eq. (10) below:

$$\tilde{\sigma} = \begin{cases} cr + \sigma \tan(\phi), & r \neq 0 \\ \sigma \tan(\phi), & r = 0 \end{cases} \quad (10)$$

2.3 Proposed model calibration process for calcium silicate and clay brick masonry elements

As already mentioned, according to a simplified micro-modelling approach, each component of a masonry element (i.e. bricks and mortar) needs to be described in terms of its mechanical properties. However, experimental campaigns on masonry elements rarely involve tests that would allow one to obtain all necessary material characterisation for brick and mortar separately. This lack of experimental data calls for a pre-processing effort that makes use of empirical formulae available in the literature to obtain first estimates of the aforementioned parameters, as described in the flowchart shown in Figure 6 and Figure 7, below. In addition, and as suggested by Mayorca and Meguro (2003), the elastic material properties of mortar need to be subsequently calibrated into equivalent values ($E_{mo,eq}$, $G_{mo,eq}$) ensuring that the initial lateral stiffness computed by the model for the URM walls matches either an expected value for such response parameter (herein termed as “theoretical initial lateral stiffness”, K_{the}) or, if available, the experimentally observed initial lateral stiffness, K_{exp} .

Then, depending on the applied stresses/strains at the joint level, the elastic parameters are adjusted locally by the code according to the implemented material model, in order to reproduce the actual behaviour in the nonlinear range. In summary, one may identify the following four main steps (see Figure 6) in the definition/calibration of the material properties for a URM structure to be modelled using the AEM.

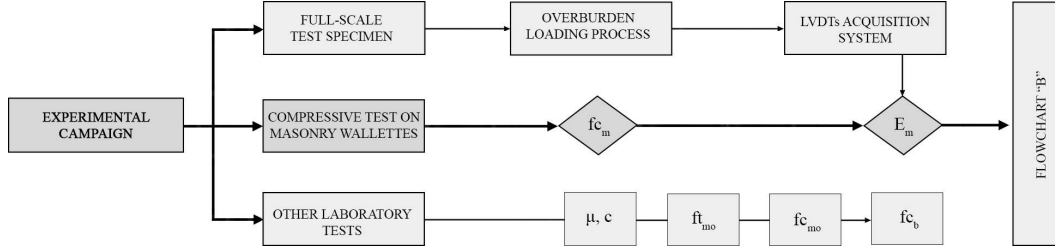


Figure 6 Flowchart A: masonry mechanical properties typically available and of use in a micro-modelling approach (adapted from Malomo et al. 2018)

1. *Obtain experimental properties of masonry, bricks and mortar.* The most commonly performed masonry material characterisation tests allow obtaining fundamental modelling parameters such as the compressive strength, Young's modulus, the friction coefficient and the cohesion of masonry (f_{c_m} , E_m , μ , c), brick and mortar compressive strength (f_{c_b} , $f_{c_{mo}}$), and the mortar tensile strength ($f_{t_{mo}}$).

2. *Infer Young's and shear modulus of bricks (E_b , G_b) from empirical formulae.* Depending on the brick type, a wide range of empirical relations, founded on experimental outcomes, can be selected. With reference to Jäger et al. (2004) and Kaushik et al. (2007), for CS and CL bricks respectively, the Young's modulus can be estimated using Eq. (11-12) by multiplying their compressive strengths by experimentally-derived constants as follows:

$$\text{CS} \quad E_b = (f_{c_b} \times 355) \quad (11) \quad \text{CL} \quad E_b = (f_{c_b} \times 375) \quad (12)$$

3. *Estimate Young's and shear modulus of mortar (E_{mo} , G_{mo}) from homogenisation formulae.* Since the Young's modulus of masonry and bricks are known, that of mortar can be computed by means of the Eqs. (13)-(16) reported below, often employed to develop a homogenisation process. In this work, all four equations described below, where ζ is the ratio of brick's height to the thickness of mortar joint, were used to infer E_{mo} , and then the ensuing average considered for the models. Furthermore, it is noted that the shear modulus G_{mo} was obtained assuming $G = E/(2(1 + \nu)) = 0.4E$ with $\nu = 0.25$, (Lekhnitskii 1963), because no experimental data for this specific parameter were available.

$$E_{mo} = \left(\frac{-4E_m E_b}{25E_m - 29E_b} \right) \quad (\text{Brooks and Baker 1998}) \quad (13)$$

$$E_{mo} = \left(\frac{E_m E_b}{E_b - 1.25\zeta(E_m - E_b)} \right) \quad (\text{Matysek and Janowski 1996}) \quad (14)$$

$$E_{mo} = \left(\frac{-E_m E_b}{5E_m - 6E_b} \right) \quad (\text{Ciesielski 1999}) \quad (15)$$

$$E_{mo} = \left(\frac{E_m E_b}{\zeta(E_m - E_b) + E_b} \right) \quad (\text{U.B.C. 1991}) \quad (16)$$

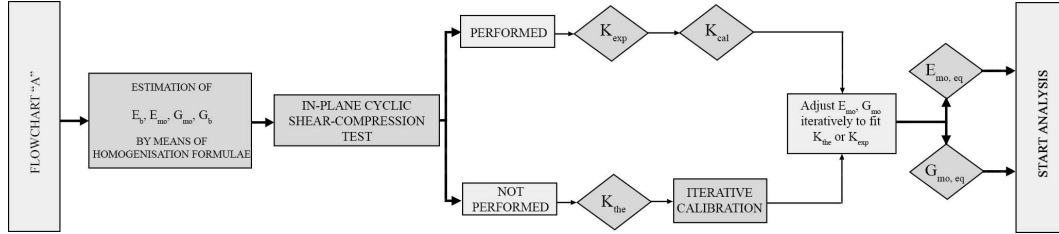


Figure 7 Flowchart B: calibration of equivalent values of E and G for the mortar in URM calcium silicate brick walls (adapted from Malomo et al. 2018)

4. Compute K_{the} and iteratively obtain values of equivalent properties of mortar ($E_{mo,eq}$, $G_{mo,eq}$). The “theoretical” initial lateral stiffness of piers can be evaluated for different boundary conditions (i.e. double-fixed, DF, and cantilevered, CL) using the formulae of Eq. (17), where δ is the lateral top displacement which is defined considering both flexural and shear response:

$$\delta_{DF} = \left(\frac{Hh^3}{12E_m} + \frac{Hh}{A_v G} \right), \quad \delta_{CL} = \left(\frac{Hh^3}{3E_m} + \frac{Hh}{A_v G} \right)$$

$$\text{with } \begin{cases} G = 0.4E \\ A = tL \\ A_v = 5/6A \end{cases} \Rightarrow K_{the} = \frac{H}{\delta} = \left(\frac{tE_m}{\left(\frac{h}{L} \right) \left(\omega \left(\frac{h}{L} \right)^2 + 3 \right)} \right) \quad (17)$$

Further, h is the height, L is the length and t is the thickness of the walls, H is the applied horizontal force, E_m is the Young’s modulus of the masonry and A_v is the shear area (equal to 5/6 of the actual lateral one, A). The parameter ω is equal to 1 in the case of double-fixed boundary conditions, whereas it can be set to 4 if a cantilevered element is contemplated. Once K_{the} is known, it can then be compared to the initial lateral wall stiffness computed by the uncalibrated AEM model. The values of E_{mo} and G_{mo} are then consequently and iteratively adjusted until the initial lateral stiffness obtained is considered to have reached an acceptable/satisfactory value; such final equivalent mortar E and G values are herein termed $E_{mo,eq}$ and $G_{mo,eq}$. The AEM modelling of the URM post-cracking behaviour is based on the elastic properties degradation, according to the criteria previously discussed. The abovementioned empirically-inferred values, and their calibrated counterparts, will be reported in the next dedicated section, i.e. when experimental outcomes will be compared with numerical predictions.

2.4 URM walls subjected to in-plane cyclic loading

Slender (i.e. CS1-2 and CL1-2-3) and squat (i.e. CS3 and CL4-5) full-scale wall specimens were tested in different experimental configurations at the laboratory of the European Centre for Training and Research in Earthquake Engineering (Eucentre, Pavia, Italy). The CS piers were characterised by a single leaf periodic arrangement (stretcher bond) of 212x103x71 mm³ CS brick units and 10 mm thick mortar joints. The CL piers, on the other hand, featured 208x100x50 mm³ CL brick units arranged in a so-called Dutch cross bond, leading to 208 mm thick double-wythe walls.

The mechanical properties of both the masonry types have been obtained through a wide range of characterisation tests (Graziotti et al. 2015, 2016c), including bending-compression, uniaxial compression, shear-compression and bond-wrench tests on both mortar and masonry samples, as depicted in Figure 8 for the case of CS masonry.

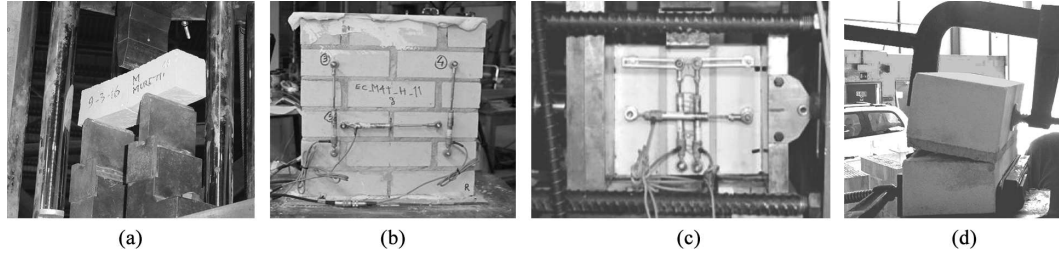


Figure 8 Mortar bending-compression test (a), compression (b), shear (c) and bond wrench test (d) on masonry samples (Graziotti et al. 2015)

In Table 1 below, the most relevant experimentally-derived masonry properties are reported in terms of mean values together with the associated coefficient of variations (C.o.V.).

Table 1 Experimental material properties of CS and CL masonries (Graziotti et al. 2015, 2016c)

	CS - $\delta_m = 1839$ [kg/m ³]						CL - $\delta_m = 1979$ [kg/m ³]					
	f_{c_m}	f_{c_b}	$f_{t_{m_0}}$	E_m	c	μ [-]	f_{c_m}	f_{c_b}	$f_{t_{m_0}}$	E_m	c	μ [-]
Mean [MPa]	6.20	18.67	0.24	4182	0.21	0.42	11.22	40	0.23	9833	0.15	0.55
C.o.V. [%]	7.04	13.67	16.32	33.27	-	-	7.43	11.21	60.11	25.42	-	-

The walls, characterised by various aspect ratios, were founded on a reinforced concrete (RC) beam clamped to the lab strong floor with post-tensioned steel bars, whereas the top RC beam, to which different overburden pressures were applied (see Table 2), was connected to the masonry piers by means of a layer of self-levelling high strength shrinkage-controlled gypsum to prevent sliding. The top lateral displacements were imposed by a horizontal servo-hydraulic actuator through a steel beam rigidly connected to the RC top-beam. Two horizontal servo-hydraulic actuators assured the boundary conditions, as well as the vertical compression. Furthermore, a restraining system was introduced in order to prevent out-of-plane deflection of the loading beam.

This notwithstanding, a spurious out-of-plane mode occurred during the first loading cycles of CS2, and the test was interrupted prematurely. For this reason, the modelling of the response of CS2 has not been included in this contribution, albeit it is available elsewhere (e.g. Malomo et al. 2018; Malomo and Pinho 2016). Similarly, since the only difference between CL5 and CL4 was the loading history (each cycle was repeated three times in CL4, as for all the specimens, whereas in CL5 only one cycle for target displacement was performed), the latter has not been modelled. Full details on both wall specimens and testing protocols can be found in Graziotti et al. (2015, 2016c).

Table 2 Test specimens: dimensions, vertical stress and boundary conditions

In-plane cyclic response of URM walls subjected to shear-compression quasi-static loading

Specimen ID	Length [m]	Height [m]	Thickness [m]	Overburden [MPa]	Boundary conditions
CS1	1.1	2.75	0.103	0.70	Fixed-Fixed
CS3	4.0	2.75	0.103	0.30	Cantilever
CL1	1.2	2.71	0.208	0.52	Fixed-Fixed
CL2	1.2	2.71	0.208	1.20	Fixed-Fixed
CL3	1.2	2.71	0.208	0.86	Fixed-Fixed
CL5	2.7	2.71	0.208	0.30	Fixed-Fixed

For each test, after imposing the vertical top compression, the loading history was applied in a displacement-controlled procedure, as reported in Table 3 and Table 4 in terms of target drift, where the last cycle performed is indicated by bold text. The tests were stopped when the walls lost their bearing capacity or in case of testing problems. CS1 initially exhibited rocking behaviour with horizontal cracks opening at the edges. Then, the cracks migrated towards the panel centre, reducing its effective height. Brick-crushing occurred in several CS units, leading to an unusually high energy dissipation, as further discussed in Graziotti et al. (2016b). The response of CS3 was mainly governed by shear mechanisms, with stepped cracks at the centre of the panel, sliding and shear failure through units.

Table 3 Displacement loading history for CS specimens. Adapted from (Graziotti et al. 2015)

	cycle	1	2	3	4	5	6	7	8	9	10	11
θ [‰]	CS1	0.19	0.26	0.39	0.51	0.76	1.01	1.51	2.02	2.53	3.03	4.04
	CS3	0.03	0.07	0.10	0.16	0.20	0.28	0.37	0.53	0.81	0.98	1.53
	cycle	12	13	14	15	16	17	18	19	20	21	22
θ [‰]	CS1	5.04	6.05	8.06	10.07	12.57	15.07	20.10	-	-	-	-
	CS3	2.06	2.53	3.06	-	-	-	-	-	-	-	-

CL brick masonry specimens, due to different dimensions and bond patters, mainly suffered flexure-governed failure modes. CL1 exhibited pure rocking behaviour during the whole test, with damage mainly due to masonry crushing mechanisms. The response of CL2 was characterised by diagonal joint sliding phenomena occurred during the last phases of the test in the bottom half of the pier. In the case of CL3, instead, a hybrid failure occurred (shear modes were observed after the attainment of the maximum flexural capacity of the pier). Although the wall exhibited intensive toe-crushing damage, flexural failure mechanisms were predominant. Finally, CL5 failed in shear, with diagonal stepped cracks visible in the left part of the panel, albeit base sliding damage was initially observed.

Table 4 Displacement loading history for CL specimens. Adapted from (Graziotti et al. 2016c)

	cycle	1	2	3	4	5	6	7	8	9	10	11
θ [‰]	CL1	0.16	0.27	0.51	0.55	0.77	1.08	1.55	2.09	2.60	3.10	4.14
	CL2	0.13	0.31	0.39	0.53	0.78	1.02	1.53	2.04	2.55	3.06	4.10
	CL3	0.15	0.31	0.37	0.49	0.74	0.99	1.51	2.01	2.52	3.03	4.02
	CL5	0.03	0.06	0.13	0.2	0.3	0.51	1.01	2.01	3.01	4.02	6.03
	cycle	12	13	14	15	16	17	18	19	20	21	22
θ [‰]	CL1	5.15	6.19	8.19	10.22	12.76	15.30	20.36	25.45	30.50	40.68	-
	CL2	5.11	6.12	8.14	10.18	12.73	-	-	-	-	-	-
	CL3	5.02	6.04	8.08	10.11	12.65	-	-	-	-	-	-
	CL5	8.04	10.05	15.28	14.34	-	-	-	-	-	-	-

Based on damage observations, the governing failure modes, as the mid-height shear failure depicted in Figure 9 for the case of CS3, were summarised in Table 5 for each specimen.

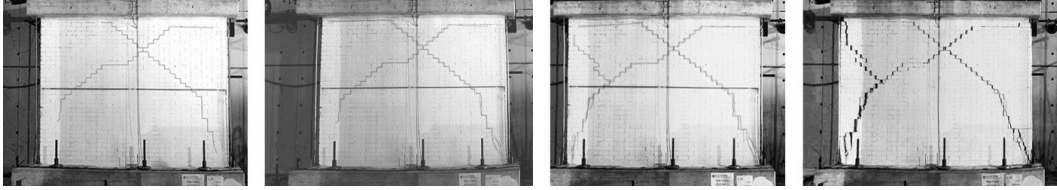


Figure 9 Experimental damage evolution of specimen CS3 (Graziotti et al. 2015)

More details regarding the experimental response in terms of lateral capacity, dissipated energy and initial stiffness will be given in the next section, together with their numerical counterparts.

Table 5 Experimental failure mechanisms / damage pattern

Specimen ID	Experimental failure mode / damage
CS1	Masonry crushing
CS3	Mid-height shear failure
CL1	Masonry crushing / base sliding
CL2	Flexural-shear failure
CL3	Flexural failure / masonry crushing
CL5	Base sliding / shear failure

2.5 Simulation of tests on both calcium silicate and brick masonry panels

A brick mesh-based modelling approach, whereby one discrete element is assigned to each brick, was initially employed, thus faithfully reproducing the experimental arrangement of the specimens' brick units. An additional discretisation was then also applied by subdividing the elements along their vertical axis with a view to try to better capture the brick splitting phenomena that was observed during the tests (the impact on the results of such refinement was however very mild). Each surface of a given rigid element was connected to the adjacent one by means of 25 springs, as depicted in Figure 10 below.

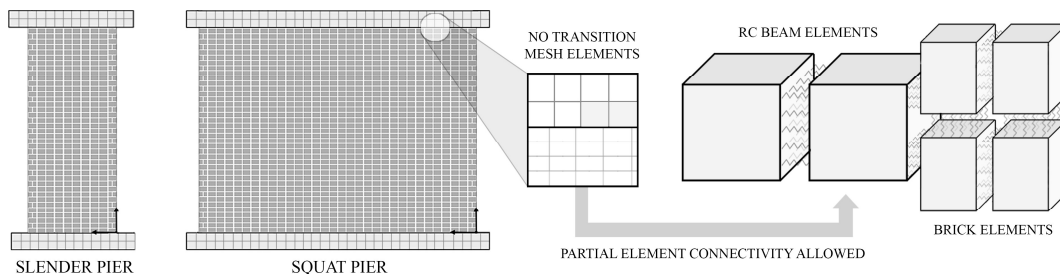


Figure 10 Screenshot of the AEM models and partial connectivity among elements (adapted from Malomo et al. 2018)

The loading and foundation RC beams were explicitly modelled, assuming a linear elastic response of their constituent material. As shown in Figure 10, in order to decrease the computational burden, a coarser mesh was assigned to the RC beams; it is noted that the

AEM, unlike other methods (such as the FEM), does not need a mesh transition from large-size elements to small elements, since partial connectivity between units is allowed.

2.5.1 Preliminary results obtained with uncalibrated mechanical properties

The values of E and G for brick and mortar as obtained by using the empirical equations reported in (11)-(16) are presented in Table 6.

Table 6 Summary of the inferred uncalibrated material properties of masonry components

Masonry type	E_b [MPa]	G_b [MPa]	E_{mo} [MPa]	G_{mo} [MPa]
CS	6628	2651	1415	566
CL	15000	6000	4042	1617

For the slender walls made of both CS and CL brick masonries (i.e. CS1, CL1-2-3), the corresponding preliminary AEM models (i.e. models built using the above experimental/inferred material properties, which have not been iteratively calibrated through the procedure proposed in this work) showed initial lateral stiffness (K_{pre}) values that overestimate the experimentally recorded values, as shown in Table 7. In addition, most of these preliminary models exhibited an early collapse (see Figure 11(a)), due to a premature compressive failure of the mortar interface springs, caused by the fact that the effect of confinement was not considered (i.e. the compressive strength of mortar was used).

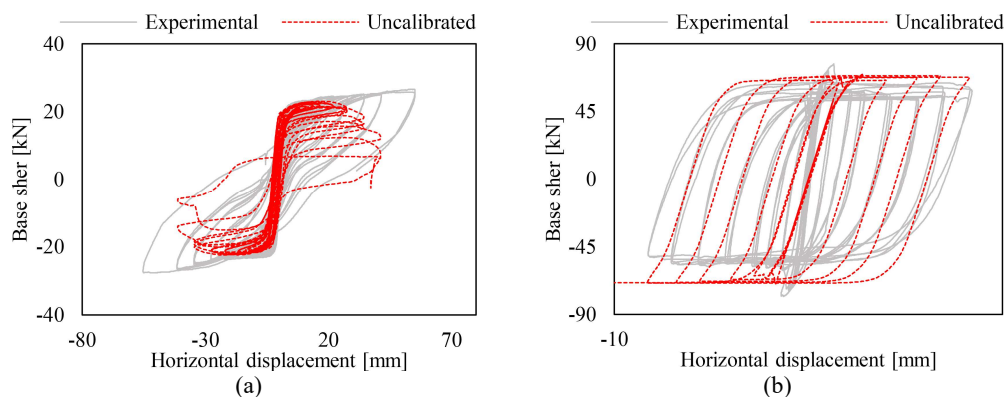


Figure 11 Comparison between preliminary and experimental results of (a) CS1 and (b) CL5

For what concerns instead the squat walls (i.e. CS3 and CL5), both the preliminary models showed an initial lateral stiffness K_{pre} that underestimates the experimental recorded value, and exhibited a pure shear behaviour that not properly accounted for the initial rocking mechanisms, thus predicting a shear capacity slightly higher than that of the test specimens, as depicted in Figure 11 (b) for the case of CS3.

2.5.2 Results obtained with calibrated mechanical properties

The calibration procedure proposed starts with the computation of the “theoretical” initial lateral stiffness (K_{the}) through the use of Eq. (17), after which values of equivalent E and G for the mortar ($E_{mo,eq}$, $G_{mo,eq}$) are iteratively determined so that the initial lateral stiffness given by the AEM model K_{cal} is similar to K_{the} .

The underlying rationale behind such approach is that K_{the} provides a relatively reliable estimate of the actual stiffness of the masonry wall/pier, notwithstanding the simplified assumptions and approximations that are at the basis of the derivation of Eq. (17), such as:

- the expression $G = 0.4E$ has inherent variability attached to it
- the value of E_m is not strictly constant, but rather varies as a function of the overburden and deformation level
- actual boundary conditions may differ slightly from perfect cantilever or full-fixity

And indeed, the comparison between the values of “theoretical” and experimental initial lateral stiffness included in Table 7 can be considered as relatively satisfactory, with the above limitations in mind. This is reassuring, given that it implies that in those (typical) cases where experimental data is not available, the employed formulae can be used with some degree of confidence. To further demonstrate this point, in the current modelling effort the mortar equivalent material properties were iteratively calibrated against K_{the} , rather than considering K_{exp} (which in this specific case was available and could have been employed).

Table 7 Comparison between experimental, theoretical, preliminary and calibrated numerical initial stiffness and associated Young’s and shear moduli

Specimen ID	K_{exp} [kN/mm]	K_{pre} [kN/mm]	K_{the} [kN/mm]	K_{cal} [kN/mm]	$E_{mo,eq}$ [MPa]	$G_{mo,eq}$ [MPa]
CS1	22.9	30.4	18.4	21	4700	1880
CS3	152.4	102.1	127.2	144	4500	1800
CL1	66.2	137.1	110.8	72.3	5150	2060
CL2	120.5	183.1	97.9	108.4	4878	1951
CL3	79.2	85	95.1	72	4131	1652
CL5	361.5	346	458.3	367	3102	1463

In what follows, starting from the slender walls, the numerical hysteretic responses are presented, also comparing them with their experimental counterparts (for which a detailed description of the observed lab response can be found in Graziotti et al. 2015, 2016c).

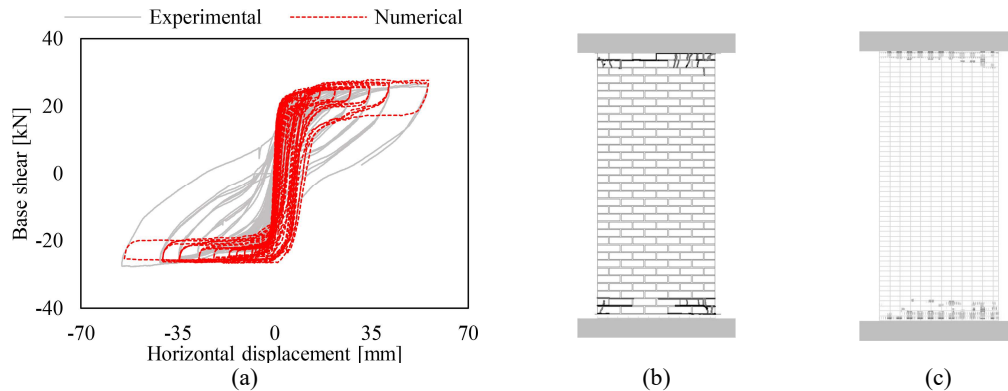


Figure 12 CS1: Experimental vs numerical hysteresis (a), experimental (b) and numerical damage (c)

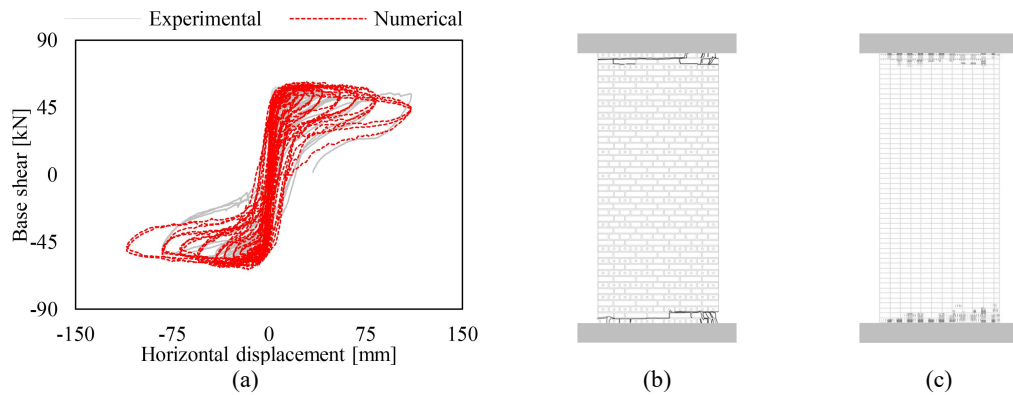


Figure 13 CL1: Experimental vs numerical hysteresis (a), experimental (b) and numerical damage

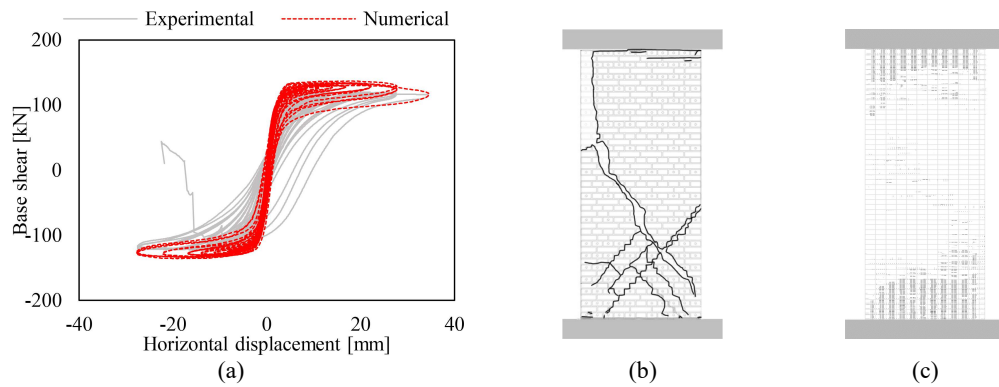


Figure 14 CL2: Experimental vs numerical hysteresis (a), experimental (b) and numerical damage

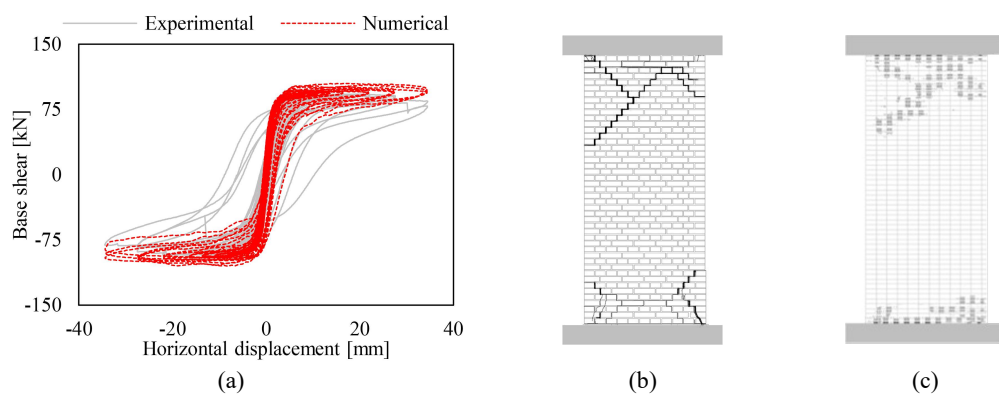


Figure 15 CL3: Experimental vs numerical hysteresis (a), experimental (b) and numerical damage

As it can be observed from Figure 12 to Figure 15 above, where the predictions referred to the slender walls are reported, the numerical models were able to capture relatively well the shear/displacement capacity of the test specimens, as well as their (rocking-governed) response mode and corresponding crack pattern. On the other hand, however, and with the exception of specimen CL2, the numerical models struggled to adequately reproduce the shape of the hysteretic curves of the specimens (i.e. their energy dissipation), an issue that, even if not unusual in the modelling of masonry walls subjected to rocking, does warrant further scrutiny in the future.

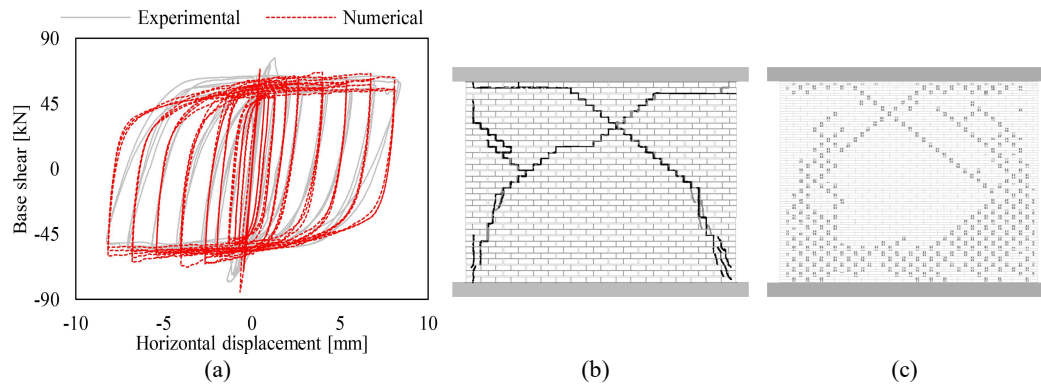


Figure 16 CS3: Experimental vs numerical hysteresis (a), experimental (b) and numerical damage

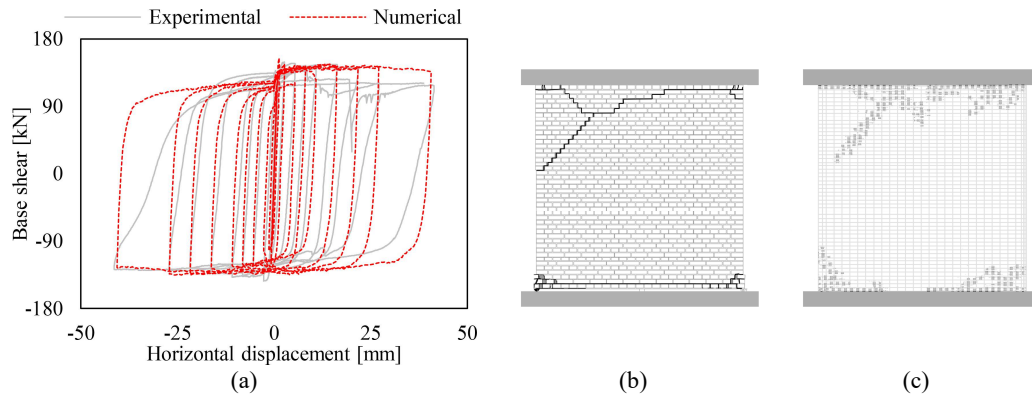


Figure 17 CL5: Experimental vs numerical hysteresis (a), experimental (b) and numerical damage

Contrary to what happened with their slender counterparts, the squat wall AEM models did manage to capture the energy dissipation of the test specimens adequately, in addition to their displacement/shear capacity and failure mode, as depicted in Figure 16 and Figure 17 above.

It is however worth noting that the perfect matching of the experimental results, and in particular of the associated X-stepped crack patterns, did require a somewhat empirical adjustment of the default values of so-called normal (NSF) and shear (SSF) post-failure stiffness of the interface springs, in order to accentuate the development of the diagonal shear crack pattern. In the code employed in this work, their default values for mortar material are both set to 0.01 (which is what one expects in a homogeneous material), typically implying pure sliding of elements once a crack is formed (although this depends also on material properties and loading configuration), and thus preventing, in some cases, the capturing of eventual diagonal shear crack development.

Therefore, and in particular for the case of squat piers, where shear crack propagation is expected, it may result opportune for the aforementioned default values to be modified, as discussed further below. Indeed, in the modelling of the two squat wall specimens (CS3 and CL5), since hand calculations showed a likelihood for shear failure to occur, the value of NSF was increased to a value close to unity (0.95, i.e. essentially no normal stiffness degradation after cracking, and hence no premature compression failure of the normal

springs located at wall mid-height, where shear cracks are expected to develop), whilst SSF was increased by a factor of 10 (0.1, i.e. a reasonable value for a heterogeneous material).

However, it is worth mentioning that reasonable results, at least in terms of hysteretic curves, can be also obtained without the introduction of such adjustments, as shown in Figure 18 below for both CS3 and CL5.

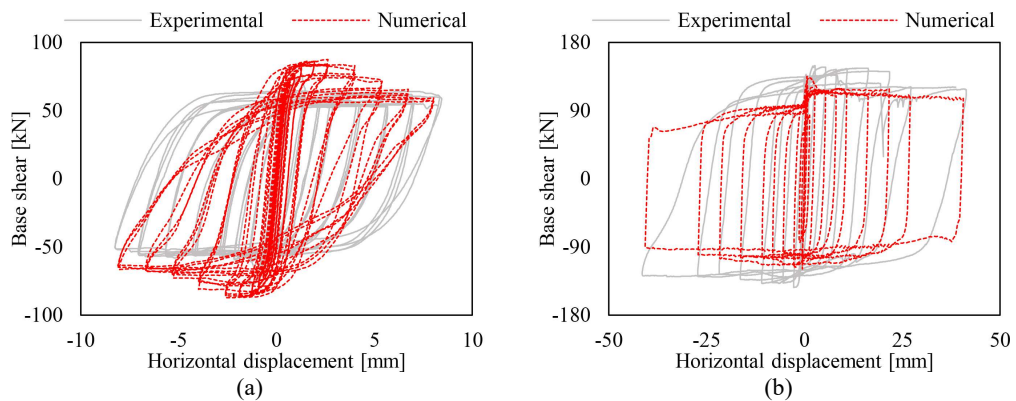


Figure 18 Experimental hysteretic response of (a) CS3 and (b) CL5 and their numerical counterparts obtained with standard values of both NSF and SSF

Indeed, observing the results obtained for CS3 using the model with standard values of NSF and NSF, it is clear that the global response of the specimen was adequately captured, both in terms of capacity and stiffness. The predicted behaviour, if compared to the experimental one, is characterised by a more pronounced rocking-bending response of the first cycles, whilst the pure shear mechanism starts afterwards, with lower dissipated energy. When applying an analogous approach for the modelling of the response of CL5, instead, the initial flexural mechanism was not accounted properly, leading to a significant underestimation of the lateral capacity. However, the shear-governed failure mode, adequately captured by the model, resulting in an acceptable prediction of dissipated energy.

The positive impression on the numerical vs. experimental comparison reported above is further confirmed by the comparisons shown in Table 8 below, where it can be observed that the AEM models estimated values of both maximum capacity and dissipated energy that feature differences with respect to the tests observations in an acceptable range.

Table 8 Comparison between experimental results of (a) CS3 and (b) CL5 and their numerical counterparts obtaining with standard values of both NSF and SSF

Specimen ID	Experimental			Numerical		
	V_{max}^+ [kN]	V_{max}^- [kN]	E_h [kJ]	V_{max}^+ [kN]	V_{max}^- [kN]	E_h [kJ]
CS1	26.5	-27.6	13.7	27.9	-26.7	8.7
CS3	76.7	-78.0	14.4	83.7	-67.4	16.1
CS3 – no post-stiffs. adjs.	76.7	-78.0	14.4	87.3	-87.0	14.6
CL1	59.1	-58.4	29.8	61.4	-61.1	31.8
CL2	119.9	-122.6	19.1	135.4	-136.5	18.1

CL3	92.5	-92.5	20.8	103.6	-104.5	17.4
CL5	148.1	-142.8	57.8	154.4	-135.3	59.4
CL5 – no post-stiffs. adjs.	148.1	-142.8	57.8	97.6	-119.1	51.3

2.6 Conclusions

The Applied Element Method (AEM) is a modelling technique based on the mechanical interaction between rigid bodies, which are connected by means of spring layers, where the material properties are lumped. The AEM was already employed in some applications concerning the simulations of URM structures (mostly large-scale buildings not experimentally tested), as well as the in-plane quasi-static response of URM components. Nevertheless, the mechanical performance of calcium silicate brick masonry has never been investigated using this numerical approach, as well as the response of Dutch-cross bond double-wythe elements. Moreover, neither a specific calibration procedure nor a careful validation against a series of experimental results is currently available in literature. The latter highlighted the advantages of a proper adjustment of the initial material properties assigned to the spring interfaces, through a methodology that is applicable to the general and common case of when no experimental results are available.

In this endeavour thus, the numerical prediction of the in-plane cyclic response of both calcium-silicate and clay brick unreinforced masonry walls using the AEM was discussed and scrutinised, through comparison against laboratory test results. Validation of this numerical approach was undertaken by an attempt to reproduce the results of in-plane shear-compression tests on six different full-scale specimens, made both of calcium-silicate and clay bricks. For the definition of the material mechanical properties of brick and mortar, a pre-processing methodology, founded on theoretical and empirical techniques able to infer such physical quantities, was elaborated. For this purpose, several expressions (mainly referred to the masonry homogenisation theory) were considered and reviewed, showing how some masonry properties (i.e. Young's and shear modulus of mortar) can be iteratively and readily calibrated to enhance the modelling results, even in the nonlinear range. Moreover, it is worth noting the advantages of a "global" calibration method (e.g. considering the wall lateral stiffness as a target parameter rather than local-scale physical quantities), whereby the additional modelling of characterisation tests is not necessarily needed.

The AEM models presented in this work captured with varying levels of accuracy the hysteretic response, the energy dissipation and the crack patterns of the test specimens. The results, whilst relatively satisfactorily as a whole, also showed that improvements are warranted. Such possible enhancements are currently being explored, as is the extension and verification of this modelling approach to different loading conditions (including out-of-plane dynamic loading) and more complex structures.

Acknowledgements

The work described in this paper was carried out within the framework of the research programme on hazard and risk of induced seismicity in the Groningen region, sponsored by the Nederlandse Aardolie Maatschappij BV (NAM). The authors also acknowledge all

those at the European Centre for Training and Research in Earthquake Engineering (EUCENTRE, Pavia, Italy) that were involved in the testing campaign referred to in this paper, as well as the technical support staff from Applied Science International LLC (ASI), for the guidance on the use of the employed AEM.

References

- Addessi, D., Mastrandrea, A., and Sacco, E. (2015). "A force-based equivalent frame element for push-over analysis of masonry structures." *Key Engineering Materials*, 624, 405–412.
- Asteris, P. G., Sarhosis, V., Mohebkhah, A., Plevris, V., Papaloizou, L., Komodromos, P., and Lemos, J. V. (2015). "Numerical modeling of historic masonry structures." *Handbook of research on seismic assessment and rehabilitation of historic structures*, IGI Global, 213–256.
- Bakeer, T. T. (2009). "Collapse analysis of masonry structures under earthquake actions." PhD Thesis - Technical University of Dresden.
- Block, P., Ciblac, T., and Ochsendorf, J. (2006). "Real-time limit analysis of vaulted masonry buildings." *Computers & Structures*, Elsevier, 84(29), 1841–1852.
- Braga, F., and Dolce, M. (1982). "A method for the analysis of antiseismic multi-storey masonry buildings (In Italian)." *Proceedings of the 6th International Brick Masonry Conference*, Rome, 1088–99.
- Brooks, J. J., and Baker, A. (1998). "Modulus of Elasticity of Masonry." *Masonry International*, 12(2), 58–63.
- Casolo, S. (2000). "Modelling the out-of-plane seismic behaviour of masonry walls by rigid elements." *Earthquake Engineering & Structural Dynamics*, Wiley-Blackwell, 29(12), 1797–1813.
- Casolo, S. (2009). "Macroscale modelling of microstructure damage evolution by a rigid body and spring model." *Journal of Mechanics of Materials and Structures*, 4(3), 551–570.
- Chen, S.-Y., Moon, F. L., and Yi, T. (2008). "A macroelement for the nonlinear analysis of in-plane unreinforced masonry piers." *Engineering Structures*, Elsevier, 30(8), 2242–2252.
- Chetouane, B., Dubois, F., Vinches, M., and Bohatier, C. (2005). "NSCD discrete element method for modelling masonry structures." *International journal for numerical methods in engineering*, Wiley-Blackwell, 64(1), 65–94.
- Ciesielski, R. (1999). "The dynamic module of elasticity of brick walls." *Proceedings of the Conference of the Committee of Civil Engineering PZITB: Lublin, Poland*.
- Costa, A. A., Penna, A., Arède, A., and Costa, A. (2015). "Simulation of masonry out-of-plane failure modes by multi-body dynamics." *Earthquake Engineering & Structural Dynamics*, Wiley-Blackwell, 44(14), 2529–2549.
- Cundall, P. A. (1971). "A computer model for simulating progressive large scale movements in blocky rock systems." *Proc. Symp. Rock Fracture (ISRM)*, Nancy.
- Cundall, P. A., and Hart, R. D. (1992). "Numerical modelling of discontinua." *Engineering computations*, 9(2), 101–113.
- D'Ayala, D., and Speranza, E. (2003). "Definition of collapse mechanisms and seismic vulnerability of historic masonry buildings." *Earthquake Spectra*, 19(3), 479–509.
- DeJong, M. J., and Dimitrakopoulos, E. G. (2014). "Dynamically equivalent rocking structures." *Earthquake Engineering & Structural Dynamics*, Wiley-Blackwell,

- 43(10), 1543–1563.
- DeLorenzis, L., DeJong, M. J., and Ochsendorf, J. A. (2007). “Failure of masonry arches under impulse base motion.” *Earthquake Engineering & Structural Dynamics*, Wiley-Blackwell, 36(14), 2119–2136.
- van Elk, J., Bourne, S. J. S., Oates, S. J. S., Bommer, J. J. J., Pinho, R., and Crowley, H. (2018). “A probabilistic model to evaluate options for mitigating induced seismic risk.” *Earthquake Spectra - submitted for publication*.
- Furukawa, A., Kiyono, J., and Toki, K. (2012). “Numerical simulation of the failure propagation of masonry buildings during an earthquake.” *Journal of Natural Disaster Science*, Japan Society for Natural Disaster Science, 33(1), 11–36.
- Graziotti, F., Penna, A., and Magenes, G. (2016a). “A nonlinear SDOF model for the simplified evaluation of the displacement demand of low-rise URM buildings.” *Bulletin of Earthquake Engineering*, Springer, 14(6), 1589–1612.
- Graziotti, F., Rossi, A., Mandirola, M., Penna, A., and Magenes, G. (2016b). “Experimental characterization of calcium-silicate brick masonry for seismic assessment.” *Proceedings of 16th International brick/block masonry conference*, Padua, Italy.
- Graziotti, F., Tomassetti, U., Rossi, A., Kallioras, S., Mandirola, M., Cenja, E., Penna, A., and Magenes, G. (2015). *Experimental campaign on cavity-wall systems representative of the Groningen building stock - Report n. EUC318/2015U*. Pavia, Italy.
- Graziotti, F., Tomassetti, U., Rossi, A., Marchesi, B., Kallioras, S., Mandirola, M., Fragomeli, A., Mellia, E., Peloso, S., Cuppari, F., Guerrini, G., Penna, A., and Magenes, G. (2016c). *Experimental campaign on a clay URM full-scale specimen representative of the Groningen building stock - Report n. EUC128/2016U*. Pavia, Italy.
- Guragain, R., Worakanchana, K., Mayorca, P., and Meguro, K. (2006). “Simulation of brick masonry wall behavior under cyclic loading using applied element method.” *Bulletin of ERS*, Institute of Industrial Science The University of Tokyo, 58(6), 531–534.
- Heyman, J. (1966). “The stone skeleton.” *International Journal of solids and structures*, Elsevier, 2(2), 249IN1257IN5265--256IN4264IN12279.
- Jäger, W., Irmschler, H., and Schubert, P. (2004). *Mauerwerk-Kalender 2004*. Ernst & Sohn Verlag für Architektur und technische Wissenschaften.
- Jean, M. (1999). “The non-smooth contact dynamics method.” *Computer methods in applied mechanics and engineering*, Elsevier, 177(3), 235–257.
- Karbassi, A., and Nollet, M.-J. (2013). “Performance-based seismic vulnerability evaluation of masonry buildings using applied element method in a nonlinear dynamic-based analytical procedure.” *Earthquake Spectra*, Earthquake Engineering Research Institute, 29(2), 399–426.
- Kaushik, H. B., Rai, D. C., and Jain, S. K. (2007). “Stress-strain characteristics of clay brick masonry under uniaxial compression.” *Journal of materials in Civil Engineering*, American Society of Civil Engineers, 19(9), 728–739.
- Kawai, T. (1978). “New discrete models and their application to seismic response analysis of structures.” *Nuclear Engineering and Design*, Elsevier, 48(1), 207–229.
- Khoo, C. L., and Hendry, A. W. (1973). “Strength tests on brick and mortar under complex stresses for the development of a failure criterion for brickwork in compression.” *Proceedings of the British Ceramic Society*, 51–66.
- Lagomarsino, S., Penna, A., Galasco, A., and Cattari, S. (2013). “TREMURI program: an

- equivalent frame model for the nonlinear seismic analysis of masonry buildings.” *Engineering Structures*, Elsevier, 56, 1787–1799.
- Lekhnitskii, S. G. (1963). *Of an anisotropic elastic body*. Holden-Day, San Francisco, USA.
- Lemos, J. V. (2007). “Discrete element modeling of masonry structures.” *International Journal of Architectural Heritage*, 1(2), 190–213.
- Lourenço, P. B. (2002). “Computations on historic masonry structures.” *Progress in Structural Engineering and Materials*, Wiley-Blackwell, 4(3), 301–319.
- Lourenço, P. B., and Ramos, L. F. (2004). “Characterization of Cyclic Behavior of Dry Masonry Joints.” *Journal of Structural Engineering*, 130(5), 779–786.
- Lourenço, P. B., Rots, J. G. J. G., and Blaauwendraad, J. (1995). “Two approaches for the analysis of masonry structures - micro and macro-modeling.” *Research article HERON - Delft Univ. of Technology (Delft, The Netherlands)*, 40(4), 313–340.
- Malomo, D., and Pinho, R. (2016). *AEM modelling of URM walls subjected to in-plane cyclic shear-compression using Extreme Loading for Structures - Report D4 - Mosayk Ltd*. Pavia, Italy.
- Malomo, D., Pinho, R., and Penna, A. (2018). “Using the applied element method for modelling calcium silicate brick masonry subjected to in-plane cyclic loading.” *Earthquake Engineering & Structural Dynamics*, 47(7), 1610–1630.
- Matysek, P., and Janowski, Z. (1996). “Analysis of factors affecting the modulus of elasticity of the walls.” *Proceedings of the Conference of the Committee of Civil Engineering PZITB: Lublin, Poland*.
- Mayorca, P., and Meguro, K. (2003). “Modeling masonry structures using the applied element method.” *Seisan-Kenkyu*, 55(6), 581–584.
- Meguro, K., and Tagel-Din, H. (2000). “Applied element method for structural analysis: Theory and application for linear materials.” *Structural Engineering/Earthquake Engineering*, 17(1).
- Meguro, K., and Tagel-Din, H. (2001). “Applied Element Simulation of RC Structures under Cyclic Loading.” *Journal of Structural Engineering*, 127(11), 1295–1305.
- Meguro, K., and Tagel-Din, H. (2002). “Applied Element Method Used for Large Displacement Structural Analysis.” *Journal of Natural Disaster Science*, 24(1), 25–34.
- Milosevic, J., Lopes, M., Bento, R., and Gago, A. S. (2012). “Triplet test on rubble stone masonry panels.” *Proceedings of the 15th World Conference on Earthquake Engineering*, Lisbon, Portugal.
- Moreau, J. J. (1988). “Unilateral contact and dry friction in finite freedom dynamics.” *Nonsmooth mechanics and Applications*, Springer, 1–82.
- Pandey, B. H., and Meguro, K. (2004). “Simulation of Brick masonry wall behavior under in plane lateral loading using applied element method.” *13th World conference on earthquake engineering, Vancouver, BC, Canada, August*.
- Parisi, F., and Augenti, N. (2012). “A shear response surface for the characterization of unit-mortar interfaces.” *Proceedings of the 15th International Brick and Block Masonry Conference*, Florianópolis, Brazil.
- Penna, A., Lagomarsino, S., and Galasco, A. (2014). “A nonlinear macroelement model for the seismic analysis of masonry buildings.” *Earthquake Engineering & Structural Dynamics*, Wiley-Blackwell, 43(2), 159–179.
- Van der Pluijm, R. (1993). “Shear behaviour of bed joints.” *Proceedings of the 6th North American Masonry Conference*, Philadelphia, USA.

- Portioli, F., and Cascini, L. (2016). "Contact Dynamics of Masonry Block Structures Using Mathematical Programming." *Journal of Earthquake Engineering*, Taylor & Francis, 1–32.
- Rafiee, A., Vinches, M., and Bohatier, C. (2008a). "Application of the NSCD method to analyse the dynamic behaviour of stone arched structures." *International Journal of Solids and Structures*, Elsevier, 45(25), 6269–6283.
- Rafiee, A., Vinches, M., and Bohatier, C. (2008b). "Modelling and analysis of the Nimes arena and the Arles aqueduct subjected to a seismic loading using the Non-Smooth Contact Dynamics method." *Engineering Structures*, Elsevier, 30(12), 3457–3467.
- Raka, E., Spacone, E., Sepe, V., and Camata, G. (2015). "Advanced frame element for seismic analysis of masonry structures: model formulation and validation." *Earthquake Engineering & Structural Dynamics*, Wiley-Blackwell, 44(14), 2489–2506.
- Roca, P., Cervera, M., Gariup, G., and others. (2010). "Structural analysis of masonry historical constructions. Classical and advanced approaches." *Archives of Computational Methods in Engineering*, Springer, 17(3), 299–325.
- Shi, G. H., and Goodman, R. E. (1988). "Discontinuous deformation analysis—a new method for computing stress, strain and sliding of block systems." *The 29th US Symposium on Rock Mechanics (USRMS)*.
- Tagel-Din, H., and Meguro, K. (1998). "Consideration of Poisson's ratio effect in structural analysis using elements with three degrees of freedom." *Bull. of Earthquake Resistant Struct. Res. Ctr*, 31, 41–50.
- Tomažević, M. (1987). "Dynamic modelling of masonry buildings: storey mechanism model as a simple alternative." *Earthquake Engineering & Structural Dynamics*, Wiley-Blackwell, 15(6), 731–749.
- Tondelli, M., Beyer, K., and DeJong, M. (2016). "Influence of boundary conditions on the out-of-plane response of brick masonry walls in buildings with RC slabs." *Earthquake Engineering & Structural Dynamics*, Wiley-Blackwell.
- U.B.C. (1991). "International Conference of Building Officials. Uniform Building Code." *International conference of building officials, USA*, Whittier, USA.
- Van Zijl, G. (1996). *Shear transfer across bed joints in masonry: A numerical study - Technical Report - Delft University of Technology*. Delft, The Netherlands.

CHAPTER 3

Out-of-plane dynamic behaviour of URM assemblies
in both one way and two-way bending conditions



CHAPTER 3 Out-of-plane dynamic behaviour of URM assemblies in both one way and two-way bending conditions

Malomo D., Comini P., Pinho R., Penna A. (2018). “Validating numerical modelling of out-of-Plane dynamic response of masonry walls through comparison with full-scale shake-table.” *Journal of Structural Engineering*, ASCE, to be submitted.

Abstract. Structural failure of existing unreinforced masonry buildings, when subjected to earthquake loading, is often caused by the out-of-plane response of masonry walls. The out-of-plane resistance of such masonry assemblies could vary considerably depending on several factors, such as boundary conditions, vertical overburden and construction technique. Amongst the latter, the cavity-wall system, originally introduced in Northwest Europe in the 19th century and then spread to several world countries including USA and Canada, China, Australia and New Zealand, has been shown to be particularly vulnerable towards out-of-plane actions. In this work, the use of a relatively new addition to the discrete elements analysis family, the Applied Element Method, was investigated and subsequently considered for reproducing the experimentally observed out-of-plane shake-table response of unreinforced masonry full-scale cavity-wall specimens subjected to both one-way and two-way bending.

Keywords: applied element method; numerical modelling; out-of-plane; shake-table; unreinforced masonry.

3.1 Introduction

The out-of-plane (OOP) failure of unreinforced masonry (URM) elements might cause significant damage due to the separation between transversal and longitudinal walls, as well as the lack or ineffectiveness of the mechanical connections amongst façades and diaphragms. Moreover, it precludes the exploitation of global capacity associated with the in-plane resistance of the structural walls, often leading to an early collapse of the structural system (e.g. D’Ayala et al. 1997; Dizhur et al. 2011; Ingham and Griffith 2010; Penna et al. 2014b).

Notwithstanding the above, relatively limited work has been carried out over the years on the verification and validation of numerical approaches for the modelling of OOP dynamic response of URM walls, as discussed further in the subsequent section. This is probably related to the fact that the necessary experimental data was up until recently not available, with only a few dynamic tests having been carried out (e.g. ABK 1981; Graziotti et al. 2016, 2018; Griffith et al. 2004; Meisl et al. 2007; Penner and Elwood 2016), and confined

to the cases of single leaf panels/façades tested in one-way bending conditions. Research on the two-way bending mechanism had instead been limited to quasi-static airbag tests on full-scale specimens (Derakhshan et al. 2018; Griffith et al. 2007), inclined platforms (Restrepo Vélez et al. 2014) and dynamic shake-table tests on both reduced-scale (e.g. Maccarini et al. (2018) and Vaculik and Griffith (2017b)) and full-scale (Candeias et al. 2017; Costa et al. 2013) brick and stone masonry subcomponents, whilst no dynamic two-way bending tests on cavity-walls were available in the literature up until the recently work of Graziotti et al. (2018).

This work therefore attempts to address the aforementioned knowledge gap, by modelling a series of full-scale URM wall specimens tested under dynamic excitation by the latter researchers. Such tests feature both one-way bending, as well as two-way bending response conditions, and consider also single-leaf and cavity-walls, using both calcium-silicate (CS) and clay (CL) bricks. Further, different axial load levels and boundary conditions are taken into account, as is the presence of openings. The adopted modelling approach (Applied Element Method), discussed and described in detail in subsequent sections of this paper, is shown to be able to adequately capture the OOP dynamic response of the different URM walls considered, tested under several combinations of boundary conditions, geometrical configurations and vertical pressures, estimating with relatively satisfactory accuracy both their base shear capacity, as well as failure mode.

3.2 Overview of typically-employed URM modelling approaches

Despite the increasing interest in both understanding and assessing the OOP response of URM elements, most of the commonly employed modelling approaches tend to tackle such phenomena by making use of relatively simplified assumptions. Moreover, notwithstanding some promising recent developments by Tomassetti et al. (2018) and Vaculik and Griffith (2017a), the analytical expressions available in literature for both one-way (Derakhshan et al. 2013, 2014; Godio and Beyer 2017; Sorrentino et al. 2008) and two-way bending conditions (Derakhshan et al. 2018; Shawa et al. 2012) are mainly applicable only to very simple geometries, idealised boundary conditions and load cases. Making use of mathematical programming, the employment of these equations can be extended successfully to the modelling of the dynamic response of blocky assemblies, as demonstrated by Costa et al. (2015) and D'Ayala and Shi (2011). Interested readers may refer to e.g. Ferreira et al. (2015) and Sorrentino et al. (2017), where a comprehensive review of these methods is presented.

Considering URM structures at the building scale, instead, several computational methodologies of different levels of complexity and computational burden have been developed for reproducing numerically the behaviour of large-scale masonry assemblies. The macroelement modelling strategy, typically implemented in equivalent-frame models (e.g. Addressi et al. 2015; Chen et al. 2008; Penna et al. 2014a; Raka et al. 2015), represents an acceptable compromise between accuracy and required analysis time. However, notwithstanding the effectiveness of these approaches in predicting the in-plane response of URM elements, the influence of the OOP mechanisms is usually neglected. In order to overcome this limitation, different upgrades to this original scheme were implemented and validated by e.g. Kallioras et al. (2018), who proposed a simplified procedure for

accounting implicitly the mechanical contribution of OOP-loaded URM components. However, both crack propagation and debris areas cannot be estimated using the latter modelling techniques. On the other hand, the use of hybrid discrete-macro element models seems to be promising, as proved by some recent applications (e.g. Cannizzaro and Lourenço 2017), albeit numerical simulations of the dynamic response of tested full-scale URM wall specimens is not presently available in literature.

More refined numerical approaches based on homogenisation theory and continuum domain have also been developed for the simulation of URM structures subjected to OOP loading. Several numerical applications concerning the use of the Finite Element Method (FEM), amongst others, are available in literature (e.g. Milani et al. 2007; Noor-E-Khuda et al. 2016), of which an exhaustive review can be found in Abrams et al. (2017), Lourenço (2009) and Roca et al. (2010). Despite being widely employed and extended, intrinsic limitations of these FEM-based approaches, and their hybrid methods counterparts, make the simulation of the OOP response of large-scale composite structures still extremely challenging, as shown by the recent work of e.g. AlShawa et al. (2017) and Chácara et al. (2017). Moreover, with the exception of the latter, most of them have been applied to the investigation of the quasi-static (cyclic or monotonic) OOP performance of URM components (e.g. Maccarini et al. 2018).

A different numerical approach, which intrinsically accounts for the mechanical interaction between units and mortar, is instead the discontinuum-based models. In such framework, the use of the Distinct Element Method (DEM) has in the past been extensively investigated, especially for the case of dry-joints between units. Initially conceived for simulating soil and rock mechanics in the early seventies (Cundall 1971), it makes use of zero-thickness spring layers to describe the interaction between adjacent rigid or deformable bodies. The masonry bond pattern, as well as the wall section morphology, can be reproduced explicitly accounting for their non-negligible influence on the OOP response of URM panels, as demonstrated e.g. by de Felice (2011) and Pulatsu et al. (2016). The work of Papantonopoulos et al. (2002), Psycharis et al. (2003) and Lemos (1998, 2007), mainly focused on dry-joint structures, further proved the capabilities of such discrete modelling approach in predicting the global collapse of monumental structures. Recently, Bui et al. (2017) proposed a series of comparisons between both in-plane and OOP experimental behaviour of dry-joint unreinforced masonry constructions and their numerical counterparts reaching an adequate level of accuracy. Also, Azevedo et al. (2000) investigated the response of mortared-joints structures for deriving seismic vulnerability functions, whilst in Tondelli et al. (2016) the influence of the boundary conditions on the OOP response of URM masonry walls was pointed out. In the work proposed by Lemos and Campos Costa (2017), instead, the DEM was employed for simulating the shake-table experimental response of a full-scale irregular block masonry specimen. Although a simplified joint model was employed for reducing the computational efforts, the overall OOP collapse failure mechanisms was adequately captured by the model. A more detailed modelling strategy, firstly validated through the simulation of the OOP quasi-static behaviour of URM components (Galvez et al. 2018b), was adopted by Galvez et al. (2018a) for simulating the shake-table collapse mode of a two-story reduced-scale URM building specimen with mortared-joints and periodic brick texture, leading to accurate results despite the very high computational cost required, as noted by the authors.

Notwithstanding the abovementioned applications, as far as the authors' are aware of, the numerical simulation of the dynamic OOP response of mortared-joint URM components has not been addressed yet.

Within the discrete elements family, the rigid body spring model (RBSM) (Kawai 1978) proved to be a valid alternative with respect to other micro-modelling methods. According to its formulation, a masonry assembly is assumed to be composed of rigid blocks connected by discrete deformable interfaces with distributed normal and tangential nonlinear springs, as described in Casolo (2000). Several applications (e.g. Casolo and Peña 2007) have shown that in-plane governed responses can be adequately simulated using RBSM. Regardless, since the recontact between neighbouring elements (if different from the ones initially set) is not accounted for, the explicit modelling of OOP collapses is unattainable using the standard formulation of RBSM (Furukawa et al. 2012). Thus, more refined hybrid computational procedures are currently being explored, as proved by the RBSM/FEM homogenised hybrid model lately developed by Silva et al. (2017), which provided a good agreement with quasi-static tests results on URM panels subjected to two-way bending OOP loading.

Meguro and Tagel-Din (2000, 2001, 2002) proposed an analogous but more computationally effective approach, the Applied Element Method (AEM), partially overcoming the abovementioned limitations. Its formulation allows the reproduction of the structural response both in the finite and discrete domains, taking into account contacts and dynamic element interactions automatically. Since the OOP failure mechanisms can be described up to complete collapse accounting for the displacements of each unit separately, the estimation of debris areas can be also considered. Moreover, the possibility of describing the interaction between in-plane and OOP actions and the associated cracks propagation with a relatively low computational cost, makes this numerical tool particularly suitable for the simulation of the global response of complex URM structures.

In this endeavour, thanks to the abovementioned features, an AEM-based structural analysis software tool - Extreme Loading for Structures (Applied Science International LLC. 2018) - was selected for reproducing the observed OOP shake-table response of full-scale URM cavity-wall specimens subjected to both one-way and two-way bending. The selection of material parameters, the representation of the test-set up and the modelling strategy are discussed and verified by comparing the experimental outcomes with their numerical counterparts.

3.3 The Applied Element Method for masonry structures

According to the AEM, a given three-dimensional structure is discretised as a virtual assembly of rigid units, carrying only mass and damping of the system. Their mechanical connection is provided by linear or nonlinear springs, uniformly distributed along the external contact surfaces as depicted in Figure 19, with normal stiffness k_{nx} , shear stiffnesses k_{sy} and k_{sz} (where the subscripts x , y , and z indicate the orientation with respect to the global coordinate system), in which the material properties are lumped.

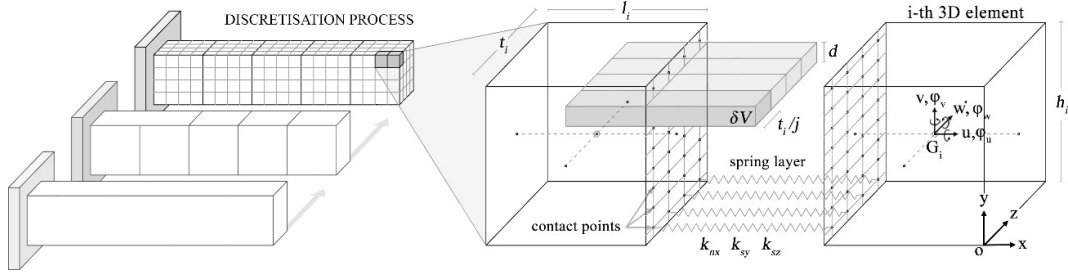


Figure 19 AEM discretisation process and connectivity among elements

With reference to Figure 19, the values assigned to both normal and shear spring stiffness (whose number j could vary depending on the desired discretisation level) are quantified respectively using Eq. (1), which involves geometrical parameters, such as the length l_i and the thickness t_i , modelling values such as the distance d between two consequent springs, and the elastic material properties E_{xx} (Young's modulus), G_{xy} and G_{xz} (shear moduli associated to the vertical and transversal directions).

$$k_{nx} = \sum_{i=1}^j \left(\frac{E_{xx} d \left(\frac{t_i}{j} \right)}{l_i} \right), \quad k_{sy} = \sum_{i=1}^j \left(\frac{G_{xy} d \left(\frac{t_i}{j} \right)}{l_i} \right), \quad k_{sz} = \sum_{i=1}^j \left(\frac{G_{xz} d \left(\frac{t_i}{j} \right)}{l_i} \right) \quad (1)$$

Naturally, in a post-cracked response stage, such elastic parameters are modified according to the material constitutive laws. The AEM employs these criteria changing the stiffness values at each loading step, taking into account the damage evolution; when a given amount of springs has failed and their stiffness is set to zero, contact between units is lost. The latter are characterised by six degrees of freedom ($u, v, w, \phi_u, \phi_v, \phi_w$), representing their rigid body motion. Nevertheless, since each group of springs completely describes stresses and deformations of a certain volume δV , the behaviour of the whole assembly is deformable.

Considering that a masonry element is usually constituted by an assembly of units (e.g. bricks or blocks) connected by mortar interfaces of variable thickness t_{mo} , the abovementioned generalised approach can be easily extended to the modelling of such composite structures, as illustrated in Figure 20 below:

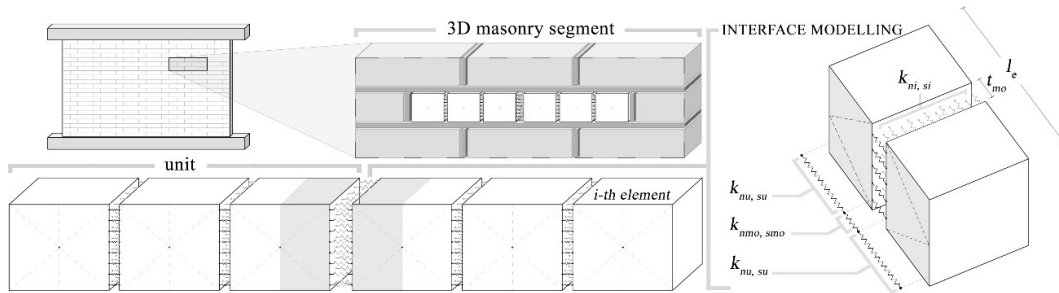


Figure 20 Discretisation of a 3D masonry segment according to the AEM

This scheme, indeed, can be explicitly reproduced using the AEM, which represents each unit separately lumping the mechanical properties of the unit-mortar interface into equivalent spring layers characterised by the stiffnesses reported in Eqs. (3)-(4), where E_u , G_u , E_{mo} and G_{mo} are the unit and mortar Young's and shear moduli respectively:

$$k_{nu} = \sum_{i=1}^j \left(\frac{E_u d \left(\frac{t_u}{j} \right)}{l_u} \right), \quad k_{su} = \sum_{i=1}^j \left(\frac{G_u d \left(\frac{t_u}{j} \right)}{l_u} \right) \quad (3)$$

$$k_{ni} = \sum_{i=1}^j \left(\frac{l_u - t_{mo}}{E_u d \left(\frac{t_u}{j} \right)} + \frac{t_{mo}}{E_{mo} d \left(\frac{t_u}{j} \right)} \right)^{-1}, \quad k_{si} = \sum_{i=1}^j \left(\frac{l_u - t_{mo}}{G_u d \left(\frac{t_u}{j} \right)} + \frac{t_{mo}}{G_{mo} d \left(\frac{t_u}{j} \right)} \right)^{-1} \quad (4)$$

It is worth noting that the equivalent interface spring stiffnesses (i.e. k_{ni} and k_{si}) were obtained assuming unit and mortar springs arranged in series at an arbitrary contact point, whilst the brick-to-brick ones (i.e. k_{nb} and k_{sb}) only describe the interaction between identical materials. Moreover, in this specific case, the shear moduli of both unit and mortar were assumed to be equal along the vertical and transversal axes. The masonry constitutive model typically implemented in AEM codes, for failure modes that come from the joint participation of unit and mortar in high compressive stress, is a linearised version of the “composite interface cap model” proposed in Lourenço et al. (1995) for micro-modelling approaches, as reported in Figure 21. The numerical idealisation of both cohesive, compressive and tensile joint behaviour, together with the considered unit material failure envelope (Khoo and Hendry 1973), are depicted in Figure 22(a)-(d).

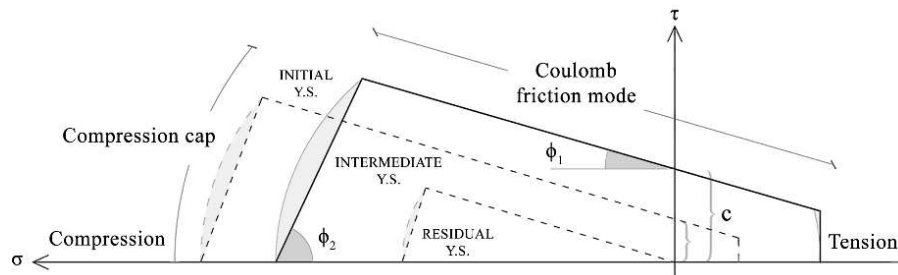


Figure 21 Linearised composite interface cap model (adapted from Lourenço et al. 1995)

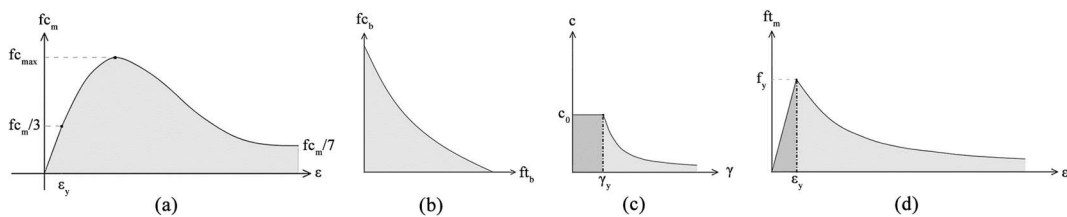


Figure 22 Compressive hardening/softening (a), Khoo-Hendry strength envelope (b), cohesion (c) and bond degradation (d) (adapted from Malomo et al. 2018c)

As already mentioned, when employing AEM, each component of a given masonry element (i.e. units and mortar) needs to be described in terms of its mechanical properties. However, experimental campaigns on masonry elements rarely involve tests that would allow one to obtain all necessary material characterisation for unit and mortar separately. Thus, undertaking the same approach described in Malomo et al. (2018c), empirical and homogenisation formulae were used to obtain first estimates of the required material parameters where direct experimental values were not available. According to Jäger et al. (2004) and Kaushik et al. (2007), indeed, the Young’s modulus of both CS and CL bricks

(E_b) can be estimated using Eqs. (5)-(6) i.e. by multiplying their compressive strength f_{c_b} by experimentally-derived constants:

$$\text{(Jäger et al. 2004)} \quad \text{CS brick} \quad E_b = (355) \cdot (f_{c_b}) \quad (5)$$

$$\text{(Kaushik et al. 2007)} \quad \text{CL brick} \quad E_b = (375) \cdot (f_{c_b}) \quad (6)$$

Hence, the expressions reported in Eqs. (7)-(10) have been employed in this endeavour in order to infer the Young's modulus of mortar (E_{mo}) as a function of the Young's modulus of masonry (E_m) and bricks (E_b), where ζ is the ratio between brick and mortar thickness. Then, the ensuing average was used for modelling purposes and the associated shear moduli were obtained assuming material isotropy (Lekhnitskii 1963). Moreover, the CS and CL bricks tensile strength was estimated assuming the 5% and 15% of their compressive strength respectively. The same range of values was successfully employed also by other researchers, e.g. Dumova-Jovanoska and Churilov (2009), Malomo et al. (2018b).

$$\text{(Brooks and Baker 1998)} \quad E_{mo} = \left(\frac{-4E_m E_b}{25E_m - 29E_b} \right) \quad (7)$$

$$\text{(Matysek and Janowski 1996)} \quad E_{mo} = \left(\frac{E_m E_b}{E_b - 1.25\zeta(E_m - E_b)} \right) \quad (8)$$

$$\text{(Ciesielski 1999)} \quad E_{mo} = \left(\frac{-E_m E_b}{5E_m - 6E_b} \right) \quad (9)$$

$$\text{(U.B.C. 1991)} \quad E_{mo} = \left(\frac{E_m E_b}{\zeta(E_m - E_b) + E_b} \right) \quad (10)$$

3.3.1 Simulation of out-of-plane mechanisms

When a masonry element is subjected to OOP action, its failure mode is considerably affected by the imposed boundary conditions, as summarised in Figure 23(a). Under appropriate geometry and boundary conditions, masonry walls can be regarded as one-way spanning walls, with a uniaxial bending behaviour, characterised by vertical or horizontal cracks depending on the span orientation. In a more general case two-way biaxial bending behaviour might be observed, with internal flexural stresses acting in both horizontal and vertical directions simultaneously, due to the different positions and restraint conditions of the supporting edges.

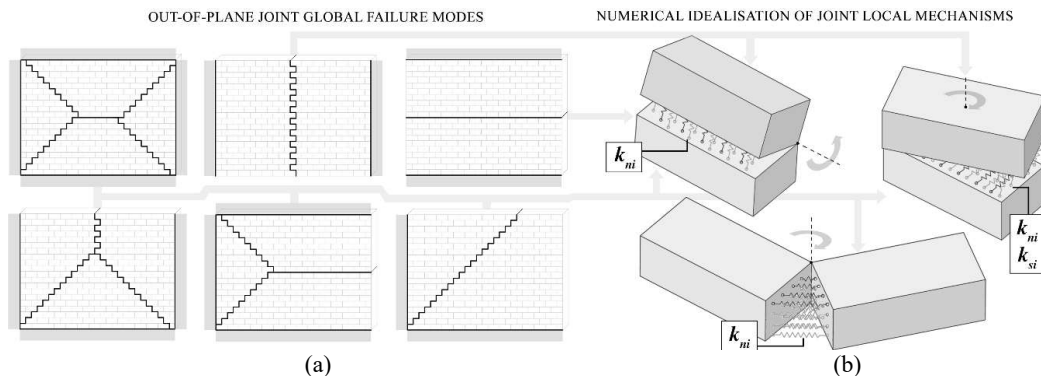


Figure 23 OOP cracking patterns depending on the wall support shape (adapted from Vaculik, 2012) (a) and AEM deformed shapes due to flexural and torsional actions (b)

In all such cases, vertical, horizontal and diagonal bending stresses act on both mortar bed- and head-joints, inducing internal flexure and torsion moments at the interfaces and through units. In the AEM framework, as shown in Figure 23(b), joint failure modes can be accounted by the equivalent interface springs by assigning flexural and torsion stresses to normal and shear spring respectively. In order to capture the units' failure, instead, an additional discretisation should be introduced, as shown in Figure 20.

In this endeavour, a coarse subdivision of all the units of the masonry elements subjected to OOP actions (i.e. excluding the return walls in case of two-way bending) proved to be sufficient for reproducing numerically the observed unit failure modes, as further discussed in the next sections.

3.3.2 First verification of AEM with material characterisation tests

In this subsection, a first comparison between experimental and numerical outcomes is proposed with a view to assess the AEM capabilities in reproducing the main OOP local failure modes. For this purpose, the results of characterisation tests on small-scale specimens carried out by Graziotti et al. (2018) were selected and consequently replicated using the AEM. Bond-wrench and torsion-compression tests on both CS and CL brick masonry samples, as well as four-point bending tests on CS wallettes (in case of CL wallettes only the numerical prediction is available, since no experimental tests were performed), were considered in such modelling exercise.

The CS brick masonry specimens were characterised by a single-leaf periodic arrangement (stretcher bond) of 212×103×71 mm units and 10 mm thick mortar joints. The same mortar bond thickness and pattern was also employed to assemble the 208×98×50 mm CL brick masonry specimens. For further test details, interested readers may refer to Sharma et al. (2018). In Table 9, the considered masonry material properties (which were also employed for all the small-scale models) are reported:

Table 9 Experimental (Sharma et al. 2018) and inferred CS/CL masonry properties

	CS - $\delta_m = 1833$ [kg/m ³]								CL - $\delta_m = 2000$ [kg/m ³]							
	f_{c_m}	f_{c_b}	f_w	E_m	c	μ	E_b	E_{m_o}	f_{c_m}	f_{c_b}	f_w	E_m	c	μ	E_b	E_{m_o}
Avg [MPa]	8.5	15.3	1.0	5430	0.8	0.5	5435	5435	4.5	46.8	0.4	6798	0.2	0.6	17550	1580
C.o.V. [%]	7.8	6.1	18.2	31.2	-	-	-	-	8.5	11.0	55.3	23.3	-	-	-	-

The comparison between experimental and numerical results shown in Figure 24 seemed to indicate that the main local OOP failure mechanisms can be adequately predicted using the considered computational method. Indeed, a good agreement in terms of overall capacity was found for the case of torsion and four-point bending tests, albeit the residual strength was not fully captured by the numerical models.

This latter aspect is due to the fact that, as already mentioned, when a given spring fails in both tension and shear, its stiffness is set to zero in the subsequent steps, causing a sudden loss of capacity right after the strength peak.

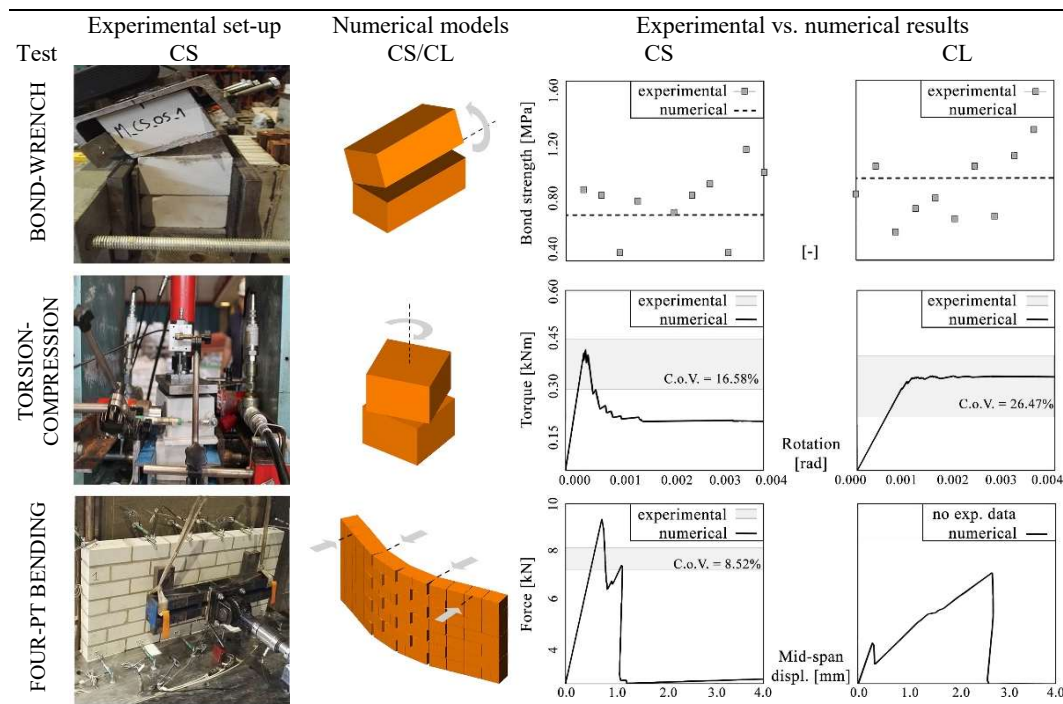


Figure 24 Comparison between characterisation test results (after Sharma et al. 2018) and their numerical counterparts (adapted from Malomo et al. 2018a)

3.4 Overview of out-of-plane shake-table tests considered in this study

As mentioned previously, a series of somewhat pioneering OOP shake-table tests were recently performed at the laboratory of Eucentre (Graziotti et al. 2016, 2018), involving both single-leaf CS and CL brick masonry panels as well as cavity CS-CL walls, characterised by different boundary conditions and ties distribution, and tested dynamically in one-way and two-way OOP bending. The employed bricks, whose dimensions were $212 \times 103 \times 71$ mm and $208 \times 98 \times 50$ mm for CS and CL brick masonry respectively, were arranged according to a stretcher bond pattern.

The mortar layers thickness was approximately 10 mm for all the specimens. For what concerns the hysteretic response and the observed crack pattern, such results will be shown in the following section, together with their numerical counterparts. In what follows, only a very brief overview of the considered test layouts, loading protocols and experimental outcomes is given, since full details on the tests may readily be found in (Graziotti et al. 2016, 2018).

3.4.1 One-way bending tests

Two different types of full-scale specimens were tested dynamically, in their OOP direction, in one-way bending conditions by Graziotti et al. (2016). The first one (i.e. SIN-03/01-00) consisted of a single leaf wall made of CS brick masonry. The remaining specimens (i.e. CAV-01-02, CAV-03-02 and CAV-01-04), instead, were constituted by an inner CS brick masonry load-bearing panel coupled with an outer veneer in CL bricks; the

All the specimens exhibited rocking behaviour with the formation of horizontal cracks at the walls bottom, top and around mid-height (MH) sections. All cracked specimens reached the OOP collapse for a value of PTA slightly higher than the activation one, as noted by Tomassetti et al. (2018a), except for SIN-03/01, for which the testing protocol has been adapted to the overburden adjustment discussed above (albeit activation and collapse PTA still seem comparable to each other).

3.4.2 One-way bending tests

Five different full-scale U-shaped walls were tested by Graziotti et al. (2018). All the specimens were constituted by an assembly of three URM panels: two return walls parallel to the direction of shaking and a main panel excited in the OOP direction. The first two walls tested (i.e. CS-010-RR/CS-005-RR and CS-000-RF), having the same geometry, only differed in the imposed vertical overburden pressure and bottom-top horizontal boundary conditions; restrained-restrained (RR) and restrained-free (RF). CSW-000-RF, instead, was characterised by the presence of an opening (1988×1630 mm) located asymmetrically in the main panel.

The fourth specimen (i.e. CL-000-RF) was made of CL bricks, whilst the last specimen tested (i.e. CV-000) was representative of a complete cavity-wall system. The distance between the two cavity-wall leaves was approximately 86 mm, and their connection was provided by 0.2 steel ties/m². The masonry material properties have been already reported in Table 9, whilst the main geometrical data of the specimens (such as the length of the central panel, l_{OOP} , and the one of the return walls, l_{ret}), as well as the different levels of vertical overburden imposed to both return walls ($\sigma_{v_{ret}}$) and central panel ($\sigma_{v_{OOP}}$) are listed in Table 13.

Table 13 Geometrical properties, overburden pressures and boundary conditions of the specimens

Specimen ID	Typology	l_{OOP} [m]	l_{ret} [m]	t [m]	h [m]	$\sigma_{v_{OOP}}$ [MPa]	$\sigma_{v_{ret}}$ [MPa]	HR	VR
CS-010-RR	CS single leaf	3.986	1.101	0.102	2.754	0.10	0.10	RR	RR
CS-005-RR	CS single leaf	3.986	1.101	0.102	2.754	0.05	0.05	RR	RR
CS-000-RF	CS single leaf	3.986	1.101	0.102	2.754	0.00	0.05	RF	RR
CSW-000-RF	CS single leaf opening	3.986	1.101	0.102	2.754	0.00	0.00	RF	RR
CL-000-RF	CL single leaf	4.023	1.080	0.098	2.760	0.00	0.05	RF	RR
CV-000-RF	CS inner wall	3.988	1.100	0.102	2.760	0.00	0.05	RF	RR
	CL outer wall	4.350	1.298	0.98	2.754	0.00	0.05	RF	RR

The experimental set-up was similar to that employed for the one-way bending tests. For what concerns the central panel, vertical restrains (VR) assured double-fixed boundary conditions along the vertical direction for all the specimens. As mentioned above, horizontal restrains (HR) that provided fixed-fixed conditions were instead assigned to the central panel of all the specimens except for the first two walls tested (i.e. CS-010-RR/CS-005-RR).

The U-shaped walls were subjected to a series of dynamic inputs of increasing intensity, up to full collapse of the specimen, considering the four different input motions (i.e. FHUIZ, FEQ2, FEQ2 and SSW) reported in Table 14.

Table 14 Exp. inputs and failure mechanism activation/collapse PTA (after Graziotti et al. 2018)

Input ID	d [s]	PTA [g]	PTA [g] corresponding to both activation of the failure mechanism and collapse														
			CS-005-RR			CS-000-RF			CSW-000-RF			CL-000-RF			CAV-000-RF		
			mech.	activ.	coll.	mech.	activ.	coll.	mech.	activ.	coll.	mech.	activ.	coll.	mech.	activ.	coll.
FHUIZ	25	0.08	-	-	-	-	-	-	-	-	-	-	-	-	-	-	
FEQ2	25	0.19	1.93	-	1.28	-	1.28	-	1.11	-	-	-	-	-	-	-	
FEQ2	25	0.31	-	-	-	0.62	-	0.91	-	1.71	1.37	1.37	-	-	-	-	
SSW	25	0.50	-	1.42	-	-	-	-	-	-	-	-	-	-	-	-	

The damage, as expected, was mainly located in the central panel, as well as at the intersection with the return walls. The latter only experienced slight damage, with the exception of the ones of the CL single leaf which developed several diagonal cracks. Moreover, contrary to what has been observed in the one-way bending tests, a considerable amount of brick units failed in bending/shear, especially for the case of CS brick masonry.

It is noted that the activation of the failure mechanism has been associated to the development of the first observable crack, to which are referred the PTA values reported in Table 14. In the case of CAV-000-RF, the collapse occurred right after the first damage detection. A comprehensive description of both testing sequence and selection of the employed input signals, as well as a detailed investigation of the dynamic responses of the specimens, can be found in Graziotti et al. (2018) and Sharma et al. (2018).

3.4.3 Estimation of debris area from the collapse of the specimens

The explicit representation of full-collapse modes, as pointed out by Bakeer (2009), is still an open challenge in numerical modelling. Recent applications (e.g. Elshaer et al. 2017; Salem et al. 2016) have shown that the AEM, amongst other approaches, seems to be able to capture adequately the progressive failure of both steel and RC complex structures, whilst only limited research pertaining the collapse analysis of URM assemblies is presently available in literature (Garofano and Lestuzzi 2016; Karbassi and Nollet 2013; Malomo et al. 2018d). This notwithstanding, encouraging results have been obtained lately when comparing the extent of the actual debris areas produced by dynamic loading and the AEM predictions (Keys and Clubley, 2017).

Given the importance of such aspect in practical applications of seismic risk (see e.g. Crowley et al. 2017, 2018), and with the aim to assess further the AEM capabilities in predicting such response parameter, the numerical predictions in terms of both area covered by debris and volume of collapsed material have in this work been compared against their experimental counterparts, whenever the latter data were available. Indeed, it is worth noting that during the one-way bending tests, polycarbonate panels were introduced on both wall sides to avoid damage to the lab equipment, which effectively prevented the estimation of the debris area associated with the collapse of the specimens.

In the case of the two-way bending experiments, instead, and as a result of the geometrical configuration and likely failure mode of the specimens themselves, the aforementioned debris containing measures needed not to be introduced, which allowed the debris area to be estimated in the majority of the tests. From a modelling viewpoint, a specific methodology was developed in order to evaluate accurately such quantities in a reasonable

timeframe. The workflow of the employed post-processing strategy is depicted in Figure 25, and it involves the use of a CAD tool, whereby each unit is automatically converted into a solid 3D element, and then the approximate debris area is inferred by considering the surface generated connecting the geometrical centroid of each unit.

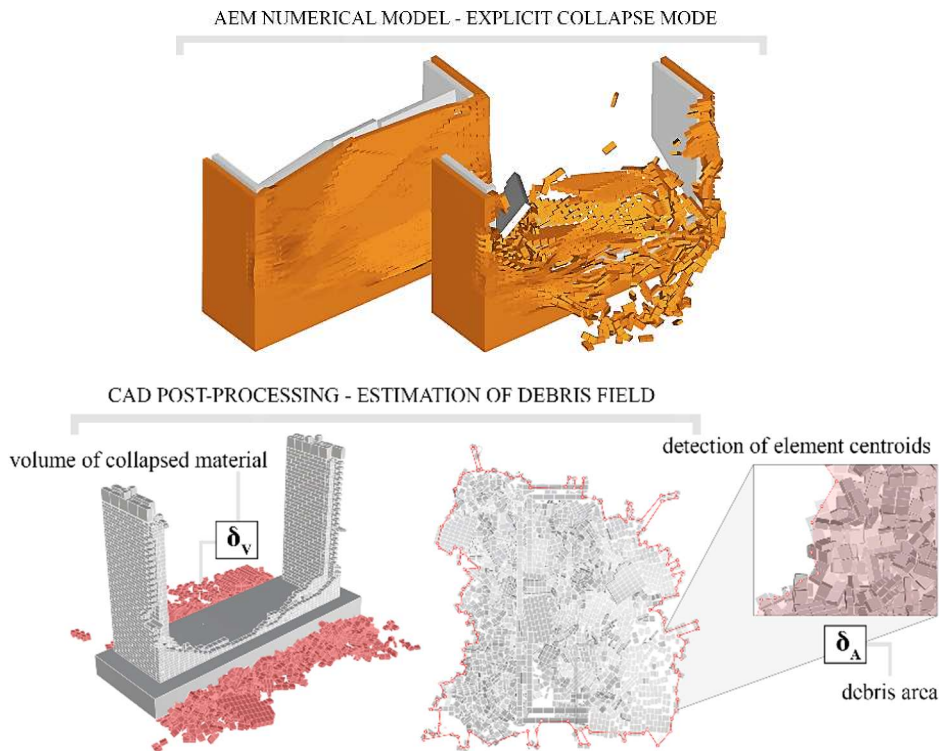


Figure 25 Workflow of the employed methodology for evaluating both the collapsed volume material and the debris area

3.5 Numerical simulation of the shake-table out-of-plane tests

In this section, the computational strategy developed, as well as a series of comparisons between experimental results and their numerical counterparts, is presented and discussed. The same modelling approach has been undertaken for both testing campaigns (i.e. one-way and two-way bending).

The experimental layouts were reproduced faithfully, assuring the same boundary conditions and loading protocols. However, aimed at reducing computational cost, the rigid steel frame structure employed during both sets of tests to avoid amplification in height of the shake-table acceleration, was considerably simplified, as depicted in Figure 26.

Indeed, in the numerical models the walls were connected by means of horizontal rigid links to a fixed linear elastic beam, to which the same seismic input that was introduced at the foundation level was also applied, thus simulating the acceleration time-history transmission to the top beam with negligible amplification that took place during the tests.

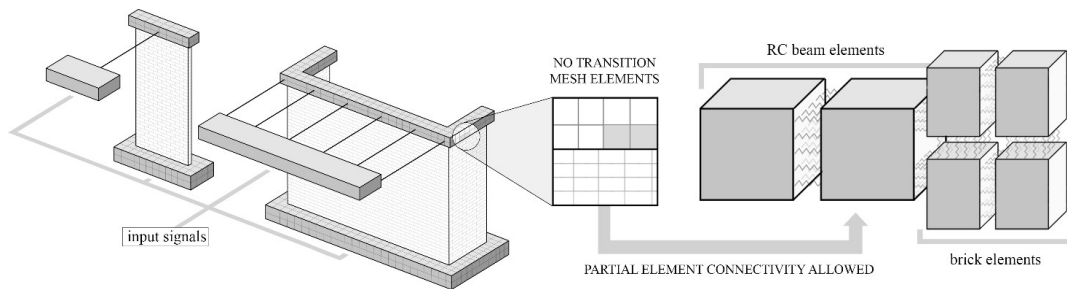


Figure 26 Numerical reproduction of the test layouts and mesh discretisation approach

The loading and foundation RC beams were explicitly modelled, assuming a linear elastic response. Rigid links, connecting the top and the bottom beams, were again used here to apply the vertical stress; initial pre-stresses, depending on the considered overburden, were assigned to the link elements reproducing the experimental ones. Further, and in order to replicate the actual stiffness of the springs employed during tests (connecting the steel top beam to the RC foundation), an equivalent Young's modulus was computed (assuming an average link section of 100 mm^2) and subsequently allotted to vertical link elements. As shown in Figure 26, a coarser mesh was assigned to the RC beams; it is noted that the AEM does not require mesh transition from large to small-size elements, since partial connectivity between units is possible. Each surface of a given rigid element (both in case of RC and URM mesh units) was connected to the adjacent one by means of 25 springs. The URM panels were discretised through a brick-based mesh, reproducing the experimental arrangement of bricks accurately. An additional discretisation was then applied subdividing each element along the vertical axis for better capturing their potential flexure and shear failure when such modes were observed experimentally (e.g. four-point OOP bending test specimen, two-way bending central panel).

For what concerns the tie-wall interfaces, which typically failed in the middle of the CL mortar bonds, the idealisation depicted in Figure 27(a)-(b) has been adopted, whereby the contact between masonry and ties occurs only through the transverse section of the ties (i.e. the ties' length is equal to that of the cavity). This is because the modelling of interpenetration phenomena between elements (such as the pull-out) would imply a very high computational burden; amongst other things, the number of dynamic contacts would increase considerably. Consequently, the adhesion stresses $\tau_p = 4.28 \text{ MPa}$ (which can be quantified dividing the associated pull-out force F_p by the embedded perimeter surface of the ties A_a), mobilised throughout $A_a \sim 534 \text{ mm}^2$, were in the models replaced by equivalent stresses $f_{teq} = (\tau_p \times A_a) / A_e$ developed on the transverse section of the ties ($A_e \sim 9 \text{ mm}^2$). Further, a linear elastic connection between CS walls and ties, with contact stiffness of CS-mortar material, was employed.

The spring layer between CL walls and ties (where tie failure typically occurred) was characterised by a strain-softening constitutive law with a post-peak softening branch and residual tensile strength (see Figure 27(c)). It is also noted that steel ties were modelled as 3D beam elements with elements with elastic-perfectly-plastic behaviour and pull-out ultimate strength F_p equal to the experimentally-recorded one, i.e. 2.29 kN (Messali et al. 2016).

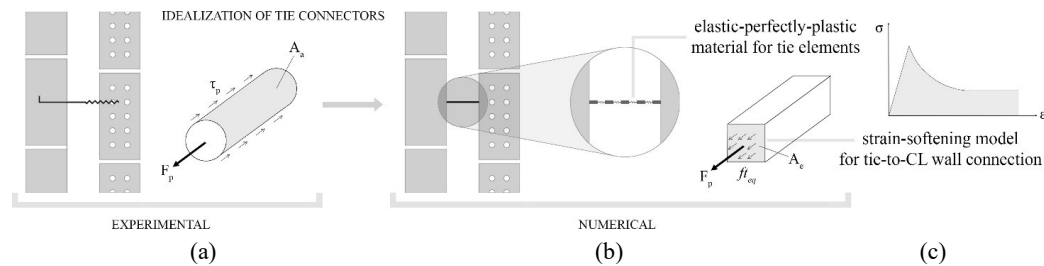


Figure 27 Experimental (a) and numerical (b) ties configuration, stress-strain relationship of CL wall-to-tie interface (c)

Finally, according to the experimental layouts, each CS wall was rigidly connected by means of L-shaped steel anchors to the top steel beam. Thus, a linear elastic interface (characterised by relatively high Young's and shear moduli) was introduced in the same position avoiding spurious relative displacements between the top beam and the CS brick masonry panels. For the same purpose, the abovementioned linear elastic interface was also employed at the interface between both CS and CL piers and the foundation beam. Further comments are provided in the following subsections, where employed modelling strategy and related assumptions are discussed more specifically depending on the considered test.

3.5.1 One-way bending tests

The structure of the four numerical models developed for simulating the OOP dynamic response of both single leaf, as well as cavity URM walls is schematically represented in Figure 28. Moreover, some of the additional modelling assumptions adopted are listed in the following:

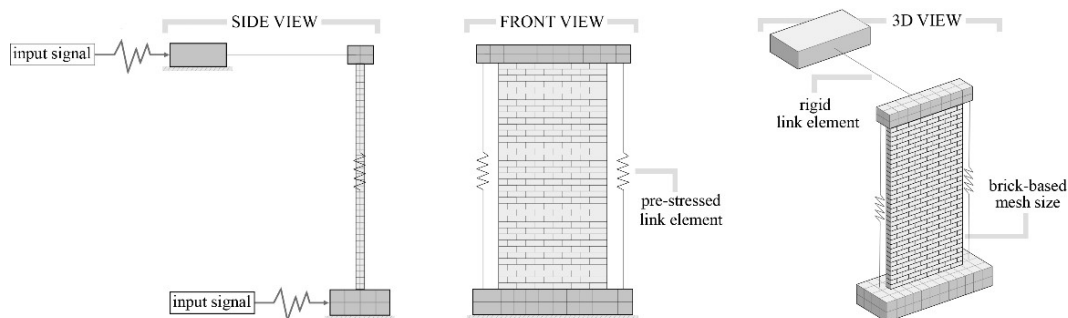
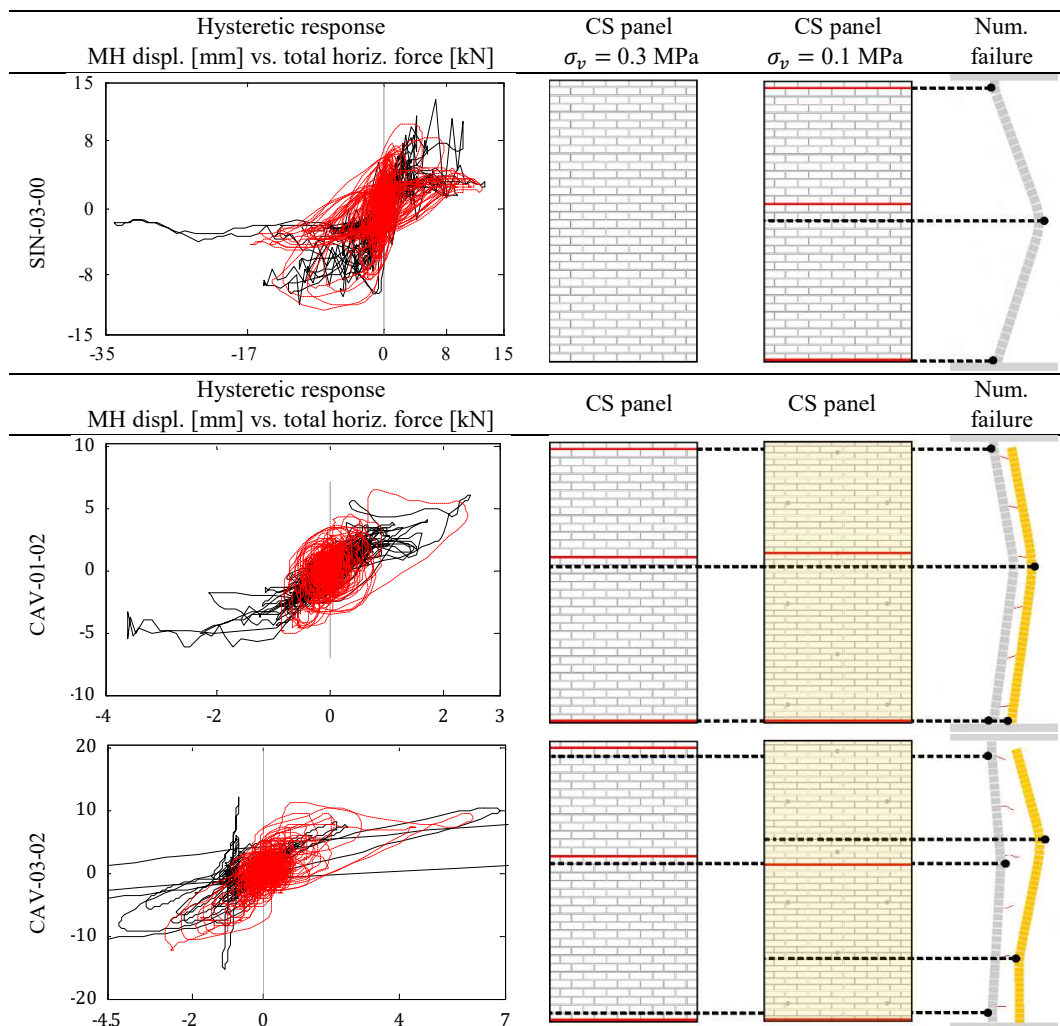


Figure 28 Structure of the AEM model developed for simulating the OOP one-way bending tests

- Since the experimental OOP failures only occurred through the bed-joints, a brick-based mesh (i.e. without vertical subdivisions) was adopted, in order to decrease the computational efforts.
- The previously mentioned overburden change in the SIN-03/01-00 specimen has been replicated during the associated numerical simulation by introducing (and removing) different link elements. Such modelling strategy allowed taking into account (with just one numerical model) of the damage evolution occurred on the same specimen during the different loading stages.

- The masonry material properties implemented in the numerical models corresponded to the ones previously reported in Table 10. Indeed, no alterations of the experimentally-derived values had to be introduced for capturing the dynamic response of the specimens.

In Figure 29, experimental and numerical crack patterns, failure modes, and the relation between horizontal displacement at MH and total horizontal force, are shown. Following an analogous approach to that suggested in the dedicated experimental paper (i.e. Graziotti et al. 2016), the experimental force has been obtained by multiplying the absolute acceleration of the centre of mass of the two bodies (idealised as rigid) by the related masses while the displacement is the one relative to the mid-height hinge location, assuming a triangular distribution of the relative acceleration along the wall height (i.e. with maximum acceleration at mid-height hinge location). Since experimental collapse tended to occur slightly later than what was numerically predicted (as summarised in Table 15 and further discussed in the next subsection), only the cycles up until numerical collapse were depicted in the hysteretic curves, for a more readily interpretation of the plots.



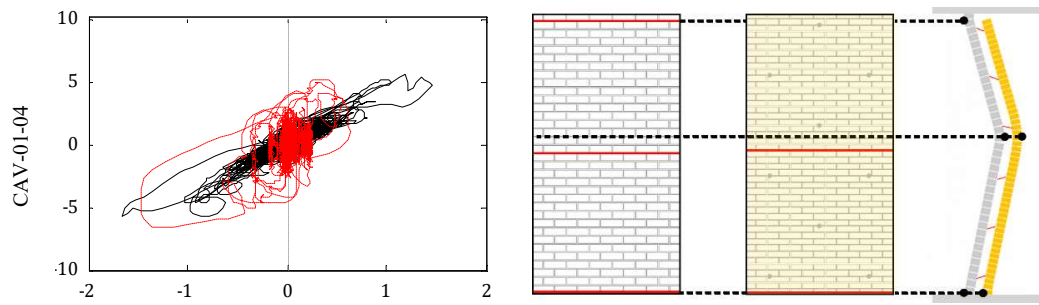


Figure 29 Experimental (in red) vs. numerical (in black) results: hysteretic behaviour and crack patterns

Regardless, both experimental (in red) and numerical (in black) displacement profiles for each cycle are reported in Figure 30 below:

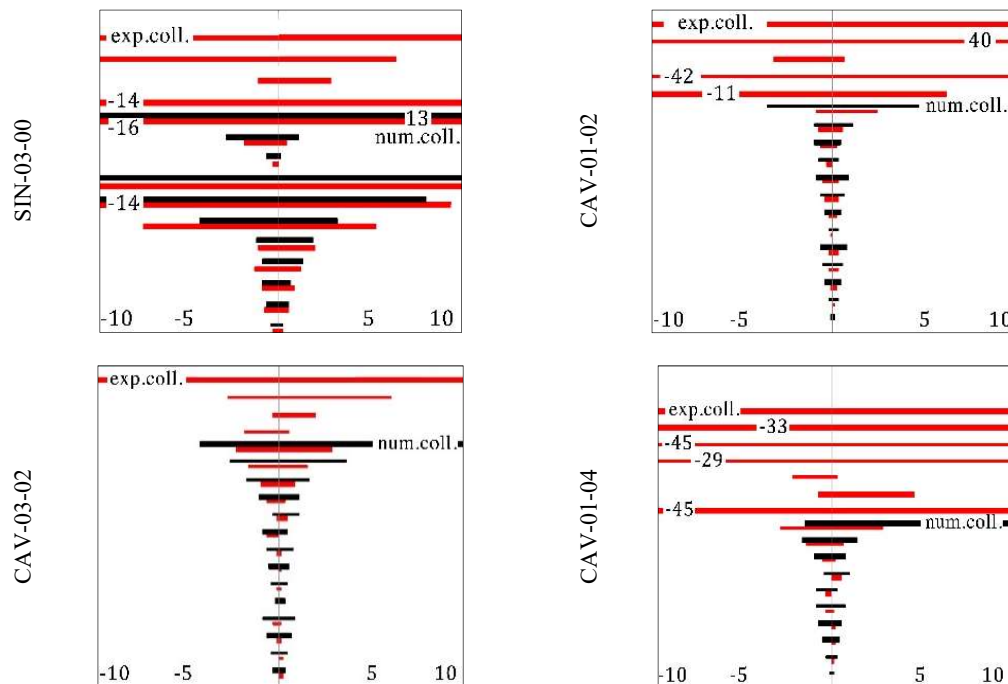


Figure 30 Experimental (in red) vs. numerical (in black) displacement profiles

The dynamic OOP one-way bending of masonry walls is a rather complex response mechanism. Hence, numerical prediction of its hysteretic behaviour and collapse capacity is inevitably and unavoidably challenging. Within such context, therefore, the comparisons depicted above can be considered as encouraging, with the numerical models producing results that appear to be within the range of their experimental counterparts. Such positive impression is further confirmed by what is shown in Table 15, where it can be observed that the estimated values of PTA feature differences with respect to the experimental observations in the range of 7-15%. As it can be gathered by comparing the numerical PTA associated to the mechanism activation and the one corresponding to collapse, the model struggled to capture the slight residual resistance exhibited by the specimens after the

attainment of the first MH crack. This might be attributable to the simplified tension cut-off criterion implemented in the employed AEM-based code, according to which the interface strength is automatically set to zero after reaching the maximum input value and thus neglecting any residual capacity. This aspect, as discussed in the next subsection, is less evident in the case of two-way bending. Indeed, in such cases, since multiple failure surfaces are involved in the mechanism activation, the failure of a single spring layer does not necessarily induce global collapse.

Table 15 Experimental vs. numerical collapse PTA and predicted debris area

Specimen ID	Exp. mech. activ. PTA [g]	Exp. collapse PTA [g]	Num. mech. activ. PTA [g]	Num. collapse PTA [g]	δ_A [m ²]	δ_V [m ³]
SIN-03-00	0.96	0.85	0.96	0.96	6.83	0.72
CAV-01-02	0.50	0.68	0.60	0.60	2.91	0.81
CAV-03-02	0.75	1.11	0.93	0.93	3.46	0.43
CAV-01-04	0.63	0.68	0.63	0.63	4.65	0.82

Given the relatively satisfying performances of the numerical models, and with a view to assess the potential life-safety risk associated with such mechanisms, an attempt was made in this endeavour for estimating numerically the collapse debris produced by each specimen, as depicted in Figure 31 for the case of CAV-01-02 (it is herein recalled that, contrary to the two-way bending test, no experimental counterpart is available in this case). The extent of the computed debris areas (δ_A) and volumes (δ_V) are reported in Table 15, with the reader being referred to the work of Crowley et al. (2017, 2018) for a description on how this type of results could be used to estimate risk to the building occupants.

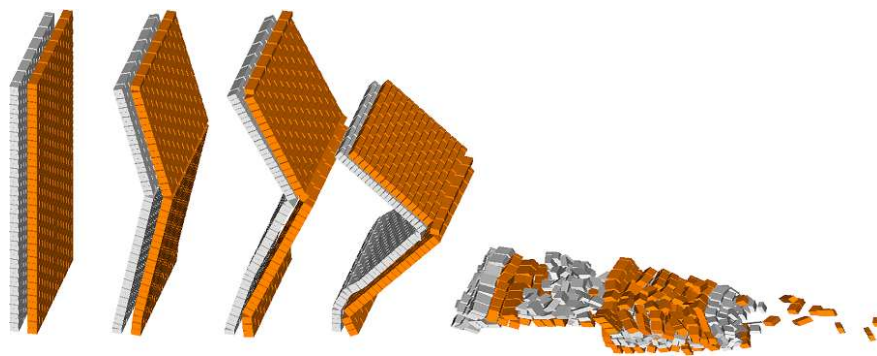


Figure 31 Numerical progressive OOP collapse of CAV-01-02 subjected to one-way bending

3.5.2 Two-way bending tests

Six different numerical models, whose configuration is depicted in Figure 32(a)-(b), were developed for reproducing numerically the experimental OOP dynamic response of the single leaf and cavity-walls subjected to two-way bending. In addition to the modelling assumptions reported at the beginning of this section, the following is also of relevance:

- Experimental collapses were often caused by hybrid modes, i.e. involving both joint and unit failure. Thus, an additional vertical discretisation of the bricks was

assigned to the elements of central panel, whilst a brick-based standard mesh has been allotted to the return walls.

- As discussed in Graziotti et al. (2018) and Sharma et al. (2018), all the test specimens were carefully instrumented with accelerometers, potentiometers, wire potentiometers and a 3D optical acquisition system, according to a pre-defined marker-grid. With a view to facilitate the comparison between numerical and experimental outcomes, such an acquisition system has been replicated in the models by introducing massless small rigid elements placed in the same locations. While OOP displacements were evaluated at MH and on the top of the central panel, depending on the considered boundary conditions (i.e. RR/RF respectively), time-histories of inertial forces were computed numerically by multiplying the acceleration recorded at massless small rigid element locations (idealised as lumped in the element centroids) with a tributary mass assigned to them, equal to the one reported in Sharma et al. (2018).
- Finally, the mechanical contribution of tie connectors was accounted undertaking the same modelling approach employed for the models subjected to one-way bending conditions. Similarly, the selected masonry material properties did not differ from the ones experimentally-determined.

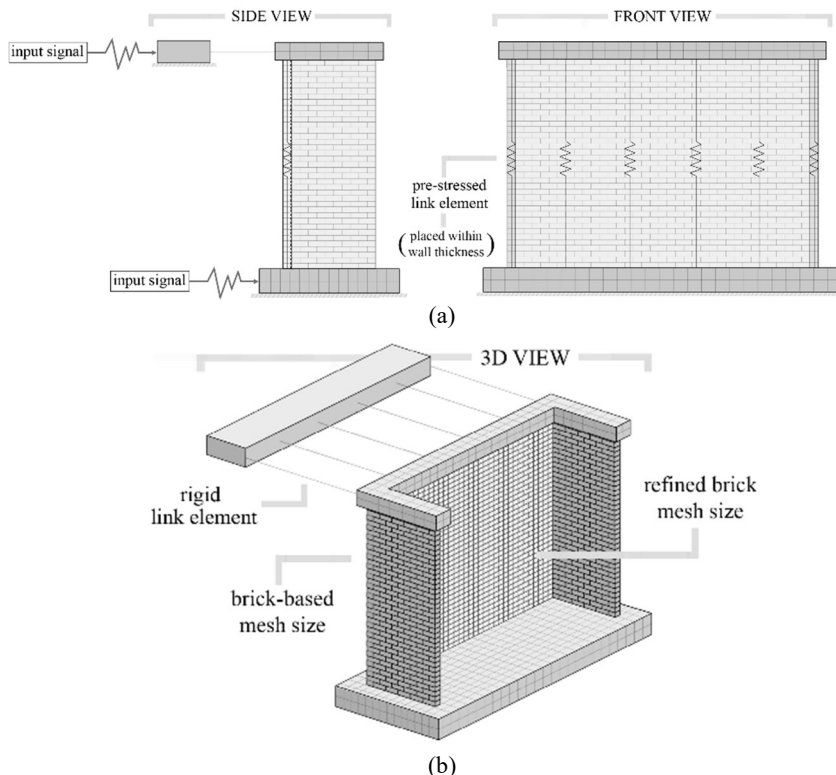
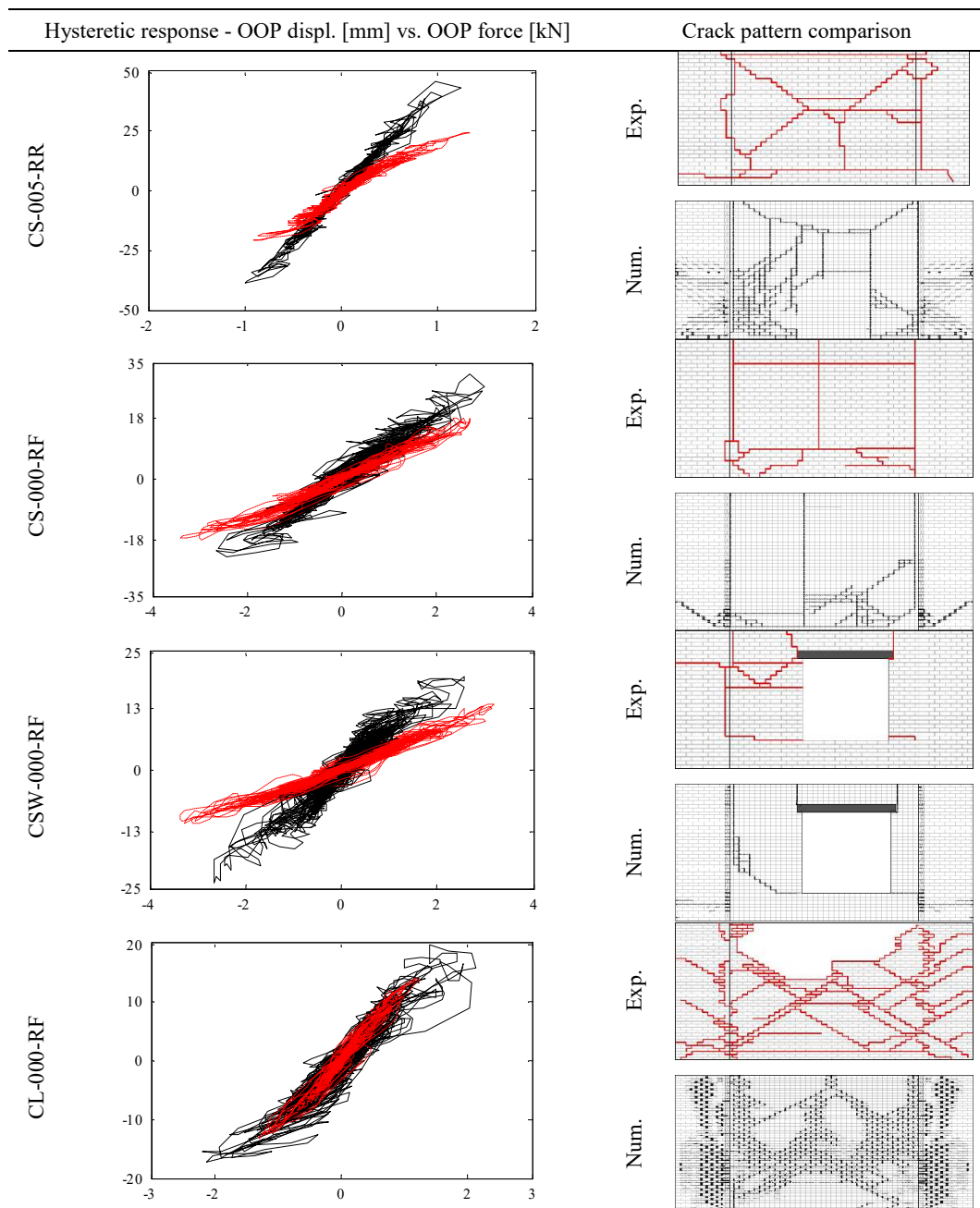


Figure 32 Structure of the AEM model developed for simulating the OOP two-way bending response: lateral (a) and 3D (b) views

In the following, the numerical collapse failure modes (the colour used for the rendering of the models changes as a function of the wall material, where CS is grey and CL is orange),

as well as the predicted hysteretic behaviours, were compared with their experimental counterparts (see Figure 33). Such quantities were expressed as OOP displacement against the corresponding OOP force. Given the differences in terms of experimental/numerical collapse PTAs reported in Table 16, only comparable data were shown.

However, with a view to represent the actual extent of displacement capacity exhibited by the specimens with respect to the predicted one, a comparison between the latter quantities is also proposed in Figure 35.



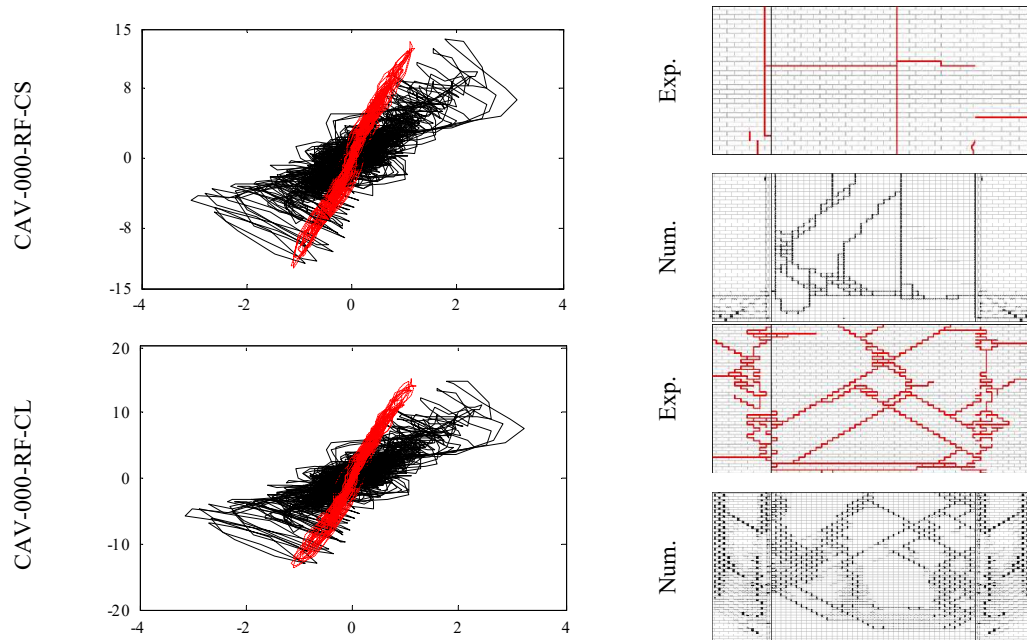


Figure 33 Experimental (in red) vs. numerical (in black) hysteretic behaviour and crack pattern

This modelling exercise substantially confirmed the capability of AEM in adequately capturing the brittle OOP response of URM components subjected to two-way bending conditions, given that the models did reproduce in a relatively satisfactory manner both the failure modes of the specimens, as well as their hysteretic response (especially considering that the OOP displacement values are very small). As depicted in Figure 34, an acceptable agreement in terms of crack patterns was also found, especially for the central panels.

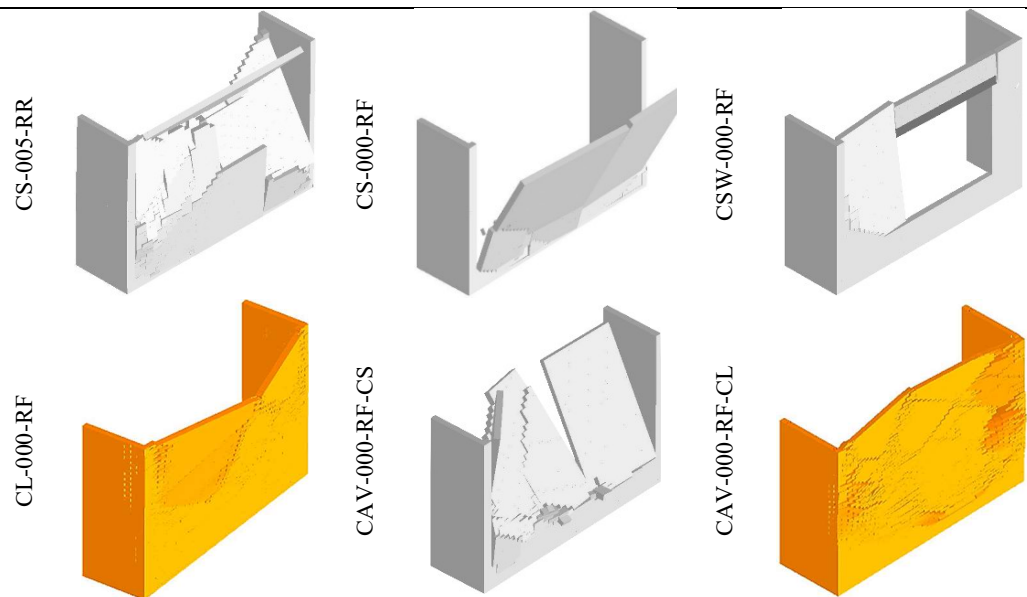


Figure 34 Screenshot of the numerical models at the onset of collapse

Still, because of the simplified joint and unit constitutive models implemented in the employed numerical tool (e.g. no post-peak softening joint behaviour is considered), when comparing the PTA at which collapses occurred experimentally with the ones predicted by the models, in some cases noticeable differences were observed, as shown in Table 16:

Table 16 Comparison between experimental and numerical failure PTA

Specimen ID	Exp. mech. activ.	Exp. collapse	Num. mech. activ.	Num. collapse
	PTA [g]	PTA [g]	PTA [g]	PTA [g]
CS-005-RR	1.93	1.42	1.18	1.93
CS-000-RF	1.28	0.62	0.95	1.10
CSW-000-RF	1.28	0.91	0.65	1.13
CL-000-RF	1.11	1.71	0.76	0.94
CAV-000-RF	1.37	1.37	0.57	0.63

This hypothesis is supported by the fact that the numerical collapse was often reached in the subsequent input sequence with respect to the one in which the activation of the failure mechanism occurred. However, looking at the experimental vs. numerical displacement capacities of Figure 35, it seems that the adopted modelling might be acceptable.

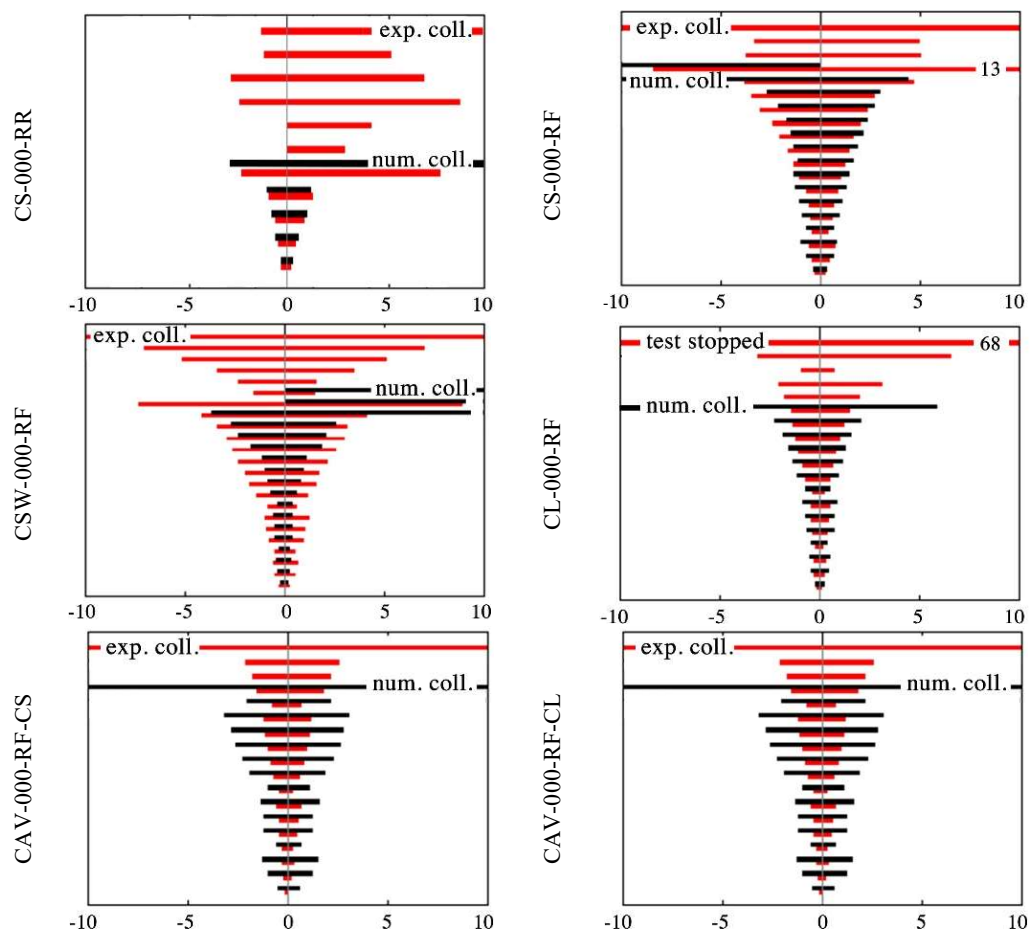


Figure 35 Experimental (in red) vs. numerical (in black) results: MH displacement profiles

Again, since satisfactory agreement between experimental and numerical response was found as a whole, the debris area (δ_A) associated to each specimen collapse mode, as well as volume of collapsed material (δ_V), were also evaluated and then compared with their experimental counterparts, as reported in Table 17, where the ratios between observed and predicted debris area and collapsed material volume (i.e. γ_A , γ_V) are also given.

Table 17 Estimation of debris area/volume of material collapsed using verified numerical models

Specimen ID	Exp. δ_A [m ²]	Num. δ_A [m ²]	Exp. δ_V [m ³]	Num. δ_V [m ³]	$0 < \gamma_A < 1$ [-]	$0 < \gamma_V < 1$ [-]
CS-005-RR	14.90	16.83	1.09	1.12	0.88	0.97
CS-000-RF	11.02	13.51	0.93	1.08	0.82	0.86
CSW-000-RF	-	4.47	-	0.45	-	-
CL-000-RF	7.16	14.39	0.31	1.12	0.50	0.28
CAV-000-RF	-	17.97	-	1.19	-	-

In some specific cases (e.g. CL-000-RF), when the collapse predicted by the numerical models occurred for a loading stage different from their experimental counterparts, inducing a slightly different damage evolution (e.g. for the case of CL-000-RF only a partial collapse of the upper portion of the central panel occurred during the test, whilst the model predicted a full collapse of the panel), non-negligible dissimilarities were found. However, considering the experimental uncertainties and variables (e.g. some of the expelled bricks interacted with the steel test-rig frame during collapse), also due to the fact that the test set-up and the instrumentation were not designed specifically for inferring these kind of collapse quantities, the application of such computational methodology to more complex structures seems to be promising.

3.6 Conclusions

Out-of-plane (OOP) damage extent may depend on several factors, such as building geometry, degree of wall-to-wall and wall-to-diaphragm connections, boundary conditions, vertical compression acting on the top of the wall and construction technique. Amongst the latter, the cavity-wall systems proved to be particularly vulnerable to OOP loading, being constituted by the assembly of a loadbearing CS inner leaf and an outer veneer usually made of CL brick masonry, with only aesthetic functions. The connection between the two leaves, separated by an air gap ordinarily filled with insulating material, is provided by metallic ties; such weak connection is typically not fully capable of coupling the dynamic response of two parallel masonry panels, rendering the mechanical contribution of the lightly loaded outer veneer to the resistance of the wall almost negligible, hence behaving as an added participating mass and thus further increasing the vulnerability of the whole system when subjected to OOP seismic sequences.

Given that relatively limited work has over the years been carried out on the verification and validation of numerical approaches for modelling this type of walls when subjected to OOP seismic input, an attempt was made in this endeavour to address the aforementioned knowledge gap by simulating a series of shake-table tests on full-scale URM wall specimens (under both one and two-way bending conditions). Use was made of a relatively new addition to the discrete element analysis family, the Applied Element Method (AEM),

which was thus scrutinised and consequently verified in this work through comparison against laboratory test results.

Given that in typical practical applications one rarely has access to experimental data on material characterisation for brick and mortar separately, a pre-processing methodology to derive such mechanical properties, and which makes use of available empirical equations, has been proposed. The modelling of the URM wall specimens then considered, in addition to the masonry units and mortar, also the presence of the tie connectors (in the case of the cavity-walls).

The analyses results seem to indicate a capability of the Applied Element Method to satisfactorily capture both the crack pattern and the collapse mode of the full-scale URM elements, as well as of their hysteretic behaviour. Moreover, a first attempt to compare the predicted debris area caused by the OOP failure was proposed, and encouraging results were obtained.

However, despite the abovementioned aspects, further improvements should be pursued in the future. Such possible enhancements are currently being explored, as is the extension and verification of this modelling approach to more complex structures.

Acknowledgements

The work described in this paper was carried out within the framework of the research programme on hazard and risk of induced seismicity in the Groningen region, sponsored by the Nederlandse Aardolie Maatschappij BV (NAM). The authors also acknowledge all those at the European Centre for Training and Research in Earthquake Engineering (Eucentre, Pavia, Italy) that were involved in the testing campaign referred to in this paper, and in particular Francesco Graziotti, Satyadhrik Sharma, Luca Grottoli and Umberto Tomassetti, for their precious assistance in accessing the test data. Finally, the collaboration of the technical support staff from Applied Science International LLC (ASI), on the use of the employed AEM software - Extreme Loading for Structures, is also acknowledged.

References

- ABK. (1981). *Methodology for Mitigation of Seismic Hazards in Existing Unreinforced Masonry Buildings: Wall Testing, Out-of-Plane, Report ABK-TR-04*. Agbabian & Associates Barnes & Associates Kariotis & Associates, El Segundo, California.
- Abrams, D. P., AlShawa, O., Lourenço, P. B., and Sorrentino, L. (2017). "Out-of-Plane Seismic Response of Unreinforced Masonry Walls: Conceptual Discussion, Research Needs, and Modeling Issues." *International Journal of Architectural Heritage*, Taylor & Francis, 11(1), 22–30.
- Addressi, D., Liberatore, D., and Masiani, R. (2015). "Force-based beam finite element (FE) for the pushover analysis of masonry buildings." *International Journal of Architectural Heritage*, Taylor & Francis, 9(3), 231–243.
- AlShawa, O., Sorrentino, L., and Liberatore, D. (2017). "Simulation Of Shake Table Tests on Out-of-Plane Masonry Buildings. Part (II): Combined Finite-Discrete Elements." *International Journal of Architectural Heritage*, Taylor & Francis, 11(1), 79–93.
- Applied Science International LLC. (2018). "Extreme Loading for Structures (2018)."

- Durham (NC), USA.
- Azevedo, J., Sincaian, G., and Lemos, J. V. (2000). "Seismic behavior of blocky masonry structures." *Earthquake Spectra*, 16(2), 337–365.
- Bakeer, T. T. (2009). "Collapse analysis of masonry structures under earthquake actions." PhD Thesis - Technical University of Dresden.
- Brooks, J. J., and Baker, A. (1998). "Modulus of Elasticity of Masonry." *Masonry International*, 12(2), 58–63.
- Bui, T. T., Limam, A., Sarhosis, V., and Hjjaj, M. (2017). "Discrete element modelling of the in-plane and out-of-plane behaviour of dry-joint masonry wall constructions." *Engineering Structures*, Elsevier, 136, 277–294.
- Candeias, P. X., Campos Costa, A., Mendes, N., Costa, A. A., and Lourenço, P. B. (2017). "Experimental Assessment of the Out-of-Plane Performance of Masonry Buildings Through Shaking Table Tests." *International Journal of Architectural Heritage*, Taylor & Francis, 11(1), 31–58.
- Cannizzaro, F., and Lourenço, P. B. (2017). "Simulation of Shake Table Tests on Out-of-Plane Masonry Buildings. Part (VI): Discrete Element Approach." *International Journal of Architectural Heritage*, Taylor & Francis, 11(1), 125–142.
- Casolo, S. (2000). "Modelling the out-of-plane seismic behaviour of masonry walls by rigid elements." *Earthquake Engineering & Structural Dynamics*, Wiley-Blackwell, 29(12), 1797–1813.
- Casolo, S., and Peña, F. (2007). "Rigid element model for in-plane dynamics of masonry walls considering hysteretic behaviour and damage." *Earthquake Engineering & Structural Dynamics*, Wiley-Blackwell, 36(8), 1029–1048.
- Chácara, C., Mendes, N., and Lourenço, P. B. (2017). "Simulation of Shake Table Tests on Out-of-Plane Masonry Buildings. Part (IV): Macro and Micro FEM Based Approaches." *International Journal of Architectural Heritage*, Taylor & Francis, 11(1), 103–116.
- Chen, S.-Y., Moon, F. L., and Yi, T. (2008). "A macroelement for the nonlinear analysis of in-plane unreinforced masonry piers." *Engineering Structures*, Elsevier, 30(8), 2242–2252.
- Ciesielski, R. (1999). "The dynamic module of elasticity of brick walls." *Proceedings of the Conference of the Committee of Civil Engineering PZITB: Lublin, Poland*.
- Costa, A. A., Arêde, A., Costa, A. C., Penna, A., and Costa, A. (2013). "Out-of-plane behaviour of a full scale stone masonry façade. Part 1: Specimen and ground motion selection." *Earthquake Engineering & Structural Dynamics*, Wiley-Blackwell, 42(14), 2081–2095.
- Costa, A. A., Penna, A., Arêde, A., and Costa, A. (2015). "Simulation of masonry out-of-plane failure modes by multi-body dynamics." *Earthquake Engineering & Structural Dynamics*, Wiley-Blackwell, 44(14), 2529–2549.
- Crowley, H., Polidoro, B., Pinho, R., and van Elk, J. (2018). "Fragility and Consequence Models for Probabilistic Seismic Risk Assessment in the Groningen Gas Field." *16th European Conference on Earthquake Engineering*, Thessaloniki, Greece.
- Crowley, H., Polidoro, B., Pinho, R., and Van Elk, J. (2017). "Framework for developing fragility and consequence models for local personal risk." *Earthquake Spectra*, 33(4), 1325–1345.
- Cundall, P. A. (1971). "A computer model for simulating progressive large scale movements in blocky rock systems." *Proc. Symp. Rock Fracture (ISRM)*, Nancy.
- D'Ayala, D., and Shi, Y. (2011). "Modeling masonry historic buildings by multi-body

- dynamics.” *International Journal of Architectural Heritage*, 5(4–5), 483–512.
- D’Ayala, D., Spence, R., Oliveira, C., and Pomonis, A. (1997). “Earthquake loss estimation for Europe’s historic town centres.” *Earthquake Spectra*, 13(4), 773–793.
- Derakhshan, H., Dizhur, D., Griffith, M. C., and Ingham, J. M. (2014). “Seismic assessment of out-of-plane loaded unreinforced masonry walls in multi-storey buildings.” *Bulletin of the New Zealand Society for Earthquake Engineering*, 47(2), 119–138.
- Derakhshan, H., Griffith, M. C., and Ingham, J. M. (2013). “Out-of-Plane Behavior of One-Way Spanning Unreinforced Masonry Walls.” *Journal of Engineering Mechanics*, 139(4), 409–417.
- Derakhshan, H., Lucas, W., Visintin, P., and Griffith, M. C. (2018). “Out-of-plane Strength of Existing Two-way Spanning Solid and Cavity Unreinforced Masonry Walls.” *Structures*, Elsevier, 13, 88–101.
- Dizhur, D., Ingham, J., Moon, L., Griffith, M., Schultz, A., Senaldi, I., Magenes, G., Dickie, J., Lissel, S., Centeno, J., and others. (2011). “Performance of masonry buildings and churches in the 22 February 2011 Christchurch earthquake.” *Bulletin of the New Zealand Society for Earthquake Engineering*, 44(4), 279–296.
- Dumova-Jovanoska, E., and Churilov, S. (2009). “Calibration of a numerical model for masonry with application to experimental results.” *Protection of historical buildings*, 1139–1145.
- Elshaer, A., Mostafa, H., and Salem, H. (2017). “Progressive collapse assessment of multistory reinforced concrete structures subjected to seismic actions.” *KSCE Journal of Civil Engineering*, Korean Society of Civil Engineers, 21(1), 184–194.
- de Felice, G. (2011). “Out-of-plane seismic capacity of masonry depending on wall section morphology.” *International Journal of Architectural Heritage*, 5(4–5), 466–482.
- Ferreira, T. M., Costa, A. A., and Costa, A. (2015). “Analysis of the Out-Of-Plane Seismic Behavior of Unreinforced Masonry: A Literature Review.” *International Journal of Architectural Heritage*, Taylor & Francis.
- Furukawa, A., Kiyono, J., and Toki, K. (2012). “Numerical simulation of the failure propagation of masonry buildings during an earthquake.” *Journal of Natural Disaster Science*, Japan Society for Natural Disaster Science, 33(1), 11–36.
- Galvez, F., Giaretton, M., Abeling, S., Ingham, J., and Dizhur, D. (2018a). “Discrete Element modelling of a two-storey unreinforced masonry scaled model.” *16th European Conference on Earthquake Engineering*, Thessaloniki, Greece.
- Galvez, F., Segatta, S., Giaretton, M., Walsh, K., Giongo, I., and Dizhur, D. (2018b). “FE and DE modelling of out-of-plane two way bending behaviour of unreinforced masonry walls.” *16th European Conference on Earthquake Engineering*, Thessaloniki, Greece.
- Garofano, A., and Lestuzzi, P. (2016). “Seismic Assessment of a Historical Masonry Building in Switzerland: The ‘Ancien Hôpital De Sion.’” *International Journal of Architectural Heritage*, Taylor & Francis, 10(8), 975–992.
- Godio, M., and Beyer, K. (2017). “Analytical model for the out-of-plane response of vertically spanning unreinforced masonry walls.” *Earthquake Engineering & Structural Dynamics*, 46(15), 2757–2776.
- Graziotti, F., Tomassetti, U., Penna, A., and Magenes, G. (2016). “Out-of-plane shaking table tests on URM single leaf and cavity-walls.” *Engineering Structures*, Elsevier, 125, 455–470.
- Graziotti, F., Tomassetti, U., Sharma, S., Grottoli, L., and Magenes, G. (2018). “Experimental response of URM single leaf and cavity-walls in out-of-plane two-way

- bending generated by seismic excitation.” *Construction and Building Materials - accepted manuscript*.
- Griffith, M. C., Lam, N. T. K., Wilson, J. L., and Doherty, K. (2004). “Experimental investigation of unreinforced brick masonry walls in flexure.” *Journal of Structural Engineering*, American Society of Civil Engineers, 130(3), 423–432.
- Griffith, M. C., Vaculik, J., Lam, N. T. K., Wilson, J., and Lumantarna, E. (2007). “Cyclic testing of unreinforced masonry walls in two-way bending.” *Earthquake Engineering & Structural Dynamics*, Wiley-Blackwell, 36(6), 801–821.
- Ingham, J., and Griffith, M. (2011). “Performance of unreinforced masonry buildings during the 2010 darfi eld (Christchurch, NZ) earthquake.” *Australian Journal of Structural Engineering*, Routledge, 11(3), 207–224.
- Jäger, W., Irmschler, H., and Schubert, P. (2004). *Mauerwerk-Kalender 2004*. Ernst & Sohn Verlag für Architektur und technische Wissenschaften.
- Kallioras, S., Graziotti, F., and Penna, A. (2018). “Numerical assessment of the dynamic response of a URM terraced house exposed to induced seismicity.” *Bulletin of Earthquake Engineering - submitted for publication*.
- Karbassi, A., and Nollet, M.-J. (2013). “Performance-based seismic vulnerability evaluation of masonry buildings using applied element method in a nonlinear dynamic-based analytical procedure.” *Earthquake Spectra*, Earthquake Engineering Research Institute, 29(2), 399–426.
- Kaushik, H. B., Rai, D. C., and Jain, S. K. (2007). “Stress-strain characteristics of clay brick masonry under uniaxial compression.” *Journal of materials in Civil Engineering*, American Society of Civil Engineers, 19(9), 728–739.
- Kawai, T. (1978). “New discrete models and their application to seismic response analysis of structures.” *Nuclear Engineering and Design*, Elsevier, 48(1), 207–229.
- Keys, R. A., and Clubley, S. K. (2017). “Establishing a predictive method for blast induced masonry debris distribution using experimental and numerical methods.” *Engineering Failure Analysis*, Pergamon, 82, 82–91.
- Khoo, C. L., and Hendry, A. W. (1973). “Strength tests on brick and mortar under complex stresses for the development of a failure criterion for brickwork in compression.” *Proceedings of the British Ceramic Society*, 51–66.
- Lekhnitskii, S. G. (1963). *Of an anisotropic elastic body*. Holden-Day, San Francisco, USA.
- Lemos, J. V., and Campos Costa, A. (2017). “Simulation of Shake Table Tests on Out-of-Plane Masonry Buildings. Part (V): Discrete Element Approach.” *International Journal of Architectural Heritage*, Taylor & Francis, 11(1), 117–124.
- Lemos, J. V. (1997). “Discrete element modelling of the seismic behaviour of stone masonry arches.” *Proceedings of the 4th International Symposium on Numerical Methods in Structural Masonry*, G. N. Pande, J. Middleton, and B. Kralj, eds., E & FN SPON, Florence, Italy, 220–227.
- Lemos, J. V. (2007). “Discrete element modeling of masonry structures.” *International Journal of Architectural Heritage*, Taylor & Francis, 1(2), 190–213.
- Lourenço, P. B. (2009). “Recent advances in masonry structures: micromodelling and homogeneization. U. Galvanetto, MH Ferri Aliabadi eds.” *Multiscale modeling in solid mechanics: computational approaches*, 251–294.
- Lourenço, P. B., Rots, J. G. J. G., and Blaauwendraad, J. (1995). “Two approaches for the analysis of masonry structures - micro and macro-modeling.” *Research article HERON - Delft Univ. of Technology (Delft, The Netherlands)*, 40(4), 313–340.

- Maccarini, H., Vasconcelos, G., Rodrigues, H., Ortega, J., and Lourenço, P. B. (2018). “Out-of-plane behavior of stone masonry walls: Experimental and numerical analysis.” *Construction and Building Materials*, Elsevier, 179, 430–452.
- Malomo, D., Comini, P., Pinho, R., and Penna, A. (2018a). “Validating numerical modelling of out-of-plane dynamic response of masonry walls through comparison with full-scale shake-table tests.” *Journal of Structural Engineering, ASCE - to be submitted*.
- Malomo, D., DeJong, M. J., and Penna, A. (2018b). *Distinct Element modelling of the in-plane failure mechanisms of URM walls. 10th International Masonry Conference*, Milan, Italy.
- Malomo, D., Pinho, R., and Penna, A. (2018c). “Using the applied element method for modelling calcium silicate brick masonry subjected to in-plane cyclic loading.” *Earthquake Engineering & Structural Dynamics*, 47(7), 1610–1630.
- Malomo, D., Pinho, R., and Penna, A. (2018d). “Using the Applied Element Method to simulate the dynamic response of full-scale URM houses tested to collapse or near-collapse conditions.” *16th European Conference on Earthquake Engineering*, Thessaloniki, Greece.
- Matysek, P., and Janowski, Z. (1996). “Analysis of factors affecting the modulus of elasticity of the walls.” *Proceedings of the Conference of the Committee of Civil Engineering PZITB: Lublin, Poland*.
- Meguro, K., and Tagel-Din, H. (2000). “Applied element method for structural analysis: Theory and application for linear materials.” *Structural Engineering/Earthquake Engineering*, Japan Society of Civil Engineers, 17(1), 21s–35s.
- Meguro, K., and Tagel-Din, H. (2001). “Applied Element Simulation of RC Structures under Cyclic Loading.” *Journal of Structural Engineering*, 127(11), 1295–1305.
- Meguro, K., and Tagel-Din, H. (2002). “Applied Element Method Used for Large Displacement Structural Analysis.” *Journal of Natural Disaster Science*, 24(1), 25–34.
- Meisl, C. S., Elwood, K. J., and Ventura, C. E. (2007). “Shake table tests on the out-of-plane response of unreinforced masonry walls. This article is one of a selection of papers published in this Special Issue on Masonry.” *Canadian Journal of Civil Engineering*, 34(11), 1381–1392.
- Messali, F., Esposito, R., and Maragna, M. (2016). “Pull-out strength of wall ties.” *Report, TU Delft, NL*.
- Milani, G., Zuccarello, F. A., Olivito, R. S., and Tralli, A. (2007). “Heterogeneous upper-bound finite element limit analysis of masonry walls out-of-plane loaded.” *Computational Mechanics*, Springer-Verlag, 40(6), 911–931.
- Noor-E-Khuda, S., Dhanasekar, M., and Thambiratnam, D. P. (2016). “An explicit finite element modelling method for masonry walls under out-of-plane loading.” *Engineering Structures*, 113, 103–120.
- Papantonopoulos, C., Psycharis, I. N., Papastamatiou, D. Y., Lemos, J. V., and Mouzakis, H. P. (2002). “Numerical prediction of the earthquake response of classical columns using the distinct element method.” *Earthquake Engineering & Structural Dynamics*, Wiley-Blackwell, 31(9), 1699–1717.
- Penna, A., Lagomarsino, S., and Galasco, A. (2014a). “A nonlinear macroelement model for the seismic analysis of masonry buildings.” *Earthquake Engineering & Structural Dynamics*, Wiley-Blackwell, 43(2), 159–179.
- Penna, A., Morandi, P., Rota, M., Manzini, C. F., Da Porto, F., and Magenes, G. (2014b).

- “Performance of masonry buildings during the Emilia 2012 earthquake.” *Bulletin of earthquake engineering*, Springer, 12(5), 2255–2273.
- Penner, O., and Elwood, K. J. (2016). “Out-of-plane dynamic stability of unreinforced masonry walls in one-way bending: Shake table testing.” *Earthquake Spectra*, 32(3), 1675–1697.
- Psycharis, I. N., Lemos, J. V., Papastamatiou, D. Y., Zambas, C., and Papantonopoulos, C. (2003). “Numerical study of the seismic behaviour of a part of the Parthenon Pronaos.” *Earthquake Engineering & Structural Dynamics*, Wiley-Blackwell, 32(13), 2063–2084.
- Pulatsu, B., Bretas, E. M., and Lourenco, P. B. (2016). “Discrete element modeling of masonry structures: Validation and application.” *Earthquakes and Structures*, 11(4), 563–582.
- Raka, E., Spacone, E., Sepe, V., and Camata, G. (2015). “Advanced frame element for seismic analysis of masonry structures: model formulation and validation.” *Earthquake Engineering & Structural Dynamics*, Wiley-Blackwell, 44(14), 2489–2506.
- Restrepo Vélez, L. F., Magenes, G., and Griffith, M. C. (2014). “Dry stone masonry walls in bending-Part I: Static tests.” *International Journal of Architectural Heritage*, 8(1), 1–28.
- Roca, P., Cervera, M., Gariup, G., and others. (2010). “Structural analysis of masonry historical constructions. Classical and advanced approaches.” *Archives of Computational Methods in Engineering*, Springer, 17(3), 299–325.
- Salem, H., Mohssen, S., Nishikiori, Y., and Hosoda, A. (2016). “Numerical Collapse Analysis of Tsuyagawa Bridge Damaged by Tohoku Tsunami.” *Journal of Performance of Constructed Facilities*, 30(6), 04016065.
- Sharma, S., Tomassetti, U., Grottoli, L., and Graziotti, F. (2018). *Out-of-plane two-way bending shaking table tests on single leaf and cavity-walls - Report n. EUCI37/2018U*. Pavia, Italy.
- Shawa, O. Al, de Felice, G., Mauro, A., and Sorrentino, L. (2012). “Out-of-plane seismic behaviour of rocking masonry walls.” *Earthquake Engineering & Structural Dynamics*, Wiley-Blackwell, 41(5), 949–968.
- Silva, L. C., Lourenço, P. B., and Milani, G. (2017). “Nonlinear Discrete Homogenized Model for Out-of-Plane Loaded Masonry Walls.” *Journal of Structural Engineering*, 143(9), 04017099.
- Sorrentino, L., D’Ayala, D., de Felice, G., Griffith, M. C., Lagomarsino, S., and Magenes, G. (2017). “Review of Out-of-Plane Seismic Assessment Techniques Applied To Existing Masonry Buildings.” *International Journal of Architectural Heritage*, 11(1), 2–21.
- Sorrentino, L., Masiani, R., and Griffith, M. C. (2008). “The vertical spanning strip wall as a coupled rocking rigid body assembly.” *Structural Engineering and Mechanics*, Techno-Press, 29(4), 433–453.
- Tomassetti, U., Graziotti, F., Penna, A., and Magenes, G. (2018a). “Modelling one-way out-of-plane response of single-leaf and cavity-walls.” *Engineering Structures*, Elsevier, 167, 241–255.
- Tomassetti, U., Sharma, S., Grottoli, L., Graziotti, F., and Magenes, G. (2018b). “Out-of-plane dynamic behaviour of URM single leaf and cavity-wall in two-way bending.”
- Tondelli, M., Beyer, K., and DeJong, M. (2016). “Influence of boundary conditions on the out-of-plane response of brick masonry walls in buildings with RC slabs.”

Earthquake Engineering & Structural Dynamics, Wiley-Blackwell.

U.B.C. (1991). "International Conference of Building Officials. Uniform Building Code."

International conference of building officials, USA, Whittier, USA.

Vaculik, J. (2012). "Unreinforced masonry walls subjected to out-of-plane seismic action."
University of Adelaide.

Vaculik, J., and Griffith, M. (2017a). "Out-of-plane load–displacement model for two-way spanning masonry walls." *Engineering Structures*, Elsevier, 141, 328–343.

Vaculik, J., and Griffith, M. C. (2017b). "Out-of-plane shaketable testing of unreinforced masonry walls in two-way bending." *Bulletin of Earthquake Engineering*, Springer Netherlands, 1–38.

CHAPTER 4

Shake-table tests on URM cavity-wall building prototypes



CHAPTER 4 Shake-table tests on URM cavity-wall building prototypes

Malomo D., Pinho R., Penna A. (2018). “Simulating the shake-table response of URM cavity-wall structures tested to collapse or near-collapse conditions.” *Earthquake Spectra*, to be submitted.

Abstract. The seismic performance of existing unreinforced masonry (URM) buildings are considerably affected by typology and level of effectiveness of both constructive details and structural components, especially if not originally designed for resisting earthquakes. Within this framework, the use of advanced numerical approaches that are capable of duly accounting for such aspects might improve significantly the assessment of the global response of URM structures. In this paper, the Applied Element Method is thus used for simulating the shake-table response of a number of full-scale building specimens representative of cavity-wall terraced houses construction, used in a number of countries exposed to tectonic or induced seismicity. A methodology for modelling the damage evolution up to complete collapse is presented, also accounting explicitly for the influence of the presence of both rigid and flexible diaphragms, degree of connections among structural members and interaction between in-plane and out-of-plane mechanisms. Although the models slightly underestimated the energy dissipation in some specific cycles prior to collapse, the predicted crack patterns, failure modes and hysteretic behaviours have shown a good agreement with their experimental counterparts.

Keywords: applied element method; cavity-wall; shake-table; collapse modelling; unreinforced masonry.

4.1 Introduction

Unreinforced masonry (URM) terraced house construction typically comes in the form of low-rise residential buildings characterised by large openings at the ground floor, timber roof and cavity-walls, constituted by the assembly of a loadbearing inner leaf plus an outer veneer with only aesthetic and insulation functions. In some of the countries where this building typology is common (e.g. New Zealand, Australia, India), and in particular in the Central and Northern European region, the inner wall is often made of calcium silicate (CS) bricks, whilst the external leaf is constructed using clay (CL) masonry instead. Aimed at assessing the seismic capacity of this specific type of URM construction, typically designed without specific seismic considerations or detailing, a number of full-scale specimens were tested on the shake-tables of both EUCENTRE (Pavia, Italy) and LNEC (Lisbon, Portugal) laboratories, including a two-storey terraced house building specimen (i.e. EUC-BUILD1, Graziotti et al. 2017) and its 2nd storey-roof (i.e. LNEC-BUILD1, Tomassetti et al. 2017) and attic-roof (i.e. LNEC-BUILD2, Correia et al. 2018) structural sub-assemblies. In the

latter case, and after the attainment of the collapse of the gable walls, the timber roof was also subjected to a supplementary quasi-static cyclic pushover test for a complete characterisation of the diaphragm response.

Detailed numerical simulations of the dynamic response up to collapse of cavity-wall terraced house building typologies are needed for the development of seismic risk models in regions where these structures are present (Crowley et al. 2017, 2018), but were not readily available in the literature, most likely because their validation required shake-table tests on complete structural systems that only now have become available, through the experimental campaign cited above. In this endeavour, therefore, and with a view to address the aforementioned knowledge gap, the applicability of the Applied Element Method (AEM), as implemented in the Extreme Loading for Structures software (ASI, 2018), was verified against tests on URM and timber components and consequently employed for reproducing the experimental response of the abovementioned specimens up to collapse or near-collapse conditions, as further discussed in what follows.

4.2 Modelling the shake-table response of URM building specimens

Penna et al. (2016) and Tomažević and Gams (2012), amongst others, successfully reproduced the shake-table tests of in-plane-governed specimens through the employment of simplified macro-modelling techniques. In order to account also for out-of-plane (OOP) failure modes, however, more refined methods, based on both continuum and discontinuum domain, are typically required. Within such context, and as reported e.g. in Roca et al. (2010) or, more recently, in Candeias et al. (2017) and Chácará et al. (2017), attempts have been to make use of Finite Element Method (FEM) approaches to reproduce large-scale shake-table tests of URM structures, with convincing results being obtained in terms of in-plane response, but still without adequately capturing out-of-plane collapse mechanisms, and the associated full displacement capacity of the system.

The development of the Distinct Element Method (DEM), initially conceived for simulating soil and rock mechanics (Cundall 1971), provided an opportunity to explicitly represent the discrete nature of masonry, and thus better capture out-of-plane response and collapse mechanisms. Several applications of DEM in the modelling of shake-table tests of URM assemblies (e.g. Bui et al. 2017, Cannizzaro and Lourenço 2017, Lemos and Campos Costa 2017, Galvez et al. 2018) have shown much-improved agreements between numerical and experimental results, including deformation patterns up to near-collapse conditions. The prediction of explicit collapse capacity, however, remained challenging, as noted by De Felice et al. (2017).

In this work, with a view to try to avoid the abovementioned difficulties (in predicting the collapse capacity of URM specimens tested under dynamic conditions), use was thus made of a relatively new addition to the discrete element family, the Applied Element Method (AEM), to model the full-scale terraced house building specimens under study. The AEM (Meguro and Tagel-Din 2000, 2001, 2002) is based on the mechanical interaction among rigid units, carrying only mass and damping of the system, connected by linear or nonlinear springs. Frictional phenomena, contacts and element impacts up to complete collapse, as shown by several applications (e.g. Elshaer et al. 2017; Salem et al. 2016), can be

adequately predicted using this modelling approach. The AEM formulation for masonry, discussed and described in subsequent sections of this paper, has been already employed for investigating both in-plane and OOP responses of experimentally-tested components (e.g. Guragain et al. 2006; Malomo et al. 2018a; b), as well as for the modelling of large-scale URM structures (e.g. Garofano and Lestuzzi 2016; Karbassi and Nollet 2013). However, as far as the authors are aware of, validation of AEM simulation through comparison against shake-table collapse testing of full-scale URM specimens has not been addressed yet. The approach followed in the current modelling validation work is schematically depicted in Figure 36 below, from where it can be gathered that the different test specimens were modelled after the experimental campaign had been completed, and in opposite order with respect to the actual testing sequence. This was done with a view to optimise the calibration process and to allow one to evaluate numerically the influence of several modelling assumptions, including idealisation of nailed/screwed connections, tie elements in cavity-walls and interlocking among transversal and longitudinal walls.

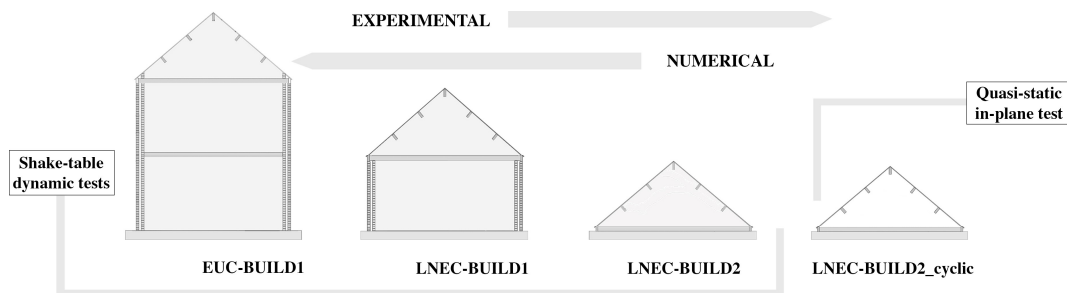
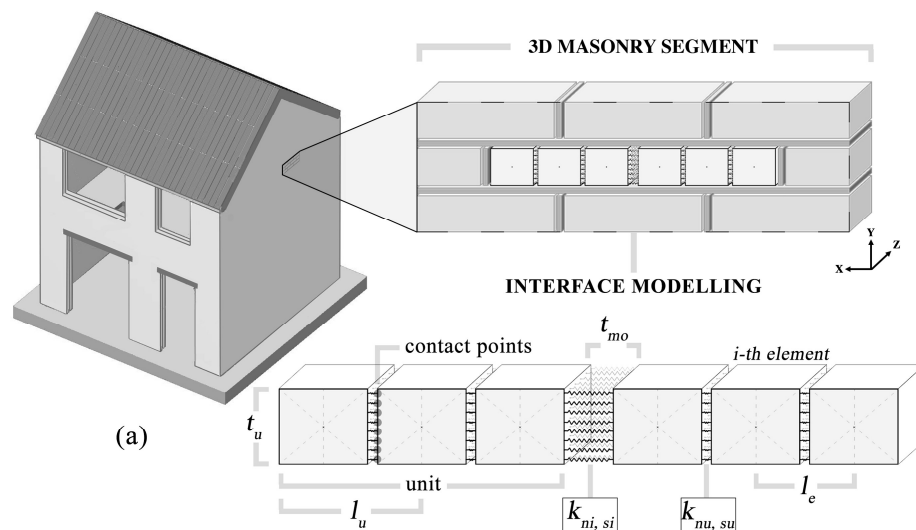


Figure 36. Graphical representation of experimental testing sequence and its numerical counterpart

4.3 The Applied Element Method for masonry structures

As mentioned above, according to the general formulation of the AEM, a given element is discretised as an assembly of rigid bodies, carrying only mass and damping of the system and characterised by six degrees of freedom.



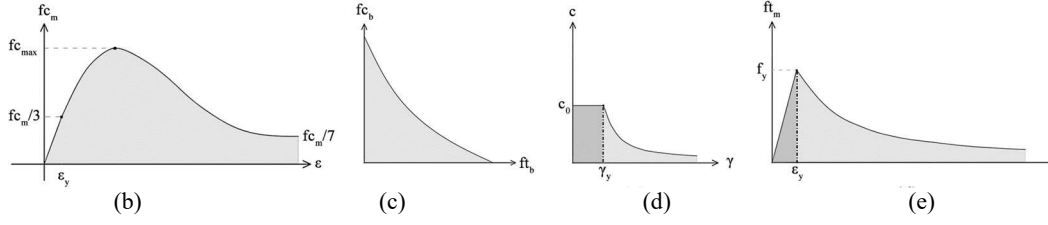


Figure 37. AEM discretisation of a 3D masonry segment (a), joint interface compressive hardening/softening (b), brick strength envelope (c), cohesive (d) and tensile (e) model

The connection among adjacent units is provided by zero-thickness linear or nonlinear interface springs, uniformly distributed along the contact surfaces, in which their mechanical properties are lumped. This intuitive computational scheme, exhaustively discussed in e.g. Meguro and Tagel-Din (2000, 2001, 2002), can be easily extended to the modelling of masonry structures, as reported in what follows.

An arbitrary masonry segment can be explicitly reproduced using the AEM by representing the actual unit arrangement as an assembly of solid rigid bodies, connected by equivalent spring layers to which the unit-mortar interface are assigned, according to a simplified micro-modelling approach. With reference to the nomenclature depicted in Figure 37(a), each spring is characterised by a normal and shear stiffness (Eqs. (3)-(4)), where E_u , G_u , E_{mo} and G_{mo} are the unit and mortar Young's and shear moduli respectively, while j and d stand for the spring number along y and z -direction respectively:

$$k_{nu} = \sum_{i=1}^j \left(\frac{E_u d \left(\frac{t_u}{j} \right)}{l_e} \right), \quad k_{su} = \sum_{i=1}^j \left(\frac{G_u d \left(\frac{t_u}{j} \right)}{l_e} \right) \quad (3)$$

$$k_{ni} = \sum_{i=1}^j \left(\frac{l_u - t_{mo}}{E_u d \left(\frac{t_u}{j} \right)} + \frac{t_{mo}}{E_{mo} d \left(\frac{t_u}{j} \right)} \right)^{-1}, \quad k_{si} = \sum_{i=1}^j \left(\frac{l_u - t_{mo}}{G_u d \left(\frac{t_u}{j} \right)} + \frac{t_{mo}}{G_{mo} d \left(\frac{t_u}{j} \right)} \right)^{-1} \quad (4)$$

It is worth noting that the equivalent interface spring stiffnesses (i.e. k_{ni} and k_{si}) were obtained assuming unit and mortar springs arranged in series at an arbitrary contact point, whilst the unit-to-unit ones (i.e. k_{nu} and k_{su}) only describe the interaction between identical materials. Such initial parameters, depending on the material constitutive laws selected, are modified at each timestep in order to account the damage evolution; when a given amount of springs has failed and their stiffness is set to zero, contact between units is lost.

Within the AEM framework, unit, joint and combined modes are described using simplified constitutive laws resulting in a definition of a linearised version of the compressive cap model originally developed by Lourenço et al. (1995), which features a simplified Mohr-Coulomb model for frictional phenomena, a tension cut-off and a compression cap. Interested readers may refer to e.g. Malomo et al. (2018a,b) for further details regarding how these expressions are employed depending on the considered failure mechanism. The numerical idealisation of both cohesive, compressive and tensile joint behaviour, together with the unit material failure envelope (Khoo and Hendry 1973), are depicted in Figure 37(b)-(e).

To faithfully represent damage mechanisms at the joint level, it is clear that each component of a given masonry element needs to be described in terms of its material properties. However, experimental campaigns rarely involve tests that would allow one to obtain all necessary material characterisation for units and mortar separately.

Thus, undertaking the approach proposed in Malomo et al. (2018b) empirical and homogenisation formulae were used to obtain first estimates of the required material parameters where direct experimental values were not available. To start with, the Young's modulus of both CS and CL bricks (E_b) are inferred by multiplying their compressive strength f_{cb} by an experimentally-derived constants, as follows:

$$\begin{array}{ll} \text{(Jäger et al., 2004)} & \text{CS brick} \quad E_b = (375) \cdot (f_{cb}) \quad (5) \end{array}$$

$$\begin{array}{ll} \text{(Kaushik et al., 2007)} & \text{CL brick} \quad E_b = (355) \cdot (f_{cb}) \quad (6) \end{array}$$

Then, the Young's modulus of mortar is obtained using Eqs. (7)-(10), based on homogenisation theory, as a function of those of masonry (E_m) and bricks (E_b), where ζ is the ratio between brick and mortar thickness. Then, the ensuing average is considered for modelling purposes and the associated shear moduli are obtained assuming material isotropy (Lekhnitskii 1963). The inferred values will be given in the next sections, together with their experimental counterparts.

$$\begin{array}{ll} \text{(Brooks and Baker, 1998)} & E_{mo} = \left(\frac{-4E_m E_b}{25E_m - 29E_b} \right) \quad (7) \end{array}$$

$$\begin{array}{ll} \text{(Matysek and Janowski, 1996)} & E_{mo} = \left(\frac{E_m E_b}{E_b - 1.25\zeta(E_m - E_b)} \right) \quad (8) \end{array}$$

$$\begin{array}{ll} \text{(Ciesielski, 1999)} & E_{mo} = \left(\frac{-E_m E_b}{5E_m - 6E_b} \right) \quad (9) \end{array}$$

$$\begin{array}{ll} \text{(U.B.C., 1991)} & E_{mo} = \left(\frac{E_m E_b}{\zeta(E_m - E_b) + E_b} \right) \quad (10) \end{array}$$

4.4 Numerical representation of building details and components

In this section, the modelling of different construction details and full-scale components, including URM walls subjected to both in-plane and OOP loading, as well as a cyclic test on a timber roof sub-structure, is presented and discussed. The findings of these numerical exercises, performed with a view to assess the AEM capabilities in adequately reproducing the response of both masonry and timber elements and for calibrating several key-parameters, were then directly implemented in the models of the specimens subjected to shake-table tests, discussed in the section that follows this one.

4.4.1 Idealisation of some construction details of terraced house test specimen

It is recalled that, as depicted in Figure 37(a), in the AEM framework interface springs are distributed uniformly along the contact surfaces, thus readily allowing the assignment of equivalent mechanical properties to such springs in order to describe the actual behaviour of a wide range of connection types (e.g. nailed, welded, interlocking, friction, etc.). In Figure 38, the most relevant connection/interface details considered in the developed AEM numerical model are illustrated, with some of which being further discussed below.

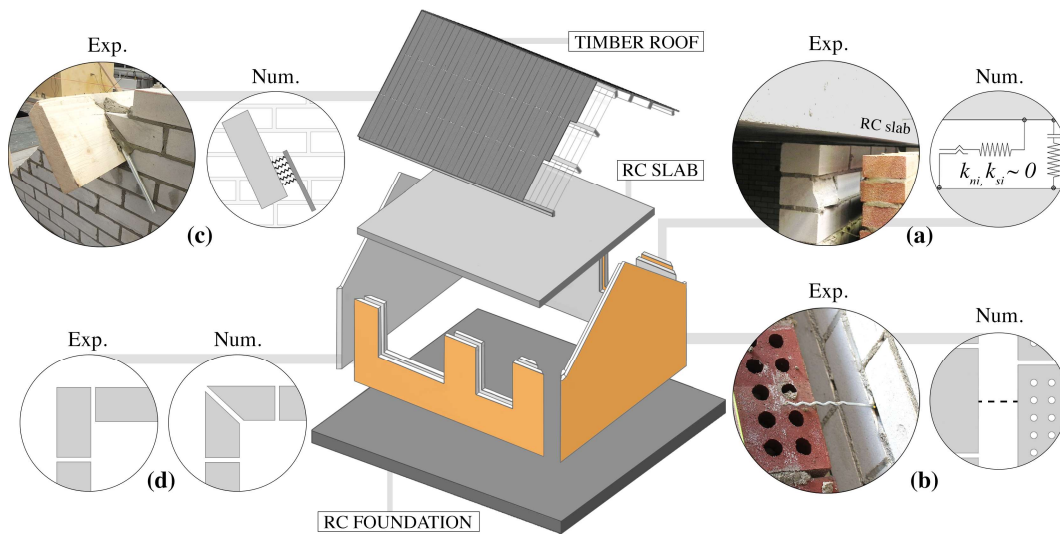


Figure 38. Constructive details of terraced house test specimen and numerical idealisations

As is typically done in common construction practice for this type of buildings, the reinforced concrete (RC) floor slabs of the specimens were supported by the CS inner leaf transverse walls only after construction completion, the gap that remained between the underneath of the 2nd floor RC slab and the top edge of the non-bearing longitudinal façades was filled with mortar. The frictional resistance that the latter may provide was likely to be limited due to lack of vertical compression, whilst the compressive strength was also likely affected by shrinkage phenomena; these two aspects have been accounted numerically by assigning reduced flexural and shear stiffness values to the corresponding interface springs (see Figure 38(a)). All details are given in Graziotti et al. (2017).

The connection of the specimen's roof substructure to the 2nd floor RC slab consisted of threaded bars screwed to the lateral timber joists; in the numerical model, interface elastic springs with very high stiffness were employed (also because no relative displacements were observed during the tests). For what concerns the ties or connectors between the two leaves of the cavity-walls, these featured a 3 mm diameter, a length of 200 mm, a “zigzag” end shape embedded within the CS bricks and an L-shaped extremity embedded on the CL panels. Their modelling was achieved through the use of bilinear beam elements placed in the model according to their actual distribution in the specimen. It is noted, however, that, in the numerical model, the contact between masonry and ties occurs only through the transverse section of the ties (see Figure 38(b)), given that the modelling of interpenetration phenomena between elements (such as the pull-out) would imply a very high computational burden. Since they typically failed within the CL mortar bonds, a bilinear constitutive law with post-peak softening branch and tension cut-off (experimentally-determined through quasi-static pull-out tests by Messali et al. (2016) was assigned to the CL wall-tie interfaces. On the CS panel side, instead, a linear elastic connection, characterised by the same flexural stiffness of the CS mortar, was employed.

Similarly, L-shaped anchors were idealised as 3D beam elements elastically connected to the joists. Their potential interaction with the gables was accounted by equivalent spring layers with only frictional resistance, as shown in Figure 38(c). Interlocking phenomena

among transversal and longitudinal walls was also implicitly represented, as indicated in Figure 38(d). Using this simplified modelling strategy, as shown in the following sub-section, an adequate agreement was found when comparing experimental and numerical OOP dynamic response of cavity-walls subjected to two-way bending.

4.4.2 Simulation of in-plane and out-of-plane tests on URM components

In this sub-section, the main findings and a selection of results related to the simulation of quasi-static and dynamic tests on full-scale cavity-wall components subjected to both in-plane and out-of-plane (OOP) loading, are presented and discussed, with particular emphasis on the loadbearing CS panels. For what concerns the modelling of in-plane cyclic tests on CS single leaf walls performed by Graziotti et al. (2015), a brick-based discretisation was employed for representing numerically the masonry panels. Then, an additional transversal subdivision was applied with a view to try to better capture the brick splitting phenomena that was observed during the tests, albeit the impact on the results of such refinement was however very mild. The joint tensile strength was assumed equal to the one inferred through bond-wrench tests, while an equivalent compressive strength (corresponding to one of the bricks) had to be assigned to the mortar material to avoid spurious interpenetration phenomena, as discussed in Malomo et al. (2018b).

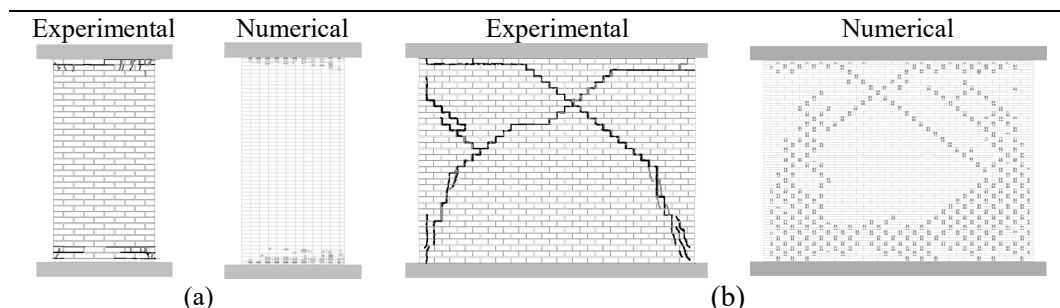


Figure 39. Slender (a) and squat (b) piers under in-plane cyclic loading: exp. vs num. crack patterns

This simplified procedure, which may overestimate the increase of mortar compressive strength due to the confinement effect, was proved to be acceptable in this modelling exercise, as shown in Figure 39, where the predicted crack patterns are compared with their experimental counterparts for the cases of slender and squat piers. Interested readers are referred to the dedicated paper by Malomo et al. (2018b), where full details are given, as well as the experimental versus numerical force-displacement envelopes.

With regards instead to the OOP one-way bending dynamic wall tests carried out by Graziotti et al. (2016), given that collapse was observed to occur always through the bed-joints, a standard brick-based mesh was adopted. When the cracks propagated through units, instead, as for the case of the central panel of the U-shaped specimens subjected to OOP two-way bending (Sharma et al. 2018), the bricks had to be discretised transversally in two regions. Regarding selection and interpretation of material properties, analogous assumptions to those made for the in-plane models were considered, whilst the contribution of tie connectors was accounted according to the methodology presented in the previous sub-section. Considering that OOP bending of masonry walls is a very brittle response

mechanism after cracking, an acceptable level of accuracy in terms of cracks propagation was obtained, as shown in Figure 40 for two of the considered CS and CL brick masonry specimens; a complete set of results for all ten walls modelled, including the corresponding hysteretic curves, can be found in Malomo et al. (2018a).

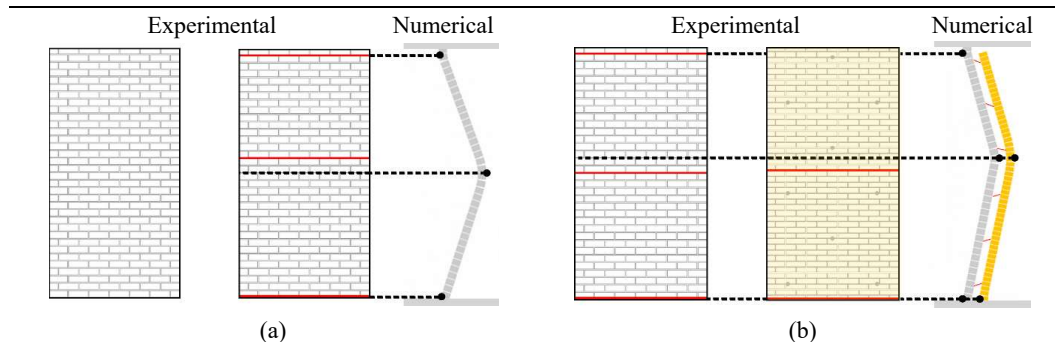


Figure 40. CS single leaf (a) and CS/CL cavity (b) walls under one-way bending OOP dynamic loading: exp. vs num. crack patterns

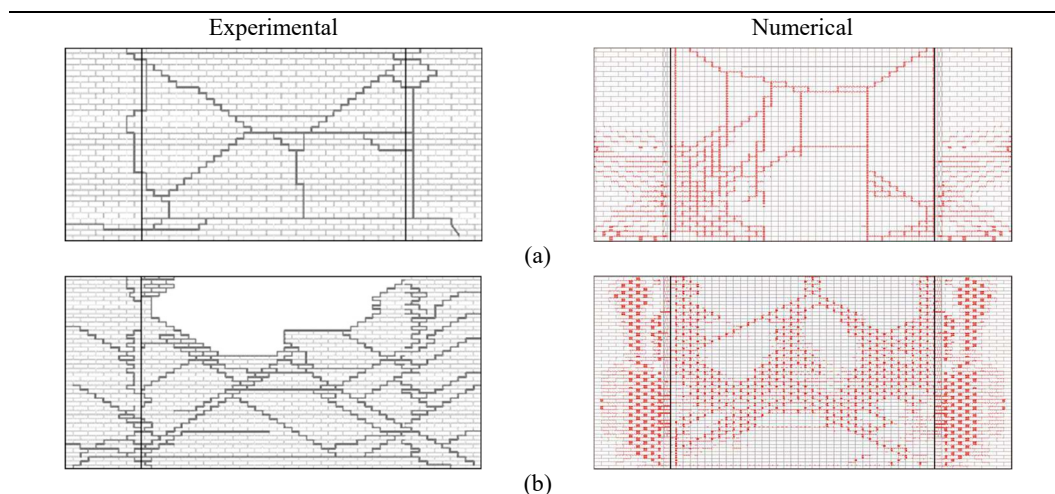


Figure 41. CS (a) and CL (b) single leaf walls under two-way bending OOP dynamic loading: exp. vs num. crack patterns

4.4.3 Modelling the in-plane cyclic performances of a timber roof sub-structure

A full-scale timber sub-structure, representative of a typical pitched roof system used in the terraced houses object of the experimental campaign considered in this study, was tested at the laboratory of LNEC (Correia et al., 2018). Such experiment followed the shake-table test on the complete specimen (i.e. LNEC-BUILD2), where the URM gable walls collapsed in an OOP fashion, as shown in the subsequent section, and it was performed after restoring the original configuration of the roof system. The latter was constituted by one ridge beam, two 1.20m-spaced joists per side among the ridge beam and two timber plates rigidly connected to RC foundation, as foreseen in Figure 42. Timber planks (182x18mm), covered by ceramic tiles, were placed on top using a couple of 60x2mm steel nails. Two quasi-static

full cycles of horizontal displacement imposed to the ridge beam through steel ties fixed to the lab strong walls, at ± 10 , ± 50 , ± 100 and ± 150 mm.

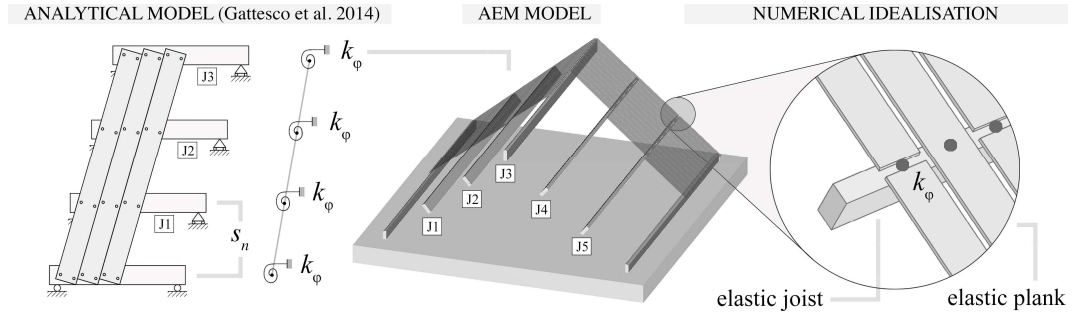


Figure 42. Configuration of LNEC-BUILD2 specimen and idealisation of nailed connections, joists and planks

The 43° pitched timber roof system was faithfully reproduced numerically by modelling each element separately, with a view to describe explicitly the relative in-plane rotations among planks and joists. Thus, the idealisation proposed in Figure 42 was adopted, according to which the contribution of nailed connections is accounted by a zero-thickness interface joint characterised by a rotational stiffness k_ϕ , while both joists and planks were modelled as solid elements with linear elastic behaviour. The system nonlinearity is essentially provided by a bilinear constitutive law with post-peak hardening assigned to the interface joints, which accurately approximates the typical response of laterally-loaded nails, as described by Foschi (1974). Considering the initial nail shear stiffness k_0 suggested by Eurocode 5 (CEN, 2004), as reported in Eq. (11) where ρ_m represents wood density and ϕ the nail diameter, and given the distance s_n between the nail couple, a first estimate of the initial rotational stiffness $k_{\phi 0}$ can be obtained through Eq. (12) as proposed by Gattesco and Macorini (2014):

$$k_0 = \left(\frac{\rho_m^{1.5} \cdot \phi^{0.8}}{30} \right) \quad (11) \quad k_{\phi 0} = \left(\frac{k_0 \cdot s_n^2}{2} \right) \quad (12) \quad k_{\phi 1} = \left(\frac{k_1 \cdot s_n^2}{2} \right) \quad (13)$$

Then, through the definition of the nail load-slip parameters k_1 , i.e. the experimentally-calibrated post-peak stiffness, and F_{max} , namely the maximum lateral capacity established from past researches (e.g. Dolan and Madsen 1992), the value of $k_{\phi 0}$ automatically changes into $k_{\phi 1}$ right after reaching F_{max} according to Eq. (13) above. Finally, both flexural and shear deformability contribution of timber boards to the in-plane response of the diaphragm were considered by defining an equivalent shear modulus G_d for plank elements, as suggested by Brignola et al. (2012), evaluated using Eq. (14) below, where X is shear factor, A board section and I moment of inertia of plank section, while G_p and E_p stand for shear and Young's modulus parallel to grain of planks respectively.

$$G_d = \left(\frac{X}{A} \right) \left(\frac{X}{G_p A} + \frac{L}{12 E_p I} \right)^{-1} \quad (14)$$

Moreover, based on experimental evidence (e.g. Wilson 2012), interlocking phenomena due to tongue and groove joint interfaces among timber boards were neglected, as well as

the contribution of tiles, which were modelled as lumped masses. In Table 18, the values associated with the abovementioned parameters are briefly summarised:

Table 18. Load-slip parameters of nailed connections and material properties of planks

NAILED CONNECTIONS	ρ_m	ϕ	s_n	k_0	k_t	$k_{\phi 0}$	$k_{\phi t}$
	[kg/m ³]	[mm]	[mm]	[N/mm]	[N/mm]	[kNmm/rad]	[kNmm/rad]
	450	2	80	554	24	1773	77
PLANK ELEMENTS	l	X	A	I	G_p	E_p	G_d
	[mm]	[-]	[mm ²]	[mm ⁴]	[MPa]	[MPa]	[MPa]
	1800	1.2	3600	120000	750	12000	121

In what follows, the numerical hysteretic curve was compared with its experimental counterpart. The specimen exhibited an elastic behaviour up until the second cycles, where some strength degradation occurred due to nail slip and partial pull-out. Then, the response remained rather stable. As it can be observed looking at Figure 43, a comparable response was obtained numerically, with the model producing acceptable results both in terms of deformed shape and hysteretic curve, albeit the capacity was slightly overestimated in the last cycles. Similarly, the evolution of displacements between the different roof joists (i.e. J1-J5), which remained linearly proportional to their elevation during the test, was adequately captured.

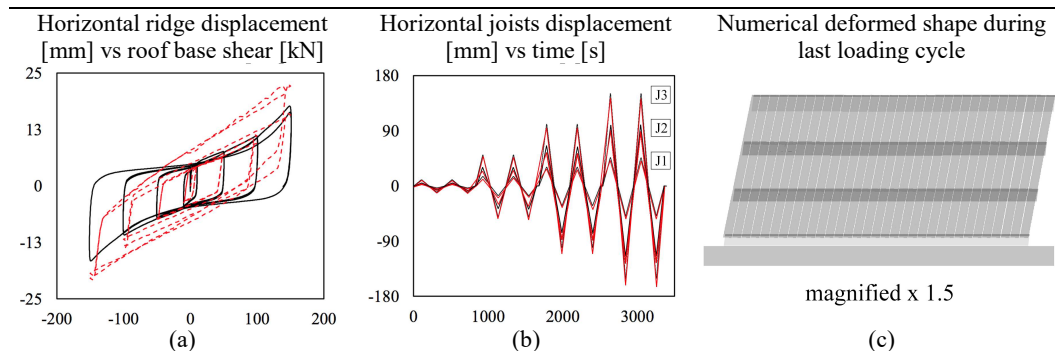


Figure 43. Exp. (black line) vs num. (red dashed line): (a) hysteretic response of the diaphragm, (b) relative displacement among timber joists J1-2-3 and (c) numerical deformed shape

4.5 Simulation of shake-table tests on URM building specimens

In this section, the experimental hysteretic behaviour, damage propagation and failure mode of the full-scale URM building specimens tested dynamically at both LNEC (i.e. LNEC-BUILD1/2) and EUCENTRE (i.e. EUC-BUILD1) laboratories are compared with their numerical counterparts. The specimens were built with analogous construction techniques and materials, but at a different time. Hence, slight differences in terms of masonry mechanical properties were obtained during characterisation tests, albeit the same CS (212x103x71mm) and CL (212x100x50mm) bricks and comparable mortar bond thicknesses (10mm) were always employed. Use was made of the modelling strategy presented in the previous section, although in some specific cases, when peculiar details or testing protocols were introduced, some modifications to the initial assumptions had to be considered on a case-by-case basis, as further discussed in the following. It is recalled that,

with a view to optimise the calibration process, the specimens were modelled in the opposite order with respect to the actual testing sequence (see Figure 36).

4.5.1 LNEC-BUILD2: attic-roof substructure

The LNEC-BUILD2 prototype was a full-scale timber roof with ceramic tiles, supported on URM gables constituted by cavity-walls (2 ties/m²) and on an RC slab, representative of the attic-roof system of EUC-BUILD1. Thus, the seismic input introduced at the base of LNEC-BUILD2 specimen corresponded to the second floor accelerations that had been recorded during the EUC-BUILD1 test. It was 5.82m long, 5.46m wide and 2.45m high with a total mass of 17.8 tons. With reference to the nomenclature reported in Figure 44, it is noted that the CL veneer was not present on the East side, because the specimen was meant to represent the end-unit of a set of terraced houses. Further details can be found in Correia et al. (2017, 2018).



Figure 44. Plan (in cm) and experimental configuration of LNEC-BUILD2 (Correia et al. 2018)

The specimen was fixed to the shake-table, and the loading protocol shown in Table 19 in terms of peak table acceleration (PTA), where the damage limit states (DLs) identified by Correia et al. (2018) are also reported, was subsequently imposed up to complete collapse.

Table 19. LNEC-BUILD2: testing sequence, experimental damage evolution and associated limit states (Correia et al. 2018)

Test ID	PTA [g]	DLs [-]	Test ID	PTA [g]	DLs [-]
FEQ1-50%	0.07	-	FEQ2-200%	0.49	DL ₂ – EG cracks
FEQ1-100%	0.14	-	FEQ2-300%	0.67	DL ₂ – EG cracks
FEQ1-150%	0.17	DL ₀ – no visible damage	FEQ2-400%	0.94	DL ₃ – several EG cracks
FEQ2-50%	0.11	DL ₀ – no visible damage	FEQ2-500%	0.96	DL ₄ – heavy damage EG; WG cracks
FEQ2-100%	0.21	DL ₁ – plaster cracks	FEQ2-600%	1.14	DL ₅ – EG collapse
FEQ2-150%	0.25	DL ₁ – plaster cracks	-	-	-

A selection of the main masonry material properties (directly implemented in the model), including compressive strength of masonry f_{cm} , flexural bond strength f_w , cohesion c and friction coefficient μ , obtained through characterisation tests on small-scale assemblies and Eqs. (7)-(10), is reported in Table 20:

Table 20. LNEC-BUILD2: experimental and inferred masonry material properties considered

	CS - density $\delta_m = 1796$ [kg/m ³]								CL - density $\delta_m = 1833$ [kg/m ³]							
	f_{cm}	f_{cb}	f_w	E_m	c	μ	E_b	E_{mo}	f_{cm}	f_{cb}	f_w	E_m	c	μ	E_b	E_{mo}
Avg [MPa]	7.0	18.7	0.3	6090	0.4	0.5	8990	2662	16.2	63.2	0.2	12661	0.4	0.7	7211	3535
C.o.V. [%]	0.1	0.1	0.2	-	-	-	0.4	-	0.1	0.1	0.5	-	-	-	0.2	-

Besides the modelling assumptions previously discussed, the following are also of relevance:

- The timber joists were pocketed into the URM walls through their entire thickness, and the remaining gap was filled with mortar. Thus, a mortar interface was introduced numerically for representing potential unseating of the joists
- Based on damage observation, the wooden plate connecting joists and CL West gable wall (which worked as a rigid-overturning preventing system) was modelled as a linear elastic continuous shell coupling the joists longitudinally through equivalent elastic spring layers
- A standard brick-based discretisation was assigned to the URM elements, since only failure through mortar joints was observed during the test.

In Figure 45, a comparison between numerical and experimental outcomes, presented in terms of hysteretic behaviour for each loading cycle (starting from FEQ2-200%, i.e. when nonlinear response became predominant), is proposed:

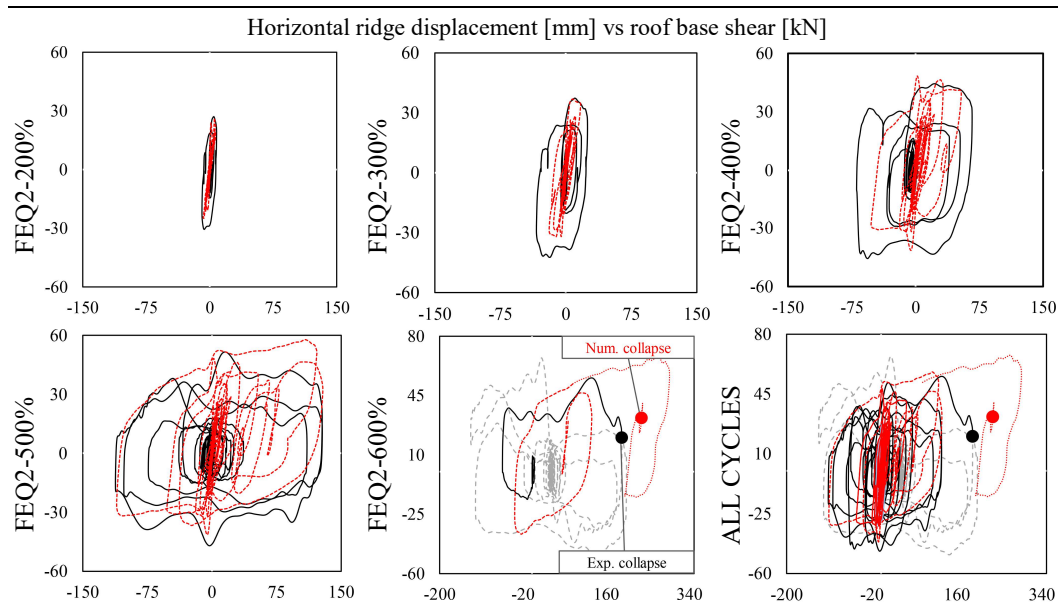


Figure 45. LNEC-BUILD2: Exp. (black line) vs num. (red dashed line) hysteretic response

The predicted force-displacement response marginally underestimated both energy dissipation and deformation capacity in the first cycles, albeit a seemingly acceptable agreement with experimental results in terms of initial and residual stiffness, base shear and overall resistance could nonetheless be found. The numerical collapse occurred at the

beginning of FEQ2-600%, when the cavity-wall gable on the West side failed in an OOP fashion, albeit the CS single leaf gable wall on the East side was already severely damaged (see Figure 46). Although the specimen exhibited a collapse mode slightly different (i.e. CS gable OOP failure), the predicted ultimate displacement capacity, appeared comparable.

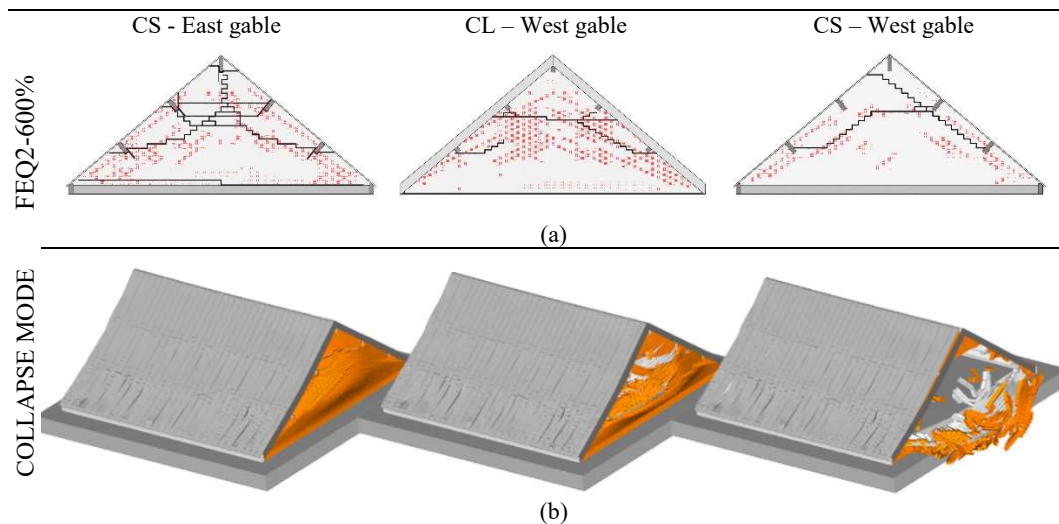


Figure 46. LNEC-BUILD2: (a) Exp. (black) vs num. (red) crack propagation at FEQ2-600% and (b) numerical collapse mode

4.5.2 LNEC-BUILD1: 2nd floor-roof substructure

The LNEC-BUILD1 building specimen was meant to represent the upper levels of the EUC-BUILD1 specimen. It consisted of a single-storey full-scale prototype 5.82 m long, 5.46 m wide and 4.93 m high with a total mass of 31.7 tons, with cavity-walls (2 ties/m²) and pitched timber roof covered by ceramic tiles. The gable-diaphragm system was substantially analogous to LNEC-BUILD2 in terms of both constructive details and overall geometry. As in the previous case, the outer CL panel was not present on the East side (see Figure 47). As discussed before, the first floor RC slab was not in contact with the longitudinal walls, which were also characterised by the presence of large openings with RC lintels, and the interface gap was filled with mortar after construction completion.



Figure 47. Plan (in cm) and experimental configuration of LNEC-BUILD1 (Tomassetti et al. 2017)

The incremental biaxial dynamic loading protocol, representative of the first-floor accelerations recorded during EUC-BUILD1 shake-table test, reported in Table 21 together with the DLs proposed by Tomassetti et al. (2017), was applied until up collapse of the specimen.

Table 21. LNEC-BUILD1: testing sequence, experimental damage evolution and associated limit states (Tomassetti et al. 2017)

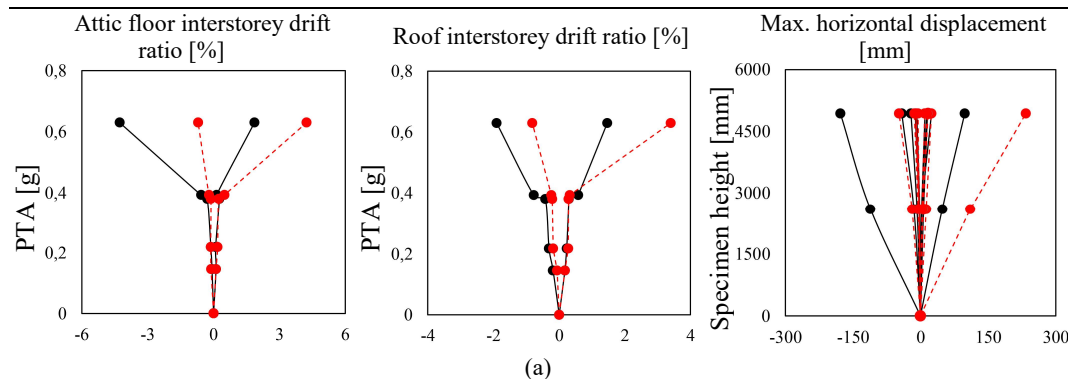
Test ID	H-PTA [g]	V-PTA [g]	DLs [-]	Test ID	H-PTA [g]	V-PTA [g]	DLs [-]
FEQ1-50%	0.06	0.04	DL ₀ – no visible damage	FEQ2-100%	0.22	0.10	DL ₂ – NW cracks
FEQ1-100%	0.12	0.07	DL ₀ – no visible damage	FEQ2-150%	0.38	0.21	DL ₃ – NW/SW cracks
FEQ1-150%	0.15	0.12	DL ₁ – plaster cracks	FEQ2-200%	0.39	0.18	DL ₄ – EW onset collapse
FEQ2-50%	0.09	0.07	DL ₁ – plaster cracks	FEQ2-300%	0.63	0.34	DL ₅ – EW collapse

The experimentally-derived masonry material properties, as well as the ones inferred using Eqs. (7)-(10), are reported in Table 22.

Table 22. LNEC-BUILD1: experimental and inferred masonry material properties considered

	CS - density $\delta_m = 1800$ [kg/m ³]								CL - density $\delta_m = 1839$ [kg/m ³]							
	f_{cm}	f_{cb}	f_w	E_m	c	μ	E_b	E_{m0}	f_{cm}	f_{cb}	f_w	E_m	c	μ	E_b	E_{m0}
Avg [MPa]	9.8	16.3	0.4	7955	0.4	0.5	8990	4537	19.4	32.5	0.2	13118	0.4	0.8	7211	3332
C.o.V. [%]	0.1	0.1	0.2	0.2	-	-	0.4	-	0.1	0.1	0.5	0.1	-	-	0.2	-

The dynamic response of the specimen was mainly governed by flexural/rocking modes, in particular of the longitudinal CS slender piers, which then led to an important uplift of the RC slab (during FEQ2-300%), which in turn triggered the OOP collapse of the consequently no longer vertically loaded CS transverse (see Tomassetti et al. 2017). Given the encouraging results obtained for LNEC-BUILD2, the model was developed considering analogous assumptions. Moreover, aimed at reproducing the experimental conditions in the static range, the top course of bricks of the North and South façades were deleted – and then restored – after the application of gravity loads. In Figure 48, the predicted attic and roof displacements, expressed in terms of attic floor and roof interstorey drift ratios (note that for the roof the drift ratio is given by the maximum relative ridge displacement divided by the inclined length of the roof), as well as the hysteretic behaviour for each test phase, were compared with their experimental counterparts.



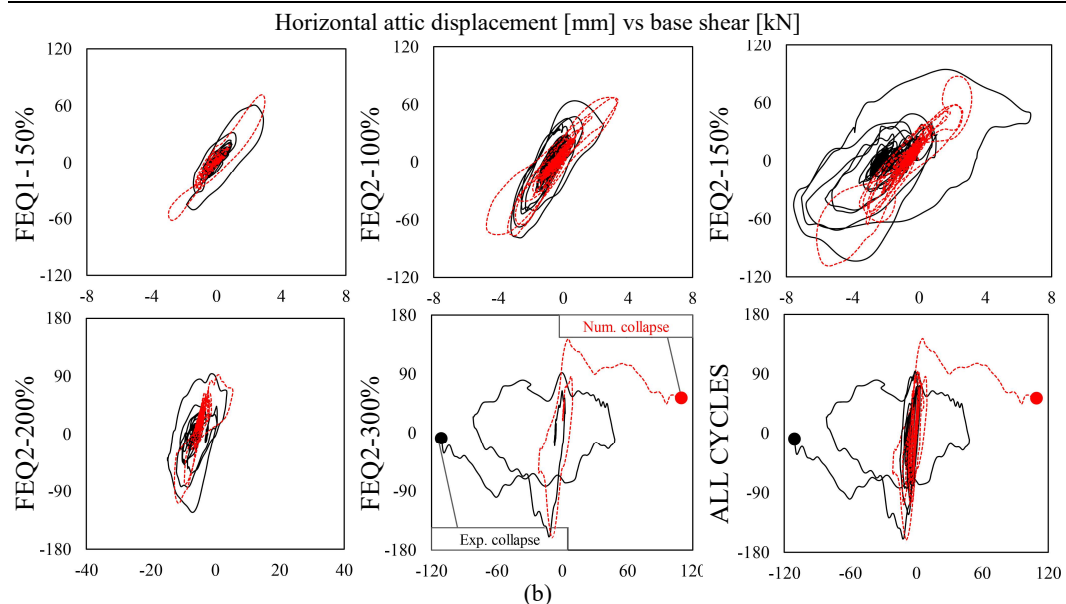
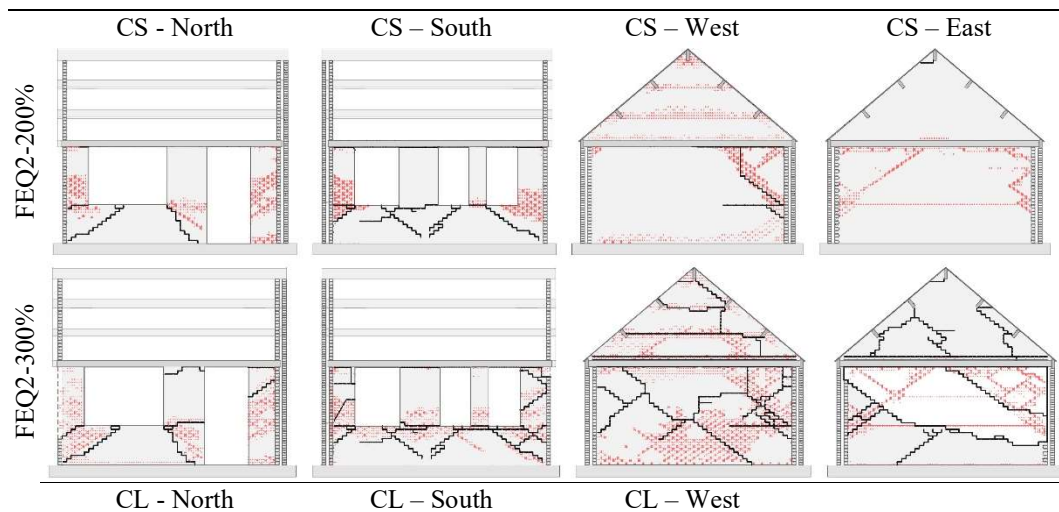


Figure 48. LNEC-BUILD1: Exp. (black) vs num. (red) (a) IDA curves and (b) hysteretic response

The response predicted by the model appears in good agreement with the one exhibited by the specimen, both in terms of overall capacity and displacement demand, though the energy dissipation was not always fully captured. This aspect might be due to the simplified tension cut-off criterion implemented in the interface springs, which in case of flexural damage neglects the post-peak energy dissipation.

Numerical collapse occurred slightly before its experimental counterpart, which may explain the differences in the hysteresis curves of FEQ2-300%. However, the damage evolution, as well as the OOP failure mechanism of the CS single leaf wall, was captured in a relatively satisfactory manner, as depicted in Figure 49.



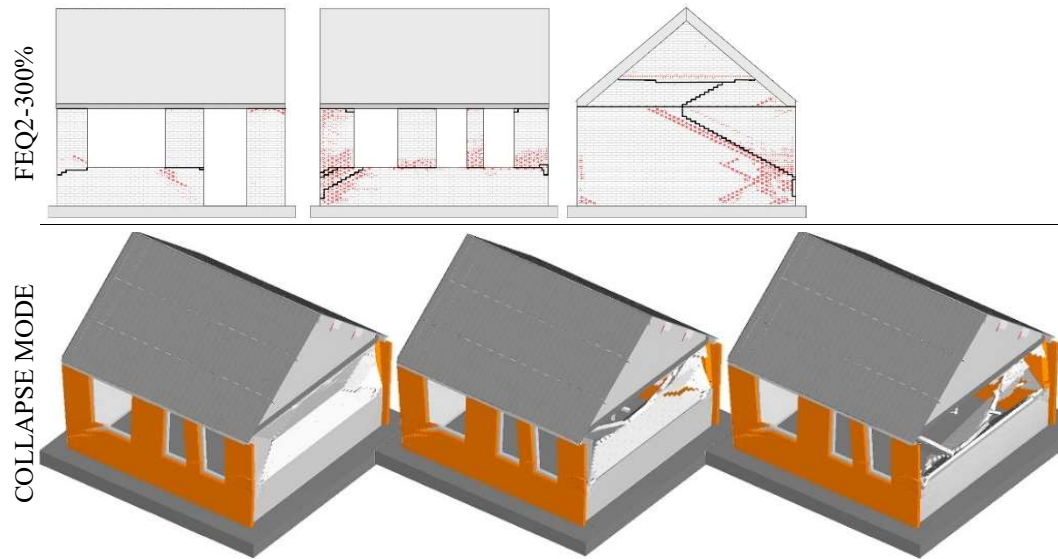


Figure 49. LNEC-BUILD1: (a) Exp. (black) vs num. (red) damage evolution and (b) numerical collapse mode

It is worth noting that the model was able to account explicitly for the interaction between the CS longitudinal piers and the RC slab, resulting in a satisfactory representation of the OOP collapse of the East CS wall induced by the diaphragm uplift, which, as noted in Figure 50, had a maximum value of 28 mm in the numerical model (whilst in the test it was not explicitly measured).

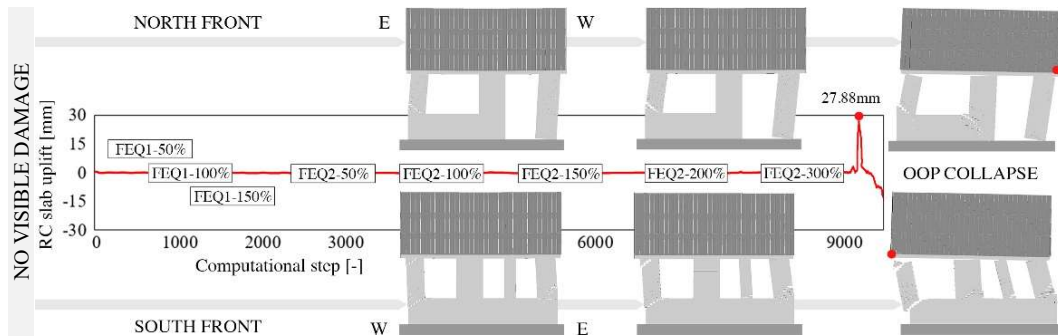


Figure 50. LNEC-BUILD1: Num. rocking response of CS longitudinal piers and RC slab uplift (varied displacement magnifications)

4.5.3 EUC-BUILD1: complete structure

The EUC-BUILD1 full-scale building prototype consisted of a two-storey cavity-wall system, 5.82m long, 5.46m wide and 7.76m high with a total mass of 56.4 tons, with RC floors, timber roof and constructive details analogous to those of LNEC-BUILD1, with the CL veneer not present on one side (see Figure 51) and the slabs only supported by CS transversal walls.



Figure 51. Plan (in cm) and experimental configuration of EUC-BUILD1 (Graziotti et al. 2017)

The testing sequence reported in Table 23 was incrementally applied to the structure, and the corresponding DLs were identified (Graziotti et al. 2017) between each loading phase.

Table 23. EUC-BUILD1: testing sequence, experimental damage evolution and associated limit states (Graziotti et al. 2017)

Test ID	PTA [g]	DLs [-]	Test ID	PTA [g]	DLs [-]
EQ1-25%	0.02	DL ₁ – no visible damage	EQ2-100%	0.16	DL ₂ – minor str. damage
EQ1-50%	0.05	DL ₁ – no visible damage	EQ2-125%	0.19	DL ₂ – minor str. damage
EQ1-100%	0.09	DL ₁ – no visible damage	EQ2-150%	0.24	DL ₃ – damage in all the CS piers
EQ1-150%	0.14	DL ₂ – minor str. damage	EQ2-200%	0.32	DL ₄ – near-collapse conditions

Table 24. EUC-BUILD1: experimental and inferred masonry material properties considered

	CS - density $\delta_m = 1835$ [kg/m ³]								CL - density $\delta_m = 1905$ [kg/m ³]							
	f_c^m	f_c^b	f_w	E_m	c	μ	E_b	E_{m0}	f_c^m	f_c^b	f_w	E_m	c	μ	E_b	E_{m0}
Avg [MPa]	6.2	18.7	0.2	4182	0.2	0.4	6628	1574	11.3	45.8	0.2	6033	0.1	0.7	17175	1624
C.o.V. [%]	0.1	0.1	0.2	0.3	-	-	-	-	0.1	0.03	0.6	0.3	-	-	-	-

The specimen (for which the masonry properties are summarised in Table 24) exhibited a pronounced flexural/rocking response, with the first significant cracks detected at EQ2-150% in the longitudinal CS panels/spandrels. No visible cracks were observed at this stage in the CL walls. Then, due to the elongation of pre-existing cracks and because of both the activation of OOP two-way bending mechanisms in the CS transversal walls, together with the substantial damage experienced by the CL façades, near-collapse conditions were reached after EQ2-200% (Graziotti et al. 2017). The numerical strategy adopted for the model of EUC-BUILD1 was analogous to the one of LNEC-BUILD1, except for the connection among the first floor RC slab/CS transversal walls (which was not present in the latter case), provided by threaded bars with a diameter of 6mm and 250mm-spaced. Based on experimental evidence, such system was idealised as a continuous equivalent elastic spring layer, which rigidly coupled the response of these elements. In Figure 52, a comparison between test and numerical outcomes is given, it can be gathered that the model seemed to have captured adequately the shake-table performance of the specimen throughout all the test. More specifically, the experimental displacement demand at the

different floor levels was satisfactorily represented numerically, as well as the roof progressive deformation. This positive impression is further confirmed by what is shown in Figure 53, where experimental and numerical crack propagation patterns appear comparable, albeit the model marginally overestimated the damage in the CS spandrels at EQ2-150% and in the CS transversal façades. Slight differences were also observed in terms of residual roof displacements and overall capacity, especially during EQ2-200%.

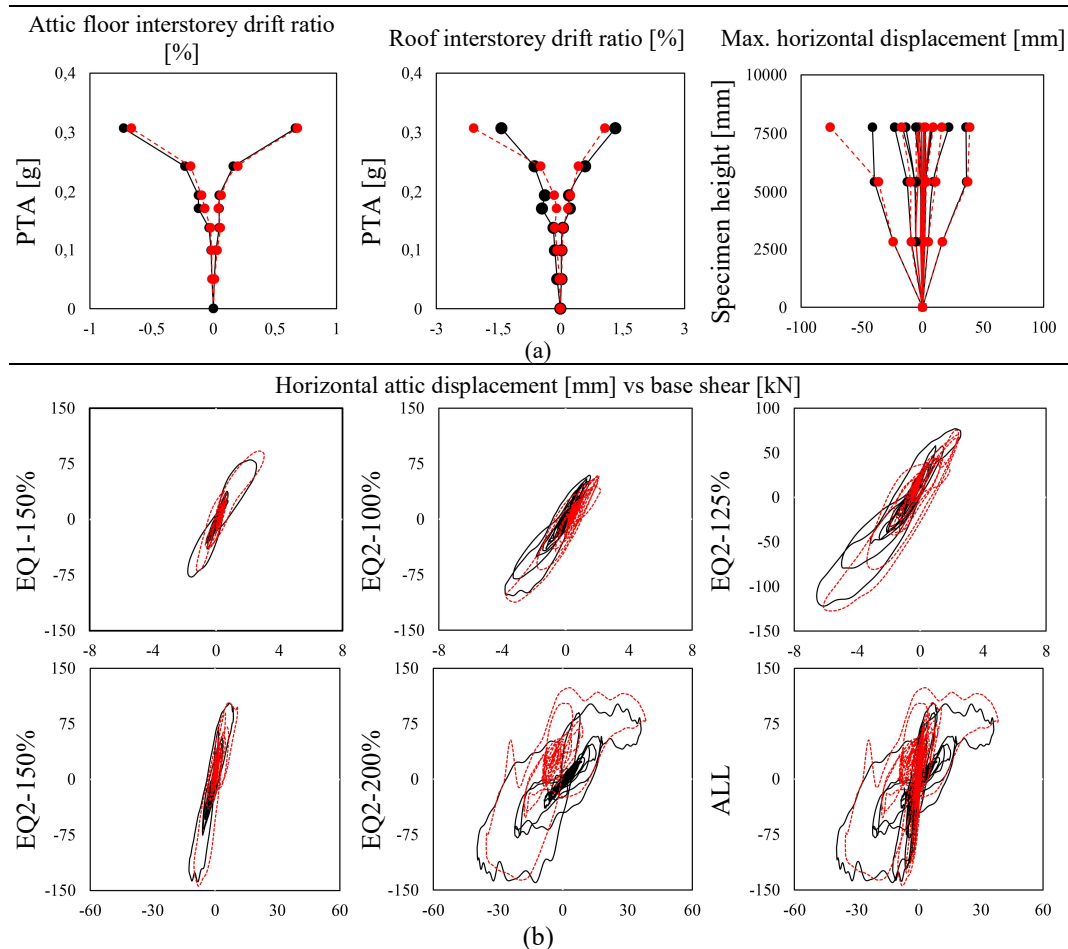
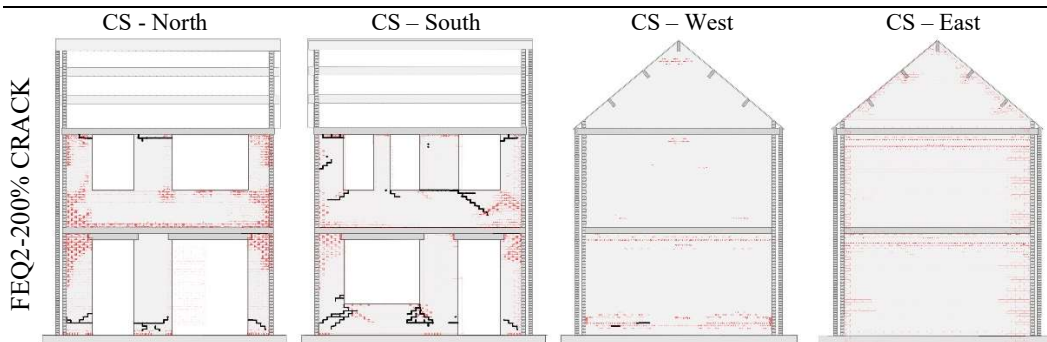


Figure 52. EUC-BUILD1: (a) Exp. (black) vs num. (red) IDA curves and (b) hysteretic response



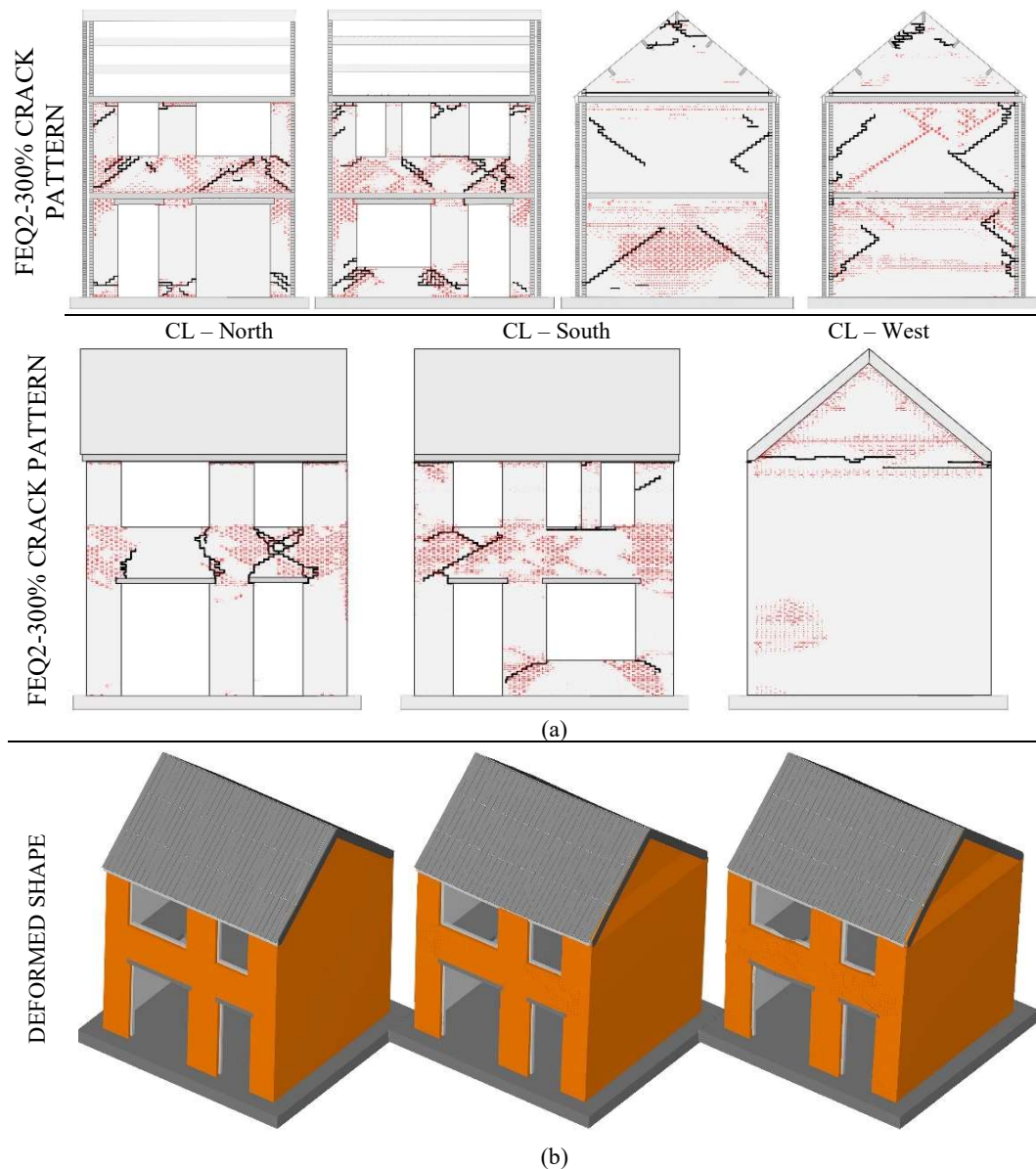


Figure 53. EUC-BUILD1: (a) Exp. (black) vs num. (red) damage evolution and (b) numerical deformed shape

Contrary to LNEC-BUILD2, the response of the roof of EUC-BUILD1 was simulated appropriately throughout all the cycles, albeit the latter was calibrated considering the same modelling assumptions. This aspect might be due to the fact that in the first case an explicit collapse occurred, possibly influencing the associated maximum roof deformations in the last cycles. Further, different spring interfaces (depending on the mortar properties) were assigned between joists and walls, which may have affected the displacement demand of the system.

4.6 Conclusions

In this work, the capability of the Applied Element Method (AEM) to simulate in-plane and out-of-plane mechanisms of URM elements, as well as the behaviour of roof timber systems, were firstly scrutinised and verified through comparison against experimental outcomes on both full-scale components and building sub-structures, up to full collapse. Then, taking advantage of the findings inferred from each numerical exercise, the modelling of a complete terraced house unit structural system, tested dynamically, was proposed. The analyses results seem to indicate that a satisfactorily level of accuracy can be reached, given that the predicted hysteretic responses, damage evolutions and collapse modes have shown a good agreement with their experimental counterparts.

Nonetheless, further improvements are still warranted, perhaps most noteworthy the possibility of including post-peak softening laws in tension for the interface joint model, given that the absence of such modelling capability seems to in some cases have led to an underestimation of the level of dissipated energy. Other possible enhancements might include the extension of the employed methodology to the simulation of more complex large-scale phenomena, such as pounding and dynamic interaction between adjacent terraced house units.

Acknowledgements

The work described in this paper was carried out within the framework of the research programme on hazard and risk of induced seismicity in the Groningen region, sponsored by the Nederlandse Aardolie Maatschappij BV (NAM). The authors also acknowledge all those at both the European Centre for Training and Research in Earthquake Engineering (Eucentre, Pavia, Italy) and Laboratório Nacional de Engenharia Civil (LNEC, Lisbon, Portugal) that were involved in the testing campaign referred to in this paper, and in particular Francesco Graziotti, Umberto Tomassetti and António Correia, for their precious assistance in accessing the test data. Finally, the collaboration of the technical support staff from Applied Science International LLC (ASI), on the use of the employed AEM software - Extreme Loading for Structures, is also acknowledged.

References

- Applied Science International LLC. (2018). "Extreme Loading for Structures (2018)." Durham (NC), USA.
- Brignola, A., Pampanin, S., and Podestà, S. (2012). "Experimental Evaluation of the In-Plane Stiffness of Timber Diaphragms." *Earthquake Spectra*, Earthquake Engineering Research Institute, 28(4), 1687–1709.
- Brooks, J. J., and Baker, A. (1998). "Modulus of Elasticity of Masonry." *Masonry International*, 12(2), 58–63.
- Candeias, P. X., Campos Costa, A., Mendes, N., Costa, A. A., and Lourenço, P. B. (2017). "Experimental Assessment of the Out-of-Plane Performance of Masonry Buildings Through Shaking Table Tests." *International Journal of Architectural Heritage*, Taylor & Francis, 11(1), 31–58.
- Cannizzaro, F., and Lourenço, P. B. (2017). "Simulation of Shake Table Tests on Out-of-Plane Masonry Buildings. Part (VI): Discrete Element Approach." *International Journal of Architectural Heritage*, Taylor & Francis, 11(1), 125–142.

- CEN European Committee for Standardization; (2004). *EN 1995-1-1:2004, Eurocode 5. Design of timber structures. Part 1-1: General rules and rules for buildings*. NA to BS EN.
- Chácara, C., Mendes, N., and Lourenço, P. B. (2017). “Simulation of Shake Table Tests on Out-of-Plane Masonry Buildings. Part (IV): Macro and Micro FEM Based Approaches.” *International Journal of Architectural Heritage*, Taylor & Francis, 11(1), 103–116.
- Ciesielski, R. (1999). “The dynamic module of elasticity of brick walls.” *Proceedings of the Conference of the Committee of Civil Engineering PZITB: Lublin, Poland*.
- Correia, A. A., Marques, A. I., V. B., Grotoli, L., Tomassetti, U., and Graziotti, F. (2017). *Shake table test up to collapse on a roof substructure of a Dutch terrace house*. Pavia, Italy.
- Correia, A. A., Tomassetti, U., Campos Costa, A., Penna, A., Magenes, G., and Graziotti, F. (2018). “Collapse shake-table test on a URM-timber roof substructure.” *16th European Conference on Earthquake Engineering*, Thessaloniki, Greece.
- Cundall, P. A. (1971). “A computer model for simulating progressive large scale movements in blocky rock systems.” *Proc. Symp. Rock Fracture (ISRM)*, Nancy.
- Dolan, J. D., and Madsen, B. (1992). “Monotonic and cyclic nail connection tests.” *Canadian Journal of Civil Engineering*, NRC Research Press, 19(1), 97–104.
- Elshaer, A., Mostafa, H., and Salem, H. (2017). “Progressive collapse assessment of multistory reinforced concrete structures subjected to seismic actions.” *KSCE Journal of Civil Engineering*, Korean Society of Civil Engineers, 21(1), 184–194.
- de Felice, G., De Santis, S., Lourenço, P. B., and Mendes, N. (2017). “Methods and Challenges for the Seismic Assessment of Historic Masonry Structures.” *International Journal of Architectural Heritage*, Taylor & Francis, 11(1), 143–160.
- Foschi, R. O. (1974). “Load-slip characteristics of nails.” *Journal of Wood Science*, 7(1), 69–76.
- Garofano, A., and Lestuzzi, P. (2016). “Seismic Assessment of a Historical Masonry Building in Switzerland: The ‘Ancien Hôpital De Sion.’” *International Journal of Architectural Heritage*, Taylor & Francis, 10(8), 975–992.
- Gattesco, N., and Macorini, L. (2014). “In-plane stiffening techniques with nail plates or CFRP strips for timber floors in historical masonry buildings.” *Construction and Building Materials*, Elsevier, 58, 64–76.
- Graziotti, F., Tomassetti, U., Kallioras, S., Penna, A., and Magenes, G. (2017). “Shaking table test on a full scale URM cavity-wall building.” *Bulletin of Earthquake Engineering*, Springer Netherlands, 15(12), 5329–5364.
- Graziotti, F., Tomassetti, U., Penna, A., and Magenes, G. (2016). “Out-of-plane shaking table tests on URM single leaf and cavity-walls.” *Engineering Structures*, Elsevier, 125, 455–470.
- Graziotti, F., Tomassetti, U., Rossi, A., Kallioras, S., Mandirola, M., Cenja, E., Penna, A., and Magenes, G. (2015). *Experimental campaign on cavity-wall systems representative of the Groningen building stock - Report n. EUC318/2015U*. Pavia, Italy.
- Guragain, R., Worakanchana, K., Mayorca, P., and Meguro, K. (2006). “Simulation of brick masonry wall behavior under cyclic loading using applied element method.” *Bulletin of ERS*, Institute of Industrial Science The University of Tokyo, 58(6), 531–534.
- Jäger, W., Irmschler, H., and Schubert, P. (2004). *Mauerwerk-Kalender 2004*. Ernst &

- Sohn Verlag für Architektur und technische Wissenschaften.
- Karbassi, A., and Nollet, M.-J. (2013). "Performance-based seismic vulnerability evaluation of masonry buildings using applied element method in a nonlinear dynamic-based analytical procedure." *Earthquake Spectra*, Earthquake Engineering Research Institute, 29(2), 399–426.
- Kaushik, H. B., Rai, D. C., and Jain, S. K. (2007). "Stress-strain characteristics of clay brick masonry under uniaxial compression." *Journal of materials in Civil Engineering*, American Society of Civil Engineers, 19(9), 728–739.
- Khoo, C. L., and Hendry, A. W. (1973). "Strength tests on brick and mortar under complex stresses for the development of a failure criterion for brickwork in compression." *Proceedings of the British Ceramic Society*, 51–66.
- Lekhnitskii, S. G. (1963). *Of an anisotropic elastic body*. Holden-Day, San Francisco, USA.
- Lourenço, P. B., Rots, J. G. J. G., and Blaauwendraad, J. (1995). "Two approaches for the analysis of masonry structures - micro and macro-modeling." *Research article HERON - Delft Univ. of Technology (Delft, The Netherlands)*, 40(4), 313–340.
- Malomo, D., Comini, P., Pinho, R., and Penna, A. (2018a). "Validating numerical modelling of out-of-plane dynamic response of masonry walls through comparison with full-scale shake-table tests." *Journal of Structural Engineering, ASCE - to be submitted*.
- Malomo, D., Pinho, R., and Penna, A. (2018b). "Using the applied element method for modelling calcium silicate brick masonry subjected to in-plane cyclic loading." *Earthquake Engineering & Structural Dynamics*, 47(7), 1610–1630.
- Matysek, P., and Janowski, Z. (1996). "Analysis of factors affecting the modulus of elasticity of the walls." *Proceedings of the Conference of the Committee of Civil Engineering PZITB: Lublin, Poland*.
- Meguro, K., and Tagel-Din, H. (2000). "Applied element method for structural analysis: Theory and application for linear materials." *Structural Engineering/Earthquake Engineering*, Japan Society of Civil Engineers, 17(1), 21s--35s.
- Meguro, K., and Tagel-Din, H. (2001). "Applied Element Simulation of RC Structures under Cyclic Loading." *Journal of Structural Engineering*, 127(11), 1295–1305.
- Meguro, K., and Tagel-Din, H. (2002). "Applied Element Method Used for Large Displacement Structural Analysis." *Journal of Natural Disaster Science*, 24(1), 25–34.
- Messali, F., Esposito, R., and Maragna, M. (2016). "Pull-out strength of wall ties." *Report, TU Delft, NL*.
- Penna, A., Senaldi, I. E., Galasco, A., and Magenes, G. (2016). "Numerical Simulation of Shaking Table Tests on Full-Scale Stone Masonry Buildings." *International Journal of Architectural Heritage*, Taylor & Francis, 10(2–3), 146–163.
- Roca, P., Cervera, M., Gariup, G., and Pela', L. (2010). "Structural analysis of masonry historical constructions. Classical and advanced approaches." *Archives of Computational Methods in Engineering*, 17(3), 299–325.
- Salem, H., Mohssen, S., Nishikiori, Y., and Hosoda, A. (2016). "Numerical Collapse Analysis of Tsuyagawa Bridge Damaged by Tohoku Tsunami." *Journal of Performance of Constructed Facilities*, 30(6), 04016065.
- Sharma, S., Tomassetti, U., Grottoli, L., and Graziotti, F. (2018). *Out-of-plane two-way bending shaking table tests on single leaf and cavity-walls - Report n. EUC137/2018U*. Pavia, Italy.

- Tomassetti, U., Correia, A. A., Marques, A., Graziotti, F., and Penna, A. (2017). “Dynamic collapse testing of a full-scale URM cavity-wall structure.” *Proceedings of ANIDIS, L’ingegneria Sismica in Italia*, Pisa University Press, Pistoia, Italy, 83–93.
- Tomažević, M., and Gams, M. (2012). “Shaking table study and modelling of seismic behaviour of confined AAC masonry buildings.” *Bulletin of Earthquake Engineering*, 10(3), 863–893.
- U.B.C. (1991). “International Conference of Building Officials. Uniform Building Code.” *International conference of building officials, USA*, Whittier, USA.
- Wilson, A. (2012). “Seismic assessment of timber floor diaphragms in unreinforced masonry buildings.” University of Auckland.

CHAPTER 5

Shake-table response of a double-leaf
unreinforced clay brick masonry house specimen



CHAPTER 5 Shake-table response of a double-leaf unreinforced clay brick masonry house specimen

Malomo, D., Pinho, R., and Penna, A. (2018). “Applied Element modelling of the dynamic response of a full-scale clay brick masonry specimen with flexible diaphragms. *International Journal of Architectural Heritage*, to be submitted.

Abstract. The seismic assessment of typical unreinforced masonry buildings in The Netherlands, recently exposed to low-intensity ground motions induced by gas extraction, is becoming the focus of both experimental and numerical research. Their design, originally not conceived for earthquake-resistance, often features the presence of both large openings and flexible diaphragms, and the lack of any specific seismic consideration or detailing further increase the associated vulnerability towards horizontal loading. In this paper, the Applied Element Method, which explicitly represents the discrete nature of masonry, is used to simulate the shake-table response of a full-scale building specimen representative of a typical Dutch detached house made of unreinforced solid clay-brick masonry. Using this modelling strategy, the damage evolution, as well as both global failure mode and hysteretic behaviour, are described. The results have shown a good agreement with the experimentally-observed response, confirming the capabilities of the Applied Element Method in reproducing effectively the large-scale response of masonry structures, whilst simultaneously keeping computational costs within acceptable limits for this time of detailed modelling.

Keywords: applied element method; numerical modelling; shake-table; flexible diaphragms; unreinforced masonry.

5.1 Introduction

The Groningen region, in the north of The Netherlands, recently experienced low-intensity ground motions due to gas extraction (Bommer and van Elk 2017; van Elk et al. 2018). Local existing unreinforced masonry (URM) structures, originally not conceived for earthquake-resistance, represent the majority of the building stock, as noted by Crowley and Pinho (2017). Most of such constructions, indeed, were designed without any seismic consideration of detailing, further increasing their vulnerability towards horizontal actions. Amongst others, the detached house typology, which commonly features one or two-storeys and flexible diaphragms, is largely widespread. Such typical Dutch URM buildings are characterised by double-wythe solid clay brick walls, irregular plan configurations, large openings and timber roof. Given the limited knowledge on the dynamic performances of this specific building type, a full-scale prototype has been tested on the shake-table of the laboratory of EUCENTRE (Pavia, Italy) in 2016. The specimen, named EUC-BUILD2, was subjected to ground motions of increasing intensity, until up to near-collapse

conditions. The associated experimental campaign, whose further details are available in e.g. Graziotti et al. (2016) and Kallioras et al. (2018), also comprised characterisation tests on small-scale masonry samples and a number in-plane quasi-static cyclic tests on URM panels subjected to different overburden pressures and boundary conditions. The experimentally-observed behaviour of the building specimen, as expected, was the result of a combination of several aspects of responses, including the nonlinear interaction between diaphragm systems and masonry elements, as well as the effect of geometrical irregularities. Moreover, the presence of peculiar constructive details (e.g. masonry trapezoidal lintels, metallic anchors among floor, timber joists and walls) contributed significantly to its complexity. With reference to the general framework, since Dutch detached houses present a large variety of architectural schemes, roof shapes and masonry properties (Arup 2015), whose influence cannot be investigated experimentally for understandable reasons, the development of reliable numerical models able to account for the abovementioned aspects might improve consistently both assessment and future seismic retrofitting activities.

Several modelling techniques of different levels of complexity and computational burden are available for reproducing analytically the behaviour of masonry structures. Simplified computational methods, such as equivalent frame (e.g. Addessi et al. 2015; Penna et al. 2014; Raka et al. 2015) and storey-mechanism (e.g. Braga and Dolce 1982; Tomaževič 1987) models, might represent an effective solution, permitting a time- and cost-saving structural analysis even in case of large-scale structures, as shown by recent applications (e.g. Kallioras et al. 2018a; Tomaževič and Gams 2012). However, as extensively discussed in Quagliarini et al. (2017), the explicit representation of out-of-plane (OOP) modes is usually neglected, often confining their application to in-plane-governed responses. Thus, more refined and computationally-demanding numerical procedures, based on both continuum and discontinuum domain, have been developed so far, and a comprehensive review of these methods can be found in e.g. Roca et al. (2010) and Lemos (2007). The use of both micro and macro Finite Element (FE) models for the modelling of entire URM buildings is widespread, and reasonable results were obtained by many authors (e.g. Castellazzi et al. 2017; Mendes and Lourenço 2014; Saloustros et al. 2018). This notwithstanding, only a few of these applications (e.g. Chácaras et al. 2017) provided comparisons with shake-table test outcomes. Similarly, although various different discrete element approaches have been considered for the simulation of large-scale URM constructions, ranging from the Non-Smooth-Contact-Dynamics (NSCD) (Chetouane et al. 2005), employed for the analysis of the Roman monumental structures (e.g. Rafiee et al. 2008), to the Distinct Element Method (DEM) (Cundall 1971), successfully applied by several researchers especially in case of dry-joint historical assemblies (e.g. Papantonopoulos et al. 2002; Psycharis et al. 2003), there is still some lacking of consistency in literature regarding the numerical representation of dynamic tests on URM building specimens. In this framework, adequate results were obtained by Galvez et al. (2018) and Lemos and Campos Costa (2017) in the modelling of a two-storey and U-shaped prototypes respectively, where deformations and collapse patterns were identifiable in the numerical simulations. However, as reported by the latter authors, despite the fact that the only reduced-scale specimens were modelled, a high computational burden was needed for performing the analyses, especially in the post-cracked range.

A different numerical approach, which partially overcomes these issues, characterises the rigid body and spring models (RBSM), typically based on the mechanical interaction between rigid units connected by linear or nonlinear springs (Kawai 1978). Originally conceived for handling static problems, many applications (e.g. Casolo and Sanjust 2009; Casolo and Uva 2013) have shown that, under several assumptions and considering relatively small structures or representative sub-systems, satisfactory results can be obtained even in the dynamic range. The basic idea of RBSM, according to which the global response of a rigid body assembly can be described considering spring elongation and failures, represents a significant advantage in terms of computational cost if compared to other methods. Indeed, reduced degrees of freedom and matrix dimensions are commonly needed, as further discussed in e.g. Casolo (2000). Several upgrades to this original scheme were also implemented by Pantò et al. (2017), who proposed a discrete macro-element model (DMEM) based on a simplified fibre-discretisation strategy and characterised by the introduction of additional spring layers for accounting diagonal shear damage. However, in the case of RBSM, as noted by Furukawa et al. (2012), the simulation of large displacement problems still represent a challenge, since the recontact between neighbouring elements (if different from the ones initially set) is usually neglected. On the other hand, the use of DMEM seems to be promising, as proved by some recent applications (e.g. Cannizzaro and Lourenço 2017), albeit numerical simulations of the dynamic response of tested full-scale URM buildings are not presently available in literature.

In this work, aimed at overcoming the abovementioned limitations, an alternative RBSM-based discrete numerical approach, the Applied Element Method (AEM) (Meguro and Tagel-Din 2000, 2001, 2002), has been selected and consequently employed for reproducing the experimental shake-table performances of a full-scale URM prototype representative of a typical Dutch detached house. Such computational technique, currently implemented in the commercial software Extreme Loading for Structures (ELS) developed by ASI (2018), which is steadily gaining popularity, has been already extensively validated through comparison with a wide range of experimental outcomes referred to the same testing campaign, including in-plane quasi-static tests on calcium-silicate URM components (Malomo et al. 2018c), OOP shake-table tests on URM U-shaped assemblies (Malomo et al. 2018a) and shake-table tests on a full-scale cavity-wall building specimen (Malomo et al. 2019b). Moreover, with a view to calibrate the model on this specific solid clay brick masonry type, several characterisation tests on small-scale masonry samples (i.e. bond-wrench, shear-compression and four-point OOP flexural tests), as well as the in-plane response of full-scale URM piers subjected to shear-compression cyclic loading, were replicated numerically. With reference to the simulation of EUC-BUILD2 prototype, since it was characterised by a large variety of constructive details and by the presence of a complex timber roof system, a specific modelling strategy was developed in order to account appropriately for their dynamic interaction with adjacent URM elements in a reasonable timeframe. The employment of this methodology, combined with the possibility of representing explicitly in-plane modes, OOP failure mechanisms and crack propagation up to collapse or near-collapse conditions, resulted in a relatively satisfactory prediction of both hysteretic behaviour and damage pattern. Finally, since a good agreement was found, and because the test was stopped before complete collapse, additional analyses were performed to determine numerically the maximum sustainable shake-table motion intensity and the governing failure mechanisms.

5.2 The Applied Element Method and the modelling of URM structures

The standard formulation of AEM, developed by Meguro and Tagel-Din (2000, 2001, 2002), can be easily adapted for simulating the mechanical response of URM elements, as shown by e.g. Mayorca and Meguro (2003). For what concerns its application towards the modelling of URM components subjected to in-plane actions, adequate results were obtained by e.g. Guragain et al. (2006), Malomo et al. (2018b) and Pandey and Meguro (2004). Similarly, the quasi-static response of OOP-loaded URM reduced-scale URM samples was investigated successfully by e.g. Karbassi and Nollet (2013) and Sathiparan et al. (2005), as well as the dynamic behaviour of URM panels subjected to both blast loading (Keys and Clubley 2017) and shake-table motions (Malomo et al. 2018b). The seismic performances of existing and monumental large-scale buildings were also assessed numerically using AEM (e.g. Garofano and Lestuzzi 2016; Karbassi and Lestuzzi 2012), albeit in most of these cases no comparisons with experimental results was available. In this respect, some recent applications have shown good agreement with the experimentally-observed shake-table responses of both reduced (Domaneschi et al. 2018; Sathiparan et al. 2012) and full-scale (Malomo et al. 2019b) building prototypes. In what follows, a brief overview of the AEM formulation for masonry structures, and an empirical-based procedure to infer unit and mortar material properties when experimental outcomes are not available, is proposed. Interested readers may refer to the publications listed at the beginning of this section for further details. According to the AEM, each unit is modelled as a rigid body, carrying only mass and damping of the system, which interacts with the adjacent ones by means of equivalent interface zero-thickness springs, representing unit-mortar mechanical properties according to a simplified micro-modelling approach (Lourenço et al. 1995). Unit failure can be accounted for by subdividing each element along the vertical or longitudinal direction. In this case, additional unit-to-unit spring layers are needed for describing effectively crushing, splitting or flexural phenomena. In Figure 54, a graphical representation of these concepts is proposed:

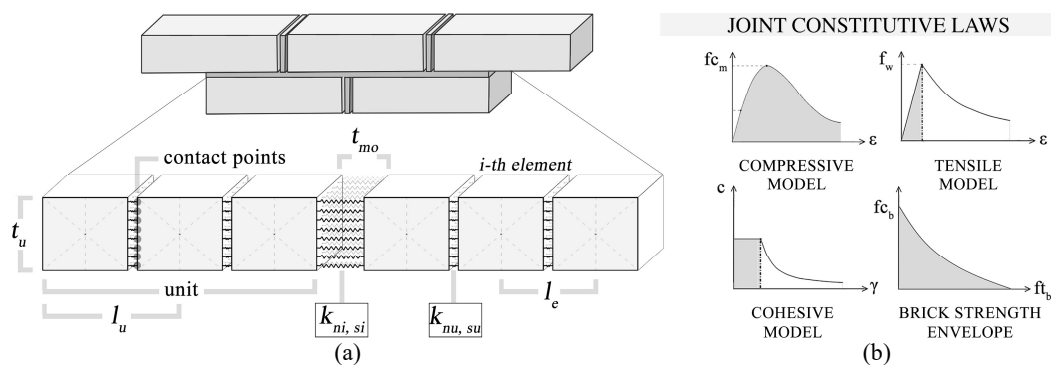


Figure 54 Three-dimensional discretisation of a masonry segment according to the AEM (a) and considered joint/unit failure criteria (b)

As it can be gathered from Figure 54, a post-peak cut-off criterion is commonly employed for spring tensile failure, whilst a nonlinear relation is assigned normal springs for simulating progressive deterioration of compressive strength. Shear damage is idealised through a Mohr-Coulomb-like bilinear law, neglecting any cohesion softening branch, which is set to zero right after reaching the maximum shear strength. Hence, the global

nonlinear behaviour of the assembly and the associated crack pattern evolution are obtained by considering the local failure of each spring according to the abovementioned criteria. Then, when a given amount of springs has failed and their stiffness is set to zero, contact between units is lost. The analytical description of both unit-to-unit (k_{nu} , k_{su}) and interface (k_{ni} , k_{si}) normal and shear spring stiffnesses, is reported in Eqs. (1)-(2), where d is the distance between two consecutive springs along the transversal direction, while E_u , E_{mo} , G_u , G_{mo} stand for the Young's and shear moduli of unit and mortar respectively.

$$k_{nu} = \sum_{i=1}^j \left(\frac{E_u d \left(\frac{t_u}{j} \right)}{l_u} \right), \quad k_{su} = \sum_{i=1}^j \left(\frac{G_u d \left(\frac{t_u}{j} \right)}{l_u} \right) \quad (1)$$

$$k_{ni} = \sum_{i=1}^j \left(\frac{l_u - t_{mo}}{E_u d \left(\frac{t_u}{j} \right)} + \frac{t_{mo}}{E_{mo} d \left(\frac{t_u}{j} \right)} \right)^{-1}, \quad k_{si} = \sum_{i=1}^j \left(\frac{l_u - t_{mo}}{G_u d \left(\frac{t_u}{j} \right)} + \frac{t_{mo}}{G_{mo} d \left(\frac{t_u}{j} \right)} \right)^{-1} \quad (2)$$

Depending on the considered mechanism and system orientation, in-plane and OOP local modes are accounted by normal, shear or both of the interface (or unit-to-unit) springs, as depicted in Figure 55:

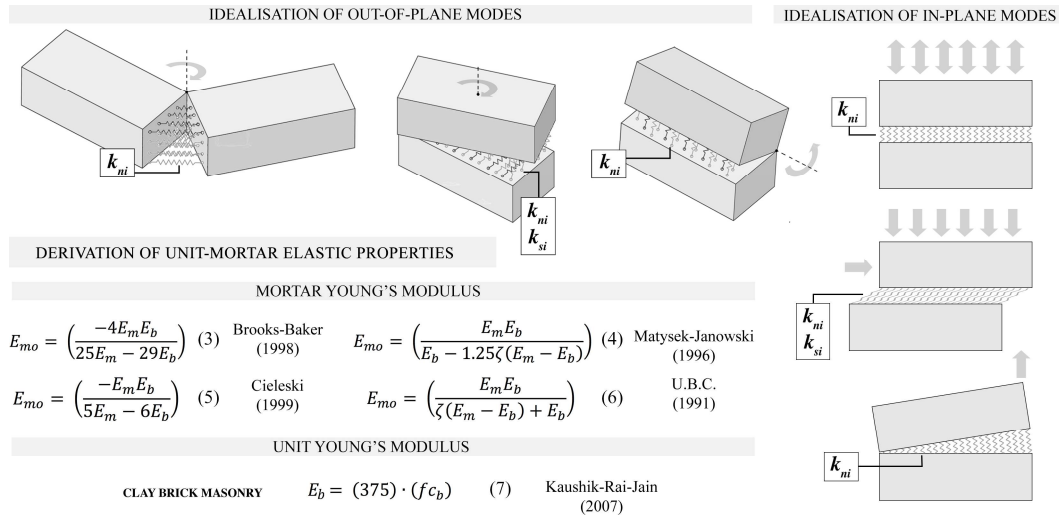


Figure 55 AEM representation of in-plane and OOP modes (a), analytical derivation of unit (Jäger et al. 2004; Kaushik et al. 2007) (b) and mortar (b) material properties (Brooks and Baker 1998; Ciesielski 1999; Matysek and Janowski 1996; U.B.C. 1991)

With reference to Figure 55, it is clear that both unit and mortar properties are needed for describing numerically joint, unit and hybrid failures. However, experimental campaigns on masonry elements rarely involve tests that would allow one to obtain all necessary material characterisation for unit and mortar separately. Thus, undertaking the same approach described in Malomo et al. (2018c), empirical and homogenisation formulae (i.e. Eqs. (3-7), see Figure 55) were used to obtain first estimates of the required material parameters where direct experimental outcomes were not available, where f_{cb} brick compressive strength, E_m masonry Young's modulus and ζ ratio of brick's height to the

thickness of mortar joint. Then, starting from the ensuing average values, an iterative calibration process was applied until obtaining satisfactory results.

5.3 Modelling of constructive details and sub-components of typical clay brick masonry Dutch detached houses

In this section, the idealisation of a large selection of typically-employed constructive details which characterised the pre-1940's URM Dutch detached houses is proposed. Then, the simplified modelling strategy developed for representing numerically the dynamic performances of the timber roof structure of EUC-BUILD2, which can be also potentially extended to the simulation of a wide range of other existing and historical buildings with common features, is presented and discussed, as well as a first verification of AEM against laboratory results obtained through in-plane and OOP tests on both URM samples and full-scale components. Interested readers may refer to the dedicated paper by Kallioras et al. (2018b) for further clarifications regarding the structural details of EUC-BUILD2 and the associated nomenclature herein employed for describing timber diaphragm components.

5.3.1 Idealisation of constructive details

The detached house URM building typology, largely widespread in the Groningen region since before World War II, presents a wide range of peculiar constructive details, including wall-to-floor and wall-to-roof nailed or screwed connections, trapezoidal-shaped masonry lintels and interlocking timber joints. In the AEM framework, the interface springs are located at specific contact points and distributed uniformly along the inner surfaces, representing the stress/strain state of a given volume δV and the contact stiffness. This modelling approach thus readily allows assigning equivalent mechanical properties to interface spring layers in order to describe the actual behaviour of a wide range of connection types, as summarised in Figure 56 for the case of EUC-BUILD2:

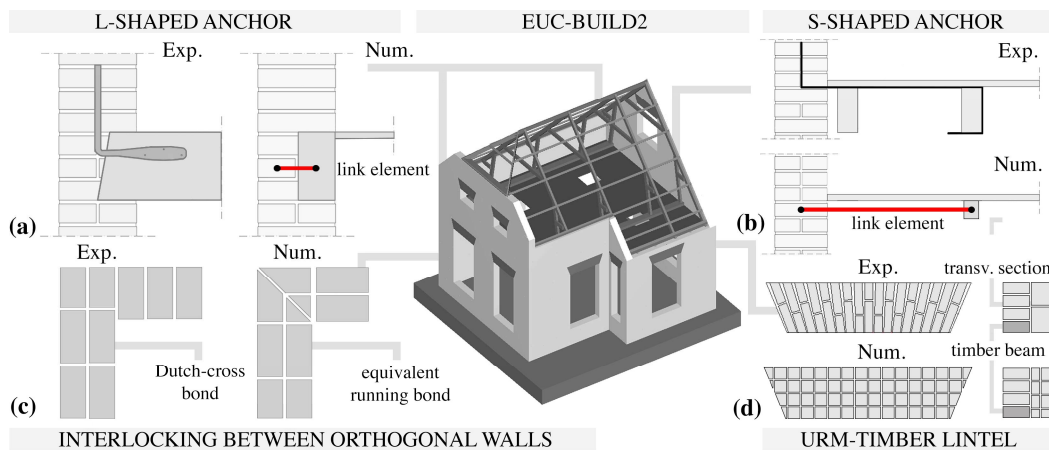


Figure 56 Numerical idealisation of constructive details of EUC-BUILD2

The timber floor joists are commonly pocketed into the masonry elements for half of the wall thickness, and the remaining gap filled with mortar. In addition, 14-mm-diameter L-shaped steel anchors, screwed to the joists and embedded into the masonry among the two wythes, were placed along West/East façades of EUC-BUILD2. These aspects have been

accounted numerically by assigning a mortar material to interface springs, together with the introduction of a bilinear link element with tension cut-off, which connected the joist extremities to the centroid of the corresponding outer bricks, with an equivalent maximum pull-out force equal to 11 kN (NZSEE 2006). Similarly, S-shaped steel anchors (900x30x5 mm), located at mid-span of each façade, provided a more effective floor-to-wall connection in the direction perpendicular to the gables (i.e. North and South sides) avoiding early OOP failure modes, have been idealised as above.

Masonry lintels of different geometries, depending on opening width, were built above all openings. They consisted in flat-arches constituted by vertically-placed cut bricks with stretchers facing outwards, supported by 100x50 mm timber beams (see Figure 56). The lintel trapezoidal shape has been faithfully reproduced numerically, even though the actual brickwork could not be explicitly described. It is herein noted, indeed, that the current version of the employed AEM code only allows the representation of a standard stretcher bond pattern, as further discussed in the following sections. Hence, lintels were modelled as an assembly of elastic beams (to which were assigned timber material properties) and equivalent homogenised masonry elements, finely subdivided both longitudinally and transversally for accounting for potential flexural and shear cracks. Interlocking phenomena among walls were implicitly represented, as gathered from Figure 56, according to the simplified approach proposed by Malomo et al. (2019b).

These modelling assumptions, whose effectiveness will be investigated in detail in the subsequent sections, resulted in a significant reduction of computational cost. Indeed, the explicit representation of small elements (e.g. anchors, connectors) would imply a considerable increase of time step required for stable dynamic analysis, which is a function, in addition of element mass and contact stiffness, of the minimum unit size.

5.3.2 Numerical representation of timber diaphragms

The typical diaphragm types of pre-1940's Dutch terraced house are usually constituted by the assembly of timber joists and planks, without the presence of additional reinforcement solutions, resulting in a relatively low in-plane stiffness. In the case of EUC-BUILD2, the timber floor was made of 200x24-mm-thick timber floorboards, nailed perpendicularly to ten 80x180 mm timber joists spanning continuously between the East and West URM walls (Figure 57). On the contrary, the roof external shape combined two different end geometries: a half-hipped roof with a clipped gable at the North façade and a full-height gable at the South façade (Kallioras et al. 2018b). The roof structure comprised four East-West timber trusses (64x114 mm), which supported longitudinal North-South purlins (44x64 mm) and a ridge beam (38x120 mm). With respect to the latter, continuous timber boards (200x18 mm) were arranged perpendicularly and connected through a couple of 150-mm-spaced 3-mm-diameter nails. Finally, clay tiles, supported by a grid of laths and counter battens, were nailed on the top. The floor system, considering also the additional masses (provided by rubber blocks), weighed 1.8 tons, approximately 0.1 tons in less than the whole roof structure.

In this endeavour, two different strategies were developed for reproducing numerically the dynamic response of the timber diaphragms briefly described above, as represented in Figure 57. Because of the complexity of the considered timber systems, and since this

experimental campaign did not feature any specific tests on timber components and connectors, simplified procedures were employed, as discussed in what follows.

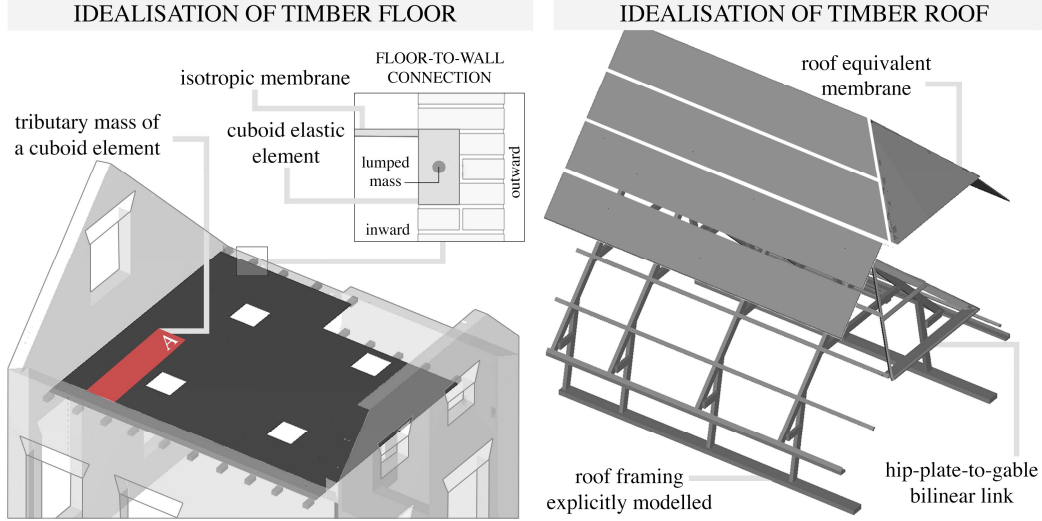


Figure 57 Modelling of both floor (a) and roof (b) timber diaphragms of EUC-BUILD2

The first-floor diaphragm has been idealised as a continuous isotropic membrane element, characterised by an equivalent shear modulus Gf_{eq} , defined using the simplified analytically-based approach proposed by Gattesco and Macorini (2014). According to the latter, and considering the nail slip modulus k_{ser} (provided by Eurocode 5 (2005)) and the associated rotational stiffness k_{ϕ} reported in Eqs. (8)-(9), a first estimate of the overall in-plane stiffness in case of loads acting perpendicularly to the joists can be obtained employing Eq. (9), with n_j and n_b number of joists and boards respectively.

$$k_{ser} = \left(\frac{\rho_m^{1.5} \phi^{0.8}}{30} \right) \quad (8)$$

$$k_{\phi} = \left(k_{ser} \frac{s_n^2}{2} \right) \quad (9)$$

$$K_d = \left(\frac{n_j n_b k_{\phi}}{H^2} \right) \quad (10)$$

$$Gf_{eq} = \left(\frac{K_d H}{t_b B} \right) \quad (11)$$

Then, Gf_{eq} can be determined with Eq. (11), where H stands for half of the diaphragm length, B is the floor span length and t_b the board thickness. The inferred values, including the considered wood density ρ_m , nail diameter ϕ and spacing s_n , are summarised in Table 25. It is worth noting that potential interlocking phenomena due to tongue and groove connections among planks, as well as their actual arrangement, could not be reproduced using this methodology. However, according to both numerical (Brignola et al. 2012) and experimental (Wilson et al. 2014) outcomes, their effect seems to be almost negligible. In order to account for the actual distribution of gravity loads, and for the mechanical interaction between floor and walls, the membrane was rigidly attached to cuboid elastic elements, representing the portion of joists embedded into the longitudinal façades, in which the mass of the system was lumped (see Figure 57). An analogous approach was employed for the modelling of the complex timber roof structure. However, in this case, the shaking direction was parallel to the purlins, to which the planks were nailed. Hence, the equivalent shear modulus Gr_{eq} assigned to the roof membrane was inferred through a

different analytical procedure, developed by Brignola et al. (2008). It accounts implicitly for nail slip and shear/flexural deformations of boards, combining such contributions of flexibility according to Eq. (11), where X (assumed equal to 1.2) is the shear factor, l_j average wheelbase between joists, G_p shear modulus of planks, E_p flexural modulus parallel to the grain of planks, A_p board section and I_p associated moment of inertia.

$$Gr_{eq} = \left(\frac{X}{A_p} \right) \left(\frac{l_j}{k_{ser} s_n^2} + \frac{X}{G_p A_p} + \frac{l_j^2}{12 E_p I_p} \right)^{-1} \quad (11)$$

In this case, the equivalent roof membrane was discontinuous, i.e. it was interrupted at each intersection with purlins, ridge and hip rafter/wall-plate beams, to which the various regions were rigidly connected. Indeed, the roof framing, which comprises rafters and purlins (inclined at an angle of 47°), strut, tie and collar tie timber beams, has been explicitly represented with a view to maximising the accuracy related to the distribution of gravity loads, which was not straightforward. In this respect, it is worth mentioning that the mass of both planks and clay tiles has been lumped into the roof trusses by assigning an equivalent density. In Table 25, the mechanical parameters employed for the modelling of timber diaphragms are summarised:

Table 25 Modelling parameters employed for the timber diaphragms of EUC-BUILD2

FLOOR system	ρ_m [kg/m ³]	ϕ [mm]	s_n [mm]	k_{ser} [N/mm]	k_ϕ [kNmm/rad]	K_d [N/mm]	Gf_{eq} [MPa]
	450	3	150	766	8618	72	1.4
ROOF system	l_j [mm]	A_p [mm ²]	s_n [mm]	E_p [MPa]	G_p [MPa]	I_p [mm ⁴]	Gr_{eq} [MPa]
	0.93	3600	120	12000	750	1.2e7	3.9

The interlocking joints connecting the roof members to each other were modelled as only-frictional spring layers. The same properties were also assigned at the interface between rafters and gables, since they only interacted through sliding/pounding phenomena. The interface among timber purlins and URM walls, as for the case of floor joists, is provided by mortar interface springs. Based on post-test damage observation, instead, a rigid connection between timber wall-plates and longitudinal façades was introduced, thus preventing spurious sliding failure.

On the contrary, although the nailed connection between hip wall-plate and North gable did not exhibit complete failure during the shake-table test, it has been represented by combining the use of an only-frictional spring layer with bilinear links with the stiffness of the employed nails (k_{ser}) and a tension cut-off equal to the maximum lateral capacity of the latter, i.e. 500 N, established according to Dolan and Madsen (1992). That was done in order to simulate potential collapse modes of the gables, which was particularly vulnerable towards OOP mechanisms.

5.3.3 Simulating in-plane and out-of-plane failure modes of URM elements

In this subsection, a first comparison between experimental and numerical results is presented. This modelling exercise, which featured the simulation of small-scale masonry samples (i.e. doublets, triplets and wallettes) subjected to bond-wrench, shear-compression

and OOP flexural tests, as well as the in-plane cyclic behaviour of full-scale URM piers (named CL1, CL2, CL3, CL5), were aimed at calibrating the mechanical properties to be assigned to the AEM model of EUC-BUILD2. Full details on both experimental protocols and interpretation of test results are given in the dedicated report by Graziotti et al. (2016). All the abovementioned masonry elements, and EUC-BUILD2 itself, were built using 208x100x50 mm clay bricks arranged in a Dutch cross-bond pattern, typically employed for pre-1940's URM constructions in The Netherlands, which basically consists in a double-wythe combination of header and stretcher bond patterns (see Figure 57). The use of this peculiar brickwork bond may have a not-negligible effect on the lateral stiffness of in-plane loaded URM components. Although no experimental evidence is presently available in literature, this observation is supported by both analytical considerations (Mann and Muller 1982) and numerical applications (e.g. Szakály et al. 2016). Moreover, the recent work proposed by (Malomo et al. 2019a), who compared the numerically-inferred in-plane responses of a wide range of URM panels characterised by different brick arrangements (i.e. stretcher, Flemish, English, header and Dutch-cross bonds) with several combinations of boundary conditions, overburden pressures (σ_v) and aspect ratios, substantially confirmed this assumption. However, as already mentioned, the current version of the employed AEM code only allows the representation of a standard stretcher bond pattern. Thus, this aspect has been accounted implicitly, as further discussed in what follows. With reference to the in-plane cyclic tests, after inferring a first estimate of mortar initial elastic properties using Eqs. (3)-(6), the latter have been iteratively calibrated, resulting in an adjustment of the interface spring stiffness according to Eq. (2), until obtaining a satisfactory agreement with the experimental counterparts. In Table 26 below, the main masonry material properties (where f_c is the compression strength of masonry, f_w is the bond tensile strength, c stands for cohesion and μ for friction coefficient), as well as the calibrated Young's moduli referred to the wall specimens (i.e. E_{mo-1} , E_{mo-2} , E_{mo-3} , E_{mo-5}), are reported. It is also noted that the associated shear moduli were inferred assuming material isotropy (Lekhnitskii 1963). To be consistent, in the modelling of characterisation tests (as well as in the case of EUC-BUILD2), the ensuing average of E_{mo-1} - E_{mo-5} , namely E_{mo-AVG} , was employed, leading to reasonable results.

Table 26 Masonry material properties and calibrated Young's moduli of the wall specimens

	δ_m [kg/m ³]	f_c	f_{cb}	f_w	E_m	c	μ [-]	E_{mo-1}	E_{mo-2}	E_{mo-3}	E_{mo-5}	E_{mo-AVG}
Avg. [MPa]	1984	11.2	40	0.2	9833	0.15	0.55	5150	4878	4131	3102	4315
C.o.V. [%]	1.0	7.4	11.2	60.1	25.4	-	-	-	-	-	-	-

For what concerns the modelling of characterisation tests, the comparison between experimental and numerical results reported in Figure 58 seemed to indicate that the both tensile and shear bond resistance at the joint level, as well as the local OOP failure mechanisms, can be adequately predicted using the AEM. An acceptable agreement in terms of overall capacity was found for the case of four-point bending test, albeit the residual strength was not fully captured by the numerical model. This latter aspect might be due to the fact that when a given spring fails, its stiffness is set to zero in the subsequent steps, causing a sudden loss of capacity right after the strength peak.

Test set-up

Num. models

Exp. vs num. results

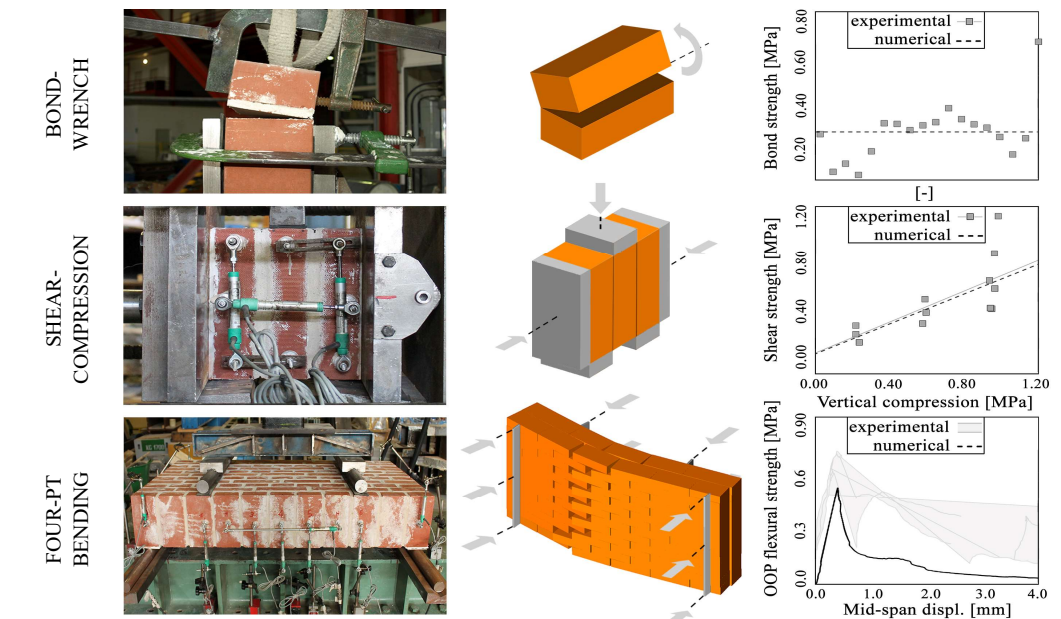
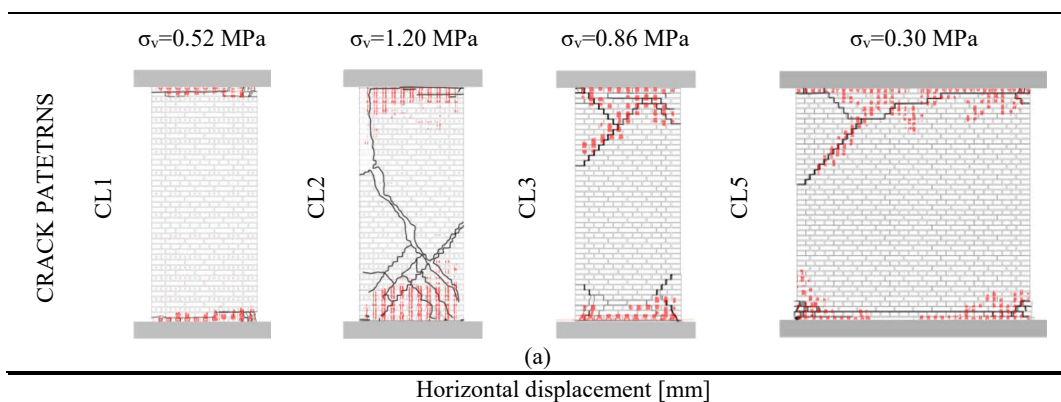


Figure 58 Comparison between characterisation test results and their numerical counterparts

As it can be observed from Figure 59, where the predictions referred to the slender walls (i.e. CL1, CL2, CL3, aspect ratio 2.25) are summarised, the numerical models were able to capture relatively well the shear/displacement capacity of the test specimens, as well as their (rocking/flexure-governed) response mode and corresponding crack pattern. On the other hand, however, and with the exception of specimen CL1, the numerical models struggled to adequately reproduce the shape of the hysteretic curves of the specimens (i.e. their energy dissipation), an issue that, even if not unusual in the modelling of masonry walls subjected to rocking, does warrant further scrutiny in the future. Contrary to what happened with their slender counterparts, the AEM model of the squat wall (i.e. CL5, aspect ratio 0.98) did manage to capture the experimental energy dissipation satisfactorily, although slight differences in terms of lateral capacity and failure mode were observed.



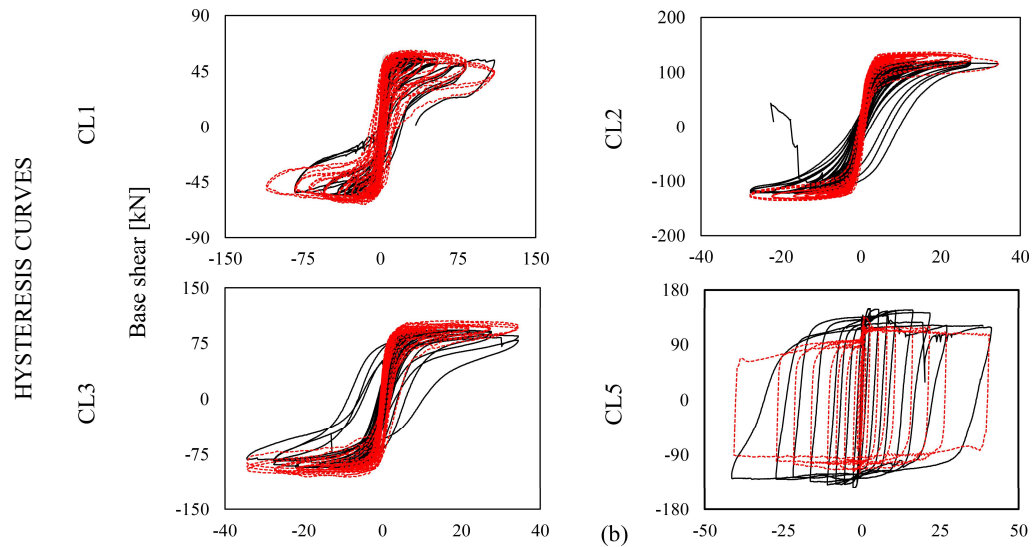


Figure 59 Comparison between in-plane cyclic test results (in black) and their numerical counterparts (red-dashed line) in terms of crack pattern (a) and hysteretic response (b)

5.4 Simulating the shake-table performances of EUC-BUILD2

In this section, the numerical results obtained for EUC-BUILD2 are compared with their experimental counterparts in terms of both hysteretic behaviour and damage propagation. The modelling strategy presented in the previous sections, as well as the findings related to the simulation of URM components, were directly implemented in the AEM model, which was representative, as a whole, of the actual dynamic response exhibited by the building specimen. Then, since the test was stopped prior to collapse, the model was subjected to additional ground accelerations with a view to represent this aspect numerically.

5.4.1 Brief overview of the specimen response

The EUC-BUILD2 full-scale building prototype was tested on the shake-table of the EUCENTRE laboratory (Pavia, Italy) in 2016 (Kallioras et al. 2018b). It consisted in a single-storey double-wythe solid clay URM system, 5.8 m long, 5.3 m wide and 3.3 m high (ridge level) with a total mass of 32.6 tons, characterised by large openings, irregular plan configuration and timber flexible diaphragms, as depicted in Figure 60:



Figure 60 Plan (in cm) and experimental configuration of EUC-BUILD2 (Kallioras et al. 2018b)

The testing sequence reported in Table 27 in terms of peak-table acceleration (PTA) was incrementally applied through shake-table motions, until reaching near-collapse conditions. At the end of each test phase, the cracks propagation was mapped, resulting in the identification of the damage states (i.e. DS₁-DS₄), as exhaustively discussed in Kallioras et al. (2018b) and briefly summarised below. It is herein noted that the suffix –A stands for aftershock, which has been imposed to the structure after SC2-400%, during which the specimen substantially experienced only a minor widening of pre-existing cracks.

Table 27 Testing sequence, experimental damage evolution and limit states of EUC-BUILD2

Test ID	PTA [g]	DS [-]	Test ID	PTA [g]	DS [-]
SC1-25%	0.03	DS ₁ – no visible damage	SC2-150%	0.23	DS ₂ – minor str. damage
SC1-50%	0.05	DS ₁ – no visible damage	SC2-200%	0.29	DS ₂ – minor str. damage
SC1-100%	0.10	DS ₁ – no visible damage	SC2-250%	0.39	DS ₂ – minor str. damage
SC1-150%	0.15	DS ₁ – no visible damage	SC2-300%	0.50	DS ₃ – moderate str. damage
SC2-50%	0.08	DS ₁ – no visible damage	SC2-400%	0.68	DS ₄ – near-collapse conditions
SC2-100%	0.14	DS ₁ – no visible damage	SC2-200%-A	0.28	DS ₄ – near-collapse conditions

The dynamic response of EUC-BUILD2 up to SC2-100% was characterised by slight damage, which became visible only after SC2-150%, when first horizontal cracks were detected right above the openings of the North gable, extending throughout the façade length. The activation of an OOP failure mechanisms on the South gable was firstly after SC2-250%, together with the formation of diagonal cracks on West wall, due to the interaction with the North façade. Moderate in-plane damage was observed during SC2-300%, which coincided with pronounced OOP modes exhibited by both the gables. According to Kallioras et al. (2018b), near-collapse conditions were reached after SC2-400%. The response of this test sequence was essentially governed by the West wall/gable-roof assembly, albeit the damage was largely widespread throughout all the building. Further details will be given in the next sub-section, where experimental results are compared with numerical predictions. However, more detailed information regarding experimental layout, loading protocol and test outcomes are available in the contribution mentioned above, to which interested readers may refer.

5.4.2 Comparison between experimental and numerical results

The performances of the AEM model, expressed in terms of hysteretic envelopes (Figure 61 (a)), IDA curves and displacement profile (Figure 61 (b)), are summarised below. The overall dynamic response of the full-scale building prototype seems to have been adequately captured numerically, given that both the predicted displacement demand and base shear capacity for each cycle appear in good agreement with their experimental counterparts (for space constraints only nonlinear-governed hysteresis were reported).

The first-floor displacements were duly represented throughout all the testing sequence, with the exception of the last cycle (i.e. SC2-400%), where the model noticeably underestimated the experimentally-observed horizontal deformation on the North side. This notwithstanding, experimental and numerical energy dissipation appear comparable, albeit slight differences were noted during SC-250%.

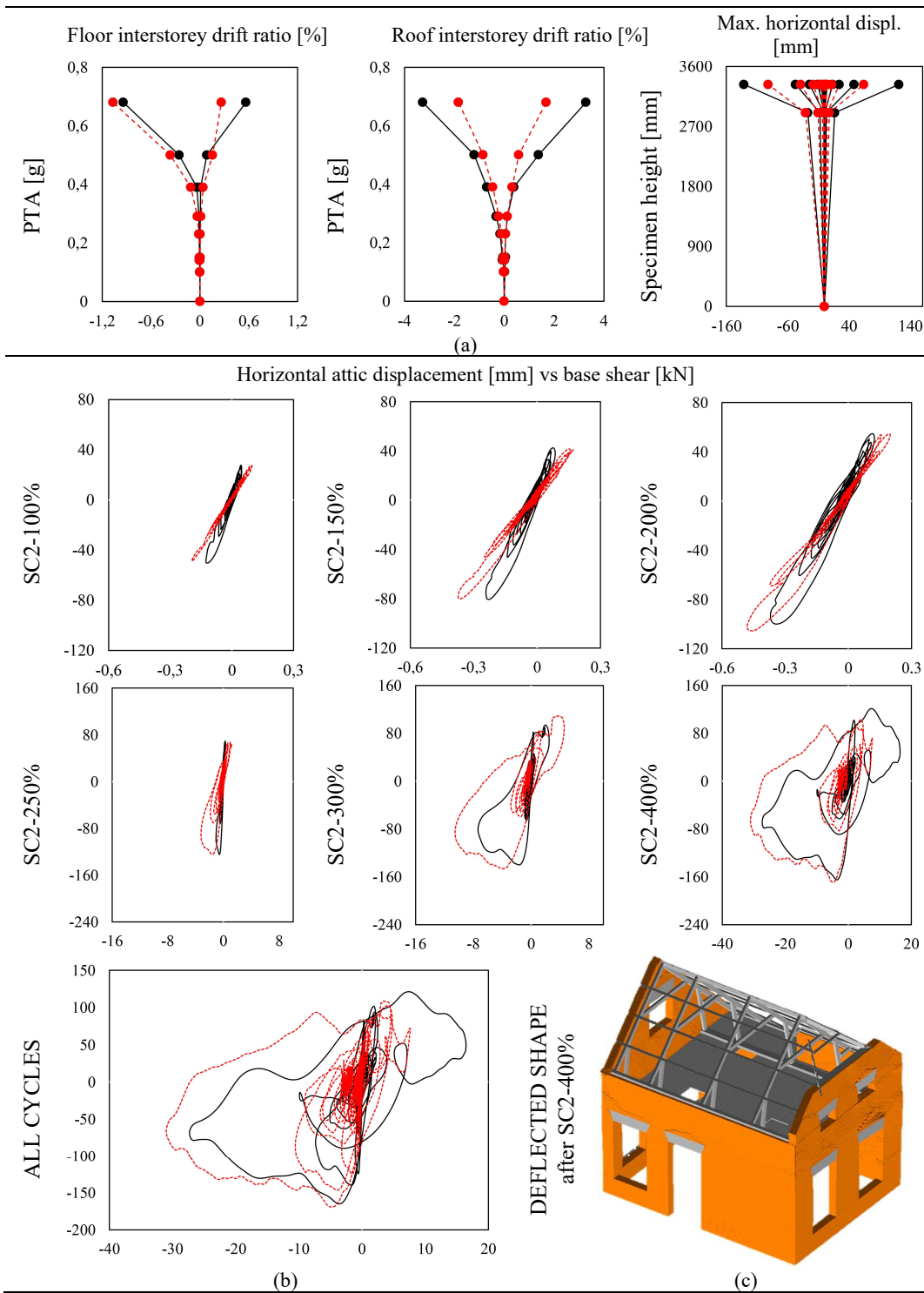


Figure 61 Experimental (black) vs numerical (red dashed line) IDA curves, displacement profile (a) and hysteretic response (b), numerical deflected shape after SC2-400%

Similarly, the roof response predicted by the model can be considered satisfactory until up to SC2-200%, i.e. when the specimen roof-gable assembly started exhibiting a pronounced nonlinear behaviour. This aspect might be directly related to the numerical idealisation of the roof structure, which does not account for cyclic stiffness degradation.

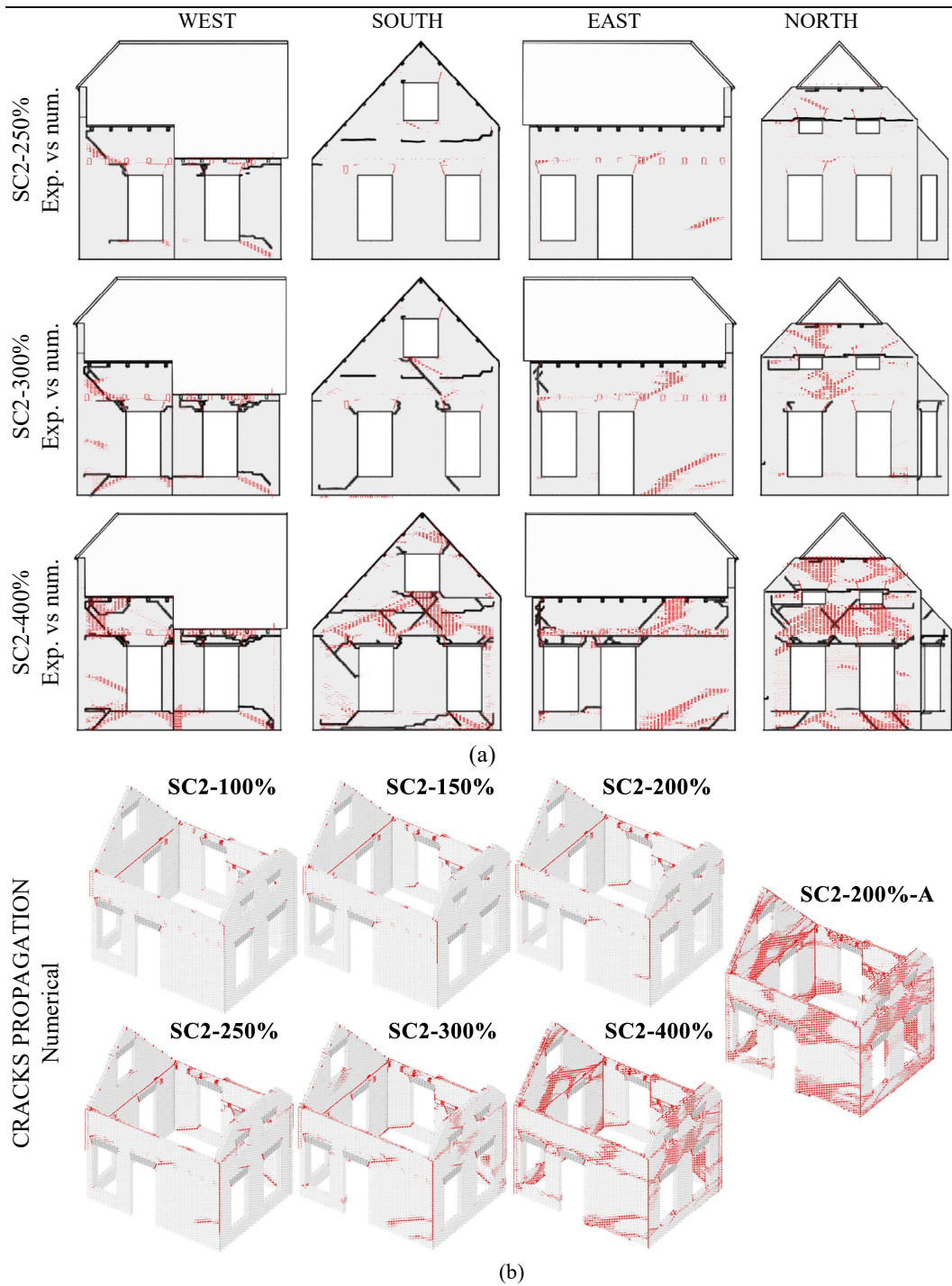


Figure 62 Experimental (black) vs numerical (red) damage evolution (a) and 3D numerical cracks propagation

The general positive impression on the numerical performances presented above is further confirmed by the damage evolution comparisons depicted in Figure 62 (a), from which it can be noted that an adequate agreement with experimental outcomes was found. Indeed, despite some observable differences in terms of crack slope (it is herein recalled that the actual brickwork bond was not explicitly reproduced) which were substantially expected, the model did manage to capture appropriately the fractures' propagation. From Figure 62 (b), where the local response of each sub-component is more appreciable, it can be gathered that the numerical prediction, as a whole, is effectively representative of the global shake-table response of the building specimen. However, especially in the East façade and with reference to the testing phases SC-250% and SC-300%, the model experienced early flexural and diagonal shear damage, as well as a premature activation of the OOP overturning mechanism of the North gable, resulting in a marginal overestimation of the overall damage extent. Given the encouraging results obtained, and because the test was stopped before collapse (i.e. right after reaching near-collapse conditions), additional ground accelerations were imposed to the (damaged) AEM model with a view to investigate numerically the maximum sustainable seismic intensity beyond the envisaged loading protocol. For this purpose, three further inputs were initially selected, namely SC3-250%, SC3-300% and SC3-400% (analogous to SC2-250%, SC2-300% and SC2-400% respectively).

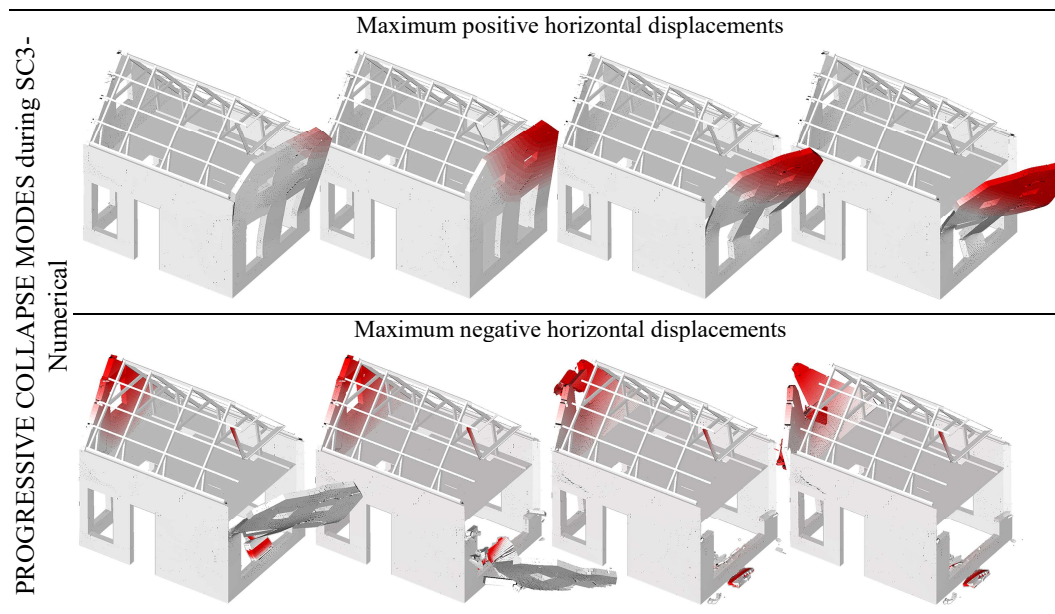


Figure 63 3D numerical collapse mode during SC3-250%

A common feature of most of the discrete element methods is that the crack pattern can change every time the simulation is running, as noted by Galvez et al. (2018). From a computational viewpoint, it implies a high sensitivity towards trivial perturbations of the geometry, often resulting in the obtainment of slightly different numerical results even using the same model. This spurious phenomenon, which is also observable during the

course of real experiments (e.g. Mouzakis et al. 2002), is particularly relevant for rigid-block-based collapse analysis, as argued by Papantonopoulos et al. (2002). In this work, considering the same numerical model, minor differences in terms of collapse mode were obtained running SC3-250%, and that was substantially attributed to what has been discussed above. This notwithstanding, given the extent of the damage and the cracks concentration in the gables after SC2-200-A, the predictions reported in **Figure 63**, according to which the collapse occurred right after reaching the peak acceleration of SC3-250%, i.e. for 0.39g, appears quite reasonable. The North façade, already heavily damaged after SC2-200%-A, started failing in an OOP fashion due to the sudden loss of contact with the roof framing. The asymmetrical overturning of the North gable was the result of a combined failure of both the bilinear link located at the mid-span of the latter and the interface among purlins, hip-wall plate and the façade. A few instants later, for analogous reasons, the South gable collapse followed, ending the numerical exercise.

5.5 Conclusions

In areas of the world that have a long history of damaging earthquakes, the construction culture and practice has been shaped throughout the time considering the associated risk, with varying degrees of success. The induced seismicity phenomenon, which exposes regions historically not prone to tectonic earthquakes to various levels of ground motion intensities due to human activities, substantially increases the need of large-scale programs aimed at investigating the actual vulnerability of the building stock, of which URM structures usually represent a large portion.

This is the case of the Groningen region, in the North of The Netherlands, which has in recent years been subjected to low-intensity shakings due to gas extraction. In this context, the assessment of URM constructions lately became the focus of both numerical and experimental research. In this framework, the typical Dutch detached house building typology, namely low-rise solid clay-brick URM assemblies characterised by the presence of large openings, irregular plan distribution and flexible diaphragms, having been conceived more than sixty years ago without any seismic consideration or detailing, proved to be particularly vulnerable towards horizontal actions. Aimed at further enhancing the understanding of the seismic response of these specific URM structures, a shake-table test on a full-scale detached house building prototype has been performed in 2016 at the laboratory of EUCENTRE, Pavia, Italy, until up to near-collapse conditions.

This notwithstanding, several in-situ surveys demonstrated that a large variety of architectural schemes, roof shapes and masonry properties, whose level of influence cannot be investigated experimentally for understandable reasons, are present in the area object of study. Thus, the development of reliable numerical models able to account for the abovementioned aspects might improve consistently both assessment and future seismic retrofitting activities. The experimentally-observed dynamic behaviour was the result of the combination of a large number of aspects of response, including the nonlinear interaction among diaphragm and masonry components, the influence of constructive details and structural morphology. Moreover, the response was mainly governed by the mechanical interaction between in-plane and out-of-plane modes, usually neglected by simplified modelling techniques.

In this work, the applicability of an advanced discontinuum-based computational approach able to account for these aspects simultaneously, the Applied Element Method (AEM), was investigated and subsequently verified by comparing numerical results with a wide range of experimental outcomes, including those obtained through bond-wrench, shear-compression and four-point bending tests on small-scale specimens, as well as by in-plane cyclic shear-compression tests on full-scale URM piers with several combinations of boundary conditions, vertical pressures and aspect ratios.

Then, the combined use of specific modelling strategies for considering implicitly the influence of a large number of typically-found constructive details, such as connections among structural members, brickwork bond and flexible timber diaphragms, provided a representative numerical description of the actual shake-table performances until up to the end of the test, both in terms of hysteretic response and damage propagation, in a reasonable timeframe. Finally, given the convincing results obtained, and since no explicit collapse has been reached experimentally for avoiding potential damage to laboratory facilities, additional ground motions were imposed to the AEM model, with a view to establish numerically the maximum level of horizontal acceleration prior to complete collapse. The results, widely discussed in the body of the paper, indicated that the system, already extensively damaged, was actually not able to sustain additional ground motions. Indeed, as expected, partial out-of-plane collapse of both the gables occurred during the application of the first extra-input sequence, mostly due to the failure of one of the restraining systems specifically introduced for the shake-table test, also severely damaged after the last experimental run. Despite the sensitivity of rigid-block-based discrete models towards when performing collapse analysis, reasonable results were obtained.

In this sense, future developments might include the possibility of performing a sensitivity study varying the effectiveness of typically-employed constructive details in order to optimise assessment activities and potential retrofitting solutions, as well as further enhancements regarding the simulation of the nonlinear response of timber diaphragms, which the model struggled to reproduce adequately especially in the last loading sequences.

5.6 Acknowledgements

The work described in this paper was carried out within the framework of the research programme on hazard and risk of induced seismicity in the Groningen region, sponsored by the Nederlandse Aardolie Maatschappij BV (NAM). The authors also acknowledge all those at the European Centre for Training and Research in Earthquake Engineering (EUCENTRE, Pavia, Italy) that were involved in the testing campaign referred to in this paper, for their precious assistance in accessing the test data. Finally, the collaboration of the technical support staff from Applied Science International LLC (ASI), on the use of the employed AEM software - Extreme Loading for Structures, is also acknowledged.

References

- Addressi, D., Mastrandrea, A., and Sacco, E. (2015). "A force-based equivalent frame element for push-over analysis of masonry structures." *Key Engineering Materials*,

- 624, 405–412.
- Applied Science International LLC. (2018). “Extreme Loading for Structures (2018).” Durham (NC), USA.
- Arup. (2015). *Investigation on roof types in the Groningen region. Report 229746_031.0_MEM1004*. Amsterdam, The Netherlands.
- Bommer, J. J., and van Elk, J. (2017). “Comment on ‘The maximum possible and the maximum expected earthquake magnitude for production-induced earthquakes at the gas field in Groningen, The Netherlands’ by Gert Zöller and Matthias Holschneider.” *Bulletin of the Seismological Society of America*, Seismological Society of America, 107(3), 1564–1567.
- Braga, F., and Dolce, M. (1982). “A method for the analysis of antiseismic multi-storey masonry buildings (In Italian).” *Proceedings of the 6th International Brick Masonry Conference*, Rome, 1088–99.
- Brignola, A., Pampanin, S., and Podestà, S. (2012). “Experimental Evaluation of the In-Plane Stiffness of Timber Diaphragms.” *Earthquake Spectra*, Earthquake Engineering Research Institute, 28(4), 1687–1709.
- Brignola, A., Podestà, S., and Pampanin, S. (2008). “In-plane stiffness of wooden floor.” *Proceedings of the New Zealand Society for Earthquake Engineering Conference*, Wairakei, New Zealand, 1–19.
- Brooks, J. J., and Baker, A. (1998). “Modulus of Elasticity of Masonry.” *Masonry International*, 12(2), 58–63.
- Cannizzaro, F., and Lourenço, P. B. (2017). “Simulation of Shake Table Tests on Out-of-Plane Masonry Buildings. Part (VI): Discrete Element Approach.” *International Journal of Architectural Heritage*, Taylor & Francis, 11(1), 125–142.
- Casolo, S. (2000). “Modelling the out-of-plane seismic behaviour of masonry walls by rigid elements.” *Earthquake Engineering & Structural Dynamics*, Wiley-Blackwell, 29(12), 1797–1813.
- Casolo, S., and Sanjust, C. A. (2009). “Seismic analysis and strengthening design of a masonry monument by a rigid body spring model: The ‘Maniace Castle’ of Syracuse.” *Engineering Structures*, Elsevier, 31(7), 1447–1459.
- Casolo, S., and Uva, G. (2013). “Nonlinear analysis of out-of-plane masonry façades: Full dynamic versus pushover methods by rigid body and spring model.” *Earthquake Engineering & Structural Dynamics*, Wiley-Blackwell, 42(4), 499–521.
- Castellazzi, G., D’Altri, A. M., de Miranda, S., and Ubertini, F. (2017). “An innovative numerical modeling strategy for the structural analysis of historical monumental buildings.” *Engineering Structures*, Elsevier, 132, 229–248.
- Chácará, C., Mendes, N., and Lourenço, P. B. (2017). “Simulation of Shake Table Tests on Out-of-Plane Masonry Buildings. Part (IV): Macro and Micro FEM Based Approaches.” *International Journal of Architectural Heritage*, Taylor & Francis, 11(1), 103–116.
- Chetouane, B., Dubois, F., Vinches, M., and Bohatier, C. (2005). “NSCD discrete element method for modelling masonry structures.” *International journal for numerical methods in engineering*, Wiley-Blackwell, 64(1), 65–94.
- Ciesielski, R. (1999). “The dynamic module of elasticity of brick walls.” *Proceedings of the Conference of the Committee of Civil Engineering PZITB: Lublin, Poland*.
- Crowley, H., and Pinho, R. (2017). *Report on the v5 fragility and consequence models for the Groningen field. Report-Groningen Field Seismic Hazard and Risk Assessment Project*.
- Cundall, P. A. (1971). “A computer model for simulating progressive large scale movements in blocky rock systems.” *Proc. Symp. Rock Fracture (ISRM)*, Nancy.
- Dolan, J. D., and Madsen, B. (1992). “Monotonic and cyclic nail connection tests.”

- Canadian Journal of Civil Engineering*, NRC Research Press, 19(1), 97–104.
- Domaneschi, M., Scutiero, G., Marasco, S., Cimellaro, G. P., Khalil, A. A., Pellicchia, C., and De Luliis, E. (2018). “A methodology to quantify debris generation after a seismic event.” *16th European Conference on Earthquake Engineering*, Thessaloniki, Greece.
- van Elk, J., Bourne, S. J. S., Oates, S. J. S., Bommer, J. J. J., Pinho, R., and Crowley, H. (2018). “A probabilistic model to evaluate options for mitigating induced seismic risk.” *Earthquake Spectra - submitted for publication*.
- Eurocode, C. E. N. (2005). “6: Design of masonry structures, Part 1--1: General rules for reinforced and unreinforced masonry structures.” *European Committee for Standardization, Belgium*.
- Furukawa, A., Kiyono, J., and Toki, K. (2012). “Numerical simulation of the failure propagation of masonry buildings during an earthquake.” *Journal of Natural Disaster Science*, Japan Society for Natural Disaster Science, 33(1), 11–36.
- Galvez, F., Giaretton, M., Abeling, S., Ingham, J., and Dizhur, D. (2018). “Discrete Element modelling of a two-storey unreinforced masonry scaled model.” *16th European Conference on Earthquake Engineering*, Thessaloniki, Greece.
- Garofano, A., and Lestuzzi, P. (2016). “Seismic Assessment of a Historical Masonry Building in Switzerland: The ‘Ancien Hôpital De Sion.’” *International Journal of Architectural Heritage*, Taylor & Francis, 10(8), 975–992.
- Gattesco, N., and Macorini, L. (2014). “In-plane stiffening techniques with nail plates or CFRP strips for timber floors in historical masonry buildings.” *Construction and Building Materials*, Elsevier, 58, 64–76.
- Graziotti, F., Tomassetti, U., Rossi, A., Marchesi, B., Kallioras, S., Mandirola, M., Fragomeli, A., Mellia, E., Peloso, S., Cuppari, F., Guerrini, G., Penna, A., and Magenes, G. (2016). *Experimental campaign on a clay URM full-scale specimen representative of the Groningen building stock - Report n. EUC128/2016U*. Pavia, Italy.
- Guragain, R., Worakanchana, K., Mayorca, P., and Meguro, K. (2006). “Simulation of brick masonry wall behavior under cyclic loading using applied element method.” *Bulletin of ERS*, Institute of Industrial Science The University of Tokyo, 58(6), 531–534.
- Jäger, W., Irmschler, H., and Schubert, P. (2004). *Mauerwerk-Kalender 2004*. Ernst & Sohn Verlag für Architektur und technische Wissenschaften.
- Kallioras, S., Graziotti, F., and Penna, A. (2018a). “Numerical assessment of the dynamic response of a URM terraced house exposed to induced seismicity.” *Bulletin of Earthquake Engineering - submitted for publication*.
- Kallioras, S., Guerrini, G., Tomassetti, U., Marchesi, B., Penna, A., Graziotti, F., and Magenes, G. (2018b). “Experimental seismic performance of a full-scale unreinforced clay-masonry building with flexible timber diaphragms.” *Engineering Structures*, Elsevier, 161, 231–249.
- Karbassi, A., and Lestuzzi, P. (2012). “Fragility Analysis of Existing Unreinforced Masonry Buildings through a Numerical-based Methodology.” *The Open Civil Engineering Journal*, 6(1), 121–130.
- Karbassi, A., and Nollet, M.-J. (2013). “Performance-based seismic vulnerability evaluation of masonry buildings using applied element method in a nonlinear dynamic-based analytical procedure.” *Earthquake Spectra*, Earthquake Engineering Research Institute, 29(2), 399–426.
- Kaushik, H. B., Rai, D. C., and Jain, S. K. (2007). “Stress-strain characteristics of clay brick masonry under uniaxial compression.” *Journal of materials in Civil Engineering*, American Society of Civil Engineers, 19(9), 728–739.

- Kawai, T. (1978). "New discrete models and their application to seismic response analysis of structures." *Nuclear Engineering and Design*, Elsevier, 48(1), 207–229.
- Keys, R. A., and Clublely, S. K. (2017). "Establishing a predictive method for blast induced masonry debris distribution using experimental and numerical methods." *Engineering Failure Analysis*, Pergamon, 82, 82–91.
- Lekhnitskii, S. G. (1963). *Of an anisotropic elastic body*. Holden-Day, San Francisco, USA.
- Lemos, J. V. (2007). "Discrete element modeling of masonry structures." *International Journal of Architectural Heritage*, 1(2), 190–213.
- Lemos, J. V., and Campos Costa, A. (2017). "Simulation of Shake Table Tests on Out-of-Plane Masonry Buildings. Part (V): Discrete Element Approach." *International Journal of Architectural Heritage*, Taylor & Francis, 11(1), 117–124.
- Lourenço, P. B., Rots, J. G. J. G., and Blaauwendraad, J. (1995). "Two approaches for the analysis of masonry structures - micro and macro-modeling." *Research article HERON - Delft Univ. of Technology (Delft, The Netherlands)*, 40(4), 313–340.
- Malomo, D., Comini, P., and Pinho, R. (2018a). *Using the Applied Element Method to model the shake-table out-of-plane testing of full-scale URM wall specimens subjected to two-way bending. Report n. D10*. Pavia, Italy.
- Malomo, D., Comini, P., Pinho, R., and Penna, A. (2018b). "Validating numerical modelling of out-of-plane dynamic response of masonry walls through comparison with full-scale shake-table tests." *Journal of Structural Engineering, ASCE - to be submitted*.
- Malomo, D., DeJong, M. J., and Penna, A. (2019a). "Influence of bond pattern on the in-plane behaviour of URM piers." *to be submitted*.
- Malomo, D., Pinho, R., and Penna, A. (2018c). "Using the applied element method for modelling calcium silicate brick masonry subjected to in-plane cyclic loading." *Earthquake Engineering & Structural Dynamics*, 47(7), 1610–1630.
- Malomo, D., Pinho, R., and Penna, A. (2019b). "Simulating the shake-table response of URM cavity-wall tested to collapse or near-collapse conditions."
- Mann, W., and Muller, H. (1982). "Failure of shear-stressed masonry. An enlarged theory, tests and application to shear walls." *Proceedings of the British Ceramic Society*, (30), 223.
- Matysek, P., and Janowski, Z. (1996). "Analysis of factors affecting the modulus of elasticity of the walls." *Proceedings of the Conference of the Committee of Civil Engineering PZITB: Lublin, Poland*.
- Mayorca, P., and Meguro, K. (2003). "Modeling masonry structures using the applied element method." *Seisan-Kenkyu*, 55(6), 581–584.
- Meguro, K., and Tagel-Din, H. (2000). "Applied element method for structural analysis: Theory and application for linear materials." *Structural Engineering/Earthquake Engineering*, Japan Society of Civil Engineers, 17(1), 21s--35s.
- Meguro, K., and Tagel-Din, H. (2001). "Applied Element Simulation of RC Structures under Cyclic Loading." *Journal of Structural Engineering*, 127(11), 1295–1305.
- Meguro, K., and Tagel-Din, H. (2002). "Applied Element Method Used for Large Displacement Structural Analysis." *Journal of Natural Disaster Science*, 24(1), 25–34.
- Mendes, N., and Lourenço, P. B. (2014). "Sensitivity analysis of the seismic performance of existing masonry buildings." *Engineering Structures*, Elsevier, 80, 137–146.
- Mouzakis, H. P., Psycharis, I. N., Papastamatiou, D. Y., Carydis, P. G., Papantonopoulos, C., and Zambas, C. (2002). "Experimental investigation of the earthquake response of a model of a marble classical column." *Earthquake Engineering & Structural Dynamics*, 31(9), 1681–1698.

- New Zealand Society for Earthquake Engineering. (2006). "NZSEE 2006. Assessment and Improvement of the Structural Performance of Buildings in Earthquakes. Recommendations of a NZSEE Study Group on Earthquake Risk Buildings." 1–94.
- Pandey, B. H., and Meguro, K. (2004). "Simulation of Brick masonry wall behavior under in plane lateral loading using applied element method." *13th World conference on earthquake engineering, Vancouver, BC, Canada, August*.
- Pantò, B., Cannizzaro, F., Calì, I., and Lourenço, P. B. (2017). "Numerical and Experimental Validation of a 3D Macro-Model for the In-Plane and Out-Of-Plane Behavior of Unreinforced Masonry Walls." *International Journal of Architectural Heritage*, 11(7), 946–964.
- Papantonopoulos, C., Psycharis, I. N., Papastamatiou, D. Y., Lemos, J. V., and Mouzakis, H. P. (2002). "Numerical prediction of the earthquake response of classical columns using the distinct element method." *Earthquake Engineering & Structural Dynamics*, Wiley-Blackwell, 31(9), 1699–1717.
- Penna, A., Lagomarsino, S., and Galasco, A. (2014). "A nonlinear macroelement model for the seismic analysis of masonry buildings." *Earthquake Engineering & Structural Dynamics*, Wiley-Blackwell, 43(2), 159–179.
- Psycharis, I. N., Lemos, J. V., Papastamatiou, D. Y., Zambas, C., and Papantonopoulos, C. (2003). "Numerical study of the seismic behaviour of a part of the Parthenon Pronaos." *Earthquake Engineering & Structural Dynamics*, Wiley-Blackwell, 32(13), 2063–2084.
- Quagliarini, E., Maracchini, G., and Clementi, F. (2017). "Uses and limits of the Equivalent Frame Model on existing unreinforced masonry buildings for assessing their seismic risk: A review." *Journal of Building Engineering*, Elsevier, 10, 166–182.
- Rafiee, A., Vinches, M., and Bohatier, C. (2008). "Modelling and analysis of the Nimes arena and the Arles aqueduct subjected to a seismic loading using the Non-Smooth Contact Dynamics method." *Engineering Structures*, Elsevier, 30(12), 3457–3467.
- Raka, E., Spacone, E., Sepe, V., and Camata, G. (2015). "Advanced frame element for seismic analysis of masonry structures: model formulation and validation." *Earthquake Engineering & Structural Dynamics*, Wiley-Blackwell, 44(14), 2489–2506.
- Roca, P., Cervera, M., Gariup, G., and others. (2010). "Structural analysis of masonry historical constructions. Classical and advanced approaches." *Archives of Computational Methods in Engineering*, Springer, 17(3), 299–325.
- Saloustros, S., Pelà, L., Cervera, M., and Roca, P. (2018). "An Enhanced Finite Element Macro-Model for the Realistic Simulation of Localized Cracks in Masonry Structures: A Large-Scale Application." *International Journal of Architectural Heritage*, Taylor & Francis, 12(3), 432–447.
- Sathiparan, N., Guragain, R., and Meguro, K. (2005). "Experimental Study on In-plane and Out-of- plane Behavior of Masonry Wallettes Retrofitted by PP-Band Meshes." *Journal of Institute of Industrial Science*, 57, 530–53(August 2015).
- Sathiparan, N., Mayorca, P., and Meguro, K. (2012). "Shake table tests on one-quarter scale models of masonry houses retrofitted with PP-band mesh." *Earthquake Spectra*, 28(1), 277–299.
- Szakály, F., Hortobágyi, Z., and Bagi, K. (2016). "Discrete element analysis of the shear resistance of planar walls with different bond patterns." *The Open Construction and Building Technology Journal*, 10(1), 220–232.
- Tomažević, M. (1987). "Dynamic modelling of masonry buildings: storey mechanism model as a simple alternative." *Earthquake Engineering & Structural Dynamics*, Wiley-Blackwell, 15(6), 731–749.
- Tomažević, M., and Gams, M. (2012). "Shaking table study and modelling of seismic

behaviour of confined AAC masonry buildings.” *Bulletin of Earthquake Engineering*, 10(3), 863–893.

U.B.C. (1991). “International Conference of Building Officials. Uniform Building Code.” *International conference of building officials, USA*, Whittier, USA.

Wilson, A., Kelly, P. A., Quenneville, P. J. H., and Ingham, J. M. (2014). “Nonlinear In-Plane Deformation Mechanics of Timber Floor Diaphragms in Unreinforced Masonry Buildings.” *Journal of Engineering Mechanics*, 140(4), 04013010.

PART B

Simulating the in-plane local mechanisms of
URM panels using the Distinct Element Method

CHAPTER 6

In-plane cyclic performances of URM walls
subjected to shear-compression



CHAPTER 6 In-plane cyclic performances of URM walls subjected to shear-compression

Malomo D., DeJong M.J., Penna A. (2018). “Distinct Element modelling of the in-plane cyclic response of URM walls subjected to shear-compression.” *Earthquake Engineering & Structural Dynamics*, submitted.

Abstract. The in-plane capacity of unreinforced masonry (URM) elements may vary considerably depending on several factors, including boundary conditions, aspect ratio, vertical overburden, and masonry arrangement. Since the overall system resistance mainly relies on the in-plane lateral capacity of URM components when out-of-plane modes are adequately prevented, the assessment of the global response of URM structures could benefit from advanced numerical approaches able to account for these factors simultaneously. In this paper, the Distinct Element Method is used to simulate the experimentally-observed responses of a series of URM full-scale specimens with mortared-joints, subjected to in-plane cyclic shear-compression loading. A new methodology for numerically describing both unit, mortar and hybrid failure modes, also including masonry crushing due to high compression stresses, is proposed. The employment of the Distinct Element Method is optimised by combining dynamic relaxation schemes with time, size, and mass scaling procedures, significantly decreasing computational cost. Empirical and homogenisation formulae for inferring the elastic properties of interface between elements are also verified, enabling the proposed approach to be applied more broadly. Using this modelling strategy, the interaction between stiffness degradation and energy dissipation rate was accounted for numerically. Although the models marginally underestimate the energy dissipation in the case of slender piers, a good agreement was obtained in terms of lateral strength, hysteretic response and crack pattern.

Keywords: unreinforced masonry; in-plane; cyclic; numerical modelling; distinct element method.

6.1 Introduction

The in-plane behaviour of unreinforced masonry (URM) piers is strongly affected by several external factors, including the boundary conditions, aspect ratio and imposed vertical compression, as well as intrinsic masonry characteristics, including mechanical properties of units and mortar, bond pattern and section morphology associated with the considered masonry type. Thus, different failure modes may occur, affecting peak strength, residual capacity and related ductility. With a view to assess the in-plane response of URM elements, several simplified methods have been proposed. Ranging from the pioneering work of Magenes and Calvi (1997), Mann and Muller (1982), Paulay and Priestley (1992) and Turnšek and Sheppard (1980) to recent advancements and proposals (e.g. Petry and Beyer 2015, Wilding and Beyer 2017) analytical modelling still represents a valid

alternative for predicting the actual force-displacement relation of in-plane loaded URM walls. When implemented in simplified numerical procedures, such as storey mechanism (e.g. Braga and Dolce 1982, Tomaževič 1987) and equivalent frame models (e.g. Penna et al. 2014, Raka et al. 2015), these formulations can be automatically selected and employed in order to describe the seismic behaviour of large-scale URM structures at relatively low computational expense. Notwithstanding the above, since out-of-plane modes are usually neglected, the interaction between in-plane and out-of-plane (OOP) failure mechanisms is not typically considered. Nonetheless, as also demonstrated by experimental evidence (e.g. Tomassetti et al. 2017), boundary conditions may change suddenly when a structural system is exposed to acceleration time histories, inducing brittle out-of-plane failures due to the increase in the rocking demand of in-plane loaded URM components. Thus, a careful assessment of URM structures at the building scale calls for more advanced numerical methods, able to account for these aspects within the same computational platform, as already noted by other researchers (e.g. de Felice 2011).

Continuum-based procedures, such as the Finite Element Method (FEM), have been adapted and applied to masonry structures, implementing nonlinear constitutive laws and by means of a material homogenisation process. In this framework, the in-plane quasi-static cyclic behaviour of URM piers has been adequately represented by several authors, with varying levels of accuracy (e.g. Haach et al. 2011, Karapitta et al. 2011). However, as widely discussed in Lourenço and Milani (2014) and Roca et al. (2010), even though FEM is probably the most employed numerical tool and extended or hybrid methods (e.g. Miglietta et al. 2017, Munjiza 2004) have been additionally implemented, the simulation of block separation, rotation, or frictional sliding remains extremely challenging. A different computational approach, which explicitly accounts for the discrete nature of masonry assemblies, characterises the discontinuum-based methods, where each unit, usually connected by zero-thickness mortar layers, is modelled separately. According to the Rigid Body and Spring Model (RBSM) (Kawai 1978), an arbitrary masonry segment is assumed to be composed of rigid blocks connected by discrete deformable interfaces with distributed normal and tangential nonlinear springs, whose elongation and failure allows the modelling of the global mechanical response of the considered system when subjected to both static and dynamic loading. Despite some satisfying applications (e.g. Casolo and Peña 2007), both crack propagation and progressive damage were not represented faithfully, since the unit arrangement is considered implicitly by introducing energy relations and homogenisation procedures. The Applied Element Method (AEM) (Meguro and Tagel-Din 2000) based on similar assumptions, represents an analogous but more efficient approach in which rigid units interact with each other through nonlinear springs, where the mechanical properties of the system are lumped. Unlike the RBSM, analysis up to complete collapse of a structure using AEM is attainable, since re-contact between neighbouring elements is computed automatically. Moreover, in the AEM framework, both Poisson effect and local rotational deformations are accounted for without the need of additional elements, unlike the RBSM. In a recent application (e.g. Malomo et al. 2018), AEM was employed to capture the in-plane cyclic response of URM elements under different boundary conditions and vertical pressures. Despite the potential of this simplified micro-modelling implicit technique, unit failure modes are commonly neglected. Indeed, when a given amount of springs have failed and their stiffness is set to zero, contact between units is lost, often compromising analysis stability.

The Distinct Element Method (DEM), initially conceived for simulating soil and rock mechanics (Cundall 1971), is a simplified micro-modelling technique which makes use of an explicit time-stepping scheme. Either rigid or deformable blocks, connected by zero-thickness spring layers representing the unit-mortar interface, can be modelled. The use of the DEM for modelling dry-joint masonry structures has been widely investigated. The work of Papantonopoulos et al. (2002) and Psycharis et al. (2003) on the seismic behaviour of Greek monumental structures, as well as the contributions of Lemos (1997) and Azevedo et al. (2000) who analysed the experimental cyclic behaviour of a stone façade and of stone columns respectively, proved the capabilities of such discrete modelling approach. More specifically, the latter author proposed a series of time-history analyses of both dry and mortared-joint structures, although no experimental counterparts were available for the selected constructions. DeJong and Vibert (2012) modelled the cyclic response of dry-stone spires both experimentally and with DEM, while recently, Bui et al. (2017) compared both in-plane and out-of-plane (OOP) experimental behaviour of dry-joint URM constructions and modelling results. The seismic response of arched structures has been also scrutinised in some depth, ranging from numerical applications concerning rigid blocks subjected to impulsive base motions (e.g. DeLorenzis et al. 2007) to full earthquake time-history analysis to support the design of a stone masonry vault (e.g. DeJong et al. 2015). Nevertheless, very few applications concerning the modelling of mortared-joints (rather than dry-joints) are documented in literature, and in most of such cases, no experimental comparisons were provided. Moreover, unit failure mechanisms were usually not considered.

In this paper, a comprehensive methodology for simulating the in-plane cyclic performance of mortared-joint URM assemblies using a DEM software, 3DEC (Itasca 2013) is proposed. Limited previous research exists regarding the numerical prediction of the associated hysteretic behaviour, crack patterns and failure modes, or detailed comparison against experimental outcomes. The developed modelling strategy was employed and subsequently evaluated by simulating the experimental tests involving a series of full-scale specimens with mortared-joints, subjected to in-plane cyclic shear-compression quasi-static loading sequences (Graziotti et al. 2015, 2016b). Different levels of vertical pressures, boundary conditions, masonry types (i.e. calcium silicate, CS, and clay, CL, brick masonries) and unit arrangements (i.e. stretcher and Dutch cross bond patterns) were considered. Further, unit failure modes, commonly neglected within this framework, were also modelled through an equivalent implicit approach. The computational platform was selected carefully, with a view of taking advantage of the findings of this work for modelling more complex structures involving interaction between in-plane and out-of-plane modes, usually not considered by simplified methods.

6.2 The Distinct Element Method for masonry structures

Each masonry unit was modelled as a discrete block using DEM. Either rigid (only an interface constitutive law is needed) or deformable (continuum constitutive law for the bricks themselves must also be included) blocks can be modelled. For deformable blocks, as depicted in Figure 64, an internal Finite Element (FE) mesh is required in order to capture unit deformations, where each tetrahedral element represents a uniform-strain domain.

Then, a set of control points, or gridpoints, are associated with the outer nodes of each FE mesh unit. The masses of the system are concentrated in these nodes, and both accelerations and displacements are computed with respect to the nodes during each time-increment. Zero-thickness spring layers, characterised by pre-defined constitutive laws, as well as by both normal (k_n) and shear (k_s) stiffnesses, are assigned at the interfaces between solid elements, representing the mechanical properties of unit-mortar assembly, thus accounting for system discontinuities.

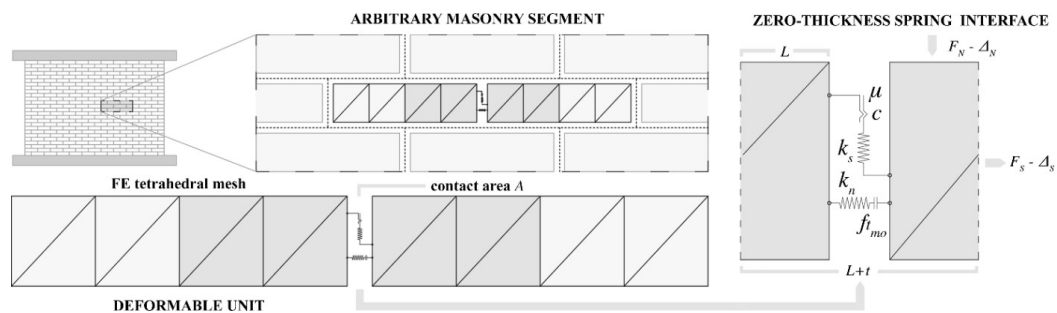


Figure 64 Discretisation of a masonry segment according to the DEM

Within the DEM framework, sliding in joints between adjacent blocks is commonly modelled using a simplified Mohr-Coulomb criterion. The “joint slip model” employed in this work is particularly suitable for simulating the cohesive-frictional response exhibited by URM assemblies subjected to shear-compression. The cohesion parameter, c , was set to zero right after reaching the maximum shear strength, thus neglecting any post-peak softening branch, resulting in a residual capacity governed by both the acting vertical stress and the specified angle of friction, ϕ . Similarly, a tension cut-off usually characterises the joint flexural response, whereas no compression failure is allowed. The effect of dilation, which takes place only when the joint is slipping, can be accounted for by introducing the parameter ψ , i.e. iteratively correcting the normal force acting at the joint level as a function of the direction of shearing. A simplified computational workflow, together with the abovementioned tensile and shear behaviour for both an intact and a sliding joint, is shown in Figure 65. Interested readers may refer to Bui et al. (2017), Cundall and Hart (1992) and Lemos (2007) for further details.

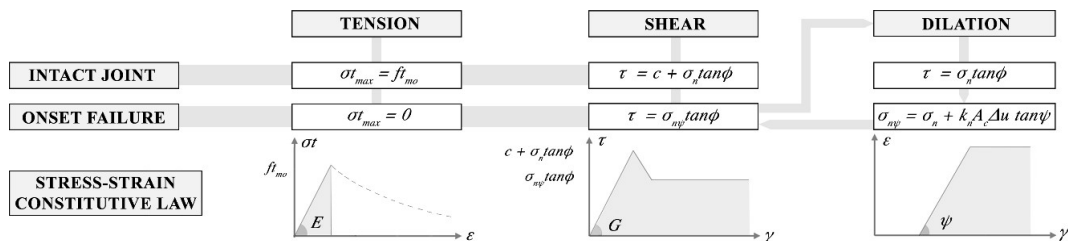


Figure 65 Tensile and shear behaviour for both intact and sliding joints

The numerical representation of unit failure modes is challenging for many DEM computational procedures, especially if based on the interaction between spring layers and solid bodies. For this purpose, two main modelling approaches might be undertaken: 1) idealise each unit as a rigid element internally subdivided by spring layers, in which the

unit material properties are lumped, or 2) unit deformability is provided by a superimposed FE mesh. Although the first one is computationally more convenient, separation due to unit failure often compromises analysis stability inducing spurious interpenetration phenomena between adjacent elements. In this contribution, bricks were modelled according to a mixed-discretisation technique (Marti and Cundall 1982), i.e. introducing a regular hexahedral mesh that was internally subdivided into six tetrahedral FE zones. In the direction perpendicular to the bed-joints, the brick element was composed by two main hexahedral sections for better capturing flexural and shear deformations, whilst no subdivisions were introduced longitudinally. Although this reduced the computational burden considerably, the aforementioned approach resulted in an appreciable overestimation of the masonry axial stiffness, so the deformability of the masonry was not properly accounted for. Such unwanted numerical phenomenon, exhaustively discussed by several authors (e.g. Bathe 2001, Chapelle and Bathe 1998), is quite common when a coarse discretisation is applied along the loading direction. To compensate, with reference to the nomenclature already reported in Figure 64, an equivalent joint contact stiffness, defined by Eq. (1), which account for both brick and mortar joint deformability, was introduced. In the case of head joints, the length L is equal to the one of the brick, while for bed joints L is the brick height. Moreover, E_b and E_{mo} stand for brick and mortar Young's modulus respectively, whilst G_b and G_{mo} indicate the associated shear moduli, inferred assuming material isotropy (Lekhnitskii 1963).

$$\begin{cases} \Delta_N = \left(\frac{F_N L}{E_b A} + \frac{F_N t}{E_{mo} A} \right) \\ \Delta_S = \left(\frac{F_S L}{G_b A} + \frac{F_S t}{G_{mo} A} \right) \end{cases} \Rightarrow \begin{cases} k_n = \frac{F_N}{\Delta_N} = \left(\frac{A}{L+t} \right) \left[\left(\frac{E_b E_{mo}}{E_b t + E_{mo} L} \right) (L+t) \right] \\ k_s = \frac{F_S}{\Delta_S} = \left(\frac{A}{L+t} \right) \left[\left(\frac{G_b G_{mo}}{G_b t + G_{mo} L} \right) (L+t) \right] \end{cases} \quad (1)$$

Several nonlinear constitutive laws might be assigned to the FE zones. With a view to describe the brittle unit failure mechanisms usually observed during experimental testing, the employment of a Mohr-Coulomb plasticity model (shear yield function) with tension cut-off (tensile yield function) provides a compromise between required material parameters, computational effort and accuracy. As in the previous case (i.e. the abovementioned joint constitutive law), compressive failure was not accounted. The shear flow rule is non-associated, unlike the tensile one. The implementation of such unit model in 3DEC involves, at each time increment, a verification of the violation of the selected elastic domain. In such case, plastic correction factors are combined with the elastic strains computed in the previous step. Thus, new stresses are evaluated and subsequently considered in the next increment. Full details are given in the technical documentation provided by Itasca (2018).

6.2.1 Simulation of in-plane failure mechanisms

The following principal in-plane failure modes and damage patterns for URM structures subjected to seismic actions are depicted in Figure 66: (a) flexural tensile crack through mortar joints, (b) masonry crushing, (c) rigid overturning, (d) shear stepped cracks through both bed and head joints, (e) sliding along the bed-joints, (f) shear failure through units. From a modelling viewpoint, it is clear that modes (a), (c), (d) and (e) should be accounted by interface springs, whereas (b) and (f) are combined failures involving both units and mortar layers. Thus, a specific computational strategy accounting for the abovementioned

mechanisms was developed. In this section, the methodology is presented, as well as the fundamental theoretical assumptions and some new modelling features implemented.

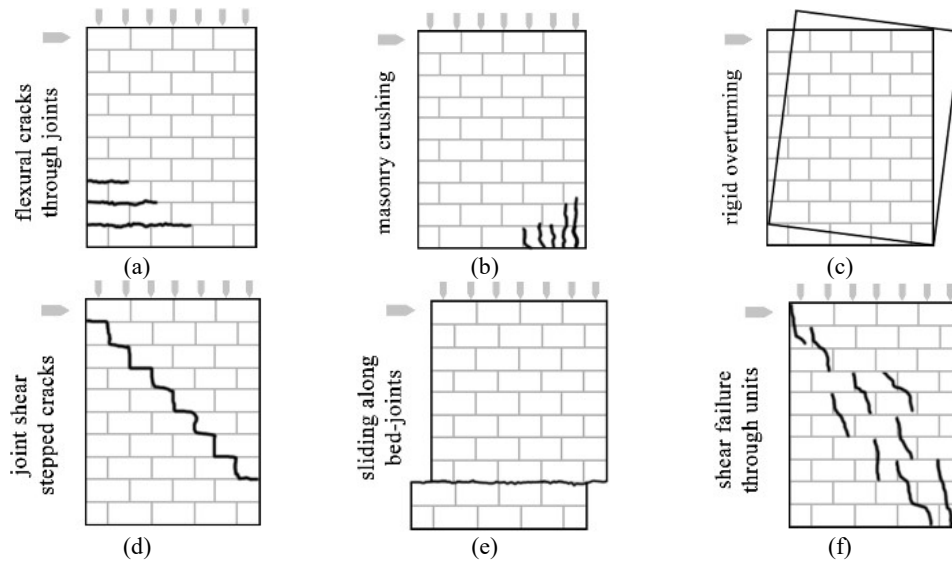


Figure 66 Considered in-plane failure mechanisms

To represent faithfully the damage mechanisms which involve the joint, unit and hybrid modes in the DE framework, it is clear that each component of a given masonry element needs to be described in terms of its mechanical properties. However, experimental campaigns rarely involve tests that would allow one to obtain all necessary material characterisation for units and mortar separately. Thus, undertaking the same approach described in Malomo et al. (2018) empirical and homogenisation formulae were used to obtain first estimates of the required material parameters where direct experimental values were not available. In Figure 67(a), where f_{c_b} is the brick compressive strength, ζ is the ratio between brick and mortar thickness, E_m and E_{m_0} stand for the Young's modulus of masonry and mortar respectively, the formulae are summarised, as well as the characterisation tests needed (see Figure 67(b)).

DERIVATION OF UNIT AND MORTAR ELASTIC PROPERTIES			
MORTAR YOUNG'S MODULUS			
$E_{m_0} = \left(\frac{-4E_m E_b}{25E_m - 29E_b} \right)$	Brooks-Baker (1998)	$E_{m_0} = \left(\frac{E_m E_b}{E_b - 1.25\zeta(E_m - E_b)} \right)$	Matysek-Janowski (1996)
$E_{m_0} = \left(\frac{-E_m E_b}{5E_m - 6E_b} \right)$	Cielecki (1999)	$E_{m_0} = \left(\frac{E_m E_b}{\zeta(E_m - E_b) + E_b} \right)$	U.B.C. (1991)
UNIT YOUNG'S MODULUS			
CALCIUM SILICATE BRICK MASONRY		CLAY BRICK MASONRY	
$E_b = (355) \cdot (f_{c_b})$	Jäger-Irmschler (2004)	$E_b = (375) \cdot (f_{c_b})$	Kaushik-Rai-Jain (2007)
$E_{m_0} - E_b$		$G_{m_0} - G_b$	
$G = E/[2(1+\nu)]$ with $\nu=0.25$			

(a)

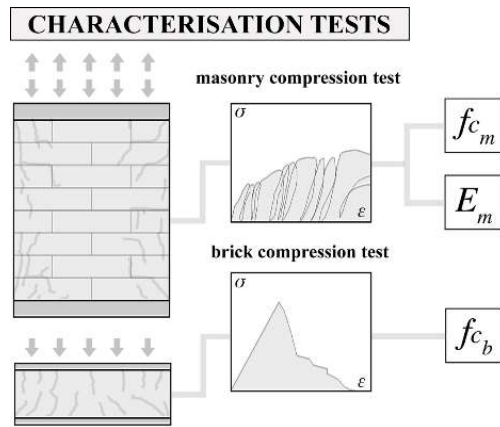


Figure 67 Derivation of brick and mortar material properties through empirical and homogenisation formulae ((Brooks and Baker 1998; Ciesielski 1999; Jäger et al. 2004; Kaushik et al. 2007; Matysek and Janowski 1996; U.B.C. 1991)) (a) and characterisation tests needed (b)

(b)

In-plane joint sliding phenomena, as discussed in the previous section, can be appropriately represented by assigning a Mohr-Coulomb-based constitutive law to interface springs. Cohesive, frictional and tensile joint behaviours were specified using material properties directly obtained through characterisation tests, without the need of altering experimental data. Results from shear-compression test on masonry triplets were considered for deriving the initial shear strength (i.e. cohesion) and friction coefficient $\mu = \tan\phi$, while the joint tensile strength was obtained from bond wrench test on masonry doublets. Finally, an automatic procedure was implemented for assigning different normal and shear stiffnesses to bed and head joints according to Eq. (1), i.e. depending on the orientation of the selected shearing plane. With reference to Figure 66, failure mode (b) is usually due to unit tensile cracking, which is subjected to tension stresses induced by compressive failure of mortar joints. To include such a mechanism without considering the interaction between mortar and brick explicitly (recall that zero-thickness mortar layers were employed), the following simplified method was developed. Small-scale CS ($3L_b \times 6H_b$), and CL ($2.5L_b \times 11H_b$) brick masonry assemblies, as discussed in more details in the following subsection, were tested numerically under incremental uniform displacement in the direction perpendicular to bed-joints.

Then, keeping constant the hexahedral FE mesh size (i.e. $0.5L_b \times H_b$), equivalent cohesive (c_{b_eq}) and frictional (ϕ_{b_eq}) input parameters were selected and consequently implemented in a Mohr-Coulomb plasticity model in order to obtain brick diagonal shear failure along the edges of the internal tetrahedral mesh elements when the compressive stresses were equal to the actual compressive strength of masonry f_c^m . Similarly, the equivalent brick tensile strength ($f_{t_b_eq}$) was inferred by replicating bending tests of simply supported bricks (Sharma et al. 2018). The specific values associated with the abovementioned parameters for both CS and CL brick masonry are given in the next subsection, together with a first verification of these modelling assumptions through comparison between characterisation test results and their numerical counterparts. However, an attempt was made in what follows to represent the extent of the inferred properties through linear expressions, as a function of f_c^b . It is worth noting that these quantities are comparable with reference experimental outcomes on similar masonry types. Analogous values were already successfully employed by other researchers (e.g. Churilov and Dumova-Jovanoska 2008).

$$ft_{b_eq} \sim (0.03) \cdot (fc_b) \quad (2) \quad c_{b_eq} \sim (1.5) \cdot (ft_{b_eq}) \quad (3) \quad \phi_{b_eq} \sim 35^\circ \quad (4)$$

The employment of this implicit numerical strategy, which led to the definition of a smooth bilinear compression cap (see Figure 69), combined with the introduction of a tension cut-off criterion, resulted in a satisfying representation of the instantaneous loss of capacity due to brittle unit tensile failure and associated cyclic energy dissipation.

6.2.2 Modelling quasi-static phenomena using explicit time-integration schemes

Numerical modelling of discontinua involves the representation of contacts, sliding and impact phenomena between discrete elements. In this context, the use of explicit dynamic solution schemes for solving complicated quasi-static problems presents several advantages. Amongst others, explicit algorithms provide unconditionally stable conditions, since the system is not iteratively forced to reach equilibrium. Contacts are treated as kinematic constraints to be adjusted after each time increment, allowing the simulation of re-contact between neighbouring elements with a reduced computational cost. However, the open challenges in applying such explicit dynamic procedure to quasi-static problems include achieving results in a realistic timeframe and avoiding unwanted inertial effects. In what follows, the applicability of explicit algorithms to the modelling of URM structures subjected to quasi-static actions is scrutinised and discussed. Further, in order to overcome such limitations, a specific methodology was developed and verified. DE-based codes are commonly based on time integration procedures that solve the equations of block system motion by explicit central finite difference methods. In practice, as widely discussed in e.g. Bathe and Saunders (1984), adequate accuracy is provided by the employment of a minimum critical timestep Δt_{cr} , defined by the Courant-Friedrichs-Lewy (CFL) condition (Courant et al. 1967), as reported in Eq. (5) below for undamped materials. It ensures that a given stress cannot propagate across more than one element in a single time step, being a function of both element (L_{min}) size and sound speed (v_c) through the considered continuum body with density δ and Young's modulus E .

$$\Delta t_{cr} \leq \left(\frac{L_{min}}{v_s} \right) \quad \text{where} \quad v_s = \sqrt{E/\rho} \quad (5)$$

The fulfilment of the CFL condition has a negligible influence on the computational cost when impulsive dynamic loading histories are applied to large-scale, high-density flexible elements. On the contrary, masonry structures are usually constituted by the assembly of small rigid units characterised by a relatively low density, which consistently increases computational burden. A wide range of numerical techniques has been implemented for optimising the use of explicit solvers in quasi-static field (Cook et al. 2002). For this purpose, the maximum value of out-of-balance forces (f_{max}) caused by inertia effects and the influence of the CFL law on the required analysis time should be investigated carefully. With reference to the latter, the main goal is to maximise Δt_{cr} by increasing the ratio L_{min}/v_s . Size-scaling procedures rely on mesh coarsening, which directly affects L_{min} . When the mechanical response is not governed by inertia effects, instead, mass-scaling constitutes an attractive solution. According to the latter, ρ is iteratively and locally adjusted in order to decrease the speed v_s . An additional effective option might be also represented by load-factoring (or time-scaling) methodologies, which involve a convenient modification of loading rate. Indeed, the magnitude of imposed velocities is increased gradually and held

constant for some time so as to achieve quasi-static conditions. Moreover, dynamic relaxation procedures, originally proposed by Otter in 1966, are commonly employed for minimising unwanted inertia forces. This approach aims at removing the kinetic energy of the model by iteratively reducing the nodal velocities. In practice, the introduction of suitable damping schemes is equivalent of immersing the structure in a viscous fluid, which also makes almost negligible the influence of geometric nonlinearities.

In this contribution, as depicted in Figure 68(a), size, mass and time-scaling techniques were used simultaneously, in combination with an adaptive dynamic relaxation method, for obtaining an acceptable compromise between accuracy and numerical calculation cost. Moreover, throughout the analysis, additional “kinetic energy checks” were implemented in the code, as further discussed in the following, in order to assure quasi-static conditions.

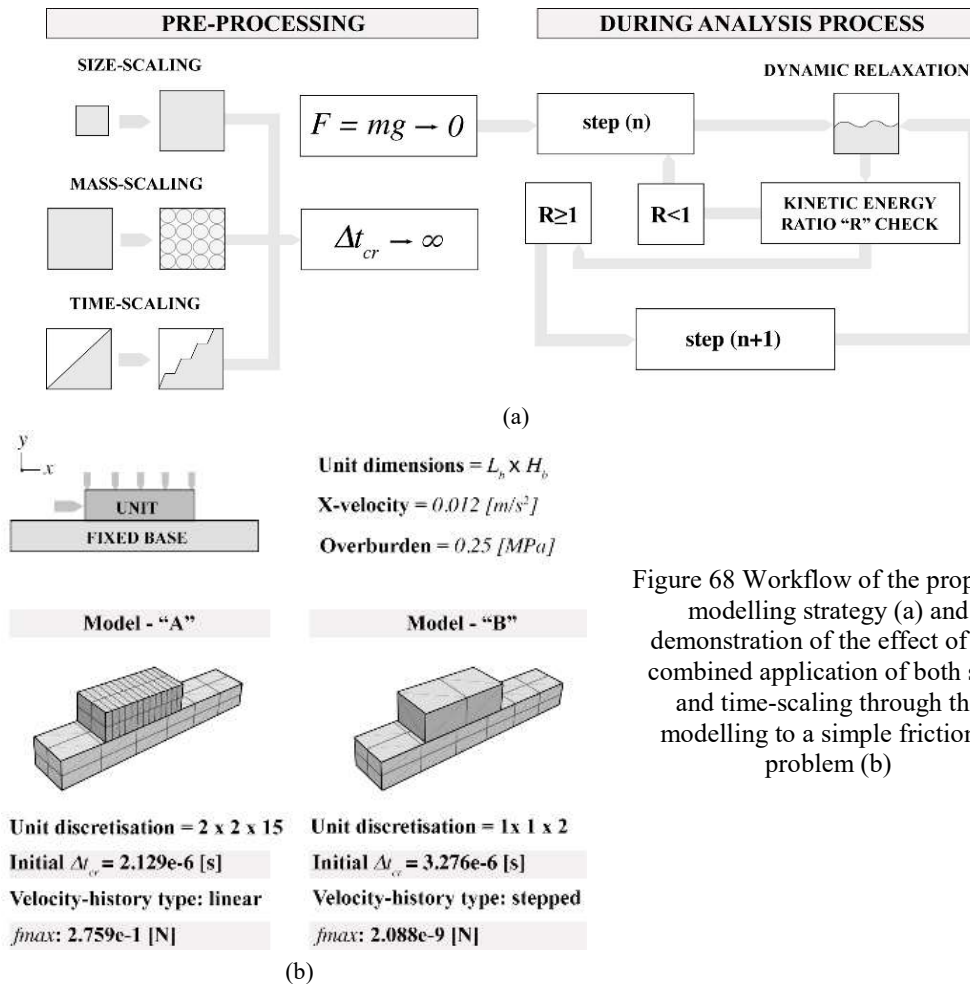


Figure 68 Workflow of the proposed modelling strategy (a) and demonstration of the effect of the combined application of both size and time-scaling through the modelling to a simple frictional problem (b)

More specifically, size-scaling was considered through the assignment of a relatively coarse mesh to the structural elements. Time-scaling was implemented by introducing a multi-stepped loading history: the horizontal velocity was increased gradually, leading to a displacement of 1 mm in 0.135 sec. Then, undertaking the approach suggested by Szakály et al. (2016) an equilibrating phase followed: velocities were set to zero and simulation was continued until the average unbalanced nodal force resultant divided by the average load

acting on the nodes became smaller than 10^5 . In the 3DEC framework, mass-scaling is automatically performed when adaptive global damping (Cundall 1982, 1987) is employed. It involves a continuous adjustment of damping coefficients in such a way that the power absorbed is a constant proportion of the rate of change of kinetic energy in the system. The iterative modification of viscosity constants is provided by a numerical servomechanism that seeks to keep the ratio (R) between the summation of nodal damping magnitude P and rate of change of nodal kinetic energy E_k equal to a target value (e.g. $R=1$ herein). In Figure 68(b), the beneficial effect of the simultaneous employment of both size and time-scaling on the extent of Δt_{cr} and f_{max} respectively has been highlighted by considering the results of the modelling of a simple quasi-static frictional problem, i.e. a sliding deformable block subjected to shear-compression induced by the application of a pre-defined horizontal velocity (i.e. 0.012 m/s^2). In order to obtain comparable outcomes, the same dynamic relaxation and mass-scaling schemes were adopted in both of the cases. However, in Model “A” neither size nor time-scaling procedures were implemented, whereas Model “B” is characterised by the combined use of the latter. Through this simple modelling exercise, it is evident that in the case of Model “B” the Δt_{cr} is significantly higher, while the value of f_{max} decreased considerably, resulting in a significant reduction in both computational time and the extent of out-of-balance forces.

6.2.3 First verification of DEM with material characterisation tests

In this subsection, a first comparison between experimental and modelling results is presented with a view to assess the DEM capabilities in reproducing the main in-plane local failure modes. Hence, a selection of characterisation tests on small-scale specimens carried out in 2015-2016 at the laboratories of DICAr (Department of Civil Engineering and Architecture, University of Pavia, Italy) has been replicated numerically. Bond wrench, shear-compression, and cyclic compression tests were considered. The CS bricks ($212 \times 102 \times 71 \text{ mm}$) were arranged according to a single-leaf periodic arrangement (stretcher bond). Dutch cross-bond, double-wythe masonry wallettes were instead assembled using CL bricks ($208 \times 102 \times 50 \text{ mm}$). The average mortar bond thickness was 10 mm for all the samples. Experimental procedures and results are exhaustively discussed in the dedicated technical reports by Graziotti et al. (2015, 2016b). In Table 28, the considered masonry material properties (which were also employed for all the small-scale models) are reported. The associated contact stiffness values (i.e. k_n , k_s) for both bed and head joints, inferred using Eq. (1), will be given in the next sections, where the modelling of full-scale wall specimens is presented and discussed.

Table 28 Experimental and inferred properties of CS and CL brick masonry (Graziotti et al. 2015, 2016b)

	CS - $\delta_m = 1839 \text{ [kg/m}^3\text{]}$						CL - $\delta_m = 1979 \text{ [kg/m}^3\text{]}$					
	f_{c_m}	f_{c_b}	$f_{t_{mo}}$	E_m	c	μ [-]	f_{c_m}	f_{c_b}	$f_{t_{mo}}$	E_m	c	μ [-]
Mean [MPa]	6.20	18.67	0.24	4182	0.21	0.42	11.22	40	0.23	9833	0.15	0.55
C.o.V. [%]	7.04	13.67	16.32	33.27	-	-	7.43	11.21	60.11	25.42	-	-
Inferred mechanical properties [MPa]	E_b	E_{mo}	$f_{t_{b_{eq}}}$	$c_{b_{eq}}$	$\phi_{b_{eq}}$	-	E_b	E_{mo}	$f_{t_{b_{eq}}}$	$c_{b_{eq}}$	$\phi_{b_{eq}}$	-
	6628	1772	0.52	0.78	35°	-	15000	3257	1.12	1.68	35°	-

Each test was simulated by directly modelling experimental layouts and boundary conditions. However, for the compression tests, a monotonic quasi-static loading protocol was substituted for the experimental (cyclic) loading to reduce computational expense. In Figure 69, numerical outcomes are plotted against experimental envelopes.

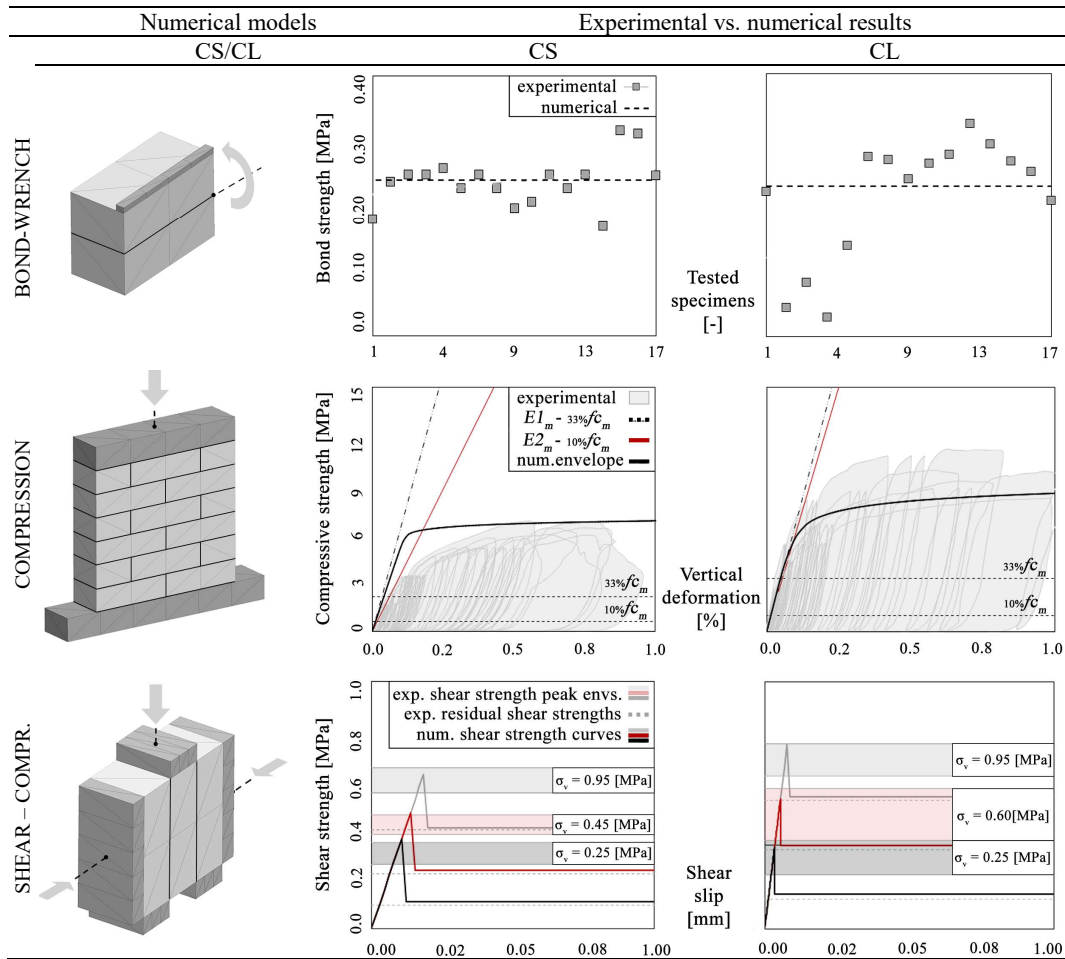


Figure 69 Preliminary verification of the modelling strategy through comparison with experimental results

The numerical models, as reported in Figure 69, adequately represented the experimental response exhibited by small-scale specimens. Indeed, both axial and lateral stiffness were captured satisfactorily, as well as the joint tensile and shear behaviour under different levels of vertical compression. Minor differences, mostly due to the simplifications introduced in the Mohr-Coulomb slip model, were found in the case of the shear-compression tests, where a post-peak softening branch was observed experimentally.

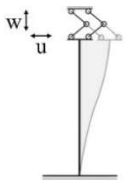
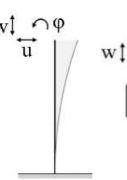
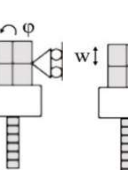
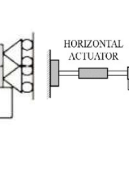
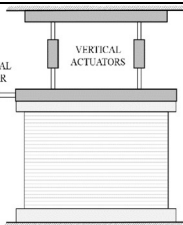
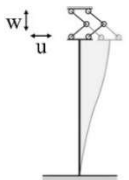
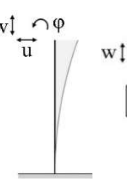
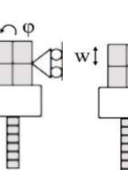
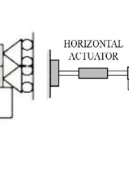
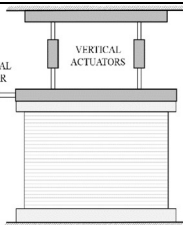
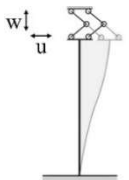
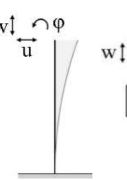
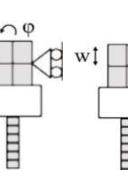
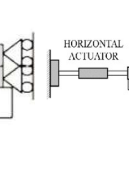
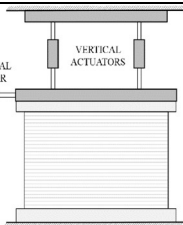
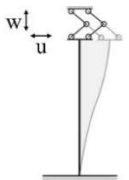
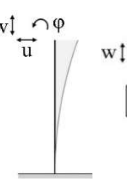
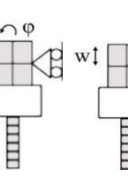
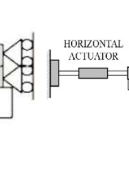
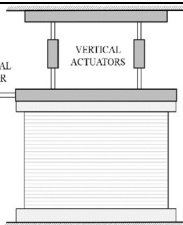
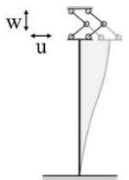
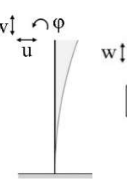
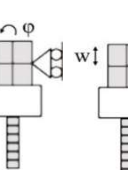
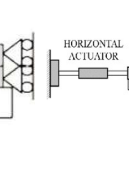
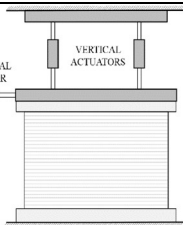
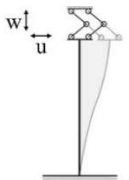
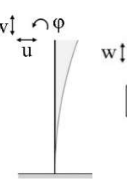
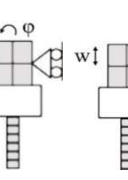
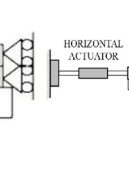
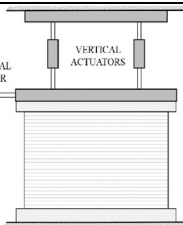
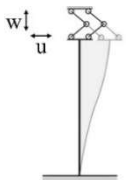
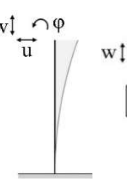
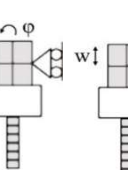
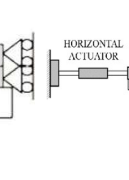
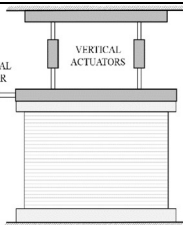
6.3 URM walls subjected to in-plane cyclic loading

A series of full-scale URM wall specimens were tested in 2015-2016 at the laboratories of Eucentre (Pavia, Italy) (Graziotti et al. 2015, 2016b). More specifically, three CS (CS1-2-3) and five CL (CL1-2-3-4-5) masonry panels were subjected to quasi-static in-plane cyclic

shear-compression loading with several combinations of boundary conditions (i.e. fixed-fixed, FF, and cantilevered, CV), overburden and aspect ratios (see Table 29). Moreover, OOP restraints were introduced through the top reinforced concrete (RC) beam. Nevertheless, during the test of CS2, a spurious OOP mechanism was observed and an additional restraint was then imposed on subsequent tests at the interface between the top RC beam and the walls tested, as depicted in Table 29, avoiding a repeat of unwanted beam rotations and ensuring fully in-plane behaviour. The walls were founded on a RC beam, which was clamped to the lab strong floor.

The displacement histories were imposed to the top beam by a horizontal servo-hydraulic actuator, whereas two horizontal servo-hydraulic actuators assured the boundary conditions, as well as the vertical pressure σ_v . Three loading cycles were performed for each target displacement δ_i , except for the case of CL5, where a single cycle was constituted by just one positive and negative application of δ_i . Thus, since the only difference between CL4 and CL5 was the loading history (i.e. each cycle was repeated just one time in CL5), the latter has not been considered in this work. Masonry material properties have already been reported in Table 28 of the previous section. Interested readers are referred to the technical reports by Eucentre (Graziotti et al. 2015, 2016b) for further details about loading protocols and experimental outcomes.

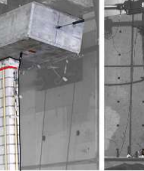
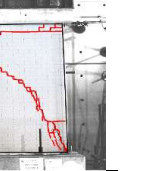
Table 29 Test set-up, dimensions, boundary conditions and OOP restrains of both CS and CL walls

Wall ID	L_w [m]	H_w [m]	t_w [m]	σ_v [MPa]	Boundary conditions		Out-of-plane restraints		Test set-up	
					FF	CV	CS2	other walls		
CS1	1.1	2.75	0.102	0.70	FF					
CS2	1.1	2.75	0.102	0.52	FF					
CS3	4.0	2.75	0.102	0.30	CV					
CL1	1.2	2.71	0.208	0.52	FF					
CL2	1.2	2.71	0.208	1.20	FF					
CL3	1.2	2.71	0.208	0.86	FF					
CL4	2.7	2.71	0.208	0.30	FF					

Wall responses and loading protocols in terms of damage patterns and imposed drift for each cycle are summarised in Table 30 and Table 31. CS1 initially exhibited rocking behaviour with horizontal cracks opening at the edges. Then, the cracks migrated towards the panel centre, reducing its effective height. Brick-crushing occurred in several CS units, leading to an unusually high energy dissipation, as further discussed in Graziotti et al. (2016a).

The behaviour of CS2 in the first cycles was characterised by pure rocking, and no relevant damage was observed. Then, a spurious OOP mechanism due to insufficient restraint provided by test setup occurred, and the test was stopped. For all other tests, the loading protocol ended when the piers were unable to sustain the imposed vertical loads anymore. The response of CS3 was mainly governed by shear mechanisms, with stepped cracks at the centre of the panel, sliding and shear failure through units.

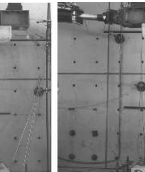
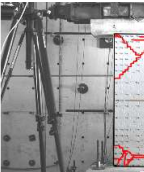
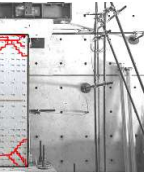
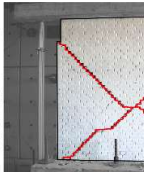
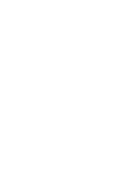
Table 30 Experimental response and loading history for CS wall specimens. Adapted from Graziotti et al. (2015)

		CS1				CS2				CS3		
Exp. response												
	cycle	1	2	3	4	5	6	7	8	9	10	11
θ [‰]	CS2	0.09	0.33	0.46	0.59	0.84	1.09	1.60	2.10	-	-	-
	CS1	0.19	0.26	0.39	0.51	0.76	1.01	1.51	2.02	2.53	3.03	4.04
	CS3	0.03	0.07	0.10	0.16	0.20	0.28	0.37	0.53	0.81	0.98	1.53
	cycle	12	13	14	15	16	17	18	19	20	21	22
	CS1	5.04	6.05	8.06	10.07	12.57	15.07	20.10	-	-	-	-
CS3	2.06	2.53	3.06	-	-	-	-	-	-	-	-	

CL brick masonry specimens, due to different dimensions and bond patterns, mainly suffered flexure-governed failure modes. CL1 exhibited pure rocking behaviour during the whole test, with damage mainly due to masonry crushing mechanisms.

The response of CL2 was characterised by diagonal joint sliding phenomena occurred during the last phases of the test in the bottom half of the pier. In the case of CL3, instead, a hybrid failure occurred (shear modes were observed after the attainment of the maximum flexural capacity of the pier). Although the wall exhibited intensive toe-crushing damage, flexural failure mechanisms were predominant. Finally, as expected, CL4 failed in shear, with diagonal stepped cracks visible in the central part of the panel.

Table 31 Experimental response and loading history for CL wall specimens. Adapted from Graziotti et al. (2016b)

		CL1			CL2			CL3			CL4	
Exp. response												
	cycle	1	2	3	4	5	6	7	8	9	10	11
θ [‰]	CL1	0.16	0.27	0.51	0.55	0.77	1.08	1.55	2.09	2.60	3.10	4.14
	CL2	0.13	0.31	0.39	0.53	0.78	1.02	1.53	2.04	2.55	3.06	4.10
	CL3	0.15	0.31	0.37	0.49	0.74	0.99	1.51	2.01	2.52	3.03	4.02
	CL4	0.03	0.04	0.08	0.16	0.20	0.29	0.38	0.51	0.77	1.03	1.53
	cycle	12	13	14	15	16	17	18	19	20	21	22
CL1	5.15	6.19	8.19	10.22	12.76	15.30	20.36	25.45	30.50	40.68	-	-
CL2	5.11	6.12	8.14	10.18	12.73	-	-	-	-	-	-	-
CL3	5.02	6.04	8.08	10.11	12.65	-	-	-	-	-	-	-
CL4	2.04	2.55	3.19	-	-	-	-	-	-	-	-	-

6.4 Simulation of the in-plane response of full-scale URM specimens

The mechanical response of URM elements subjected to in-plane cyclic loading sequences commonly involves progressive strength reduction, stiffness degradation and $P-\Delta$ effects.

When using advanced modelling methods, rather than simplified approaches, such quantities cannot be directly implemented in the code for fitting experimental data, being implicitly accounted through several modelling assumptions (e.g. constitutive laws and discretisation procedures). Thus, an attempt was made in this section to verify the effectiveness of the employed modelling strategy by comparing a wide range of key experimental and numerical parameters. Maximum capacity, lateral stiffness and total energy dissipation were considered, as well as the final crack patterns through joints and bricks. Further, dimensionless stiffness and hysteretic energy ratios for each cycle were also computed for assessing the ability of DEM to correctly predict the interaction between stiffness degradation and energy dissipation rate. For the same purpose, with reference to the abovementioned quantities, a statistical evaluation of relative average and relative standard errors between numerical predictions and experimental data was conducted. It is worth noting that such indices might also be of interest for both analytical models founded on optimisation procedures and energy-based design criteria. Experimentally-derived and inferred masonry material properties reported in Table 28 for both CS and CL brick masonry were again employed in this modelling exercise.

To faithfully represent the different experimental layouts and loading protocols, seven different DEM models, based on the assumptions discussed in the previous sections, were developed for reproducing numerically the cyclic in-plane response of both CS and CL full-scale wall-specimens. Top and bottom RC beams were modelled by a single block, internally subdivided into smaller FE regular portions (i.e. $0.5L_b \times 1.5H_b$), according to the abovementioned mixed-discretisation technique, as depicted in Figure 70.

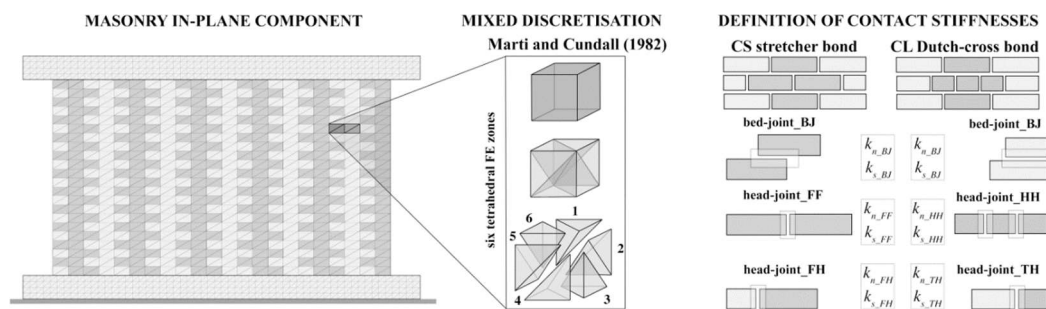


Figure 70 Discretisation and contact stiffness depending on the considered joint and bond pattern

Different equivalent densities and boundary conditions, depending on the considered overburden pressures and experimental configurations respectively, were assigned to the top RC beam. The RC foundation was considered as fully fixed. Then, the envisaged cyclic displacement loading protocols were imposed through the application of multi-stepped velocity time-histories to decrease the influence of inertia forces, as discussed in the previous section. Similarly, the use of adaptive damping was again combined with mass and size scaling procedures to decrease computational efforts.

With respect to the mesh size adopted for both of the RC beams, a slightly different hexahedral subdivision (i.e. $0.5L_b \times H_b$) was assigned to the bricks, whose actual arrangement (i.e. stretcher and Dutch-cross bond) was represented accurately. The modified Mohr-Coulomb plasticity model with tension cut-off and compression cap

described previously was assigned to all the CS and CL brick elements. Since the contact stiffnesses of the joints depend on the longitudinal/transversal distance L between two adjacent brick centroids (see Eq. (1)), different k_n , k_s were assigned to bed and head mortar layers according to the considered bond patterns. Both normal and shear stiffnesses associated with the selected bond patterns are reported in Table 32, distinguishing between the ones assigned to bed and head joints respectively, where FF indicates the joint stiffnesses computed considering the centroid distance between two consecutive bricks ($L=L_b$), while FH refers to joints where the centroid distance between adjacent full and half-length bricks ($L=0.75 L_b$) was used.

Finally, TH ($L=0.625 L_b$) is associated with the centroid distance between three-quarters and half-length brick, whereas head joint stiffnesses associated with the distance between two adjacent half bricks ($L=0.5 L_b$) were represented by the acronym HH. It is herein recalled that a Mohr-Coulomb slip model with tension cut-off characterised the behaviour of both bed and head joints.

Table 32 Normal and shear stiffnesses assigned to both bed and head joints depending on the centroid distance L

Property	Nomenclature	CS	CL
Bed-joint normal stiffness [MPa/m]	k_n	6.97e4	1.66e5
Bed-joint shear stiffness [MPa/m]	k_s	3.17e4	7.56e4
FF head-joint normal stiffness [MPa/m]	k_{n_FF}	2.34e4	4.01e4
FF head-joint shear stiffness [MPa/m]	k_{s_FF}	1.062e4	1.82e4
FH head-joint normal stiffness [MPa/m]	k_{n_FH}	3.11e4	5.33e4
FH head-joint shear stiffness [MPa/m]	k_{s_FH}	1.42e4	2.42e4
TH head-joint normal stiffness [MPa/m]	k_{n_TH}	-	4.57e4
TH head-joint shear stiffness [MPa/m]	k_{s_TH}	-	2.08e4
HH head-joint normal stiffness [MPa/m]	k_{n_HH}	-	8.02e4
HH head-joint shear stiffness [MPa/m]	k_{s_HH}	-	3.64e4

6.4.1 Hysteretic response and bilinear idealisation

In this subsection, several key-parameters such as ultimate displacement and capacity, initial stiffness and energy dissipation were compared with their numerical counterparts to assess the model capability in reproducing the experimental hysteretic responses. For the same purposes, as depicted from Figure 71 to Figure 73, equivalent bilinear envelopes, developed according to the procedure suggested by Costa et al. (2011), were also computed, and involves the definition of an equivalent elastic stiffness parameter k_{el_eq} , obtained by considering a secant value at $0.70V_{max}$, where V_{max} is the maximum base shear of the cyclic envelope.

Then, the ultimate displacement δ_u is evaluated when a strength reduction equal to the 20% of V_{max} is observed. The ultimate lateral capacity V_u , corresponding to the horizontal branch of the bilinear curve, can be found by ensuring that the area below the cyclic envelope corresponds to the one generated by the bilinear curve profile. Finally, the elastic displacement δ_e and ultimate ductility μ_u were defined by the ratios V_u/k_{el_eq} and δ_u/δ_e respectively.

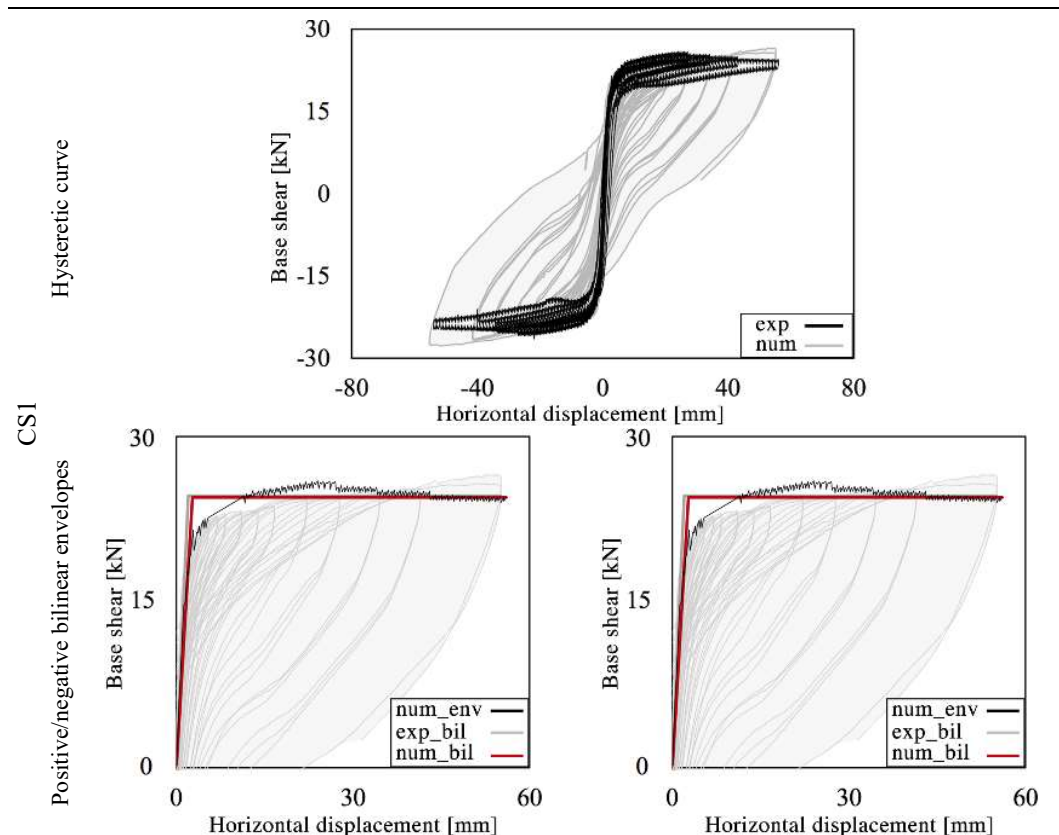
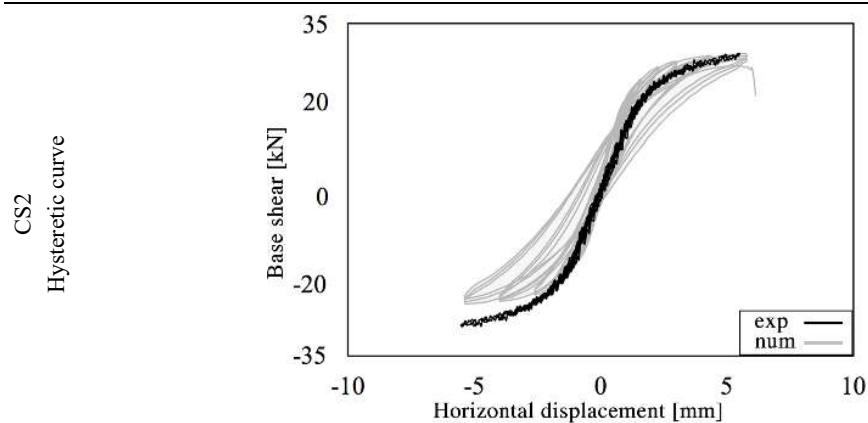


Figure 71 CS piers: experimental (Graziotti et al. 2015) vs. numerical hysteresis curves and bilinear envelopes

The DE models satisfactorily represented, as a whole, the in-plane hysteretic behaviour of the CS piers. Nevertheless, especially in the case of CS1, where the experimental energy dissipation was unusually high, the dissipation was not fully captured. This is a common issue in numerical modelling of rocking masonry walls even using other modelling approaches, e.g. Malomo et al. (2018) and Penna et al. (2014). The response of CS2 has reproduced appropriately, despite slight differences in reference to the final dissipated energy and ductility.



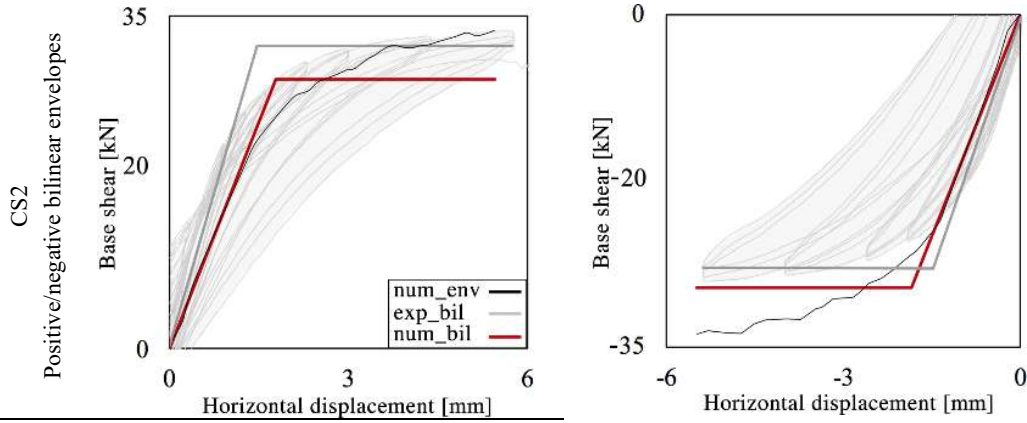


Figure 72 CS piers: experimental (Graziotti et al. 2015) vs. numerical hysteresis curves and bilinear envelopes

The numerical model of CS3 was able to predict the initial cohesive strength peak, as well as the cyclic dissipated energy and ultimate capacity. This notwithstanding, an early reduction of the lateral strength, which was not observed experimentally, characterised the last numerical cycles affecting considerably the total amount of dissipated energy.

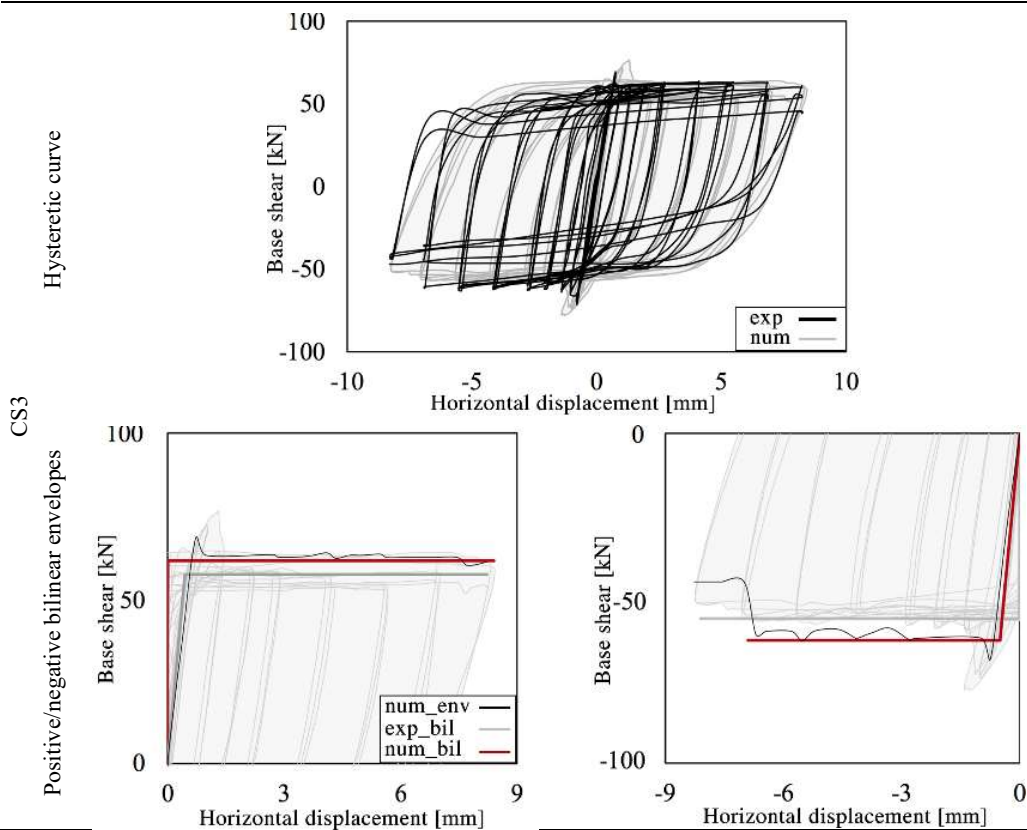


Figure 73 CS piers: experimental (Graziotti et al. 2015) vs. numerical hysteresis curves and bilinear envelopes

However, a reasonable agreement in terms of numerical backbone curves and bilinear envelopes was found, which is reassuring. The positive impression on the numerical vs. experimental comparison reported above is further confirmed by what is shown in Table 33, where the most relevant values associated with the cyclic behaviour of the URM piers are reported. It can be observed that the DEM models estimated values of maximum capacity V_{max}^+ , V_{max}^- , lateral stiffness k_{el} and energy dissipation E_h that feature differences with respect to the tests observations in an acceptable range. Similarly, for what concerns the bilinear idealisations, suitable values of k_{el_eq} , and V_u^+ , V_u^- were also obtained.

Table 33 CS piers: comparison between experimental and numerical initial stiffness, positive-negative maximum capacity and relevant parameters for bilinear envelopes

Wall ID	Experimental							Numerical						
	k_{el} [kN/mm]	V_{max}^+ [kN]	V_{max}^- [kN]	V_u^+ [kN]	V_u^- [kN]	k_{el_eq} [kN/mm]	E_h [kJ]	k_{el} [kN/mm]	V_{max}^+ [kN]	V_{max}^- [kN]	V_u^+ [kN]	V_u^- [kN]	k_{el_eq} [kN/mm]	E_h [kJ]
CS1	22.9	26.5	-27.6	24.6	-25.4	14.2	13.7	22.5	25.6	-25.7	24.5	-24.7	10.1	5.5
CS2	24.0	28.6	-24.1	28.6	-24.1	16.9	0.5	23.5	30.9	-31.0	24.3	-24.6	13.5	0.3
CS3	152.6	76.7	-78.0	61.5	-56.1	130.5	14.4	153.2	63.8	-65.8	57.2	-62.7	126.0	15.1

The simulation of the in-plane cyclic response of CL piers led to analogous results, as summarised in Figure 74 to Figure 77.

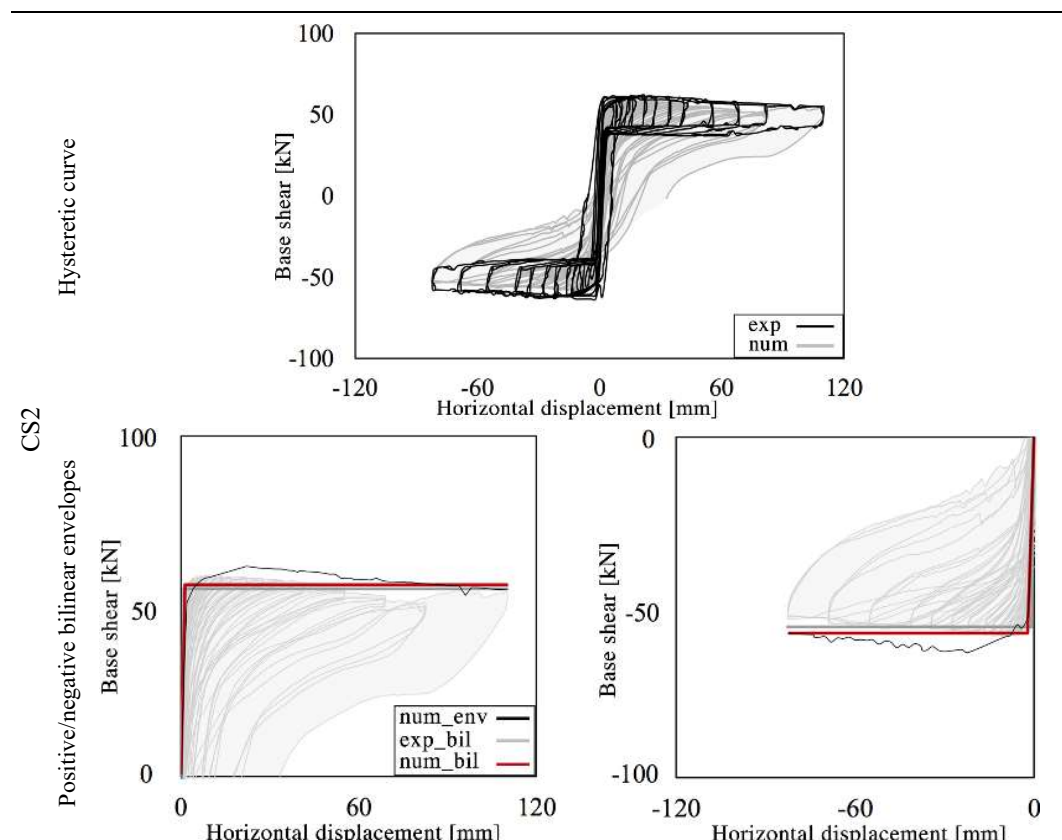


Figure 74 CL piers: experimental (Graziotti et al. 2016b) vs. numerical hysteresis curves and bilinear envelopes

Indeed, the model of CL1 was able to account for the energy dissipation caused by the intensive rocking behaviour of its experimental counterpart. It is also worth noting that the $P-\Delta$ effect, which was particularly evident, was captured convincingly.

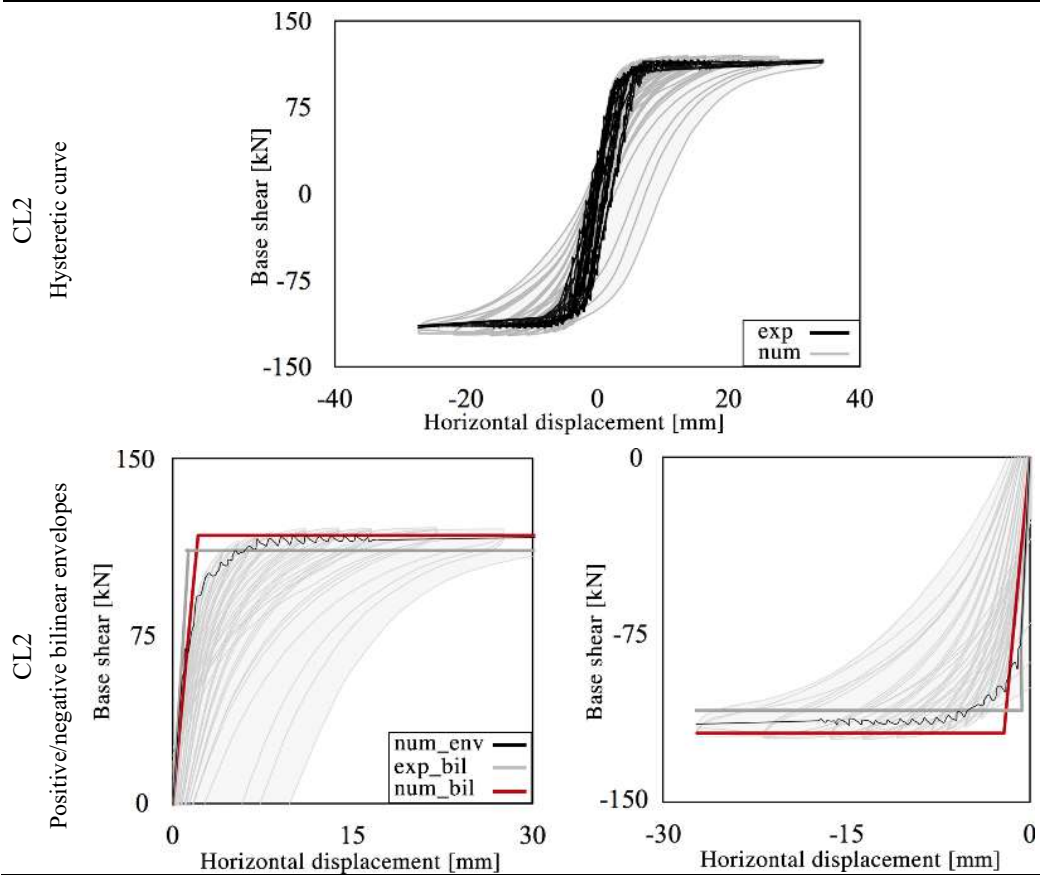
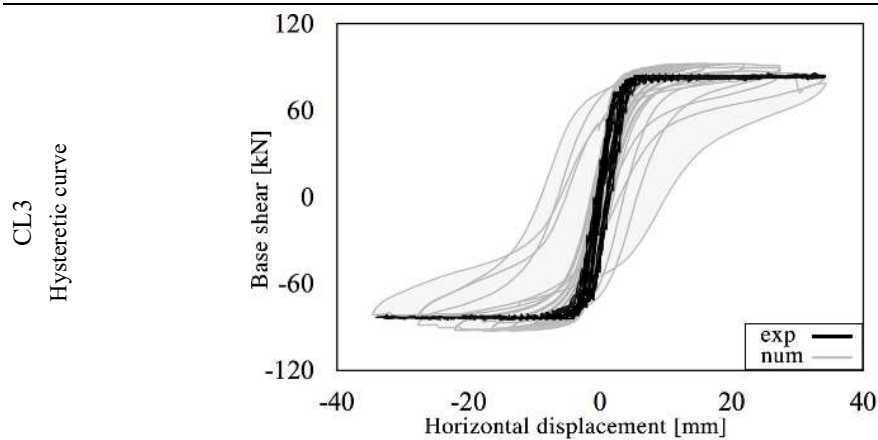


Figure 75 CL piers: experimental (Graziotti et al. 2016b) vs. numerical hysteresis curves and bilinear envelopes



In-plane cyclic performances of URM walls subjected to shear-compression

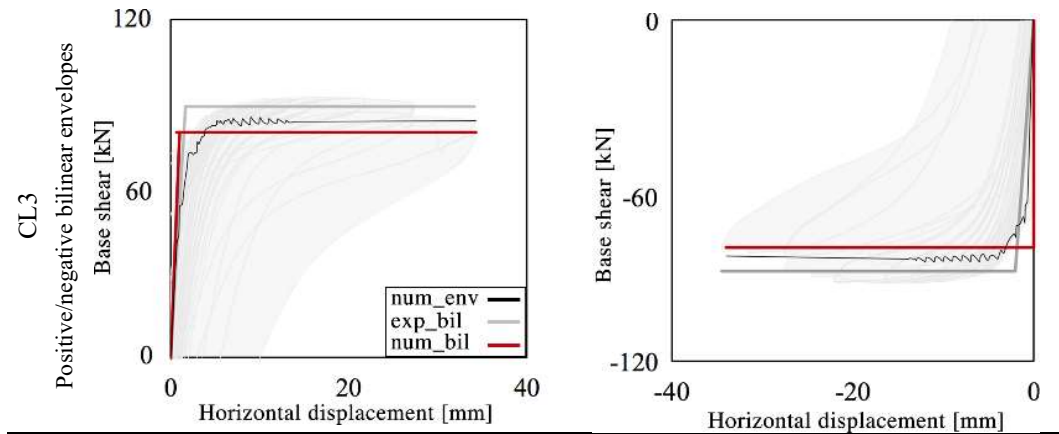


Figure 76 CL piers: experimental (Graziotti et al. 2016b) vs. numerical hysteresis curves and bilinear envelopes

The initial experimental responses of CL2 and CL3, mainly governed by rocking modes, were satisfactorily modelled. In the last cycles, instead, when flexural failures became predominant, the energy dissipation was not adequately represented. However, both the crack patterns were reproduced accurately, as reported in the next subsection.

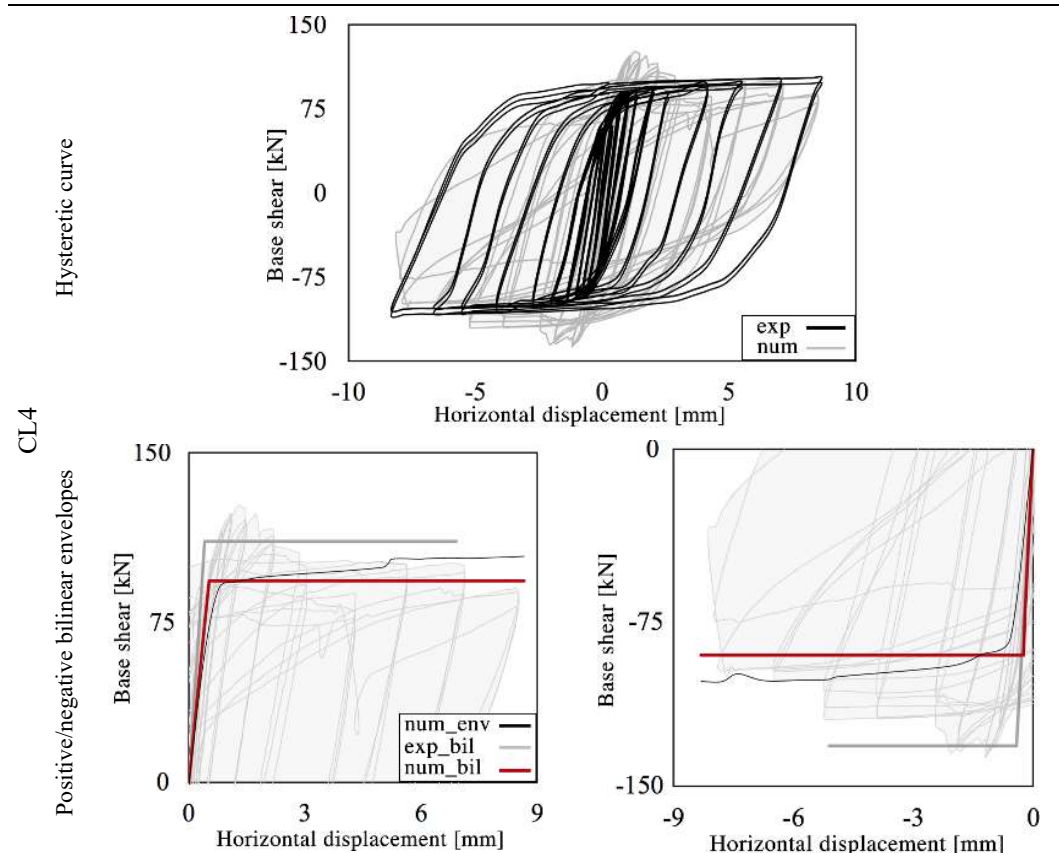


Figure 77 CL piers: experimental (Graziotti et al. 2016b) vs. numerical hysteresis curves and bilinear envelopes

The differences in energy dissipation might be due to the simplified tensile and cohesive laws implemented in the employed Mohr-Coulomb model, according to which the post-peak softening branches are neglected. Finally, even though the hysteretic response of CL4 was properly replicated by the DE model, the cohesive peak was not captured, and neither was the strength degradation of the last cycles. However, both residual capacity and overall energy dissipation were faithfully described.

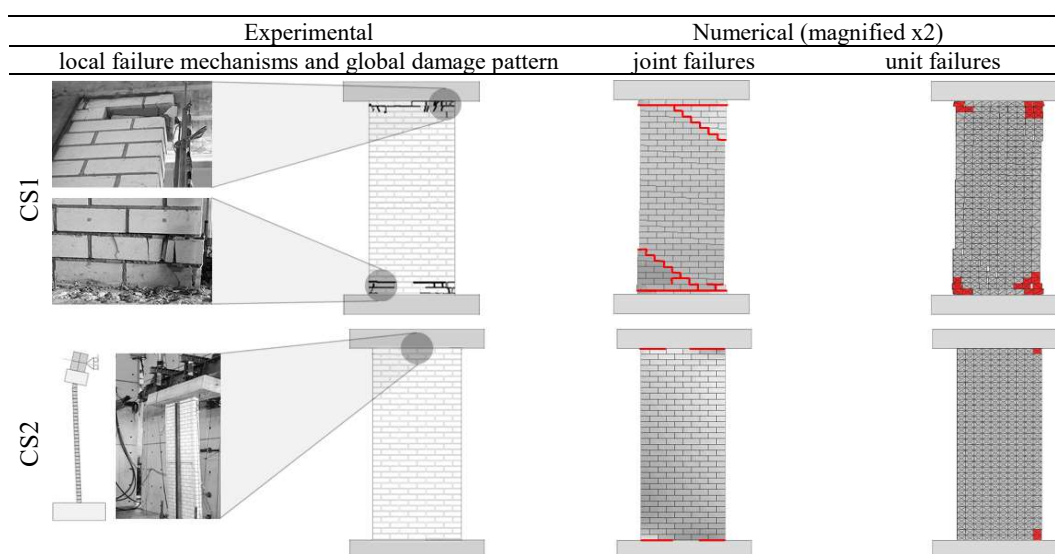
As summarised in Table 34, the comparison between experimental and numerical results substantially confirmed the effectiveness of the modelling approach presented in this work. Again, differences were observed in terms of total dissipated energy, although both lateral capacity and initial stiffness were properly represented in most of the cases. Accordingly, only slight differences between bilinear envelopes were detected.

Table 34 Comparison between experimental and numerical hysteretic response of CL walls

Wall ID	Experimental							Numerical						
	k_{el} [kN/mm]	V_{max}^+ [kN]	V_{max}^- [kN]	V_u^+ [kN]	V_u^- [kN]	k_{el_eq} [kN/mm]	E_h [kJ]	k_{el} [kN/mm]	V_{max}^+ [kN]	V_{max}^- [kN]	V_u^+ [kN]	V_u^- [kN]	k_{el_eq} [kN/mm]	E_h [kJ]
CL1	67.5	59.1	58.4	55.1	55.7	68.2	29.8	66.1	60.6	60.8	56.53	57.6	32.2	29.7
CL2	87.5	119.9	122.6	116.6	119.9	56.4	19.1	82.6	115.6	116.9	110.87	111.3	98.2	13.3
CL3	68.6	92.5	92.5	89.5	-88.4	47.8	20.8	72.8	85.9	-84.9	80.97	80.1	149.1	9.6
CL4	359.3	126.1	137.1	109.6	132.1	292.2	19.6	355.2	102.9	-103.0	91.64	92.1	233.2	21.7

6.4.2 Joint crack pattern and failure through units

This subsection provides a comparison between predicted in-plane local failure modes and their experimental counterparts, considering both joint failures and cracking through units. Then, with reference to the combination of global damage patterns and hysteretic responses, an attempt was made to identify the governing failure mechanisms associated with the ultimate capacity of the specimens.



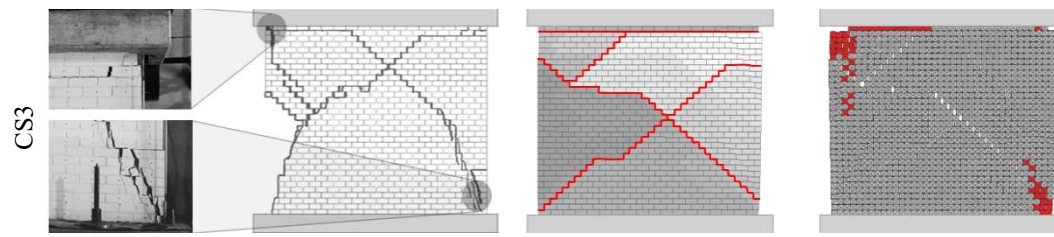


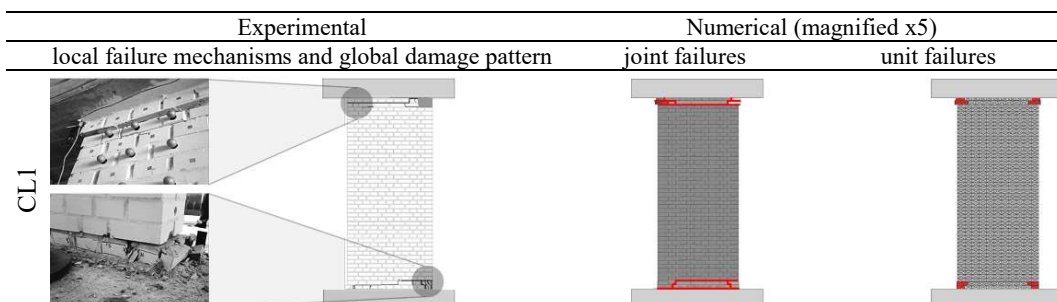
Figure 78 Experimental (black) vs. numerical (red) in-plane local failure mechanisms of CS walls

As discussed in what follows, the damage predicted by the numerical models satisfactorily replicated the experimental crack patterns in most of the cases. The DE models of CS1 (see Figure 78), in addition to masonry crushing phenomena, also exhibited stepped cracks at the interface with the RC beams. This aspect is probably due to the fact that, although unit failures were satisfactorily modelled, the experimentally-observed brick expulsion of the last cycles could not be captured. Hence, the increase in the rocking demand caused spurious stress concentrations, leading to the formation of joint diagonal cracks.

The behaviour described by the CS2 model was governed by rocking mechanism, which caused unit failures at the interface with the RC beams. Even though the experimental counterpart did not suffer such damage mode, the overall response of the specimen was sufficiently captured. CS3 exhibited diagonal joint cracks, as well as unit failures at the heel/toe. Such phenomena were properly simulated numerically, where the formation of X-stepped cracks at the centre of the panel occurred in combination to unit failures along the wall boundaries.

Similarly to what was observed during the related test, the crack pattern obtained for CL1 was a combination of base/top joint sliding and unit crushing, as depicted in Figure 79.

The simulation of CL2 and CL3, instead, predicted the development of diagonal joint cracks at the bottom and at the bottom/top of the wall respectively, as observed experimentally. Regarding unit crushing, the models adequately represented such failure modes up to the very last cycles, where a substantial damage level was reached. Finally, the X-stepped joint crack pattern exhibited by CL4 was accurately replicated by the model, which slightly overestimated the propagation of unit failure mechanisms toward the centre of the panel.



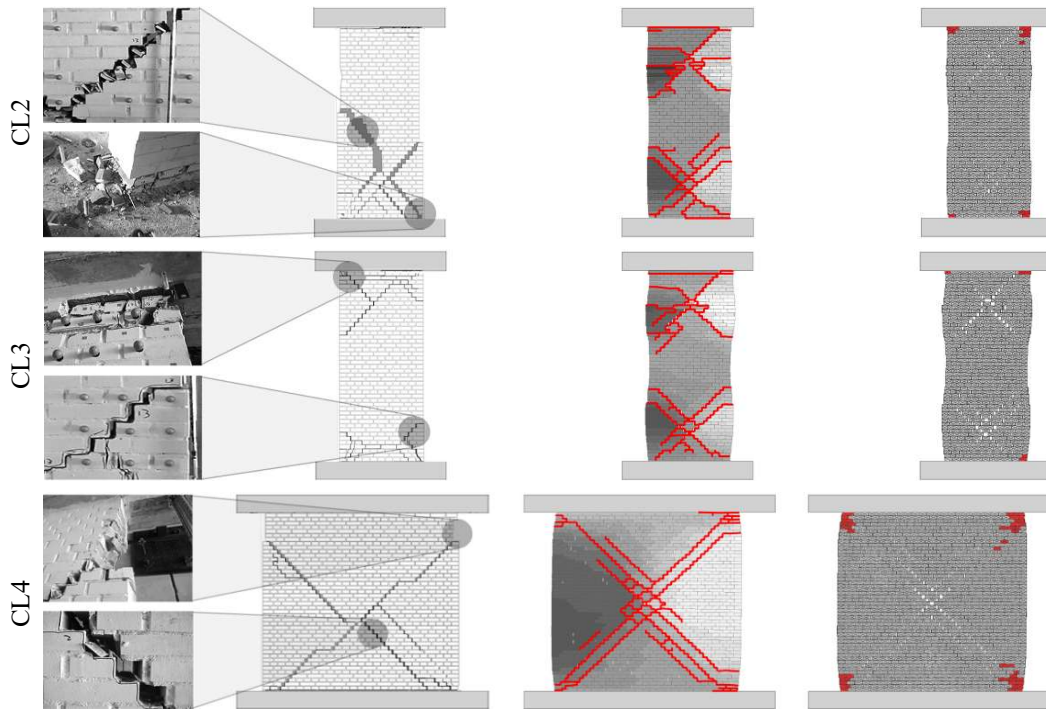


Figure 79 Experimental (black) vs. numerical (red) in-plane local failure mechanisms of CL walls

Given the results presented in this subsection, and scrutinising the hysteretic behaviour exhibited by the DE models, an attempt was made in Table 35 to identify the failure mechanisms that governed the numerical damage modes at the global scale. As summarised below, an adequate agreement between experimental and predicted responses was obtained.

Table 35 Experimental and numerical failure mode /damage

Wall ID	Experimental failure mode / damage	Predicted failure mode / damage
CS1	Masonry crushing	Masonry crushing
CS2	-	Slight damage due to top/base sliding and unit failure
CS3	Mid-height shear failure	Mid-height shear failure / masonry crushing
CL1	Masonry crushing / base sliding	Masonry crushing / base sliding
CL2	Flexural-shear failure	Flexural failure / masonry crushing
CL3	Flexural failure / masonry crushing	Flexural failure / masonry crushing
CL4	Mid-height shear failure	Mid-height shear failure

6.4.3 Effect of cyclic loading

The response of URM walls subjected to cyclic loading schemes usually involves progressive strength and stiffness degradation depending on several factors, such as boundary conditions, applied vertical pressure and associated failure mechanisms. In this framework, the evaluation of energy dissipation represents an adequate indicator of the abovementioned phenomena, being directly related to the cyclic deterioration of such mechanical quantities.

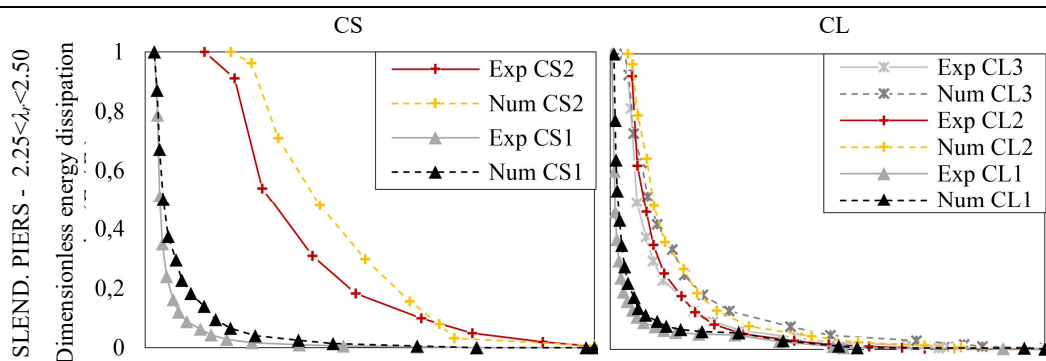
However, when comparing numerical and experimental hysteretic responses, the dissipated energy is often computed considering only its total (or final) extent, thus without investigating the interaction with both stiffness and strength degradation for each cycle, leading to a partial assessment of the model adequacy in predicting the actual behaviour of a given structural element. In this subsection, to overcome the abovementioned limitations, a comparison in terms of dimensionless stiffness and energy dissipation ratios is proposed. It is based on the definition of two different parameters, as shown in Eqs. (7)-(8).

The first one, k_d , represents the ratio between initial stiffness k_{el} and k_i (i.e. the stiffness of the i -th cycle), whilst E_d stands for E_i (the dissipated energy up to the i -th cycle) divided by the total dissipated energy E_h . The lateral strength progressive degradation is implicitly accounted for by the adopted definition of secant (or apparent) stiffness, described in e.g. Mayes and Clough (1975) and Soroushian et al. (1988), as reported in Eq. (9), where positive/negative values of maximum capacity and displacement were named $V_{max,i}^+$, $V_{max,i}^-$, $S_{max,i}^+$, $S_{max,i}^-$, respectively:

$$k_d = \left(\frac{k_{el}}{k_i} \right) \quad (7) \quad E_d = \left(\frac{E_i}{E_h} \right) \quad (8) \quad k_i = \frac{|V_{max,i}^+| + |V_{max,i}^-|}{|S_{max,i}^+| + |S_{max,i}^-|} \quad (9)$$

The assessment of the actual lateral stiffness of URM elements, and its progressive reduction when cyclic loading histories are considered, especially in case of highly nonlinear or rocking-dominated responses, might require advanced analytical procedures and it is still object of debate.

Thus, it is worth mentioning that the stiffness parameter k_i should be intended as a simplified conventional index. Also note that the energy dissipated at each cycle was evaluated by locating the minima of the work function and calculating by iterative integrations the area under the curve, as reported in Malomo et al. (2018). The results are summarised in Figure 80, where the data are organised in terms of aspect ratio λ_r (i.e. slender or squat piers) and masonry type (i.e. CS or CL):



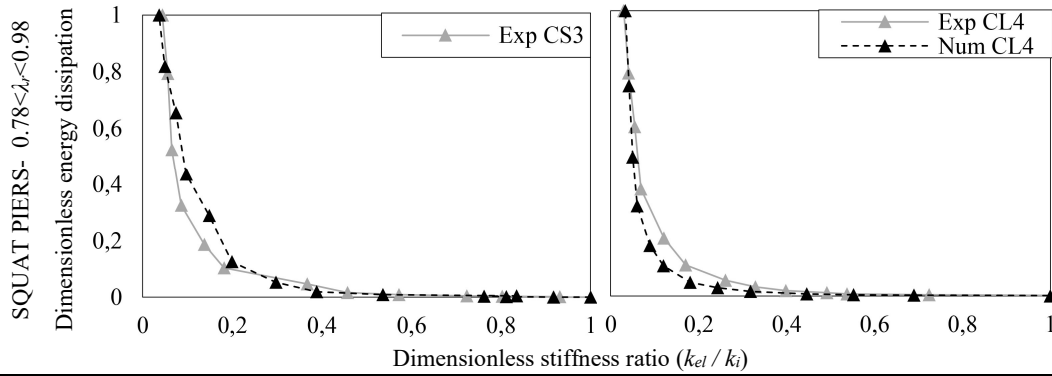


Figure 80 Comparison between experimental and numerical effect of cyclic loading

As depicted in Figure 80, although differences in total dissipated energy were observed, especially for the case of slender piers, the models captured with varying levels of accuracy the interaction between strength and stiffness degradation, as well as the energy dissipation rate. Since the resulting relationships could alternatively be directly employed in simplified and energy-based methods, e.g. Wen (1976), the equations associated with both experimental and numerical $k_d - E_d$ curves, obtained considering power trend lines ($0.84 < R^2 < 0.97$), are also reported in Table 36.

Table 36 Simplified expressions for evaluating the $k_d - E_d$ relationship

		Eq. [$k_d - E_d$]	
	Experimental		Numerical
CS1	$k_d = (2.0e^{-4}E_d)^{-2.4}$	CS1	$k_d = (6.0e^{-4}E_d)^{-2.4}$
CS2	$k_d = (1.6e^{-2}E_d)^{-2.5}$	CS2	$k_d = (4.9e^{-2}E_d)^{-6.5}$
CS3	$k_d = (1.5e^{-3}E_d)^{-2.3}$	CS3	$k_d = (1.3e^{-3}E_d)^{-2.5}$
CL1	$k_d = (4.5e^{-3}E_d)^{-1.1}$	CL1	$k_d = (4.6e^{-3}E_d)^{-1.2}$
CL2	$k_d = (4.4e^{-3}E_d)^{-1.9}$	CL2	$k_d = (2.2e^{-3}E_d)^{-2.1}$
CL3	$k_d = (5.5e^{-3}E_d)^{-1.7}$	CL3	$k_d = (1.3e^{-2}E_d)^{-1.5}$
CL4	$k_d = (8.0e^{-4}E_d)^{-2.4}$	CL4	$k_d = (4.0e^{-4}E_d)^{-2.5}$

6.4.4 Adequacy of numerical results

In this subsection, a further attempt was made to scrutinise the performance of the numerical models in order to quantify their capabilities in predicting the actual response of the specimens. Thus, with reference to representative hysteretic key-parameters (i.e. maximum capacity $V_{max,i}$ and energy dissipation E_i of the i -th cycle), a statistical evaluation of both relative average (ζ_{av} , Γ_{av}) and relative standard (ζ_{st} , Γ_{st}) errors was proposed.

Moreover, initial stiffness, maximum capacity and total dissipated energy ratios, were considered. Possible discrepancies in terms of bilinear envelopes were also considered by introducing the dimensionless parameter Δ_{bil} , i.e. the average standard error between the areas computed under positive/negative branches of both experimental and numerical curves. As suggested by Faella et al. (1992), the function errors defined by Eqs. (10)-(13) were considered, where n_c represents the number of loading cycles:

$$\left\{ \begin{array}{l} \zeta_{av} = \left(\frac{\chi_E}{\psi_E} \right) \\ \zeta_{st} = \left(\frac{\omega_E}{\psi_E} \right) \end{array} \right. \text{with} \quad \chi_E = \left(\frac{\sum_{i=1}^{n_c} |E_i^{exp} - E_i^{num}|}{n_c} \right), \quad \psi_E = \left(\frac{\sum_{i=1}^{n_c} |E_i^{exp}|}{n_c} \right), \quad \omega_E = \left(\frac{\sum_{i=1}^{n_c} |E_i^{exp} - E_i^{num}|^2}{n_c} \right)^{0.5} \quad (10)$$

$$\left\{ \begin{array}{l} \Gamma_{av} = \left(\frac{\chi_V}{\psi_V} \right) \\ \Gamma_{st} = \left(\frac{\omega_V}{\psi_V} \right) \end{array} \right. \text{with} \quad \chi_V = \left(\frac{\sum_{i=1}^{n_c} |V_{max,i}^{exp} - V_{max,i}^{num}|}{n_c} \right), \quad \psi_V = \left(\frac{\sum_{i=1}^{n_c} |V_{max,i}^{exp}|}{n_c} \right), \quad \omega_V = \left(\frac{\sum_{i=1}^{n_c} |V_{max,i}^{exp} - V_{max,i}^{num}|^2}{n_c} \right)^{0.5} \quad (12)$$

The employment of these equations allows a more accurate assessment of the numerical modelling reliability by evaluating the normalised deviation between numerical and experimental results for each cycle, as well as their statistical dispersion. Table 37 shows that the progressive decrease of lateral capacity was captured satisfactorily, as well as the associated peak values. For energy dissipation, relatively high percentages of deviation were obtained, especially in the case of slender piers, as expected. This might be explained by the fact that the final experimental cycles were characterised by a relatively high energy dissipation increments, which were not captured numerically. This aspect is also confirmed by the extent of ζ_{st} , which was considerably influenced by the different distribution of E_i during the final testing sequences.

Similarly, the hysteretic performances of CS3 were conditioned by a premature loss of strength occurred in the last loading phase. Moderate error characterised the response of CL4, where both energy dissipation and lateral capacity were accurately replicated. The initial stiffnesses were adequately represented, as reflected by the ratio $k_{el}^{exp}/k_{el}^{num}$. Consequently, a good agreement with reference to bilinear envelopes was also found for all the specimens, which is reassuring. Finally, based on the comparison between experimental and numerical damage, a conventional percentage error (0-100%) was assigned to each model with a view to quantify the accuracy of failure mode prediction (relevant for CS2 only).

Table 37 Statistical evaluation of modelling accuracy through the calculation of percentile deviation from experimental results

Wall	ζ_{av}	ζ_{st}	Γ_{av}	Γ_{st}	$k_{el}^{exp}/k_{el}^{num}$	$V_{max}^{exp}/V_{max}^{num}$	E_h^{exp}/E_h^{num}	Δ_{bil}	Failure mode error
ID	[%]	[%]	[%]	[%]	[%]	[%]	[%]	[%]	[%]
CS1	47.49	99.62	4.83	5.59	1.84	5.21	47.48	2.88	captured - 0
CS2	28.95	52.34	13.29	18.47	2.31	17.45	28.95	15.81	not fully captured - 30
CS3	19.11	31.97	11.76	13.78	0.38	9.11	19.01	10.95	captured - 0
CL1	26.58	41.84	5.03	6.61	2.20	3.44	26.50	1.81	captured - 0
CL2	16.87	39.15	4.60	5.22	5.93	4.47	15.48	5.19	captured - 0
CL3	34.94	73.08	6.22	6.76	5.83	7.21	34.92	8.98	captured - 0
CL4	7.73	14.91	16.40	22.14	1.16	21.85	1.51	9.23	captured - 0

The observations above are further confirmed by Figure 81(a)-(b), where a graphical representation of modelling accuracy depicts the percentage deviations computed above.

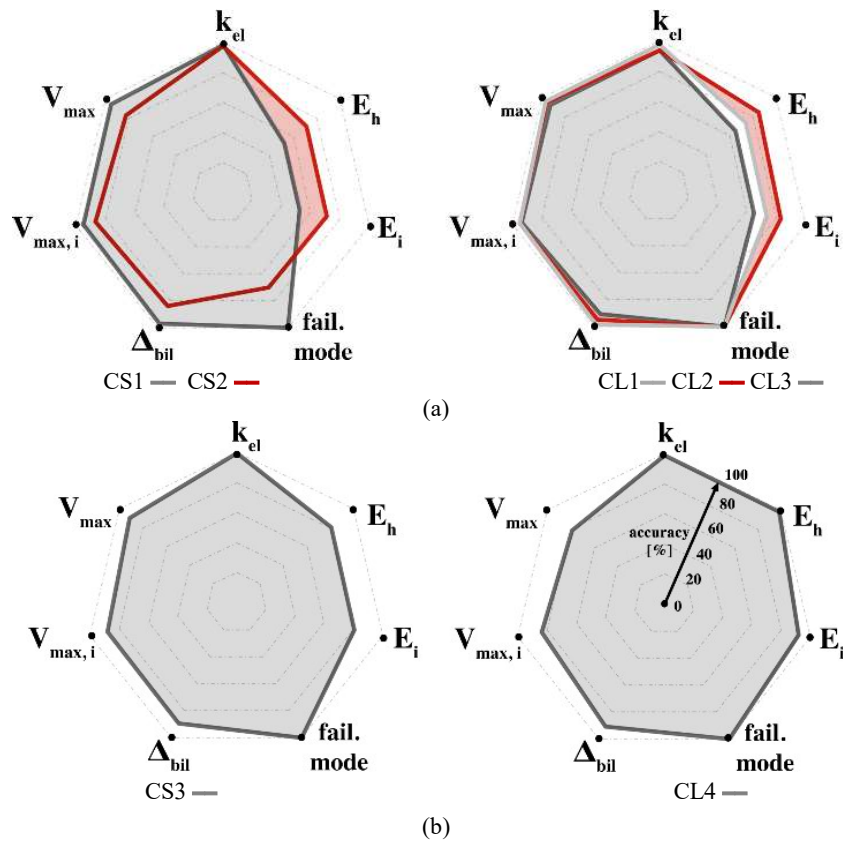


Figure 81 Representation of modelling accuracy in terms of initial stiffness, peak and i-th lateral strength, bilinear envelope, total and i-th dissipated energy, failure mode of both slender (a) and squat piers (b)

6.5 Conclusions

The in-plane response of URM components plays an important role in the overall seismic capacity of masonry buildings.

Thus, in this paper, a modelling approach is proposed to enable the use of DEM to reproduce the experimentally-observed responses of a series of URM full-scale specimens with mortared-joints, subjected to in-plane cyclic shear-compression quasi-static loading sequences, while considering the effects of boundary conditions, applied vertical pressure, bond pattern, masonry type and aspect ratio. In this approach, a strategy was developed in order to optimise the use of DEM reducing computational cost without compromising accuracy.

On the one hand, dynamic relaxation schemes were employed to decrease unwanted inertia effects, on the other a combination of size, mass, and time scaling procedures was proposed in order to reach a reasonable analysis time. Based on damage observations, masonry constitutive models have also been enhanced, including the possibility of describing brick crushing due to high compression stresses. After a first verification against experimental

results from characterisation tests, the same modelling strategy was applied to the simulation of URM walls subjected to quasi-static shear-compression cycles.

The DE models captured, with varying levels of accuracy, the experimental damage and the hysteretic behaviour, as well as the progressive deterioration of both in-plane stiffness and lateral strength. To objectively assess the capabilities of the models to adequately predict the actual performances of the URM panels, a statistical comparison between numerical and experimental outcomes has been undertaken. Despite some differences in terms of dissipated energy, a careful investigation of the effects of cyclic loading showed that the interaction between stiffness degradation and energy dissipation rate was satisfactorily accounted for numerically. Similarly, comparisons between equivalent bilinear envelopes substantially confirmed the reliability of the models, which appropriately simulated, as a whole, the global response of the specimens.

Regardless, further improvements are warranted, including the consideration of post-peak softening behaviour, as well as a verification of the effectiveness of the proposed simplified compressive failure model for different masonry types. Other possible enhancements might include the extension of the employed modelling strategy to more complex structures.

Acknowledgements

The first author gratefully acknowledges the financial support provided by University of Pavia – Research and Third Mission Unit (mobility grants for doctoral candidates – n.1914/2016- 92592). Part of this work was carried out with the financial support of the ReLUIIS-DPC Project 2017-2018 PR1 ‘Masonry structures’ funded by the Italian Department of Civil Protection.

References

- Azevedo, J., Sincaian, G., and Lemos, J. V. (2000). “Seismic behavior of blocky masonry structures.” *Earthquake Spectra*, 16(2), 337–365.
- Bathe, K.-J. (2001). “The inf-sup condition and its evaluation for mixed finite element methods.” *Computers & structures*, Elsevier, 79(2), 243–252.
- Bathe, K. J., and Saunders, H. (1984). *Finite element procedures in engineering analysis*. American Society of Mechanical Engineers.
- Braga, F., and Dolce, M. (1982). “A method for the analysis of antiseismic masonry multi-storey buildings.” *Proceedings of 16th International Brick and Block Masonry Conference*, Rome, Italy, 1089–1099.
- Brooks, J. J., and Baker, A. (1998). “Modulus of Elasticity of Masonry.” *Masonry International*, 12(2), 58–63.
- Bui, T. T., Limam, A., Sarhosis, V., and Hjiiaj, M. (2017). “Discrete element modelling of the in-plane and out-of-plane behaviour of dry-joint masonry wall constructions.” *Engineering Structures*, Elsevier, 136, 277–294.
- Casolo, S., and Peña, F. (2007). “Rigid element model for in-plane dynamics of masonry walls considering hysteretic behaviour and damage.” *Earthquake Engineering & Structural Dynamics*, Wiley-Blackwell, 36(8), 1029–1048.
- Chapelle, D., and Bathe, K.-J. (1998). “Fundamental considerations for the finite element analysis of shell structures.” *Computers & Structures*, Elsevier, 66(1), 19–36.

- Churilov, S., and Dumova-Jovanoska, E. (2008). "Calibration of a numerical model for masonry with application to experimental results." *Proceedings of the 6th International Conference Analytical Models and New Concepts in Concrete and Masonry Structures*, Łódź, Poland, 9–11.
- Ciesielski, R. (1999). "The dynamic module of elasticity of brick walls." *Proceedings of the Conference of the Committee of Civil Engineering PZITB: Lublin, Poland*.
- Cook, R. D., Malkus, D. S., Plesha, M. E., and Witt, R. J. (2002). *Concepts and Applications of Finite Element Analysis*. John Wiley & Sons, Inc., New York, USA.
- Costa, A. A., Penna, A., and Magenes, G. (2011). "Seismic performance of autoclaved aerated concrete (AAC) masonry: from experimental testing of the in-plane capacity of walls to building response simulation." *Journal of Earthquake Engineering*, Taylor & Francis, 15(1), 1–31.
- Courant, R., Friedrichs, K., and Lewy, H. (1967). "On the partial difference equations of mathematical physics." *IBM journal of Research and Development*, IBM, 11(2), 215–234.
- Cundall, P. A. (1971). "A computer model for simulating progressive large scale movements in blocky rock systems." *Proc. Symp. Rock Fracture (ISRM)*, Nancy.
- Cundall, P. A. (1982). "Adaptive density-scaling for time-explicit calculations." *Numerical Methods in Geomechanics*, Edmonton, Canada, 23–26.
- Cundall, P. A. (1987). "Distinct element models of rock and soil structure." *Analytical and computational methods in engineering rock mechanics*, 129–163.
- Cundall, P. A., and Hart, R. D. (1992). "Numerical modelling of discontinua." *Engineering computations*, 9(2), 101–113.
- DeJong, M. J., Giardina, G., Plunkett, W., and Ochsendorf, J. A. (2015). "Seismic design of a stone vault." *Society for Earthquake and Civil Engineering Dynamics Conference*, Cambridge, United Kingdom.
- DeJong, M. J., and Vibert, C. (2012). "Seismic response of stone masonry spires: Computational and experimental modeling." *Engineering Structures*, Elsevier, 40, 566–574.
- DeLorenzis, L., DeJong, M. J., and Ochsendorf, J. A. (2007). "Failure of masonry arches under impulse base motion." *Earthquake Engineering & Structural Dynamics*, Wiley-Blackwell, 36(14), 2119–2136.
- Faella, G., Manfredi, G., and Realfonzo, R. (1992). "Cyclic behaviour of tuff masonry walls under horizontal loadings." *Proceedings of the 6th Canadian Masonry Symposium*, Saskatchewan, Canada.
- de Felice, G. (2011). "Out-of-plane seismic capacity of masonry depending on wall section morphology." *International Journal of Architectural Heritage*, 5(4–5), 466–482.
- Graziotti, F., Rossi, A., Mandirola, M., Penna, A., and Magenes, G. (2016a). "Experimental characterization of calcium-silicate brick masonry for seismic assessment." *Proceedings of 16th International brick/block masonry conference*, Padua, Italy.
- Graziotti, F., Tomassetti, U., Rossi, A., Kallioras, S., Mandirola, M., Cenja, E., Penna, A., and Magenes, G. (2015). *Experimental campaign on cavity-wall systems representative of the Groningen building stock - Report n. EUC318/2015U*. Pavia, Italy.
- Graziotti, F., Tomassetti, U., Rossi, A., Marchesi, B., Kallioras, S., Mandirola, M., Fragomeli, A., Mellia, E., Peloso, S., Cuppari, F., Guerrini, G., Penna, A., and Magenes, G. (2016b). *Experimental campaign on a clay URM full-scale specimen representative of the Groningen building stock - Report n. EUC128/2016U*. Pavia,

- Italy.
- Haach, V. G., Vasconcelos, G., and Lourenço, P. B. (2011). "Parametrical study of masonry walls subjected to in-plane loading through numerical modeling." *Engineering Structures*, Elsevier, 33(4), 1377–1389.
- Itasca Consulting Group Inc. (2013). "3DEC. Three Dimensional Distinct Element Code."
- Itasca Consulting Group Inc. (2018). "3DEC – Three Dimensional Distinct Element Code, Ver. 5.20 User's Manual."
- Jäger, W., Irmschler, H., and Schubert, P. (2004). *Mauerwerk-Kalender 2004*. Ernst & Sohn Verlag für Architektur und technische Wissenschaften.
- Karapitta, L., Mouzakis, H., and Carydis, P. (2011). "Explicit finite-element analysis for the in-plane cyclic behavior of unreinforced masonry structures." *Earthquake Engineering and Structural Dynamics*, Wiley-Blackwell, 40(2), 175–193.
- Kaushik, H. B., Rai, D. C., and Jain, S. K. (2007). "Stress-strain characteristics of clay brick masonry under uniaxial compression." *Journal of materials in Civil Engineering*, American Society of Civil Engineers, 19(9), 728–739.
- Kawai, T. (1978). "New discrete models and their application to seismic response analysis of structures." *Nuclear Engineering and Design*, Elsevier, 48(1), 207–229.
- Lekhnitskii, S. G. (1963). *Of an anisotropic elastic body*. Holden-Day, San Francisco, USA.
- Lemos, J. V. (1997). "Discrete element modelling of the seismic behaviour of stone masonry arches." *Proceedings of the 4th International Symposium on Numerical Methods in Structural Masonry*, G. N. Pande, J. Middleton, and B. Kralj, eds., E & FN SPON, Florence, Italy, 220–227.
- Lemos, J. V. (2007). "Discrete element modeling of masonry structures." *International Journal of Architectural Heritage*, Taylor & Francis, 1(2), 190–213.
- Lourenço, P., and Milani, G. (2014). "Homogenization and Seismic Assessment: Review and Recent Trends." *Mechanics of Masonry Structures SE - 7*, Springer, Vienna, 293–341.
- Magenes, G., and Calvi, G. M. (1997). "In-plane seismic response of brick masonry walls." *Earthquake Engineering & Structural Dynamics*, 26(11), 1091–1112.
- Malomo, D., Pinho, R., and Penna, A. (2018). "Using the applied element method for modelling calcium silicate brick masonry subjected to in-plane cyclic loading." *Earthquake Engineering & Structural Dynamics*, 47(7), 1610–1630.
- Mann, W., and Muller, H. (1982). "Failure of shear-stressed masonry. An enlarged theory, tests and application to shear walls." *Proceedings of the British Ceramic Society*, (30), 223.
- Marti, J., and Cundall, P. (1982). "Mixed discretization procedure for accurate modelling of plastic collapse." *International Journal for Numerical and Analytical Methods in Geomechanics*, 6(1), 129–139.
- Matysek, P., and Janowski, Z. (1996). "Analysis of factors affecting the modulus of elasticity of the walls." *Proceedings of the Conference of the Committee of Civil Engineering PZITB: Lublin, Poland*.
- Mayes, R. L., and Clough, R. W. (1975). *State-of-the-art in Seismic Shear Strength of Masonry: An Evaluation and Review, Report No. EERC 75-21*. Berkeley, California.
- Meguro, K., and Tagel-Din, H. (2000). "Applied element method for structural analysis: Theory and application for linear materials." *Structural Engineering/Earthquake Engineering*, Japan Society of Civil Engineers, 17(1), 21s--35s.
- Miglietta, P. C., Bentz, E. C., and Grasselli, G. (2017). "Finite/discrete element modelling

- of reversed cyclic tests on unreinforced masonry structures.” *Engineering Structures*, 138, 159–169.
- Munjiza, A. (2004). *The combined finite-discrete element method. The Combined Finite-Discrete Element Method*, Wiley, New York, USA.
- Otter, J. R. H. (1966). “Dynamic relaxation compared with other iterative finite difference methods.” *Nuclear Engineering and Design*, 3(1), 183–185.
- Papantonopoulos, C., Psycharis, I. N., Papastamatiou, D. Y., Lemos, J. V., and Mouzakis, H. P. (2002). “Numerical prediction of the earthquake response of classical columns using the distinct element method.” *Earthquake Engineering & Structural Dynamics*, Wiley-Blackwell, 31(9), 1699–1717.
- Paulay, T., and Priestley, J. N. (1992). *Seismic Design of Reinforced Concrete and Masonry Buildings*. Wiley, New York, USA.
- Penna, A., Lagomarsino, S., and Galasco, A. (2014). “A nonlinear macroelement model for the seismic analysis of masonry buildings.” *Earthquake Engineering & Structural Dynamics*, Wiley-Blackwell, 43(2), 159–179.
- Petry, S., and Beyer, K. (2015). “Force-displacement response of in-plane-loaded URM walls with a dominating flexural mode.” *Earthquake Engineering and Structural Dynamics*, Wiley-Blackwell, 44(14), 2551–2573.
- Psycharis, I. N., Lemos, J. V., Papastamatiou, D. Y., Zambas, C., and Papantonopoulos, C. (2003). “Numerical study of the seismic behaviour of a part of the Parthenon Pronaos.” *Earthquake Engineering & Structural Dynamics*, Wiley-Blackwell, 32(13), 2063–2084.
- Raka, E., Spacone, E., Sepe, V., and Camata, G. (2015). “Advanced frame element for seismic analysis of masonry structures: model formulation and validation.” *Earthquake Engineering & Structural Dynamics*, Wiley-Blackwell, 44(14), 2489–2506.
- Roca, P., Cervera, M., Gariup, G., and Pela’, L. (2010). “Structural analysis of masonry historical constructions. Classical and advanced approaches.” *Archives of Computational Methods in Engineering*, 17(3), 299–325.
- Sharma, S., Tomassetti, U., Grottoli, L., and Graziotti, F. (2018). *Out-of-plane two-way bending shaking table tests on single leaf and cavity-walls - Report n. EUCI37/2018U*. Pavia, Italy.
- Soroushian, P., Obaseki, K., and Ki-Bong Choi. (1988). “Nonlinear Modelling and Seismic Analysis of Masonry Shear Walls.” *Journal of Structural Engineering*, 114(5), 1106–1119.
- Szakály, F., Hortobágyi, Z., and Bagi, K. (2016). “Discrete element analysis of the shear resistance of planar walls with different bond patterns.” *The Open Construction and Building Technology Journal*, 10(1), 220–232.
- Tomassetti, U., Correia, A. A., Marques, A., Graziotti, F., and Penna, A. (2017). “Dynamic collapse testing of a full-scale URM cavity-wall structure.” *Atti del XVII Convegno ANIDIS L’ingegneria Sismica in Italia*, Pisa University Press, 83–93.
- Tomažević, M. (1987). “Dynamic modelling of masonry buildings: Storey mechanism model as a simple alternative.” *Earthquake Engineering & Structural Dynamics*, Wiley-Blackwell, 15(6), 731–749.
- Turnšek, V., and Sheppard, P. (1980). “Shear and Flexural Resistance of Masonry Walls.” *International Research Conference on Earthquake Engineering*, Skopje, Japan, 517–573.
- U.B.C. (1991). “International Conference of Building Officials. Uniform Building Code.”

International conference of building officials, USA, Whittier, USA.

Wen, Y. K. (1976). "Method for Random Vibration of Hysteretic Systems." *Journal of the Engineering Mechanics Division*, 102(2), 249–263.

Wilding, B. V., and Beyer, K. (2017). "Force–displacement response of in-plane loaded unreinforced brick masonry walls: the Critical Diagonal Crack model." *Bulletin of Earthquake Engineering*, Springer Netherlands, 15(5), 2201–2244.

CHAPTER 7

Influence of bond pattern on the in-plane behaviour of
URM piers



CHAPTER 7 Influence of bond pattern on the in-plane behaviour of URM piers

Malomo, D., DeJong, M.J. and Penna, A. (2018). “Numerical assessment of the influence of bond pattern on the in-plane behaviour of URM piers.”, to be submitted

Abstract. The overall seismic capacity of unreinforced masonry (URM) systems with box-behaviour mainly rely on the in-plane strength of structural components. The effect of both internal and external factors on their strength and displacement capacity has been extensively investigated in recent years. Despite it is widely accepted that the brickwork bond typology might affect considerably both in-plane and out-of-plane performances of URM members, this aspect seems to be not fully addressed neither experimentally nor numerically. In this paper, calibrated numerical models, developed within the framework of the Distinct Element Method, are used to simulate the quasi-static lateral response of URM piers under several combinations of boundary conditions, vertical pressures and aspect ratios, accounting explicitly for a large number of typically-employed periodic and quasi-periodic bond patterns. A new methodology for representing effectively the mechanical interaction among adjacent units of different dimensions, as well as their failure when high shear-compression biaxial stress states are considered, is presented. The employment of time, size, mass scaling and dynamic relaxation procedures, combined with the introduction of equivalent interface properties for representing the effect of cyclic damage through monotonic loading schemes, provided a significant reduction of computational cost, thus enabling a comprehensive parametric study to be carried out within an acceptable timeframe. The results have shown that the brickwork bond type has a not-negligible influence on the response of laterally-loaded URM panels, indicating that it might be worth considering this aspect in the assessment of existing URM structures.

Keywords: unreinforced masonry; bond pattern; in-plane; numerical modelling; distinct element method

7.1 Introduction

The response of unreinforced masonry (URM) assemblies, when subjected to lateral loading, may vary considerably depending on a wide number of both internal and external factors. Experimental evidence has shown that the properties of unit and mortar (Salmanpour et al. 2015), unit shape and bond thickness (Calderini et al. 2009), as well as boundary conditions (Petry and Beyer 2015), overburden pressure (Rosti et al. 2016), aspect ratio (Petry and Beyer 2014) and loading rate (Tomažević et al. 1996), significantly affect their overall in-plane performances. Both consolidated rules and many codes of practice understandably suggest to reduce wall slenderness for avoiding premature loss of equilibrium due to seismic events, as noted by Cecchi and Milani (2008). Thus, existing

and new masonry structures in earthquake-prone regions are commonly built using a large variety of double-wythe masonry textures, which may have a not-negligible effect on the behaviour of URM components subjected to horizontal actions. Indeed, it is well-established that if combined actions are applied to URM members, which are intrinsically characterised by various degrees of anisotropy, they typically exhibit a high variability of lateral stiffness, ductility, peak strength and deformation capacity due to the interaction among bond pattern and loading direction (Dhanasekar et al. 1985; Drysdale and Khattab 1995; Page 1981, 1983). This is particularly evident in the case of dry and weak-mortared joints masonry elements with high compressive strength regular units subjected to shear-compression, where failure typically occur along joint interfaces (Bacigalupo et al. 2011). Further, according to the theory proposed by Mann and Muller (1982), the in-plane contribution of the head joints might need to be neglected (or reduced), since they are often unable to transfer shear stresses. Head joints, in fact, are frequently not properly filled with mortar, or they crack prematurely due to shrinkage. As an example, Maheri et al. (2008), conducting tests on URM walls subjected to both in-plane and out-of-plane actions, observed a substantial stiffness and shear capacity reduction (i.e. 30-50%) considering different degrees of head joints filling. Moreover, frictional resistance may be limited due to lack of vertical compression. Thus, the in-plane performances of laterally-loaded URM panels built with bond patterns characterised by the presence of more head joints along a given brick course with respect to the standard running bond (e.g. header or Dutch cross bonds) might differ significantly from one to another.

However, despite the increasing interest in both understanding and assessing the abovementioned aspects, also witnessed by some recent contributions (e.g. Mojsilović 2011; Thamboo and Dhanasekar 2016; Vasconcelos and Lourenço 2009), it seems that there is still some lacking of consistency in literature regarding their experimental investigation. In this work, with a view to address such knowledge gap, a comprehensive numerical study for assessing the influence of the brickwork bond type on the lateral response of URM piers subjected to shear-compression is proposed. The employment of an advanced micro-modelling approach, of which full details are given in the subsequent section, was scrutinised and verified against laboratory results. Then, considering the most widespread periodic and quasi-periodic bond arrangements, a parametric study was conducted accounting for several combinations of boundary conditions, overburden pressures and aspect ratios. In order to investigate further the potential variability of this phenomenon with respect to the use of various brick types, the analyses were conducted on both calcium-silicate (CS) and clay (CL) masonry elements, characterised by different brick aspect ratios λ_b and compressive strength f_{c_m} . Finally, normalising the obtained values of lateral stiffness, strength and displacement capacity with respect to the ones obtained for the standard running bond walls, analytical relations were derived by fitting numerical results, thus providing a simplified evaluation of the effect of masonry texture on the in-plane behaviour of URM elements.

7.2 Overview of typically employed URM modelling approaches

Most of the commonly employed in-plane analytical approaches, ranging from the first pioneering applications (e.g. Magenes and Calvi 1997; Mann and Muller 1982; Paulay and Priestley 1992; Turnšek and Čačovič 1971) to more recent developments (Benedetti and

Steli 2008; Calderini et al. 2010; Wilding and Beyer 2017), neglect or account for the effect of the brickwork bond in a simplified way, e.g. by considering the ratio between unit length and height or more refined friction-based local criteria, thus idealising the lateral response of a given URM panel as an equivalent running bond element with reduced shear strength due to the different inclination of potential sliding planes. Regardless, the numerical outcomes presented in this work seem to suggest that this cannot be applied as a general rule. Analogous considerations can be extended to simplified numerical methods, such as equilibrium-based (e.g. Roca 2006) and equivalent-frame (e.g. Penna et al. 2014; Raka et al. 2015) computational techniques, in which the abovementioned analytical formulations are implemented and automatically selected in order to describe the seismic behaviour of large-scale URM structures at relatively low computational expense.

With reference to irregular URM block assemblies, their intrinsic mechanical heterogeneity and geometrical variability would unavoidably make both experimental and numerical studies concerning the influence of the bond patterns only representative of a limited region or construction culture. In this context, the selection of realistic volume elements (RVE), whose heterogeneous properties are homogenised using micromechanics theory (e.g. Anthoine 1995; Cluni and Gusella 2004; Zucchini and Lourenço 2002), might be extremely challenging. However, recent advancements have shown that using stochastic procedures (Spence et al. 2008) and digital image processing (Falsone and Lombardo 2007), in combination with Finite Element Method (FEM) (Massart et al. 2018), local joint damage can be predicted accurately also accounting for the actual brick arrangement. On the contrary, the RVE identification in case of periodic masonry types, is more straightforward. Thus, aimed at developing homogenised mechanical properties and macroscopic failure domains, several theoretical and numerical investigations have been proposed so far (e.g. Addressi et al. 2010; De Buhan and de Felice 1997; Cecchi and Sab 2004; Salerno and de Felice 2009). Concerning quasi-periodic masonry textures, instead, only a few contributions (mainly focused on out-of-plane actions) are presently available in literature (e.g. Cecchi and Milani 2008; Milani et al. 2013). Amongst the latter, the work of Milani and Cecchi (2013) pointed out the influence of the herringbone bond pattern on the mechanical response of an in-plane loaded masonry dome by comparing homogenised and heterogeneous FEM models, observing a substantial increase of peak strength with respect to a standard running bond pattern. Regardless, the degree of accuracy which characterises the abovementioned applications is still a long way from being largely employed by both researchers and practitioners, probably due to their own complexity, albeit the use of FEM-based homogenisation approaches for existing non-periodic URM structures is widespread, as reported in e.g. Roca et al. (2010).

A different numerical methodology is represented by discontinuum-based models, according to which the discrete nature of masonry is explicitly accounted for. Despite the relatively large analysis time usually requested, recent computational developments have allowed these techniques to be progressively applied in engineering practice, namely in the failure analysis of structural components and large-scale buildings, under both static and earthquake loading, as noted by Lemos (2007). In this framework, the rigid body and springs models (RBSM) (Kawai 1978), based on the mechanical interaction among non-deformable units connected to each other by means of linear or nonlinear springs, are steadily gaining popularity, given the possibility of describing effectively large

deformations and collapse modes in an acceptable timeframe. However, masonry texture is often implicitly represented by means of energy relations (Casolo 2009) or by assigning empirically-calibrated joint properties (Malomo et al. 2018b).

The Distinct Element Method (DEM), instead, originally conceived by Cundall (1971) for simulating soil and rock mechanics, proved to be particularly suitable for local mechanisms analysis of non-periodic blocky assemblies. Its applicability to the modelling of the lateral response of URM components subjected to both monotonic (e.g. Bui et al. 2017; Dumova-Jovanoska and Churilov 2009) and cyclic (e.g. Azevedo et al. 2000; Lemos 1997) loading schemes has been investigated by several authors, especially in case of dry-joints masonry assemblies. However, only limited numerical tests pertaining the in-plane influence of brickwork bond has been carried out so far, although it is worth mentioning the work of de Felice (2011), who investigated the effect of different section morphologies on the out-of-plane response of irregular stone panels, substantially highlighting that the standard rigid body rocking curves always overestimate their actual strength and displacement capacities.

When combined DEM with FE discretisation procedures (e.g. Marti and Cundall 1982), unit deformability and associated damage can be considered (Munjiza 2004). As in the previous case, the simulation of planar walls has been addressed by several authors, including Miglietta et al. (2017) and Smoljanović et al. (2015), whose works were mainly devoted to the analysis of mortared and dry-joint clay and stone running-bond masonry piers subjected to cyclic actions. With reference to arched URM structures, the effect of unit arrangement and loading direction has been recently studied by Sarhosis et al. (2014) and Kassotakis et al. (2017). Different combinations of brickwork bonds, including English, herringbone and mixed unit arrangements, typically employed in East Europe for infill-walls, were tested numerically by Szakály et al. (2016) under monotonically increasing horizontal shear and considering several vertical pressures and aspect ratios, pointing out that the introduction of vertical bricks does not necessarily lead to an increased shear resistance, as well as the dependency of the failure mechanisms on the selected bond pattern. However, the models were not calibrated on experimental outcomes, and failure through units was not considered. Moreover, the abovementioned findings cannot be directly employed for the modelling of loadbearing masonries, since compressive stresses, material and geometrical properties were meant to represent masonry infill components. In Baraldi et al. (2018), numerical, and analytical predictions were compared to each other with a view to assess the effect of aspect and unit height-to-width ratios on the monotonic in-plane performances of URM panels characterised by weak/dry joints, showing good agreement. Notwithstanding the great potential of such computational methods, the assumptions of infinitely elastic/rigid units connected by cohesionless interfaces, as well as the selected bond patterns, appear not fully applicable to the assessment of existing URM structures.

In this paper, the influence of the most typically-employed brickwork types (i.e. Flemish English, Dutch cross-bond, header and running bond) on the in-plane response of loadbearing URM walls was investigated by means of DEM-based numerical models, implemented within the 3DEC (Itasca, 2013) framework. Their reliability was firstly assessed by reproducing numerically the force-displacement behaviour of seven full-scale CS and CL running/Dutch cross bond brick masonry walls tested at the laboratory of

EUCENTRE (Pavia, Italy), under shear-compression cyclic loading and considering several combinations of boundary conditions, vertical pressures and aspect ratios (Graziotti et al. 2015, 2016). These masonry types can be considered as representative of a wide number of URM structures all over the world, having been largely employed since a long time for both residential and monumental buildings in many regions of Europe, Asia and North America. Moreover, the difference in terms of f_{c_m} among CS and CL masonries, also allowed to investigate the effect of crushing failure in relation to unit size/arrangement. For this purpose, a smooth-bilinear compression cap, originally not provided in the 3DEC formulation and already validated in previous researches by the same authors (e.g. Malomo et al. 2018b), was assigned to deformable units for representing explicitly local damage due to high shear-compression biaxial stress states. Based on damage observation and theoretical formulations, and with a view to account for the effect of cyclic damage using monotonic loading schemes, equivalent shear strength properties were assigned to interface head joints. The computational expense was further reduced through the introduction of time, size, mass scaling and dynamic relaxation procedures, which also assured quasi-static loading conditions. Given the satisfactory results obtained, such methodology was extended to the numerical assessment of the bond pattern influence on the in-plane performances of URM elements, combining four different levels of overburden, three different wall aspect ratios and both cantilevered and fixed-fixed boundary conditions.

For each analysis, failure modes, peak shear strengths, as well as lateral stiffnesses and displacement capacities, were compared to each other, focusing on the differences exhibited by the considered periodic and quasi-periodic masonry textures with respect to the standard running bond pattern. Finally, with a view to calibrate simplified models, several analytical expressions were inferred by post-processing numerical outcomes.

7.3 Simulating the in-plane response of URM assemblies using the DEM

Using the DEM, masonry texture can be explicitly represented as a virtual assembly of deformable units discretised through a superimposed FE mesh, where each tetrahedral discrete region represents a uniform-strain domain. The connection among units is usually provided by zero-thickness nonlinear spring layers, in which the unit-mortar properties are lumped, according to a simplified micro-modelling approach (Lourenço et al. 1995).

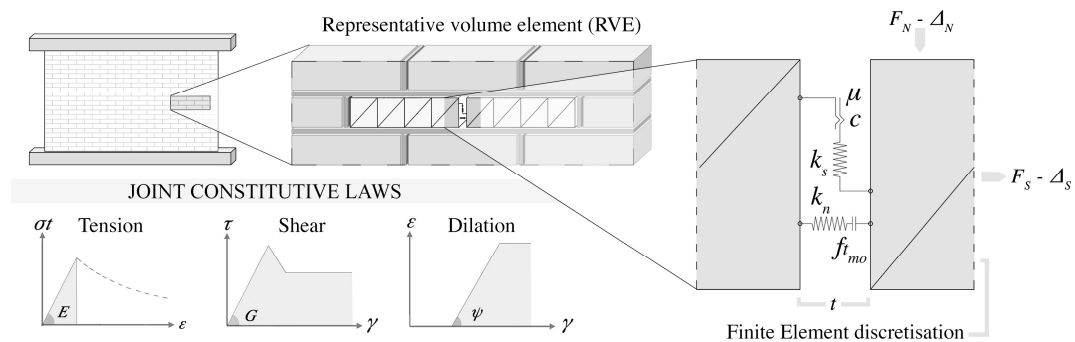


Figure 82 Discretisation of a masonry segment according to the DEM

Failure phenomena through mortar joints under biaxial in-plane actions, including the development of both flexural-tensile and shear stepped cracks, rigid overturning and base sliding mechanisms, are commonly modelled introducing linearised tensile and Mohr-Coulomb-based shear constitutive laws, also potentially accounting for dilation. In this work, as depicted in Figure 82, simplified frictional-cohesive and brittle-tensile strength criteria were assigned to interface springs. A faithful representation of both unit failure and hybrid masonry crushing phenomena is vital for simulating adequately the in-plane response of URM components subjected to high compressive stresses. The numerical representation of these aspects is still challenging for many discontinuum-based approaches, albeit several improvements have recently been achieved (e.g. D’Altri et al. 2018; Sarhosis and Lemos 2018). According to most of the available RBSMs, the crack path through units should be determined *a priori*, and it may occur only along the unit spring layers. However, due to the fact that when a given spring fails contact is lost in the subsequent computational step, this strategy often produces spurious interpenetration phenomena among adjacent blocks, increasing consistently the analysis time. Aimed at overcoming this limitation, and because neither joint nor unit compressive failure is considered in the standard formulation of the employed code, the simplified methodology lately proposed by Malomo et al. (2018a) has been herein employed. In practice, each deformable unit is internally meshed using the mixed discretisation technique developed by Marti and Cundall (1982), and characterised by a Mohr-Coulomb plasticity model (shear yield function) with tension cut-off (tensile yield function).

$$ft_{b_eq} \sim (0.03) \cdot (fc_b) \quad (1) \quad c_{b_eq} \sim (1.5) \cdot (ft_{b_eq}) \quad (2) \quad \phi_{b_eq} \sim 35^\circ \quad (3)$$

Then, the introduction of equivalent properties (i.e. equivalent cohesion c_{b_eq} , friction angle ϕ_{b_eq} and tensile strength ft_{b_eq}) inferred through linear expressions as a function of the unit compressive strength fc_b (see Eq. (1-3)), provides a satisfactory representation of the compressive failure envelope typically exhibited by the considered masonry typologies, resulting in the definition of the smooth bilinear compression caps reported in Figure 83 (with E_{1m} and E_{2m} Young’s moduli of masonry evaluated at 10-30% of fc_m), where numerical outcomes are compared with experimental results on both CS and CL masonry wallettes subjected to uniaxial cyclic compression (Graziotti et al. 2015). Further, since the effectiveness of the inferred equivalent parameters has been calibrated for a specific mesh size, i.e. $0.5L_b$ (brick length) $\times H_b$ (brick height), the same unit discretisation was considered for the following numerical investigations.

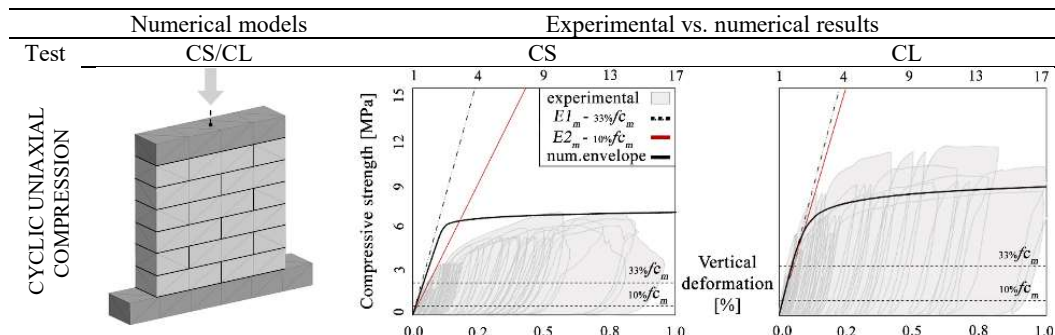


Figure 83 Comparison between experimental cyclic uniaxial compression tests and numerical compression caps (Malomo et al. 2018a)

Although such coarse subdivision of units resulted in a significant reduction of computational burden, an appreciable overestimation of the masonry axial stiffness was observed. Thus, aimed at accounting for both unit and mortar joint deformability and with reference to the nomenclature reported in Figure 82, equivalent normal and shear joint stiffnesses (i.e. k_n , k_s), defined by Eq. (4), were introduced. In the case of head joints, the length L is equal to the one of the brick, while for bed joints L is the brick height. Moreover, A is contact area, E_b and E_{mo} stand for brick and mortar Young's modulus respectively, whilst G_b and G_{mo} indicate the associated shear moduli, inferred assuming $G=0.4E$.

$$\begin{cases} \Delta_N = \left(\frac{F_N L}{E_b A} + \frac{F_N t}{E_{mo} A} \right) \\ \Delta_S = \left(\frac{F_S L}{G_b A} + \frac{F_S t}{G_{mo} A} \right) \end{cases} \Rightarrow \begin{cases} k_n = \frac{F_N}{\Delta_N} = \left(\frac{A}{L+t} \right) \left[\left(\frac{E_b E_{mo}}{E_b t + E_{mo} L} \right) (L+t) \right] \\ k_s = \frac{F_S}{\Delta_S} = \left(\frac{A}{L+t} \right) \left[\left(\frac{G_b G_{mo}}{G_b t + G_{mo} L} \right) (L+t) \right] \end{cases} \quad (4)$$

Since the experimental campaign to which this work is referred did not involve tests for obtaining the abovementioned unit and mortar elastic properties, first estimates were empirically-derived using Eqs. (5-10), summarised in Table 38, where E_m is the Young's modulus of masonry and ζ is the ratio between brick and mortar thickness t_{mo} :

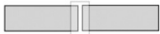
Table 38 Empirical expressions for inferring unit and mortar material properties

BRICK	(Jäger et al. 2004)	$E_b = (375) \cdot (f_{c_b})$	(5)
	(Kaushik et al. 2007)	$E_b = (355) \cdot (f_{c_b})$	(6)
MORTAR	(Brooks and Baker 1998)	$E_{mo} = \left(\frac{-4E_m E_b}{25E_m - 29E_b} \right)$	(7)
	(Matysek and Janowski 1996)	$E_{mo} = \left(\frac{E_m E_b}{E_b - 1.25\zeta(E_m - E_b)} \right)$	(8)
	(Ciesielski 1999)	$E_{mo} = \left(\frac{-E_m E_b}{5E_m - 6E_b} \right)$	(9)
	(U.B.C. 1991)	$E_{mo} = \left(\frac{E_m E_b}{\zeta(E_m - E_b) + E_b} \right)$	(10)

Since the contact stiffnesses of the joints depend on the longitudinal/transversal distance L between two adjacent brick centroids, different k_n , k_s were assigned to bed and head mortar layers according to the considered bond patterns. Both normal and shear stiffnesses associated to the selected bond patterns are reported in Table 39, distinguishing between the ones assigned to bed and head joints respectively, where FF indicates the joint stiffnesses computed considering the centroid distance between two consecutive bricks ($L=L_b$), while FH refers to joints where the centroid distance between adjacent full and half-length bricks ($L=0.75 L_b$) was used. Finally, TH ($L=0.625 L_b$) is associated with the centroid distance between three-quarters and a half-length brick, whereas HH stands for the head joint stiffnesses among two adjacent half bricks ($L=0.5 L_b$).

Table 39 Stiffnesses assigned to both bed and head joints depending on the centroid distance L

Joint configuration	Property	Nomenclature	CS	CL
 bed-joint_BJ	Bed-joint normal stiffness [MPa/m]	k_n	6.97e4	1.66e5
	Bed-joint shear stiffness [MPa/m]	k_s	3.17e4	7.56e4

	FF head-joint normal stiffness [MPa/m]	k_{n_FF}	2.34e4	4.01e4
	FF head-joint shear stiffness [MPa/m]	k_{s_FF}	1.062e4	1.82e4
	FH head-joint normal stiffness [MPa/m]	k_{n_FH}	3.11e4	5.33e4
	FH head-joint shear stiffness [MPa/m]	k_{s_FH}	1.42e4	2.42e4
	TH head-joint normal stiffness [MPa/m]	k_{n_TH}	-	4.57e4
	TH head-joint shear stiffness [MPa/m]	k_{s_TH}	-	2.08e4
	HH head-joint normal stiffness [MPa/m]	k_{n_HH}	-	8.02e4
	HH head-joint shear stiffness [MPa/m]	k_{s_HH}	-	3.64e4

7.4 Modelling strategy and first verification against experimental results

In this section, the modelling strategy adopted for representing numerically the cyclic force-displacement envelope, as well as the local failure mechanisms, of laterally-loaded URM piers is presented. Particular attention will be devoted to the optimisation techniques implemented in the employed DEM code for reducing the computational cost without affecting analysis accuracy. Then, considering several quasi-static cyclic shear-compression tests performed at the EUCENTRE laboratory on both CS and CL full-scale wall specimens, a first validation of the methodology is proposed. Full details on the abovementioned experimental campaigns, including further information regarding test set-up, results and their interpretations are given in Graziotti et al. (2015, 2016). In Figure 84, together with a screenshot of the DEM model, the numerical idealisation of test set-up and the adopted discretisation approach, are depicted:

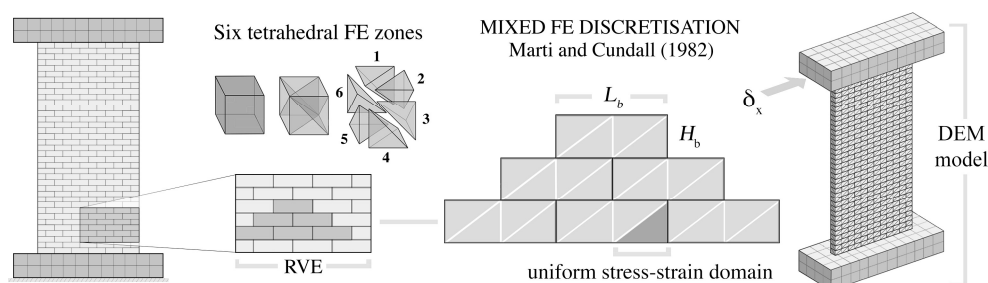


Figure 84 Screenshot of the model, applied discretisation and numerical test set-up

7.4.1 Using explicit time-integration schemes for solving quasi-static problems

The use of explicit dynamic solution schemes for quasi-static problems presents several advantages, including an effective representation of relative sliding and separation phenomena among discrete units. Indeed, unconditionally stable conditions assure the analysis completion even in case of high nonlinear behaviours, multiple contacts/re-contacts and large deformations, making its employment naturally suitable for the numerical analysis of both flexure and shear-dominated responses of blocky assemblies. This notwithstanding, obtaining results in a realistic timeframe avoiding unwanted inertial effects is still an open challenge. Regarding this last issue, the introduction of a proper dynamic relaxation scheme (Otter 1966), which iteratively reduces the nodal velocities by removing the kinetic energy of the system, represents an attractive solution. In this work, velocity-proportional adaptive global damping (Cundall 1982) was used to adjust the damping factor continuously in such a way that the power absorbed is a constant proportion

of the rate of change of kinetic energy in the system. The iterative modification of viscosity constants is provided by a numerical servomechanism that seeks to keep the ratio (R) between the summation of nodal damping magnitude P and rate of change of nodal kinetic energy equal to a target value (e.g. $R=1$ herein). Moreover, throughout the analysis, additional “kinetic energy checks” were implemented in the code, as further discussed in Malomo et al. (2018a), in order to assure quasi-static conditions. A common issue when employing advanced numerical models is unavoidably represented by the required analysis time. Thus, an attempt was made in this endeavour to optimise the employment of the selected computational code by increasing the extent of the minimum critical timestep Δt_{cr} , defined by the Courant-Friedrichs-Lewy (CFL) condition (Courant et al. 1967). It ensures that a given stress cannot propagate across more than one element in a single time step, being a function of both element (L_{min}) size and sound speed (v_s) through the considered continuum body with density δ and Young’s modulus E , thus providing adequate accuracy.

$$\Delta t_{cr} \leq \left(\frac{L_{min}}{v_s} \right) \quad \text{where} \quad v_s = \sqrt{E/\rho} \quad (11)$$

As it can be gathered from Eq. (11), which mathematically describe the CFL condition for undamped materials, the main objective is to maximise Δt_{cr} by increasing the ratio L_{min}/v_s . As widely discussed in e.g. Cook et al. (2002), the performances of explicit solvers applied to quasi-static problems can be significantly enhanced by introducing size and mass scaling procedures, which have a direct effect on the CFL law. In this work, such numerical techniques were employed simultaneously by assigning a coarse FE to the units (increasing L_{min}) and through iterative adjustment of ρ in order to decrease the speed v_s locally.

7.4.2 Evaluation of cyclic force-displacement envelopes using monotonic analysis

Experimental loading protocols usually consist in a series of periodically-imposed target lateral displacements, applied multiple times with relatively low velocity. From a numerical viewpoint, especially when using micro-modelling approaches, their implementation often implies a significant computational cost, which was understandably not compatible with the purposes of this work. Thus, displacement-controlled monotonic pushover analyses were performed instead, according to the methodology suggested by Szakály et al. (2016), i.e. increasing gradually the magnitude of applied velocities, leading to a displacement of 1 mm in 0.135 sec. This procedure, often called time scaling, also provides for an additional equilibrating phase. Indeed, every 1 mm, velocities were set to zero and simulation was continued until the average unbalanced nodal force resultant divided by the average load acting on the nodes became smaller than 10^5 , assuring quasi-static conditions.

The effect of cyclic loading on the in-plane response of URM elements typically comprises stiffness degradation, progressive strength reduction and various levels of energy dissipation depending on several factors, such as boundary conditions, aspect ratios and top vertical pressure. Moreover, in relation to the loading direction, these parameters may vary significantly (albeit this was not the case of the selected experimental tests). These aspects cannot clearly be taken into account when monotonic actions are considered. However, as shown in the next sub-section, an acceptable agreement with test outcomes for both CS and CL brick masonry was found when reduced values of shear strength (i.e. zero cohesion and halved friction angle) are assigned to head joints. As noted by Magenes and Calvi (1992),

this could be interpreted as if the local friction cracks in the head joints develops prematurely, before the attainment of the failure condition given by bed joint or brick tensile mechanisms. Given the encouraging results obtained in terms of both force-displacement envelopes and crack patterns (see Figure 85, Figure 86), this assumption (also supported by the Mann and Muller theory) has been extended to the parametric study.

7.4.3 First verification with experimental tests

Three CS (CS1-2-3) and five CL (CL1-2-3-4-5) full-scale URM panels were subjected to quasi-static in-plane cyclic shear-compression loading with several combinations of boundary conditions, overburden and aspect ratios (see Table 41) at the laboratory of EUCENTRE in 2015-2016. It is noted that, since CL4 and CL5 only differed for the loading history (i.e. cycles were not repeated in CL5), the latter has not been considered in this work. The CS bricks (212×102×71 mm) were arranged according to a single-leaf running bond pattern. Dutch cross-bond, double-wythe masonry walls were instead assembled using CL solid bricks (208×102×50 mm). The average t_{mo} was 10 mm for all the samples.

Table 40 CS and CL experimental (Graziotti et al. 2015, 2016) and inferred material properties

	CS - $\delta_m = 1839$ [kg/m ³], $\lambda_b = 0.33$ [-]						CL - $\delta_m = 1979$ [kg/m ³], $\lambda_b = 0.24$ [-]					
	$f_c m$	$f_c b$	f_w	E_m	c	μ [-]	$f_c m$	$f_c b$	f_w	E_m	c	μ [-]
Mean [MPa]	6.20	18.67	0.24	4182	0.21	0.42	11.22	40	0.23	9833	0.15	0.55
C.o.V. [%]	7.04	13.67	16.32	33.27	-	-	7.43	11.21	60.11	25.42	-	-
Inferred mechanical properties [MPa]	E_b	E_{mo}	$f_{t_b, eq}$	$c_{b, eq}$	$\phi_{b, eq}$	-	E_b	E_{mo}	$f_{t_b, eq}$	$c_{b, eq}$	$\phi_{b, eq}$	-
	6628	1772	0.52	0.78	35°	-	15000	3257	1.12	1.68	35°	-

The walls, whose material properties are summarised in Table 40 (where δ_m is masonry density, f_w bond tensile strength, c cohesion and μ friction coefficient), were founded on a reinforced concrete (RC) beam clamped to the lab strong floor, which has been explicitly replicated numerically, as well as the top one. The displacement histories were imposed to the latter by a horizontal servo-hydraulic actuator, whereas two horizontal servo-hydraulic actuators assured both boundary conditions and desired vertical compressions σ_0 . In Table 41, the experimental configurations and main dimensions (i.e. length L_w , height H_w and thickness t_w) of the specimens are reported, together with the associated aspect ($\lambda_w = H_w/L_w$), shear-span ($\alpha_v = H_0/L_w$, with $H_0 = H_w$ or $H_0 = 0.5H_w$ in case of cantilevered or fully fixed conditions respectively) and axial load ($\sigma_L = \sigma_0/f_c m$) ratios.

Table 41 Test specimens: dimensions, vertical stress and boundary conditions

Wall ID	L_w [m]	H_w [m]	t_w [m]	σ_0 [MPa]	Boundary conditions	λ_w [-]	α_v [-]	σ_L [%]
CS1	1.10	2.75	0.102	0.70	Fixed-Fixed	2.50	1.25	11
CS2	1.10	2.75	0.102	0.52	Fixed-Fixed	2.50	1.25	8
CS3	4.00	2.75	0.102	0.30	Cantilevered	0.69	0.69	5
CL1	1.20	2.71	0.208	0.52	Fixed-Fixed	2.26	1.13	5
CL2	1.20	2.71	0.208	1.20	Fixed-Fixed	2.26	1.13	11
CL3	1.20	2.71	0.208	0.86	Fixed-Fixed	2.26	1.13	8
CL4	2.70	2.71	0.208	0.30	Fixed-Fixed	1.00	0.50	3

In what follows, a comparison between numerical outcomes and their experimental counterparts is presented. As depicted in Figure 85, albeit the in-plane response of the full-scale specimens might have been influenced by the cyclic nature of the tests, both capacity and failure mechanisms were adequately reproduced by the models (subjected instead to monotonic incremental loading sequences), as further discussed below. The bilinear idealisations plotted in Figure 85 were developed according to the approach suggested by Costa et al. (2011), i.e. calculating the effective stiffness k_{eff} as the secant to experimental/numerical envelope at 70% of the maximum capacity V_p . Then, V_b was evaluated ensuring that the areas above the envelope and below the bilinear curve are equal.

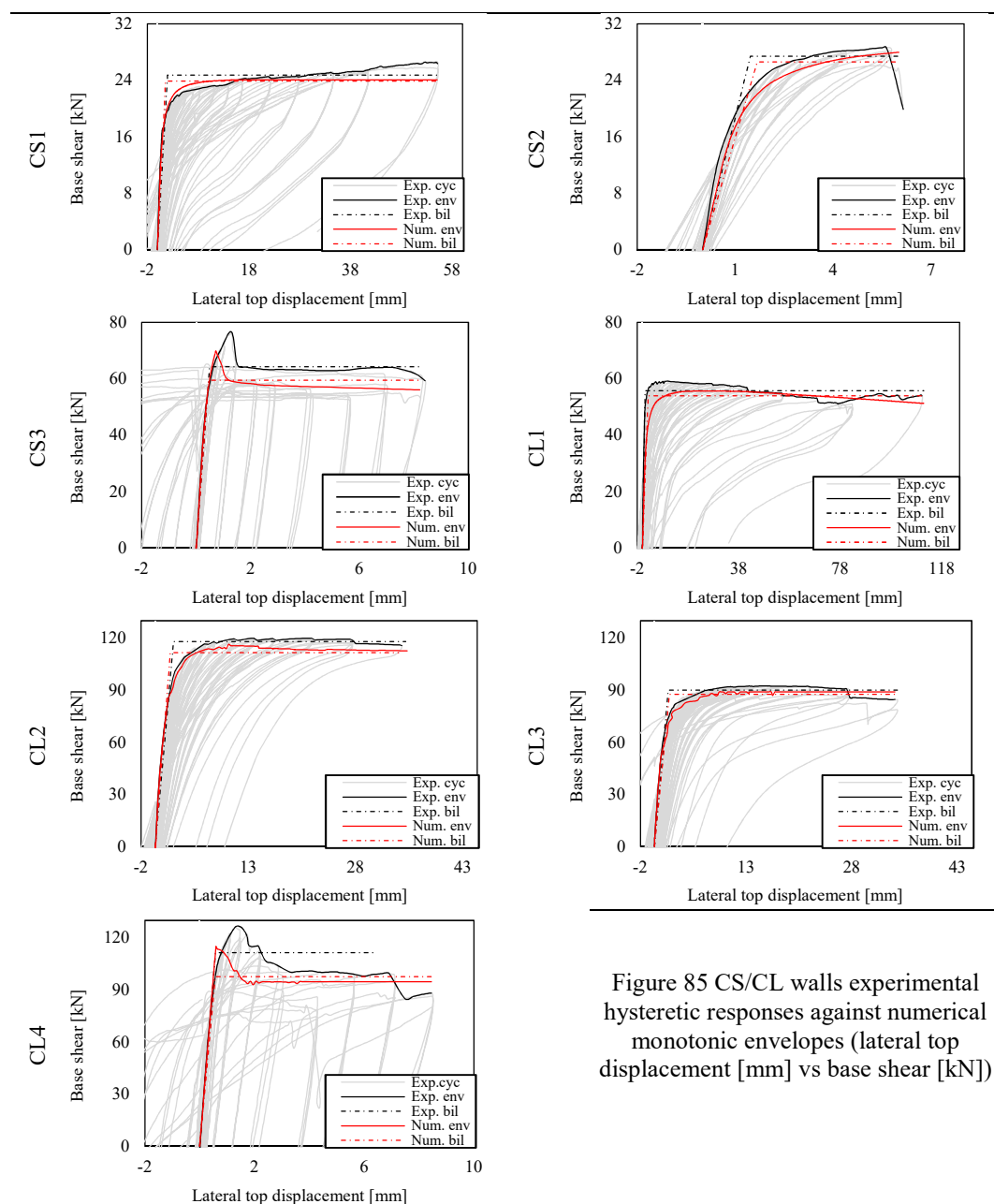


Figure 85 CS/CL walls experimental hysteretic responses against numerical monotonic envelopes (lateral top displacement [mm] vs base shear [kN])

It is worth noting that the models adequately accounted for the $P-\Delta$ effect, which led to a not-negligible progressive reduction of the lateral strength especially in the case of CL1. The experimental hysteretic curve of CS1, instead, reveals how during the test a peculiar crack propagation, migrating toward the centre of the panel, produced the shortening of its effective height, resulting in an unusually high energy dissipation and hardening response, which the model could not reproduce. During the test of CS2, instead, a spurious rotation of the top RC beam occurred because of insufficient restrain conditions and its very different in-plane and out-of-plane slenderness, ending the test prematurely. However, the model did manage to capture appropriately the initial test phases.

Comparing experimental backbones against numerical monotonic envelopes, an acceptable agreement was found, as a whole. Indeed, both cohesive strength peaks exhibited by squat walls and residual resistances, as well as the initial stiffness of all the specimens, were duly accounted for numerically. The latter parameter, herein named k_i , was determined by the first data point of the considered envelope, and in many cases that corresponded to approximately the 10% of V_p .

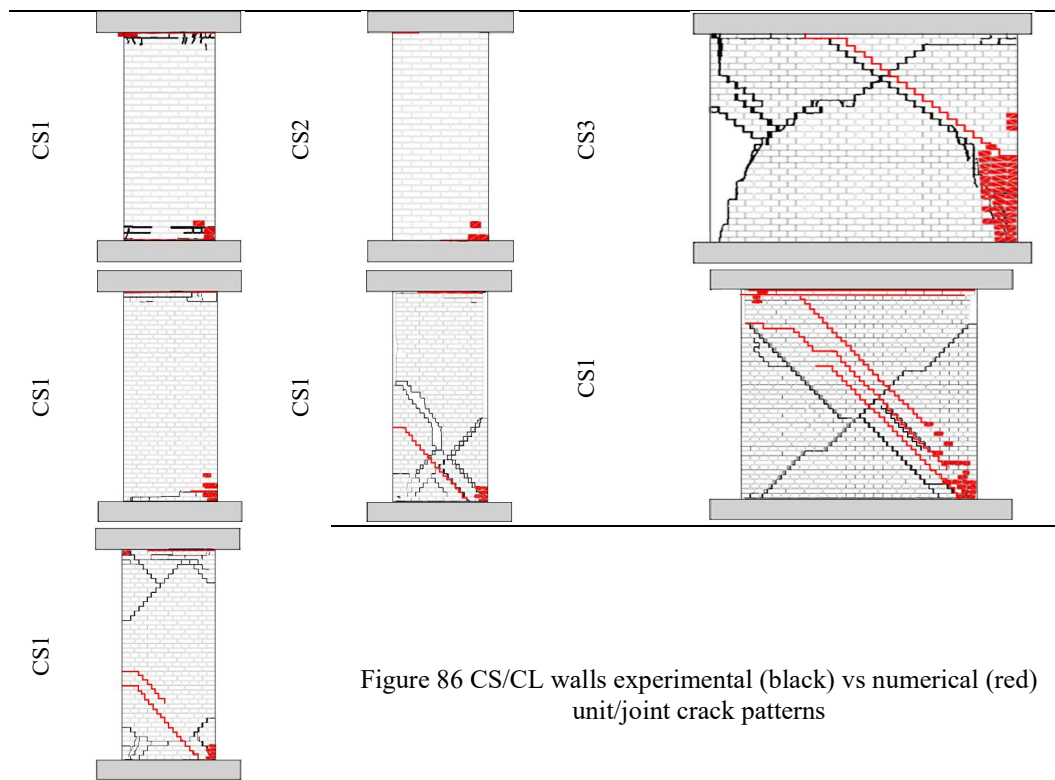


Figure 86 CS/CL walls experimental (black) vs numerical (red) unit/joint crack patterns

Looking at Figure 86, where experimental and numerical unit/joint crack patterns are compared, it seems that the predicted failure modes are quite representative of the experimental ones. Obviously, given the differences in terms of imposed displacement histories, such comparison involves some degree of abstraction. However, considering the same tests, it might be of interest noting that applying an analogous modelling strategy (except for the assignment of head joint properties) and introducing cyclic loading protocols, an adequate agreement was found (Malomo et al. 2018a), which is reassuring.

The general positive impression on the outcomes of this modelling exercises is further confirmed by what is shown in Table 42, where the average percentile deviation calculated with respect to the experimentally-recorded values of both peak (ΔV_p) and bilinear (ΔV_b) capacities, as well as of the initial (Δk_i) and effective (Δk_{eff}) stiffness is reported. Regarding the latter, although a slightly larger scatter is clearly observable, it seems to be within an acceptable range.

Table 42 Numerical peak/bilinear capacity, initial/effective stiffness and associated percentile deviation with respect to experimental outcomes

Wall ID	$V_{p,num}$ [kN]	$V_{b,num}$ [kN]	ΔV_p [%]	ΔV_b [%]	$k_{i,num}$ [kN/mm]	$k_{eff,num}$ [kN/mm]	Δk_i [%]	Δk_{eff} [%]
CS1	24.01	23.87	10.37	3.06	21.33	15.36	6.86	22.88
CS2	27.97	26.61	2.25	7.48	23.67	15.94	1.37	15.23
CS3	69.84	59.4	9.82	3.54	147	115.23	3.67	12.15
CL1	55.73	53.89	6.05	2.25	71	41.23	5.19	17.67
CL2	116.37	111.62	3.03	4.46	91	54.09	4.00	17.09
CL3	89.76	87.56	3.05	2.22	63	41.54	8.16	10.67
CL4	115.45	97.6	9.22	12.30	351.33	171.22	2.22	10.89

7.5 Parametric analysis

After the validation of the numerical models, a parametric analysis was performed for assessing the influence of different brickwork types on the in-plane performances of URM piers subjected to shear-compression. Four main typologies of periodic and quasi-periodic bond patterns were considered given their extensive use all over the world, and the predicted wall responses (obtained varying several key-parameters, as further explained in the following) compared with the ones of standard running bond (RUN) panels. More specifically, Flemish (FLE), English (ENG), Dutch-cross (DUT), and header (HEA) bonds were selected. Having been characterised by various combinations of brick dimensions and arrangements, the slopes (φ) of the lines connecting consecutive head joints along the height of the panel substantially differ one to another. Thus, different potential “sliding planes” may be identified, as shown in Figure 87:

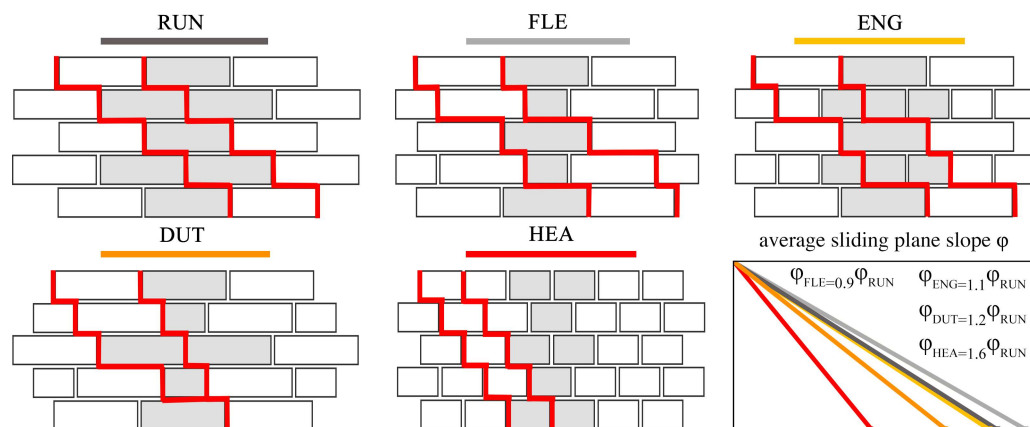


Figure 87 Considered bond patterns and identification of different potential sliding planes

7.5.1 Methodology and definition of key-parameters

The adopted methodology is herein presented and discussed, as well as the definition of the most significant factors which have been investigated and parameterised during the analyses, whose results will be given in the next subsections. The main variables under study are listed below:

1. Masonry texture, i.e. RUN, FLE, ENG, DUT, HEA
2. Masonry type, CS/CL, characterised by different mechanical (see Table 40) and geometrical (λ_b , φ) properties
3. Wall aspect ratio λ_w
4. Boundary conditions, cantilevered/fully-fixed
5. Overburden pressure σ_0 , considered as a percentage of f_c

The CS specimens consisted of single-leaf walls, while CL bricks were arranged in double-wythe. Given the initial hypothesis of weak head joints and the differences in terms of f_c and λ_b , these systems can be regarded, in terms of potential bond pattern effect, as representative of a lower and upper bound respectively. Thus, depending on the considered brickwork type, a higher degree of response variability is expected for the case of CS assemblies, which is supposed to be much affected by different joint configurations.

In more details, three different aspect ratios λ_w , namely 0.5, 1 and 2.5, corresponding to long (LG), squat (SQ) and slender (SL) walls respectively, were considered in this modelling exercise, as depicted in Figure 88. Then, for each λ_w , four levels of overburden σ_0 (determined in relation to the masonry type, CS/CL, i.e. taking the 3, 6, 9 and 12% of f_c) were imposed to the top RC beam. In the case of squat and long panels the top RC beams were restrained reproducing both cantilevered (CV) and fixed-fixed (FF) boundary conditions, resulting in the definition of multiple values of shear span ratio α_v (i.e. 0.25, 0.50, 1). For slender piers, instead, only fully-fixed boundary conditions were imposed ($\alpha_v = 1.25$). In Table 43, the abovementioned parameters are summarised:

Table 43 Geometrical properties and mechanical configurations of the considered walls

Wall ID	L_w [m]	H_w [m]	t_w [m]	t_w [m]	Boundary conditions	H_0	λ_w [-]	α_v [-]	σ_L [%]
SL	1.10	2.75	0.102	0.208	FF	1.38	2.50	1.25	3/6/9/12
SQ	2.75	2.75	0.102	0.208	FF/CV	1.38/2.75	1	0.5/1	3/6/9/12
LONG	5.50	2.75	0.102	0.208	FF/CV	1.38/2.75	0.50	0.25/0.5	3/6/9/12

For each monotonic analysis, initial stiffness, maximum shear/displacement capacities and failure mode were monitored and subsequently compared. With a view to optimise such process and to make more readable the results, these quantities will be related to both α_v and σ_L . As in the previous case, a bilinear idealisation was employed for evaluating effective stiffness and equivalent lateral shear. The ratios k_{eff}/k_i and V_b/V_p were also considered for each specimen, although no significant trends were observed in this respect.

Further, it is recalled that masonry crushing phenomena were also accounted for numerically, given that each masonry texture may induce the development of different unit failure mechanisms.

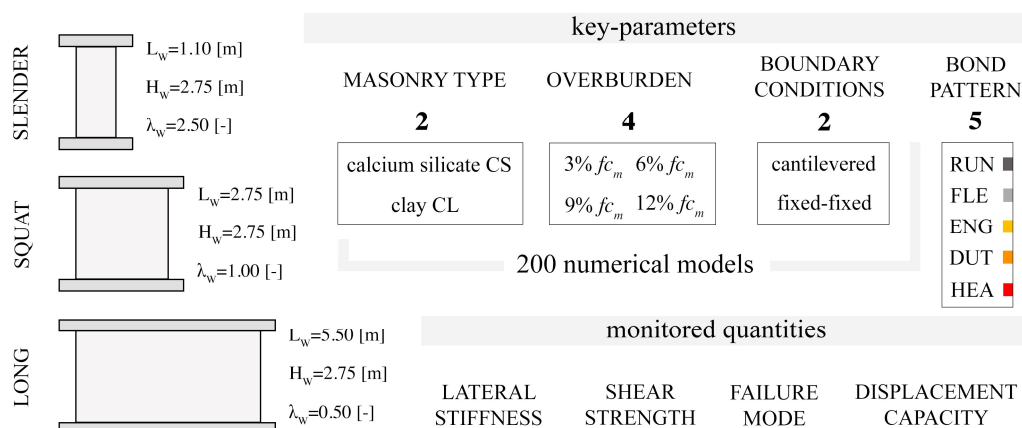


Figure 88 Workflow of the proposed parametric analysis

Undertaking a similar approach to that suggested by Haach et al. (2011), the predicted failure mechanisms were standardised according to the following description, which comprises both flexure (F), shear (S) and hybrid-governed behaviours:

- Rocking/flexure modes (F), when a horizontal/diagonal crack opened in the base of the wall due to the tensile stresses and the wall rotates around the bottom corner
- Crushing (F/C), when early horizontal flexural cracking reduces the effective cross-section of the walls and toe-crushing of wall occurs due to the concentration of high compressive stresses at the toes of the wall
- Top (TS) and base (BS) shear sliding, when straight crack through unit-mortar interfaces are detected
- Diagonal shear (DS), mainly associated with diagonal cracking (stepped cracks along mortar joints or through both units and bonds)
- Hybrid mechanisms, in case of combined failure modes, where the order of the letters stands for the sequence of the observed damage (e.g. F/C/DS, C/TS/DS)

In the next subsections, an interpretation of numerical results obtained using calibrated DEM models and applying the methodology discussed above, is presented. Given the relatively large extent of inferred data, the influence of brickwork bond will be presented in terms of stiffness, lateral strength and displacement capacity/failure mode individually.

7.5.2 Lateral stiffness

The initial stiffness of cyclically-loaded URM piers is usually evaluated as the slope of the line connecting the positive and negative extreme points of the first hysteresis loop. In this work, dealing with monotonic force-displacement curves, k_i was determined considering approximately the 10% of V_p . In general, not-negligible differences in terms of k_i were noticed among the selected brickworks, and, as expected, the parameter ϕ seems to play a relevant role. As it can be gathered from Figure 89 for the case of squat CS panels with $\alpha_v = 0.5$ and $\sigma_L = 6\%$, the distribution of joint normal stress magnitude along the panels may vary considerably depending on the brick arrangement, resulting in the definition of various inclinations of the “diagonal strut” even in the first loading stages, thereby justifying the inverse correlation often observed between ϕ and k_i .

However, the numerical models seem to indicate that this cannot be taken to apply as a general rule: when comparing the initial response of RUN and FLE walls, indeed, although the latter is characterised by a lower value of φ , the associated k_i parameter is consistently reduced. In this respect, the parameter $\lambda_j = A_b(A_{hj}\varphi)^{-1}$, where $A_b=L_bH_b$ and A_{hj} is the area of head joints referred to a RVE, might represent a better indicator, as depicted below:

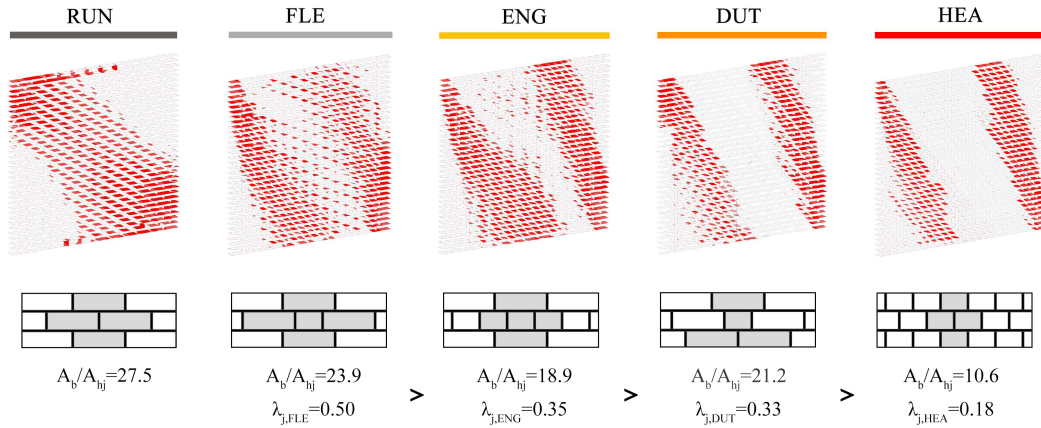


Figure 89 Propagation of joint normal stresses along CS squat walls in the first stages of loading and head joint-to-brick ratio for each brickwork

All the specimens exhibited higher lateral stiffness when increasing axial load (and obviously with decreased aspect ratio), as also reported by several authors (e.g. Salmanpour et al. 2015; Vanin et al. 2017). However, no significant differences with respect to the axial load ratio σ_L were detected when normalising the *i-bond* initial stiffnesses with the ones of the RUN walls, although they seem to be reduced with increased σ_L . Similarly, clear trends were not recognisable in terms of k_{eff}/k_i , which ranged from 0.75 to 0.98 for all the walls.

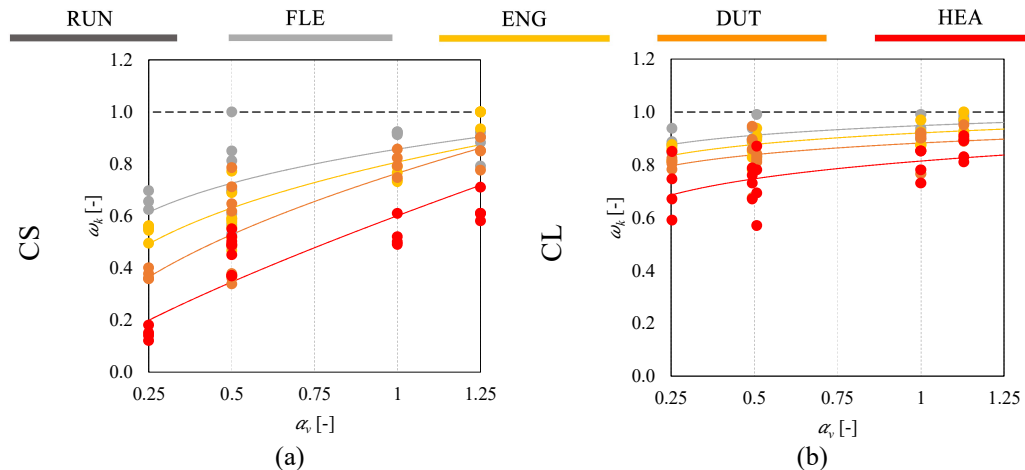


Figure 90 Influence of bond pattern on the initial lateral stiffness: shear span ratio vs normalised initial stiffness of the *i-th* wall for both CS (a) and CL (b)

On the contrary, when the normalised k_i of the *i-th* brickwork ω_k (i.e. $k_{i,BOND^i}/k_{i,RUN}$) is plotted against α_s (see Figure 90), the initial stiffnesses of the various specimens seem to be consistently reduced with decreased α_s , and this is much more evident in the case of CS

piers, characterised by a higher λ_b value, which can be directly correlated to φ . The HEA wall models suffered a significant reduction of k_i , up to 80% for CS brick masonry with $\alpha_v = 0.25$, as well as both ENG and DUT piers, which exhibited a rather similar initial lateral response for both the masonry types. The normalised k_i factor of FLE panels made of CS bricks slightly differ from the unity in case of $\alpha_v > 1.25$, albeit a substantial reduction was observed with decreased α_v . Considering the same masonry texture with CL bricks, instead, the difference with RUN walls becomes almost negligible for $\alpha_v > 1.25$.

Overall, the numerical outcomes shown above seem to indicate that k_i may vary considerably depending on the bond morphology, and as expected it is noticeably influenced by φ - λ_b . Regardless, the predicted distribution of compressive stresses in the panels, induced by lateral loading, would suggest that k_i is also controlled by the extent of head joints along a given brick course, which can be adequately represented by the ratio λ_j referred to a given RVE.

It was found that the dissimilarities described above are mainly related to the parameter α_v , which accounts for both aspect ratio and boundary conditions. With reference to Figure 90, the best data fitting was obtained assuming a power-law distribution, with $0.50 < R^2 < 0.70$. Hence, aimed at providing a simplified analytical expression for considering the abovementioned aspects, the expression reported in Table 44 (i.e. Eq. (12)), which can be easily adapted for inferring the ω_k for each brickwork bond as a function of α_v by changing the β_1 - β_2 coefficients, is proposed.

Table 44 Proposed simplified expression and β_1 and β_2 values for each brickwork and masonry type

Equation	Masonry type	FLE		ENG		DUT		HEA	
$\omega_k = \beta_1(\alpha_v)^{\beta_2}$ (12)	CS	β_1	β_2	β_1	β_2	β_1	β_2	β_1	β_2
		0.86	0.24	0.81	0.36	0.76	0.53	0.60	0.80
	CL	β_1	β_2	β_1	β_2	β_1	β_2	β_1	β_2
		1.06	0.05	1.04	0.06	1.06	0.08	1.14	0.14

7.5.3 In-plane strength

In this subsection, the lateral strengths exhibited by the URM walls with different masonry textures is compared against the ones of the RUN panels. Particular emphasis will be given to the evaluation of the maximum shear capacity V_p , since the majority of the simplified assessment procedures mainly rely on the latter rather than the residual strength V_r . However, referring to relatively low values of α_v (i.e. < 1), it might be worth mentioning that the ratio V_r/V_p seemed to be close to unity when considering the monotonic force-displacement curves of ENG, DUT and HEA walls. RUN and FLE piers, instead, exhibited more pronounced cohesive peaks (see Figure 91), resulting in lower values of V_r/V_p .

This can be attributable to the higher values of lateral stiffness which characterises the latter elements, as well as to the activation of different failure modes (e.g. top and bottom sliding). Indeed, as further discussed in the next subsection, early diagonal cracking mechanisms often occurred in case of ENG, DUT, and HEA walls, precluding the exploitation of the overall shear capacity associated to cohesive-frictional phenomena.

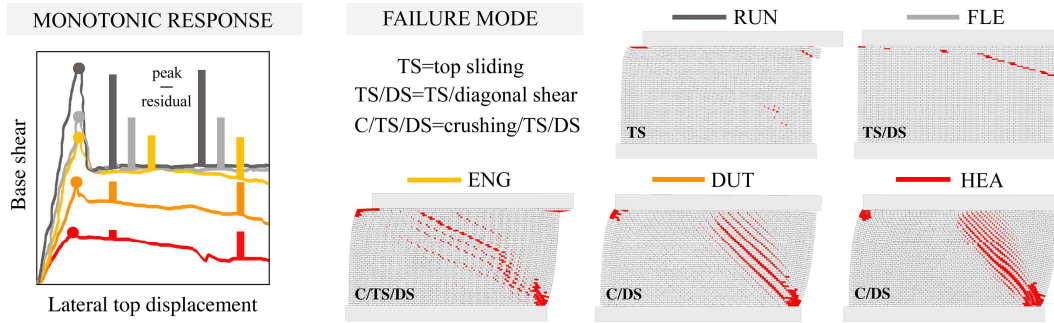


Figure 91 Comparison between the shear responses in the case of CL long walls

As for k_i , the bilinear idealisation of the envelope curves has not provided significant indications. In fact, the value of V_b corresponded approximately to $0.94-0.97V_p$ in almost all cases, which is also consistent with the experimental findings reported in e.g. (Salmanpour et al. 2015; Tomaževič 1999). As depicted in Figure 92(a)(b), the relations between V_p and the axial load ratio σ_L indicate that a substantial increase in lateral capacity with increased pre-compression. This is in accordance to both experimental evidence (e.g. Drysdale et al. 1999) and numerical applications (e.g. Haach et al. 2011).

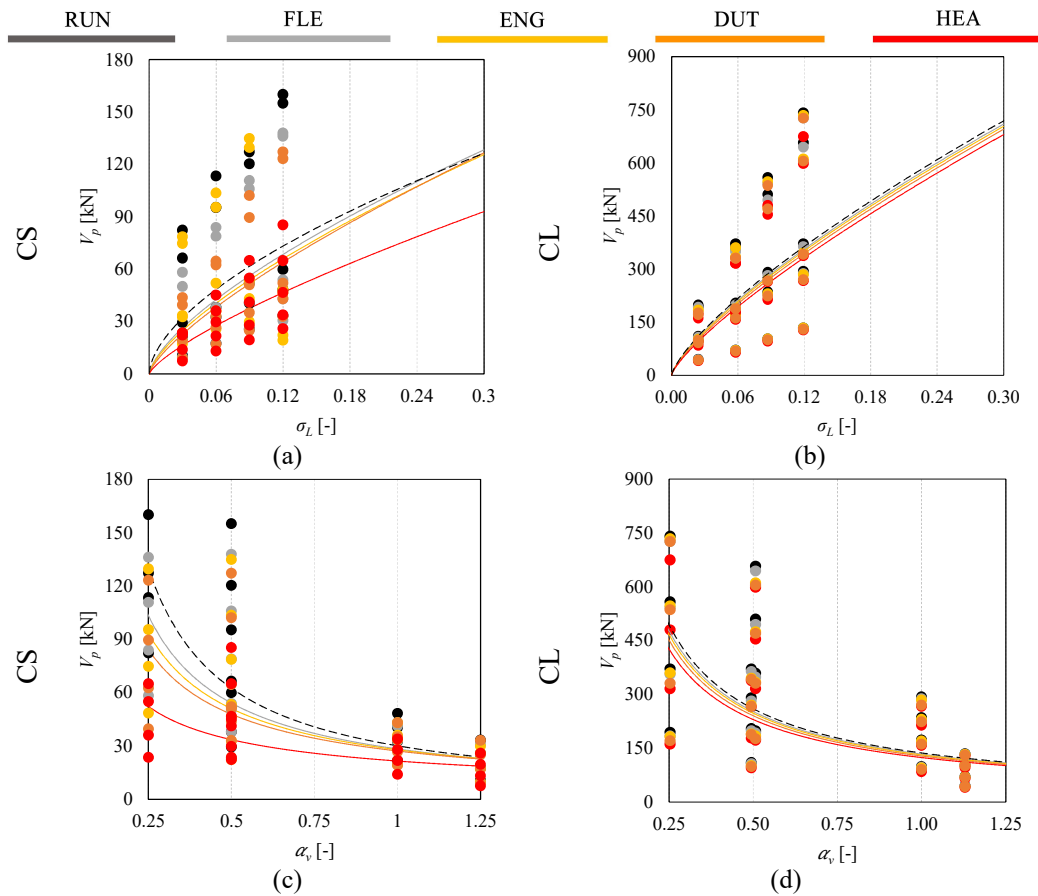


Figure 92 Influence of bond pattern on the lateral capacity V_p : axial load ratio vs V_p for CS (a) and CL (b) walls, shear span ratio vs V_p for CS (c) and CL (d) walls

The latter authors found that right after $\sigma_L = 0.4-0.5$, crushing failure takes a key-role in the in-plane resistance of concrete block walls, resulting in a sudden loss of base shear. In this work, similar phenomena were occasionally observed in case of both CS/CL squat and long walls with $\sigma_L = 0.12$. However, the general trend (herein extended through a power law interpolation up to $\sigma_L = 0.30$) would suggest that for CS and CL brick masonry this aspect is not always predominant. Looking at Figure 92(c)(d), it is seen that V_p increases as the shear span ratio α_v decreases, as also confirmed by experimental evidence (e.g. Anthoine et al. 1995; Kikuchi et al. 2003; Schultz et al. 1998). As previously noted, the CS masonry walls appear more sensitive with respect to the change of bond configuration, while only small variations were detected for CL panels. This is more evident when considering the normalised distribution of capacity ω_p , equal to the ratio $V_{p,BONDI}/V_{p,RUN}$, as depicted in Figure 93, from which it can be gathered that even in the case of CL brick masonry not-negligible differences with respect to the RUN walls, ranging from 18 (HEA) to 5% (FLE), were detected. In this case both σ_L and α_v seem to considerably affect the in-plane response of the various brickworks. The best fitting of numerical data were obtained using a power law interpolation function, with average values of R^2 between 0.40 and 0.65. A slightly lower correlation factor was found for the HEA walls, which under specific combinations of vertical pressure and boundary conditions exhibited premature diagonal cracking.

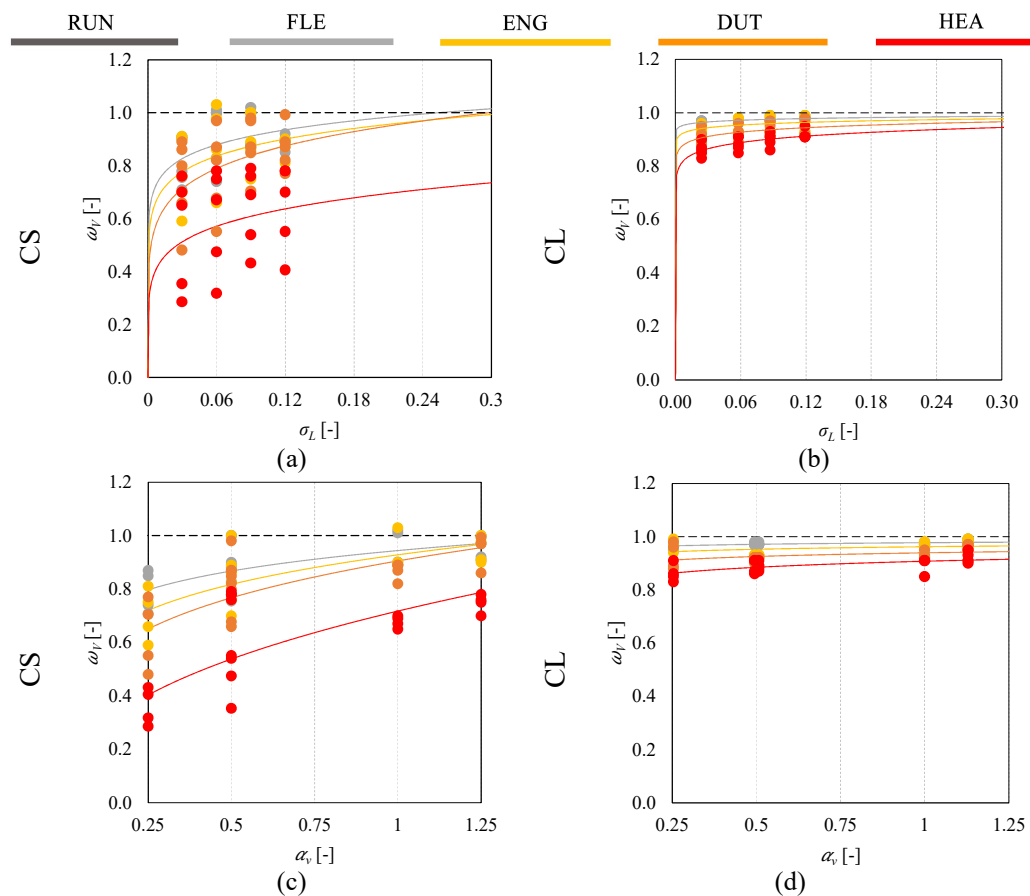


Figure 93 Influence of bond pattern on the lateral capacity V_p : axial load ratio vs normalised V_p for CS (a) and CL (b) walls, shear span ratio vs normalised V_p for CS (c) and CL (d) walls

Thus, with a view to combine simultaneously in a simplified analytical expression the abovementioned relations, a multi-criteria optimisation technique was applied through mathematical programming. In practice, after defining *a priori* a convenient objective function and the number of variables, an evolutionary algorithm (Michalewicz and Janikow 1991) seek to select iteratively potential values within the specified range for minimising the overall mean squared error. Since the increase of both σ_L and α_v induces an increased value of ω_v , and because the adopted power law function seems to adequately represent the trend of numerical outcomes, the following relation is proposed:

$$\omega_v = \gamma_1 (\alpha_v)^{\gamma_2} (\sigma_L)^{\gamma_3} \quad (13)$$

The optimal solution provided by the iterative adjustment of the γ_1 , γ_2 and γ_3 coefficients let to acceptable results, with an average error of 5-7%. In Table 45, the γ factors are reported:

Table 45 Values of γ_1 , γ_2 and γ_3 depending on both bond pattern and masonry type

Masonry type	FLE			ENG			DUT			HEA		
	γ_1	γ_2	γ_3									
CS	0.99	0.11	0.03	1.00	0.16	0.04	1.02	0.02	0.03	1.12	0.44	0.18
CL	1.01	0.003	0.003	1.01	0.05	0.02	1.08	0.02	0.10	1.02	0.04	0.04

Then, three-dimensional failure surfaces of both CS and CL brick masonry piers subjected to in-plane loading were directly inferred considering Eq. (13), as represented in Figure 94. The differences among the various walls characterised by the selected bond patterns are clearly observable, as well as the influence of masonry type.

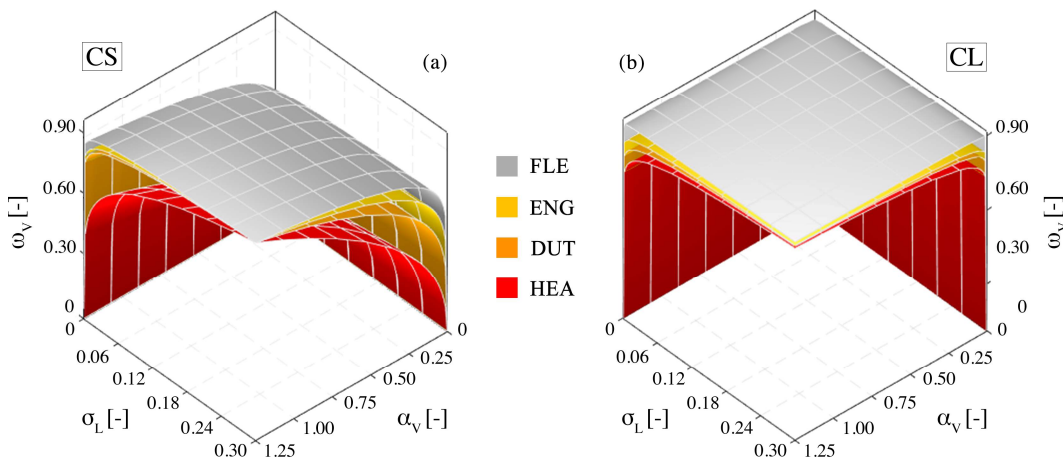


Figure 94 Failure surfaces of laterally-loaded CS (a) and CL (b) piers characterised by different masonry textures depending on shear span and axial load ratios

7.5.4 Failure mode and displacement capacity

Initiation and propagation of fractures through blocky assemblies are unavoidably dependent on both geometrical and mechanical properties of each component. When considering different arrangements of units, the effect of relative rotations and

displacements among adjacent bodies, in fact, may induce stress and strain localisation, producing several combinations of peculiar crack patterns. This is something that has been already widely investigated, for instance, in the field of rock mechanics, as discussed in e.g. Lisjak and Grasselli (2014) and Mahabadi et al. (2012). On the contrary, apart from a few contributions (e.g. Casapulla et al. 2013, Portioli et al. 2013, Vanin and Foraboschi 2012), only limited research pertaining the influence of unit shape and mortar joint morphology (rather than dry joint) on both failure mechanisms and displacement capacity of URM elements is currently available in literature.

In the following, the observed failure modes and associated ultimate displacement capacities δ_u of each specimen are summarised. According to the standardisation of in-plane mechanisms previously introduced, the governing failure modes exhibited by each wall and their dependency on both σ_L and α_i are investigated, resulting in the definition a simplified analytical correlation function in terms of normalised displacement capacity ω_D (i.e. $\delta_{u,BOND^i}/\delta_{u,RUN}$). However, it is worth mentioning that some experimental applications (e.g. Abrams 1996; Paulson and Abrams 1990) have shown that the imposed loading rate may affect considerably the deformation performances of shear walls. When monotonic loads are applied, as noted by Petry and Beyer (2014), the δ_u of URM elements might differ significantly from the one obtained considering cyclic or pseudo-dynamic testing protocols, and, because of the lack of dedicated experimental tests, this aspect is still object of debate. Nonetheless, the findings herein presented seem to indicate clearly that due to the activation of different types of mechanisms, the δ_u of laterally loaded piers may vary significantly depending on the considered masonry texture.

In this respect, it is worth mentioning that when sliding failure along bed joints was predominant, the models occasionally struggled to capture explicitly the progressive lateral strength reduction, producing smooth bilinear curves. Thus, in all these cases, the use of bilinear idealisation for evaluating the ultimate displacement capacity was not suitable. To be consistent, δ_u has been determined for all the models according to a local criterion, i.e. assuming that the onset of failure is reached whenever head joints are aligned.

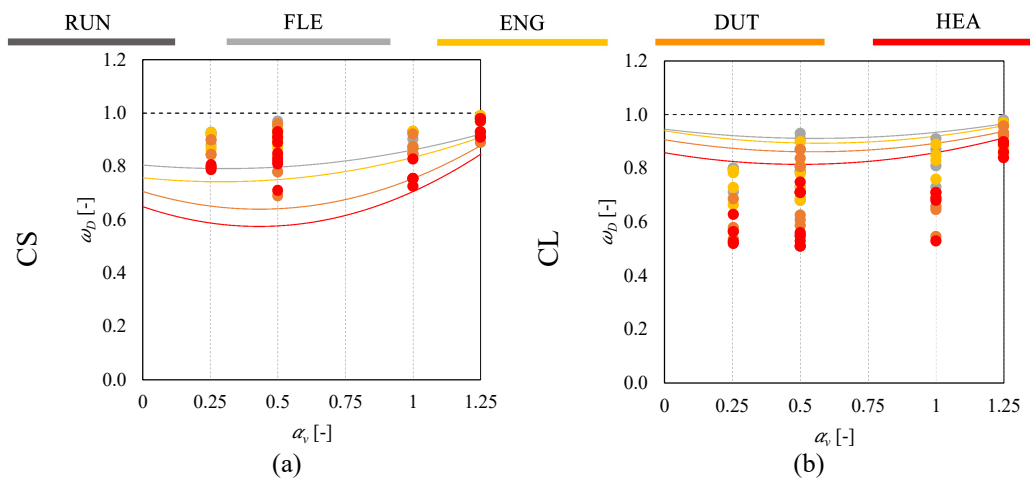


Figure 95 Influence of bond pattern on displacement capacity: shear span ratio vs normalised lateral displacement of the i -th wall for both CS (a) and CL (b) walls

As pointed out by Wilding and Beyer (2018), an effective approach to distinguish between shear and flexure controlled walls is to use the shear span ratio. Given the close relation between predicted failure mode and displacement capacity, major differences among the selected brickworks were noted referring to α_v , rather than σ_L , whose effect was less evident. In Figure 95, the dimensionless ratio ω_D of both CS and CL walls is plotted against the shear span ratio. It is interesting noting that the best fitting was obtained using a polynomial regression function (Eq. (13)), showing that ω_D noticeably decrease especially for $0.5 < \alpha_v < 1.0$. This is because within this specific range significant dissimilarities were detected in terms of failure mode. Indeed, while RUN and FLE walls mostly exhibited top and bottom sliding mechanisms (at least in the first loading stages), ENG, DUT and HEA panels prematurely failed in diagonal shear, thereby justifying such discrepancy (see Figure 96). Good correlation factors ($0.35 < R^2 < 0.65$) were found especially for CS masonry elements, in which this particular phenomenon was more predominant.

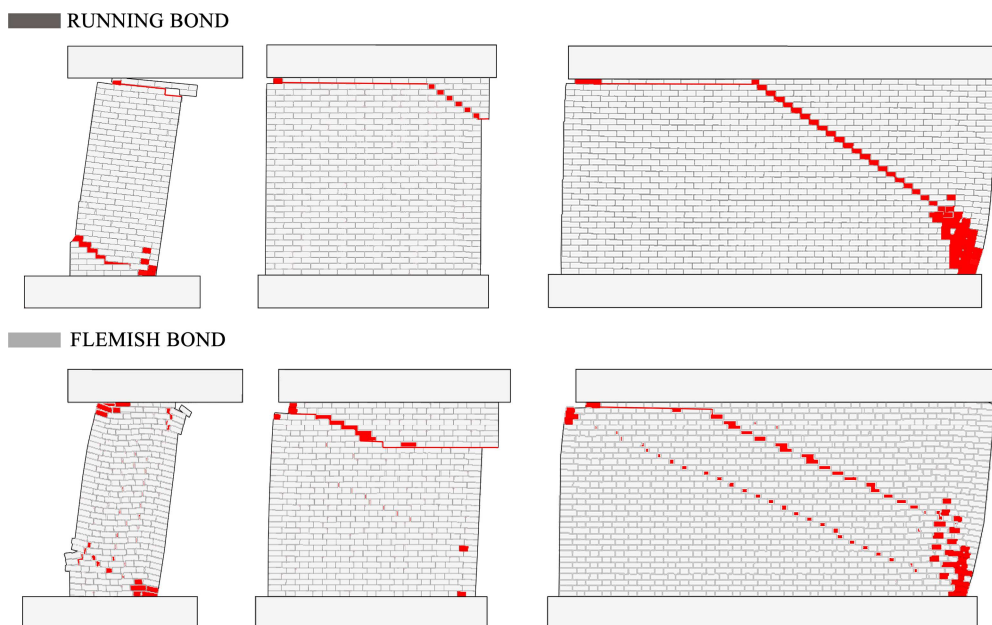
$$\omega_D = \rho_1(\alpha_v)^2 + \rho_2(\alpha_v) + \rho_3 \quad (13)$$

In Table 46, the correlation factors ρ for both CS/CL masonry types, are briefly summarised:

Table 46 Values of ρ_1 , ρ_2 and ρ_3 depending on both bond pattern and masonry type

Masonry type	FLE			ENG			DUT			HEA		
CS	ρ_1	ρ_2	ρ_3									
	0.15	-0.09	0.81	0.18	-0.10	0.76	0.36	-0.31	0.71	0.40	-0.35	0.65
CL	ρ_1	ρ_2	ρ_3									
	0.11	-0.15	0.95	0.14	-0.16	0.94	0.15	-0.17	0.91	0.18	-0.17	0.86

It might worth noting that for equal external conditions, masonry type and failure mode, the activation of multiple sliding planes was observed in all the cases except for the RUN piers. Moreover, it was seen that the extent of parallel stepped cracks is inversely proportional to λ_j , as it can be gathered from Figure 96 for fixed-fixed CS walls.



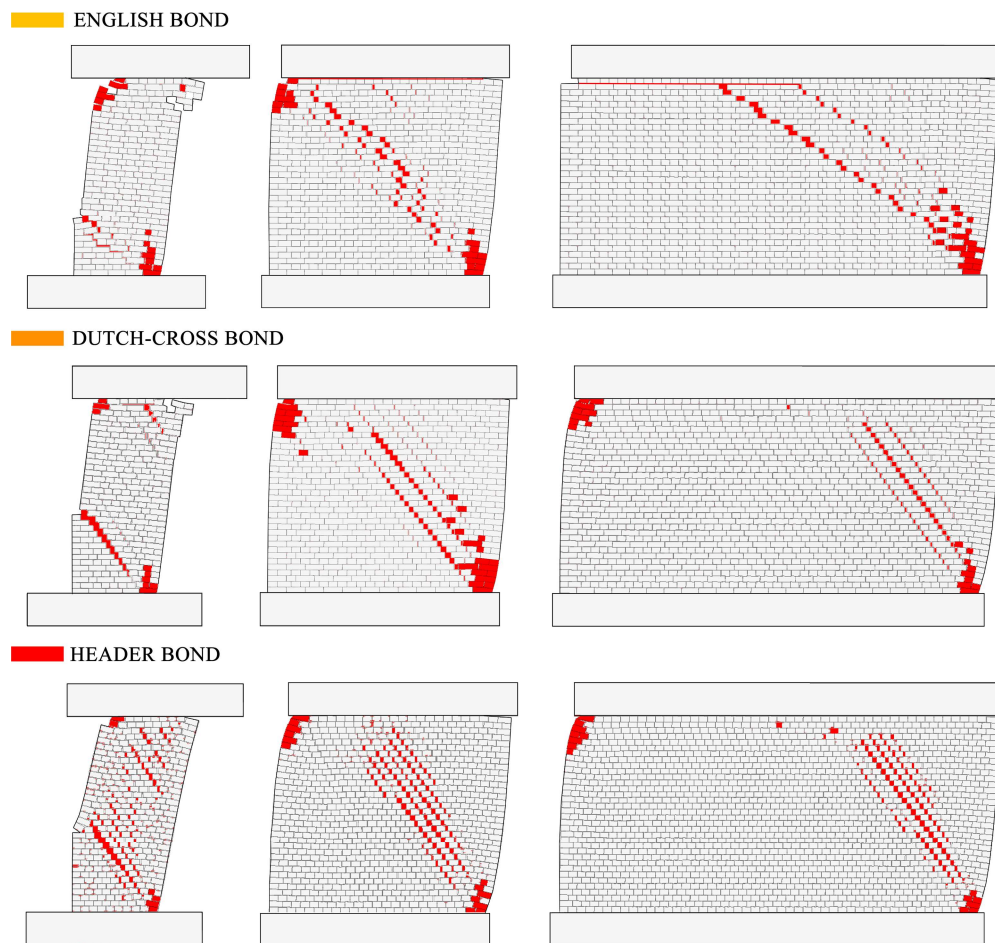


Figure 96 Influence of bond pattern on failure mode: joint cracks and unit damage for CS fully fixed walls (various magnifications)

This aspect, which is also well supported by experimental outcomes (e.g. Graziotti et al. 2016; Messali and Rots 2018), substantially increase the vulnerability of URM elements towards horizontal actions, further reducing the ultimate displacement capacity and inducing rather brittle failure modes. On the contrary, the extent of masonry crushing damage seems to be more apparent in the long walls constituted by the assembly of smaller units, somehow compensating the differences in terms of ω_D . Indeed, it was noticed that in the latter case relative rotations among adjacent bricks they are subjected to lower flexural stresses, which are transferred to both bed and head joints, producing stress localisations. This is clearly observable in the case of slender HEA piers, where cracks initiated in the centre of the panel. Analogous failure modes were detected by Anthoine et al. (1995) testing cyclically English bond panels.

In the case of cantilevered walls, a similar trend was found for all the specimens, albeit the piers rotated around the bottom corner in different manners, due to the various inclination of the crack opened in base because of tensile failure of joints (also visible in Figure 96). CL elements, tested numerically both in fully fixed and in cantilevered conditions,

presented comparable behaviours with the CS ones, albeit the ratio ω_D and the associated failure mode were much less sensitive to bond pattern effects.

In the contour plots of Figure 97- Figure 98, the main findings related to both failure modes and displacement capacity of the brickworks under study are summarised. They were developed assigning to each variable (i.e. failure mode or ω_D) an ID number, and then interpolating values at neighbouring points through cubic convolution. Figure 97 (a)(b)(c)(d) are meant to represent the variability of failure modes depending on both shear span ratio (left y-axis) and axial load ratio (right y-axis) for each brickwork (x-axis), also distinguishing between CS (left column) and CL (right column) brick masonry. In Figure 97(a)(b), every shade of colour is assigned to a specific flexure/hybrid/shear failure mechanism. In Figure 97(c)(d), instead, this approach is simplified by identifying three main governing modes, namely flexure/hybrid/shear.

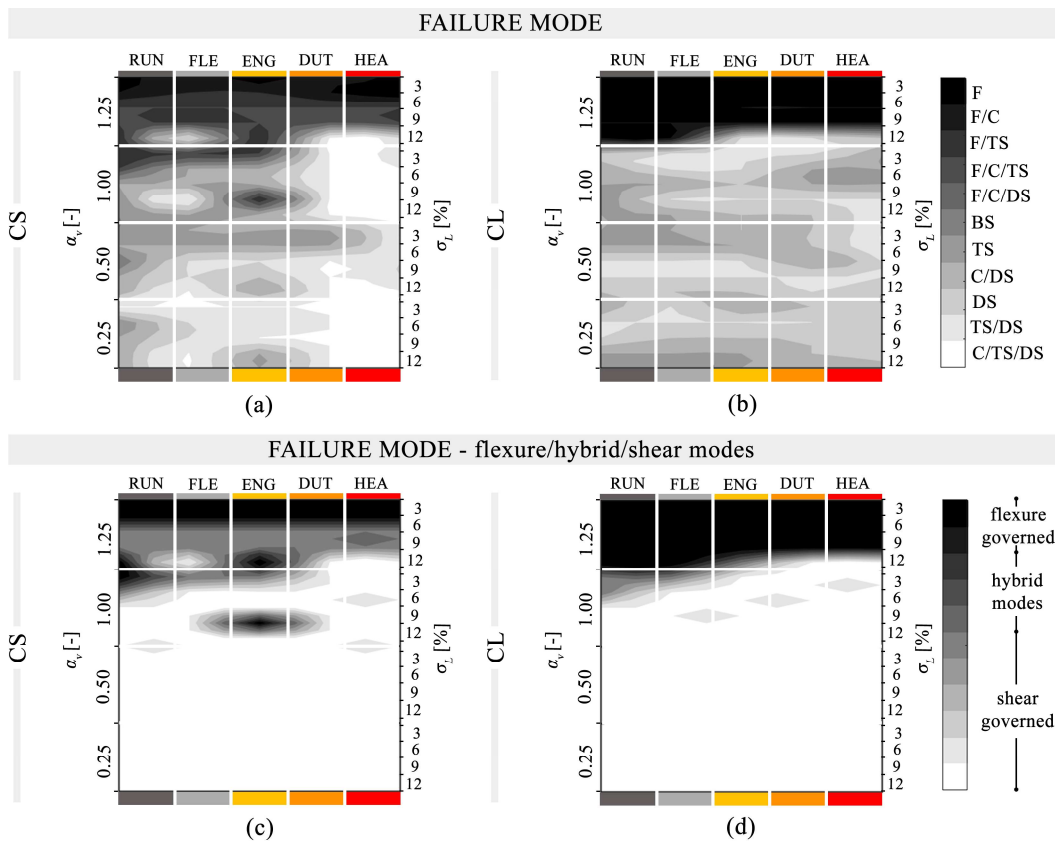


Figure 97 Influence of bond pattern on failure mode: relation between bond pattern and failure mode depending on both shear span and axial load ratio

The same scheme was also employed in Figure 98, where the extent of normalised displacement capacity ω_D for each brickwork is reported. The more the colour is dark the more the displacement capacity of the i -th brickwork is lesser than the one of the corresponding RUN wall (e.g. black, $\omega_D = 0.5$).

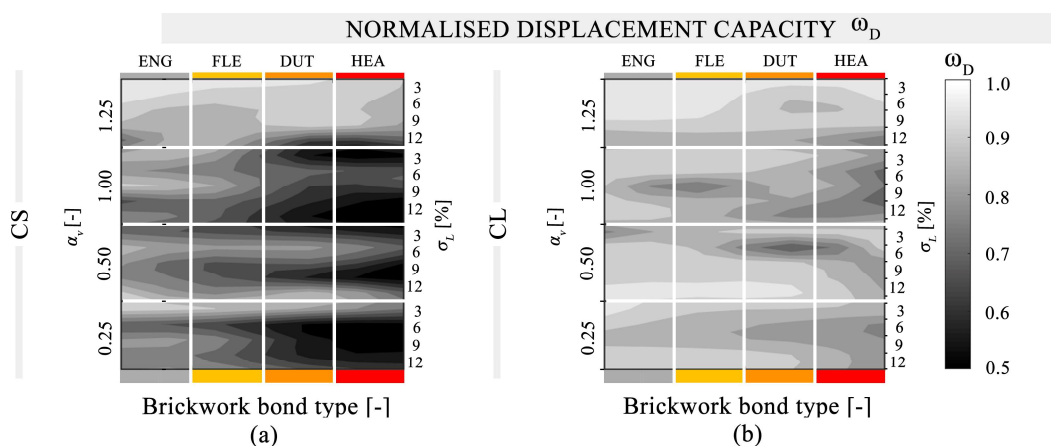


Figure 98 Influence of bond pattern on displacement capacity: normalised displacement capacity depending on both shear span and axial load ratio

As expected, a clear correlation between Figure 97 and Figure 98 is visible, especially for CS piers. Indeed, when diagonal cracking is predominant (light grey to white, Figure 97(a), for instance, the associated displacement is consistently reduced, up to 50% (dark grey to black, Figure 98(a)).

The colours are much more uniform in the case of CL elements, revealing their less sensitivity with respect to different masonry textures. With reference to the general framework, numerical outcomes would suggest that the deformation capacity of URM walls is strongly dependent on unit size and arrangement, inducing a large variety of peculiar failure mechanisms which might considerably affect their in-plane performances. Moreover, the effect of the axial load ratio was found to be less important compared to the shear span ratio, which in this context can be deemed as a key-parameter.

7.6 Conclusions

The in-plane performances of URM components, when subjected to biaxial stress states, may vary significantly depending on the interaction among load direction, joint orientation and bond pattern. Moreover, the mechanical contribution of mortar head joints might be often reduced, since they are often unable to transfer shear stresses because they crack prematurely due to shrinkage, being frequently not properly filled. In addition, experimental evidence shown that the considered boundary conditions, aspect ratio and pre-compression level also play a relevant role. However, the combination of the abovementioned internal and external factors has not yet been fully investigated neither experimentally nor numerically. Consequently, most of the analytical and computational procedures developed so far neglect or only simplistically account for the effect that various masonry textures may have on the lateral response of URM members.

In this work, calibrated models, developed in the framework of the Distinct Element Method (DEM), were used to perform a comprehensive parametric analysis with a view to investigate both strength and displacement capacity, as well as the horizontal stiffness, of monotonically-loaded URM piers constituted by many typically-employed periodic and

quasi-periodic brickwork bond types, under the assumption of weak head joints. Several combinations of overburden pressure, aspect ratio and boundary conditions were considered, as well as two main masonry typologies made of calcium-silicate and clay bricks characterised by different unit dimensions and compressive strengths. The use of DEM was enhanced by introducing additional features, including the possibility of simulating crushing phenomena, and optimised through the development of a specific modelling strategy which provided a significant reduction of computational cost. In order to make readily employable the findings of this work for simplified numerical methods, analytical formulations were also proposed by fitting numerical data.

The results seem to indicate that the brickwork type may considerably affect the in-plane behaviour of URM panels subjected to shear-compression. The number of masonry textures investigated (i.e. running, Flemish, English, Dutch-cross and header bond) makes it possible to draw up preliminary statistics on strength and displacement capacity variability of URM walls depending on the considered bond pattern:

- In general, the running bond walls performed better than the others
- For similar values of bond tensile and shear strength, the masonry typology, and in particular the unit size (on which also depends on the height of the head joints), plays a relevant role
- The proposed simplified ratio λ_j , which may be evaluated selecting a representative volume element (RVE) of the masonry element under study, proved to be an effective indicator of the in-plane performances of the considered brickworks, being directly proportional to initial stiffness, shear strength and displacement capacity
- It was observed that even during the first stages of loading, the propagation of normal stresses through the various brickworks noticeably differs from each other, strongly influencing the initial lateral response
- Significant differences in terms of in-plane strength were observed, and for equal masonry type, they tend to increase with increased axial and shear span ratio
- Failure mode and displacement capacity are unavoidably related. In this respect, a critical range of the shear span ratio α_v has been identified. Indeed, for $0.5 < \alpha_v < 1.0$, while running and Flemish bond walls underwent top and bottom sliding, English, Dutch-cross and Header bond panels prematurely failed in diagonal shear, thereby exhibiting reduced displacement capacity. For these walls, a strong decay in resistance to earthquake is to be expected.

References

- Abrams, D. P. (1996). "Effects of scale and loading rate with tests of concrete and masonry structures." *Earthquake Spectra*, 12(1), 13–28.
- Addessi, D., Sacco, E., and Paolone, A. (2010). "Cosserat model for periodic masonry deduced by nonlinear homogenization." *European Journal of Mechanics-A/Solids*, Elsevier, 29(4), 724–737.
- Anthoine, A. (1995). "Derivation of the in-plane elastic characteristics of masonry through homogenization theory." *International Journal of Solids and Structures*, Pergamon, 32(2), 137–163.
- Anthoine, A., Magonette, G., and Magenes, G. (1995). "Shear-compression testing and analysis of brick masonry walls." *Proceedings of the 10th European conference on earthquake engineering*, Rotterdam, The Netherlands, 1657–1662.
- Azevedo, J., Sincaian, G., and Lemos, J. V. (2000). "Seismic behavior of blocky masonry structures." *Earthquake Spectra*, 16(2), 337–365.
- Bacigalupo, A., Cavicchi, A., and Gambarotta, L. (2011). "A Simplified Evaluation of the Influence of the Bond Pattern on the Brickwork Limit Strength." *Advanced Materials Research*, Trans Tech Publications, 368–373, 3495–3508.
- Baraldi, D., Reccia, E., and Cecchi, A. (2018). "In plane loaded masonry walls: DEM and FEM/DEM models. A critical review." *Meccanica*, Springer Netherlands, 53(7), 1613–1628.
- Benedetti, A., and Steli, E. (2008). "Analytical models for shear-displacement curves of unreinforced and FRP reinforced masonry panels." *Construction and Building Materials*, Elsevier, 22(3), 175–185.
- Brooks, J. J., and Baker, A. (1998). "Modulus of Elasticity of Masonry." *Masonry International*, 12(2), 58–63.
- De Buhan, P., and de Felice, G. (1997). "A homogenization approach to the ultimate strength of brick masonry." *Journal of the Mechanics and Physics of Solids*, Pergamon, 45(7), 1085–1104.
- Bui, T. T., Limam, A., Sarhosis, V., and Hjiij, M. (2017). "Discrete element modelling of the in-plane and out-of-plane behaviour of dry-joint masonry wall constructions." *Engineering Structures*, Elsevier, 136, 277–294.
- Calderini, C., Cattari, S., and Lagomarsino, S. (2009). "In-plane strength of unreinforced masonry piers." *Earthquake Engineering and Structural Dynamics*, 38(2), 243–267.
- Calderini, C., Cattari, S., and Lagomarsino, S. (2010). "The use of the diagonal compression test to identify the shear mechanical parameters of masonry." *Construction and Building Materials*, Elsevier, 24(5), 677–685.
- Casapulla, C., Portioli, F., Maione, A., and Landolfo, R. (2013). "A macro-block model for in-plane loaded masonry walls with non-associative Coulomb friction." *Meccanica*, Springer Netherlands, 48(9), 2107–2126.
- Casolo, S. (2009). "Macroscale modelling of microstructure damage evolution by a rigid body and spring model." *Journal of Mechanics of Materials and Structures*, 4(3), 551–570.
- Cecchi, A., and Milani, G. (2008). "A kinematic FE limit analysis model for thick English bond masonry walls." *International Journal of Solids and Structures*, Pergamon, 45(5), 1302–1331.
- Cecchi, A., and Sab, K. (2004). "A comparison between a 3D discrete model and two homogenised plate models for periodic elastic brickwork." *International Journal of*

- Solids and Structures*, Pergamon, 41(9–10), 2259–2276.
- Ciesielski, R. (1999). “The dynamic module of elasticity of brick walls.” *Proceedings of the Conference of the Committee of Civil Engineering PZITB: Lublin, Poland*.
- Cluni, F., and Gusella, V. (2004). “Homogenization of non-periodic masonry structures.” *International Journal of Solids and Structures*, Elsevier, 41(7), 1911–1923.
- Cook, R. D., Malkus, D. S., Plesha, M. E., and Witt, R. J. (2002). *Concepts and Applications of Finite Element Analysis*. John Wiley & Sons, Inc., New York, USA.
- Costa, A. A., Penna, A., and Magenes, G. (2011). “Seismic performance of autoclaved aerated concrete (AAC) masonry: from experimental testing of the in-plane capacity of walls to building response simulation.” *Journal of Earthquake Engineering*, Taylor & Francis, 15(1), 1–31.
- Courant, R., Friedrichs, K., and Lewy, H. (1967). “On the partial difference equations of mathematical physics.” *IBM journal of Research and Development*, IBM, 11(2), 215–234.
- Cundall, P. A. (1971). “A computer model for simulating progressive large scale movements in blocky rock systems.” *Proc. Symp. Rock Fracture (ISRM)*, Nancy.
- Cundall, P. A. (1982). “Adaptive density-scaling for time-explicit calculations.” *Numerical Methods in Geomechanics*, Edmonton, Canada, 23–26.
- D’Altri, A. M., de Miranda, S., Castellazzi, G., and Sarhosis, V. (2018). “A 3D detailed micro-model for the in-plane and out-of-plane numerical analysis of masonry panels.” *Computers & Structures*, Pergamon, 206, 18–30.
- Dhanasekar, M., Kleeman, P. W., and Page, A. W. (1985). “Biaxial stress-strain relations for brick masonry.” *Journal of structural Engineering*, American Society of Civil Engineers, 111(5), 1085–1100.
- Drysdale, R. G., and Khattab, M. M. (1995). “In-plane behavior of grouted concrete masonry under biaxial tension-compression.” *ACI Structural Journal*, 92(6), 653–664.
- Drysdale, R., Hamid, A., and Baker, L. (1999). *Masonry Structures--Behavior and Design*, The Masonry Society. Boulder, Colorado, Boulder, Colorado, United States.
- Dumova-Jovanoska, E., and Churilov, S. (2009). “Calibration of a numerical model for masonry with application to experimental results.” *Protection of historical buildings*, 1139–1145.
- Falsone, G., and Lombardo, M. (2007). “Stochastic representation of the mechanical properties of irregular masonry structures.” *International Journal of Solids and Structures*, Pergamon, 44(25–26), 8600–8612.
- de Felice, G. (2011). “Out-of-plane seismic capacity of masonry depending on wall section morphology.” *International Journal of Architectural Heritage*, 5(4–5), 466–482.
- Graziotti, F., Tomassetti, U., Rossi, A., Kallioras, S., Mandirola, M., Cenja, E., Penna, A., and Magenes, G. (2015). *Experimental campaign on cavity-wall systems representative of the Groningen building stock - Report n. EUC318/2015U*. Pavia, Italy.
- Graziotti, F., Tomassetti, U., Rossi, A., Marchesi, B., Kallioras, S., Mandirola, M., Fragomeli, A., Mellia, E., Peloso, S., Cuppari, F., Guerrini, G., Penna, A., and Magenes, G. (2016). *Experimental campaign on a clay URM full-scale specimen representative of the Groningen building stock - Report n. EUC128/2016U*. Pavia, Italy.
- Haach, V. G., Vasconcelos, G., and Lourenço, P. B. (2011). “Parametrical study of masonry walls subjected to in-plane loading through numerical modeling.” *Engineering*

- Structures*, Elsevier, 33(4), 1377–1389.
- Itasca Consulting Group Inc. (2013). “3DEC. Three Dimensional Distinct Element Code.”
- Jäger, W., Irmschler, H., and Schubert, P. (2004). *Mauerwerk-Kalender 2004*. Ernst & Sohn Verlag für Architektur und technische Wissenschaften.
- Kassotakis, N., Sarhosis, V., Forgács, T., and Bagi, K. (2017). “Discrete element modelling of multi-ring brickwork masonry arches.” *Proceedings of the 13th Canadian Masonry Symposium*, Halifax, Canada.
- Kaushik, H. B., Rai, D. C., and Jain, S. K. (2007). “Stress-strain characteristics of clay brick masonry under uniaxial compression.” *Journal of materials in Civil Engineering*, American Society of Civil Engineers, 19(9), 728–739.
- Kawai, T. (1978). “New discrete models and their application to seismic response analysis of structures.” *Nuclear Engineering and Design*, Elsevier, 48(1), 207–229.
- Kikuchi, K., Yoshimura, K., Tanaka, A., and Yoshida, K. (2003). “Effect of wall aspect ratio on seismic behaviour of reinforced fully grouted concrete masonry walls.” *Proceedings of 9th North American masonry conference*, Clemson, South Carolina, United States, 214–225.
- Lemos, J. V. (1997). “Discrete element modelling of the seismic behaviour of stone masonry arches.” *Proceedings of the 4th International Symposium on Numerical Methods in Structural Masonry*, G. N. Pande, J. Middleton, and B. Kralj, eds., E & FN SPON, Florence, Italy, 220–227.
- Lemos, J. V. (2007). “Discrete element modeling of masonry structures.” *International Journal of Architectural Heritage*, Taylor & Francis, 1(2), 190–213.
- Lisjak, A., and Grasselli, G. (2014). “A review of discrete modeling techniques for fracturing processes in discontinuous rock masses.” *Journal of Rock Mechanics and Geotechnical Engineering*, Elsevier, 6(4), 301–314.
- Lourenço, P. B., Rots, J. G. J. G., and Blaauwendraad, J. (1995). “Two approaches for the analysis of masonry structures - micro and macro-modeling.” *Research article HERON - Delft Univ. of Technology (Delft, The Netherlands)*, 40(4), 313–340.
- Magenes, G., and Calvi, G. M. (1992). “Cyclic behaviour of brick masonry walls.” *Proceedings of the 10th world conference on earthquake engineering*.
- Magenes, G., and Calvi, G. M. (1997). “In-plane seismic response of brick masonry walls.” *Earthquake Engineering and Structural Dynamics*, Wiley-Blackwell, 26(11), 1091–1112.
- Mahabadi, O. K., Lisjak, A., Munjiza, A., and Grasselli, G. (2012). “Y-Geo: New Combined Finite-Discrete Element Numerical Code for Geomechanical Applications.” *International Journal of Geomechanics*, 12(6), 676–688.
- Maheri, M. R., Najafgholipour, M. A., and Rajabi, A. R. (2008). “The influence of mortar head joints on the in-plane and out-of-plane seismic strength of brick masonry walls.” *Iranian Journal of Science and Technology Transaction*, 35(C1), 63–79.
- Malomo, D., DeJong, M. J., and Penna, A. (2018a). “Distinct Element modelling of the in-plane cyclic response of URM piers subjected to shear-compression.” *to be submitted*.
- Malomo, D., Pinho, R., and Penna, A. (2018b). “Shake-table response of a double-leaf unreinforced clay brick masonry building.” *to be submitted*.
- Mann, W., and Muller, H. (1982). “Failure of shear-stressed masonry. An enlarged theory, tests and application to shear walls.” *Proceedings of the British Ceramic Society*, (30), 223.
- Marti, J., and Cundall, P. (1982). “Mixed discretization procedure for accurate modelling of plastic collapse.” *International Journal for Numerical and Analytical Methods in*

- Geomechanics*, 6(1), 129–139.
- Massart, T. J., Sonon, B., Ehab Moustafa Kamel, K., Poh, L. H., and Sun, G. (2018). “Level set-based generation of representative volume elements for the damage analysis of irregular masonry.” *Meccanica*, Springer Netherlands, 53(7), 1737–1755.
- Matysek, P., and Janowski, Z. (1996). “Analysis of factors affecting the modulus of elasticity of the walls.” *Proceedings of the Conference of the Committee of Civil Engineering PZITB: Lublin, Poland*.
- Messali, F., and Rots, J. G. (2018). “In-plane drift capacity at near collapse of rocking unreinforced calcium silicate and clay masonry piers.” *Engineering Structures*, Elsevier, 164, 183–194.
- Michalewicz, Z., and Janikow, C. Z. (1991). “Genetic algorithms for numerical optimization.” *Statistics and Computing*, Kluwer Academic Publishers, 1(2), 75–91.
- Miglietta, P. C., Bentz, E. C., and Grasselli, G. (2017). “Finite/discrete element modelling of reversed cyclic tests on unreinforced masonry structures.” *Engineering Structures*, 138, 159–169.
- Milani, G., and Cecchi, A. (2013). “Compatible model for herringbone bond masonry: Linear elastic homogenization, failure surfaces and structural implementation.” *International Journal of Solids and Structures*, 50(20–21), 3274–3296.
- Milani, G., Esquivel, Y. W., Lourenço, P. B., Riveiro, B., and Oliveira, D. V. (2013). “Characterization of the response of quasi-periodic masonry: Geometrical investigation, homogenization and application to the Guimarães castle, Portugal.” *Engineering Structures*, Elsevier, 56, 621–641.
- Mojsilović, N. (2011). “Strength of masonry subjected to in-plane loading: A contribution.” *International Journal of Solids and Structures*, Pergamon, 48(6), 865–873.
- Munjiza, A. (2004). *The combined finite-discrete element method. The Combined Finite-Discrete Element Method*, Wiley, New York, USA.
- Otter, J. R. H. (1966). “Dynamic relaxation compared with other iterative finite difference methods.” *Nuclear Engineering and Design*, 3(1), 183–185.
- Page, A. (1981). “The biaxial compressive strength of brick masonry.” *Proceedings of the Institution of Civil Engineers*, Thomas Telford - ICE Virtual Library, 893–906.
- Page, A. W. (1983). “The strength of brick masonry under biaxial tension-compression.” *International journal of masonry construction*, 3(1), 26–31.
- Paulay, T., and Priestley, J. N. (1992). *Seismic Design of Reinforced Concrete and Masonry Buildings*. Wiley, New York, USA.
- Paulson, T. J., and Abrams, D. P. (1990). “Correlation Between Static and Dynamic Response of Model Masonry Structures.” *Earthquake Spectra*, 6(3), 573–591.
- Penna, A., Lagomarsino, S., and Galasco, A. (2014). “A nonlinear macroelement model for the seismic analysis of masonry buildings.” *Earthquake Engineering & Structural Dynamics*, Wiley Online Library, 43(2), 159–179.
- Petry, S., and Beyer, K. (2014). “Influence of boundary conditions and size effect on the drift capacity of URM walls.” *Engineering Structures*, Elsevier, 65, 76–88.
- Petry, S., and Beyer, K. (2015). “Cyclic test data of six unreinforced masonry walls with different boundary conditions.” *Earthquake Spectra*, Earthquake Engineering Research Institute, 31(4), 2459–2484.
- Portioli, F., Cascini, L., Casapulla, C., and D’Aniello, M. (2013). “Limit analysis of masonry walls by rigid block modelling with cracking units and cohesive joints using linear programming.” *Engineering Structures*, Elsevier, 57, 232–247.
- Raka, E., Spacone, E., Sepe, V., and Camata, G. (2015). “Advanced frame element for

- seismic analysis of masonry structures: model formulation and validation.” *Earthquake Engineering & Structural Dynamics*, Wiley Online Library, 44(14), 2489–2506.
- Roca, P. (2006). “Assessment of masonry shear-walls by simple equilibrium models.” *Construction and Building Materials*, 20(4), 229–238.
- Roca, P., Cervera, M., Gariup, G., and Pela’, L. (2010). “Structural analysis of masonry historical constructions. Classical and advanced approaches.” *Archives of Computational Methods in Engineering*, 17(3), 299–325.
- Rosti, A., Penna, A., Rota, M., and Magenes, G. (2016). “In-plane cyclic response of low-density AAC URM walls.” *Materials and Structures/Materiaux et Constructions*, Springer Netherlands, 49(11), 4785–4798.
- Salerno, G., and de Felice, G. (2009). “Continuum modeling of periodic brickwork.” *International Journal of Solids and Structures*, Pergamon, 46(5), 1251–1267.
- Salmanpour, A. H., Mojsilović, N., and Schwartz, J. (2015). “Displacement capacity of contemporary unreinforced masonry walls: An experimental study.” *Engineering Structures*, Elsevier, 89, 1–16.
- Sarhosis, V., and Lemos, J. V. (2018). “A detailed micro-modelling approach for the structural analysis of masonry assemblages.” *Computers and Structures*, Pergamon, 206, 66–81.
- Sarhosis, V., Oliveira, D. V., Lemos, J. V., and Lourenco, P. B. (2014). “The effect of skew angle on the mechanical behaviour of masonry arches.” *Mechanics Research Communications*, Pergamon, 61, 53–59.
- Schultz, A. E., Hutchinson, R. S., and Cheok, G. S. (1998). “Seismic performance of masonry walls with bed joint reinforcement.” *Structural Engineers World Congress*, San Francisco, United States.
- Smoljanović, H., Nikolić, Ž., and Živaljić, N. (2015). “A combined finite-discrete numerical model for analysis of masonry structures.” *Engineering Fracture Mechanics*, Pergamon, 136, 1–14.
- Spence, S. M. J., Giofrè, M., and Grigoriu, M. D. (2008). “Probabilistic Models and Simulation of Irregular Masonry Walls.” *Journal of Engineering Mechanics*, 134(9), 750–762.
- Szakály, F., Hortobágyi, Z., and Bagi, K. (2016). “Discrete element analysis of the shear resistance of planar walls with different bond patterns.” *The Open Construction and Building Technology Journal*, 10(1), 220–232.
- Thamboo, J. A., and Dhanasekar, M. (2016). “Behaviour of thin layer mortared concrete masonry under combined shear and compression.” *Australian Journal of Structural Engineering*, 17(1), 39–52.
- Tomažević, M. (1999). *Earthquake-Resistant Design of Masonry Buildings*. Imperial College Press, London, United Kingdom, London, United Kingdom.
- Tomažević, M., Lutman, M., and Petković, L. (1996). “Seismic Behavior of Masonry Walls: Experimental Simulation.” *Journal of Structural Engineering*, 122(9), 1040–1047.
- Turnšek, V., and Čačovič, F. (1971). “Some experimental results on the strength of brick masonry walls.” *Proc. of the 2nd International Brick Masonry Conference*, 149–156.
- U.B.C. (1991). “International Conference of Building Officials. Uniform Building Code.” *International conference of building officials, USA*, Whittier, USA.
- Vanin, A., and Foraboschi, P. (2012). “In-plane behavior of perforated brick masonry walls.” *Materials and Structures/Materiaux et Constructions*, Springer Netherlands,

- 45(7), 1019–1034.
- Vanin, F., Zaganelli, D., Penna, A., and Beyer, K. (2017). “Estimates for the stiffness, strength and drift capacity of stone masonry walls based on 123 quasi-static cyclic tests reported in the literature.” *Bulletin of Earthquake Engineering*, Springer Netherlands, 15(12), 5435–5479.
- Vasconcelos, G., and Lourenço, P. B. (2009). “In-Plane Experimental Behavior of Stone Masonry Walls under Cyclic Loading.” *Journal of Structural Engineering*, 135(10), 1269–1277.
- Wilding, B. V., and Beyer, K. (2017). “Force–displacement response of in-plane loaded unreinforced brick masonry walls: the Critical Diagonal Crack model.” *Bulletin of Earthquake Engineering*, Springer Netherlands, 15(5), 2201–2244.
- Wilding, B. V., and Beyer, K. (2018). “The effective stiffness of modern unreinforced masonry walls.” *Earthquake Engineering and Structural Dynamics*, Wiley-Blackwell, 47(8), 1683–1705.
- Zucchini, A., and Lourenço, P. B. (2002). “A micro-mechanical model for the homogenisation of masonry.” *International Journal of Solids and Structures*, Pergamon, 39(12), 3233–3255.

CHAPTER 8

A Homogenised Distinct Macro-block for simulating
the in-plane cyclic response of URM walls



CHAPTER 8 A Homogenised Distinct Macro-block for simulating the in-plane cyclic response of URM walls

Malomo D., DeJong M.J., Penna A. (2018). “1. A Finite-Distinct macroelement approach for simulating the in-plane cyclic response of URM walls.” *In Proceedings of the 13th North American Masonry Conference*

Abstract. The interaction between in-plane and out-of-plane actions, often neglected by simplified numerical approaches, significantly affects the overall seismic response of URM structures. The use of advanced numerical modelling, on the other hand, often entails a relatively high computational cost, limiting applicability to the analysis of local mechanisms. In this work, to combine the efficiency of macroelement strategies with the benefits of discrete element methods, a new macro-element approach to model in-plane cyclic behaviour of URM panels is presented. Shear damage is accounted by a homogenised Finite Element macro-block, while flexural and sliding phenomena are represented through equivalent interface spring layers between discrete elements. The methodology is evaluated through comparison with both micro-modelling results and experimental outcomes on full-scale wall specimens characterised by different aspect ratios, boundary conditions and overburden pressures. In particular, the abilities of the proposed method to predict stiffness and strength degradation, energy dissipation and $P-\Delta$ effects, are quantified. Moreover, contrarily to most of the macroelements presently available in literature, the damage propagation can be reproduced explicitly. Being implemented in an explicit Distinct Element code, naturally suitable for large-displacement analysis, out-of-plane modes and collapses can also be considered by modelling each unit separately. The employment of this hybrid modelling strategy is demonstrated through an initial application, leading to adequate results within a reasonable timeframe.

Keywords: finite-distinct element method; numerical modelling; in-plane; unreinforced masonry

8.1 Introduction

Structural failure of unreinforced masonry (URM) buildings, when subjected to earthquake loading, often comprises the activation of complex and sometimes conflicting aspects of responses, as noted by Calvi et al. (1996). Indeed, depending on the effectiveness of floor-to-wall connections, masonry and diaphragm type, interaction between in-plane and out-of-plane actions, as well as the degree of both elevation and plan irregularity, several combinations of failure modes might occur. This is particularly relevant in the case of historical and existing constructions, frequently constructed prior to the introduction of seismic design prescriptions. In this context, micro-modelling methods might contribute significantly towards both vulnerability assessment and definition of suitable retrofitting

solutions, having been conceived for representing explicitly the discrete nature of masonry and the mechanical interaction among distinct elements.

The Distinct Element Method (DEM), developed by Cundall (1971) in the early seventies for solving rock and soil mechanics problems, can be probably deemed as one of the first micro-models ever developed. According to the DEM, each unit is modelled separately, while their mechanical interaction is provided by linear or nonlinear zero-thickness interface springs, in which the unit-mortar material properties are lumped. The applicability of DEM to masonry structures has been investigated by several authors, as broadly discussed in Lemos (2007), including the simulation of both quasi-static and dynamic behaviour of reduced-scale masonry prototypes (e.g. Galvez et al. 2018; Lemos and Campos Costa 2017) and components, such as panels (e.g. Bui et al. 2017; Malomo et al. 2018), columns (e.g. Papantonopoulos et al. 2002), spires (e.g. DeJong and Vibert 2012) and arches (e.g. DeLorenzis et al. 2007; Kassotakis et al. 2017). However, the irregular geometry of both in-plane layout and thickness composition make often preferable the adoption of continuum models with an equivalent homogenised material (e.g. Milani et al. 2013; Salerno and de Felice 2009; Zucchini and Lourenço 2002). Still, the problem of a significant computational burden often limits the applicability of these techniques to the analysis of local mechanisms and small-scale structures.

Thus, aimed at decreasing analysis time, a wide range of simplified numerical approaches have been implemented so far. Equivalent truss (e.g. Calderoni et al. 1987), storey mechanisms (e.g. Tomažević 1987) and macroelement models (e.g. Chen et al. 2008; Penna et al. 2014; Raka et al. 2015) might represent suitable alternatives in some specific cases, as reported in Magenes et al. (2000). Regardless, since out-of-plane modes are usually neglected, their use is currently confined to the analysis of in-plane governed responses (Quagliarini et al. 2017). Upgrades to this initial schemes have been recently proposed by Kallioras (2017) and Pantò et al. (2017), assigning equivalent properties to out-of-plane loaded members and introducing a three-dimensional discrete macro-element respectively. Despite the latter promising advancements, the development of effective modelling strategies for representing numerically the interaction among in-plane and out-of-plane modes still represents an open challenge.

In this work, aimed at combining the efficiency of the macroelement strategy and the advantages of homogenisation procedures with the accuracy of DEM-based methods, a Homogenised Distinct Macro-block model (HDM), namely a new finite-distinct macroelement approach, is validated against laboratory tests on full-scale piers subjected to in-plane cyclic loading. Shear damage is accounted by a homogenised Finite Element macro-block, to which the mass of the system is assigned, while flexural and sliding phenomena are represented through equivalent interface spring layers. Further, an attempt was made to include the possibility of reproducing damage propagation explicitly, unlike the majority of typically employed macroelements. The performances of the model are scrutinised and consequently compared to the ones obtained using a standard micro-modelling approach, investigating benefits and disadvantages of its potential employment. Having been implemented within the 3DEC commercial software framework (Itasca, 2013), whose use is largely widespread and suitable for many fields of structural engineering, it might be also of interest for both practitioners and applied researchers. Further, the explicit time-integration scheme on which the selected computational platform

is founded would make the HDM model also compatible with large-displacement analysis, providing unconditionally stable conditions. In this respect, out-of-plane modes, depending on the analysis objectives, can be still explicitly accounted for by modelling each brick separately, thus readily enabling a multi-scale hybrid approach.

8.2 Homogenised Distinct Macro-block (HDM) representative of a masonry panel

Masonry piers subjected to lateral loading may exhibit several failure modes, depending on boundary conditions, applied vertical pressure and aspect ratio. Under shear-compression biaxial stress states, as proved by experimental evidence (e.g. Magenes and Calvi 1997; Petry and Beyer 2015; Vanin et al. 2017), cracks may propagate along bed and head joints, though units or both. From a numerical viewpoint, as suggested by Haach et al. (2011), it is possible to standardise the typical local in-plane failure modes and the associated damage according to simplified description depicted in Figure 99:

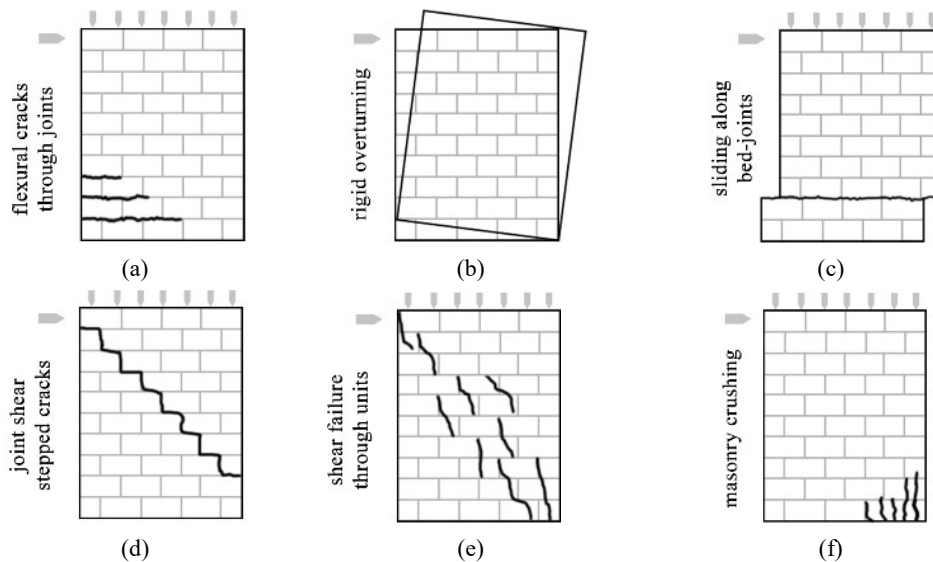


Figure 99 Typically-observed in-plane failure modes (adapted from Malomo et al. 2018)

1. *Flexure-governed* behaviours, which usually comprise flexural cracks through joints (a), masonry crushing phenomena (f) and rigid overturning and rocking modes (c)
2. *Shear-governed* behaviours, which often induce joint stepped cracks (d), sliding along bed-joints (b) and shear failure through units (e)

The proposed HDM model, as it can be gathered from Figure 100, consists in the assembly of a FE macro-block and two zero-thickness interface spring layers, located at the top and bottom central block extremities. As further discussed in the next subsection, in spite of its simplicity, such a basic mechanical scheme is able to simulate adequately the main in-plane failure mechanisms of a portion of masonry wall subjected to horizontal and vertical loads. With reference to Figure 99, interface springs account for flexural (a), rocking (b) and sliding (c) modes, while diagonal (d) and unit (e) shear failure mechanisms are represented by the FE block. At this stage, the cyclic loss of strength and the energy dissipation due to

toe/heel damage (f), commonly related to the increase in rocking demand, is not explicitly accounted for. Regarding this last point, further improvements are currently being explored. However, it is worth noting that in most of the selected experimental tests this phenomenon was not predominant. Further, the comparisons between experimental/numerical results shown in the following seems to indicate that during the last loading cycles, whenever masonry crushing occurred, because of the normal stress localisation at the corners (which induced bending failure of FE zones), the model was able to reproduce the progressive strength deterioration exhibited by the specimens, as well as the actual damage propagation.

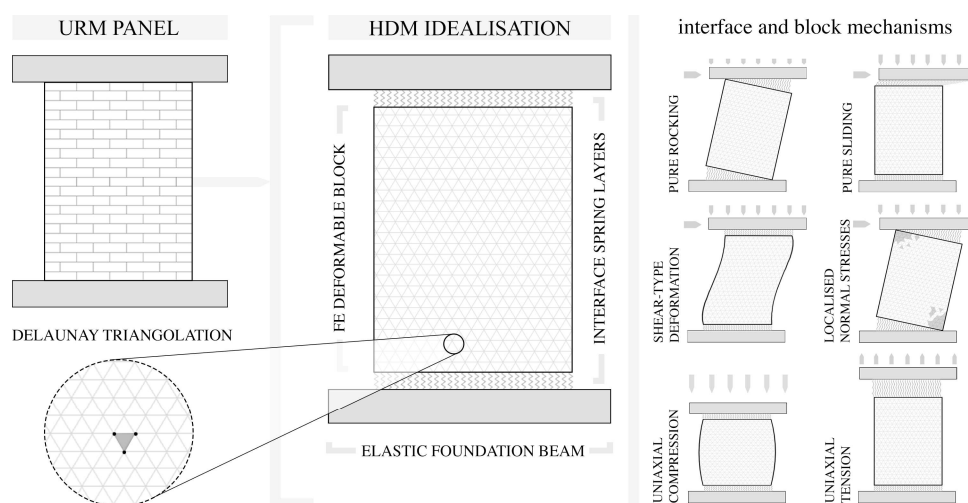


Figure 100 Homogenised Distinct Macro-block representative of a URM component

Flexural and top/base sliding mechanisms are controlled by normal and shear stiffnesses of interface springs, while cyclic stiffness and strength degradation due to shear damage is considered adjusting continuously the macro-block mechanical properties according to a linearised softening function, governed by the extent of accumulated plastic strain.

In what follows, the main theoretical elements, the constitutive laws implemented and the calibration of such numerical system are scrutinised. For the sake of clarity, aspects related to interface springs and macro-block will be presented individually. It is worth mentioning that in absence of some specific characterisation tests (e.g. diagonal compressive test) needed for the HDM calibration, use was made of the DE micro-models validated by Malomo et al. (2018), conveniently adapted for this purpose.

8.2.1 Interface springs

In the framework of the HDM model, zero-thickness spring layers are employed for representing flexural and top/bottom sliding phenomena, connecting the macro-block to adjacent elements, e.g. loading and foundation beams when the simulation of in-plane tests on URM components are considered. In the latter case, since the wall-to-beams connection is usually provided by mortar bonds, normal k_n and shear k_s stiffnesses of interface springs can be evaluated as the ratio between the Young's (or shear) modulus of mortar E_{mo} (or G_{mo}) and the length H , equal to $0.5(H_b + H_u)$, where H_b and H_u are beam and unit height respectively. In practice, as illustrated in Figure 101, H is meant to represent the centroid-to-centroid distance between the beam and corresponding top/bottom unit.

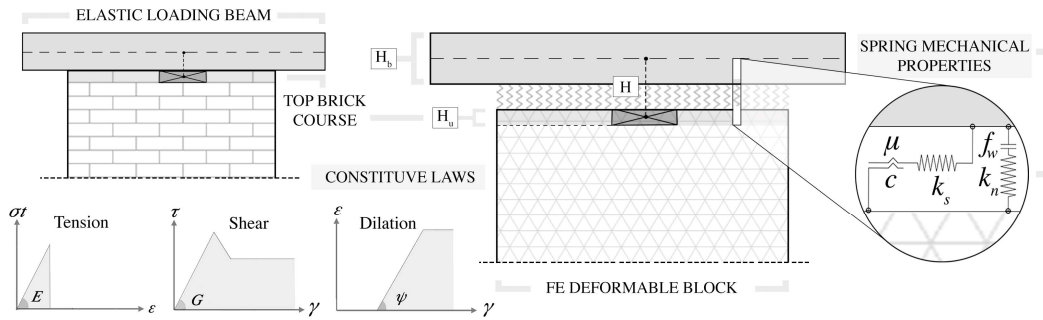


Figure 101 Interface spring layers and implemented constitutive laws

The experimental campaign to which this work is referred, as widely discussed in e.g. Graziotti et al. (2015, 2016), comprised several tests on both small and full-scale masonry prototypes, made of both calcium silicate (CS) and clay (CL) bricks. However, such efforts were mainly devoted to the study of masonry assemblies rather than the investigation of the response of single components (i.e. brick and mortar). The Young's moduli of both CS and CL bricks (E_b), needed for the evaluation of the mortar ones, were inferred using Eqs. (5)-(6), Table 47, as a function of its compressive strength f_{c_b} , obtained through uniaxial monotonic compressive test. Then, first estimates of Young's moduli of CS/CL mortar E_{mo} were derived through Eqs. (7)-(10) summarised below, where E_m stands for masonry Young's modulus (experimentally-determined by means of cyclic uniaxial compressive test) and ζ is the ratio between brick and mortar thickness t_{mo} , and the ensuing average value was adopted. Finally, the shear modulus G_{mo} was computed assuming material isotropy (i.e. $G_{mo} = 0.4 E_{mo}$).

Table 47 Empirical expressions for inferring unit and mortar material properties

BRICK	(Jäger et al. 2004)	$E_b = (375) \cdot (f_{c_b})$	(5)
	(Kaushik et al. 2007)	$E_b = (355) \cdot (f_{c_b})$	(6)
MORTAR	(Brooks and Baker 1998)	$E_{mo} = \left(\frac{-4E_m E_b}{25E_m - 29E_b} \right)$	(7)
	(Matysek and Janowski 1996)	$E_{mo} = \left(\frac{E_m E_b}{E_b - 1.25\zeta(E_m - E_b)} \right)$	(8)
	(Ciesielski 1999)	$E_{mo} = \left(\frac{-E_m E_b}{5E_m - 6E_b} \right)$	(9)
	(U.B.C. 1991)	$E_{mo} = \left(\frac{E_m E_b}{\zeta(E_m - E_b) + E_b} \right)$	(10)

As depicted in Figure 101, a Mohr-Coulomb slip model is assigned to interface springs for representing cohesive-frictional phenomena. The cohesion parameter, c , is set to zero right after reaching the maximum shear strength, thus neglecting any post-peak softening branch, resulting in a residual capacity governed by both the acting vertical stress and the specified angle of friction, ϕ . Similarly, a tension cut-off characterises the joint flexural response, whereas no compression failure is allowed. The effect of dilation, which takes place only when the joint is slipping, can be accounted for by introducing the parameter ψ , i.e. iteratively correcting the joint normal forces as a function of the direction of shearing. With a view to assessing the capabilities of the interface spring layers in adequately reproducing

both shear-compression and tensile behaviours of CS/CL brick-mortar assemblies, characterisation tests on small-scale specimens carried out in 2015-2016 at the DICAr laboratory (Department of Civil Engineering and Architecture, University of Pavia, Italy) were reproduced numerically (see Figure 102).

More specifically, masonry triplets subjected to quasi-static shear-compression loading, as well as masonry doublets tested according to the bond-wrench protocol, were considered. In Table 48, where f_{cm} and f_w are masonry compression and bond tensile strength respectively, both experimental and inferred (in italics) masonry properties are briefly summarised:

Table 48 CS and CL experimental (Graziotti et al. 2015, 2016b) and inferred material properties

	CS – masonry density = 1839 [kg/m ³]							CL – masonry density = 1979 [kg/m ³]								
	f_{cm}	f_{cb}	f_w	E_m	c	μ [-]	E_b	E_{mo}	f_{cm}	f_{cb}	f_w	E_m	c	μ [-]	E_b	E_{mo}
Mean [MPa]	6.20	18.67	0.24	4182	0.21	0.42	6628	1772	11.22	40	0.23	9833	0.15	0.55	15000	3257
C.o.V. [%]	7.04	13.67	16.32	33.27	-	-	-	-	7.43	11.21	60.11	25.42	-	-	-	-

The average mortar bond thickness was 10 mm for all the samples, while the CS (212×102×71 mm) and CL bricks (208×102×50 mm) substantially differed in terms of dimensions. Since a good agreement was found when comparing numerical results with their experimental counterparts, no adjustment of initial properties was applied.

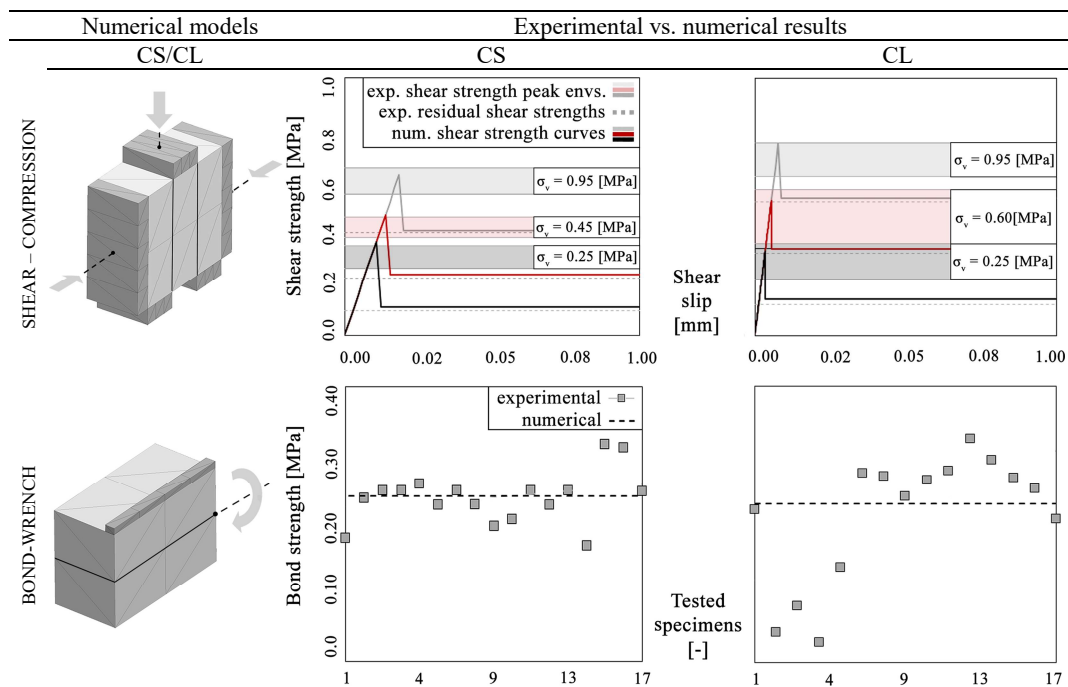


Figure 102 Calibration of interface springs through comparison with characterisation tests

8.2.2 Homogenised FE macro-block

The macro-block consists of a three-dimensional deformable solid body, in which the mass of the wall is lumped, discretised according to a FE Delaunay-based triangular mesh.

It is meant to represent wall diagonal shear deformability and associated damage phenomena. Although axial and flexural behaviours are usually controlled by interface springs when dealing with URM (with which are supposed to be arranged in series), the associated deformability was also included in the macro-block formulation. That was aimed at simulating Poisson effect and to readily extend the proposed methodology to different construction techniques and boundary conditions (e.g. precast assemblies, infill panels). As illustrated in Figure 103, a Mohr-Coulomb strain-softening plasticity model was allotted to the FE zones. It allows cohesion progressive reduction after the onset of plastic yield. Indeed, monitoring the total plastic shear strains γ at each timestep, the softening parameters are incremented according to a pre-defined linearised exponential expression, providing a gradual deterioration of initial shear resistance due to cyclic loading. Differently, no post-peak residual tensile strength was considered, meaning that when a given FE zone fails in tension, its mechanical contribution becomes negligible.

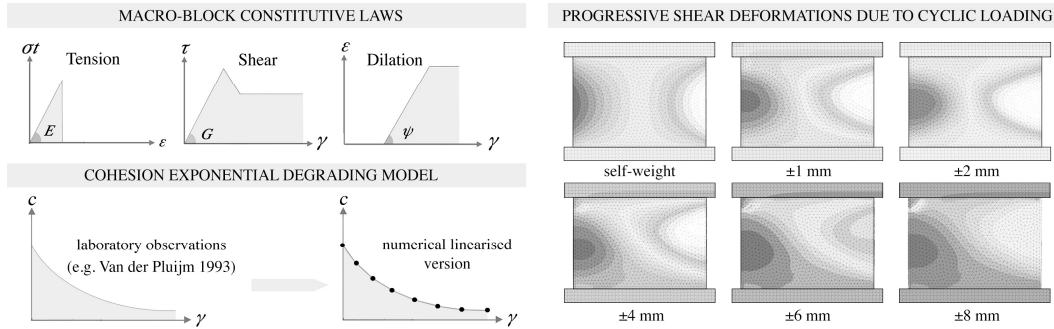


Figure 103 Mohr-Coulomb strain-softening plasticity model and shear/flexural deformations of a FE macro-block subjected to shear-compression under cantilevered boundary conditions

Aimed at accounting for cohesion degradation, Lourenço et al. (1995) proposed an expression based on fracture mechanics and supported by experimental observations (e.g. Van der Pluijm 1993). Thus, the exponential function ω_c reported in Eq. (11), often implemented in both discrete and continuum-based numerical methods, was selected, linearised and implemented in the employed DEM code.

$$\omega_c = c \left(\frac{-c}{G_f^{II}} \gamma \right) \quad (11)$$

It makes use of the second mode fracture energy G_f^{II} , which can be readily inferred in the case of the selected masonry types. Indeed, the Dutch guidelines for the seismic assessment of existing URM buildings (NPR 9998:2017) indicate 250 J/m² and 300 J/m² as the values to be adopted for CS and CL brick masonry respectively.

According to Turnšek and Čačovič (1971), the limit strength domain of a masonry element can be defined through a single “global” parameter of the material, namely the tensile strength of masonry. Similarly, the equivalent tensile strength τ_{eq} of the macro-block was evaluated through direct comparison with the outcomes of a diagonal-compression test. As already mentioned, because experimental outcomes were not available, verified micro-models were employed for replicating such test numerically for both the masonry types.

The specimen set-up resembled the one proposed by the American Society for Testing Materials (ASTM E 519-02 2002). A vertical displacement was incrementally applied to the top elastic plate with negligible velocity, while the bottom one was fully fixed, making it possible to capture adequately the post-peak strength. The calibration procedure entailed an iterative adjustment of τ_{eq} until reaching a satisfactory agreement with the micro-model outcomes. Usually, both shear and tension failure modes are involved in diagonal-compression tests, as pointed out by Frocht (1931), Yokel and Fattal (1976). Thus, this modelling exercise also provided further indications about the adequacy of considered shear-model and regarding the selection of G_m , i.e. the shear modulus to be assigned to the macro-block. In Figure 104, the comparison between the macro-block results and their micro counterparts are presented:

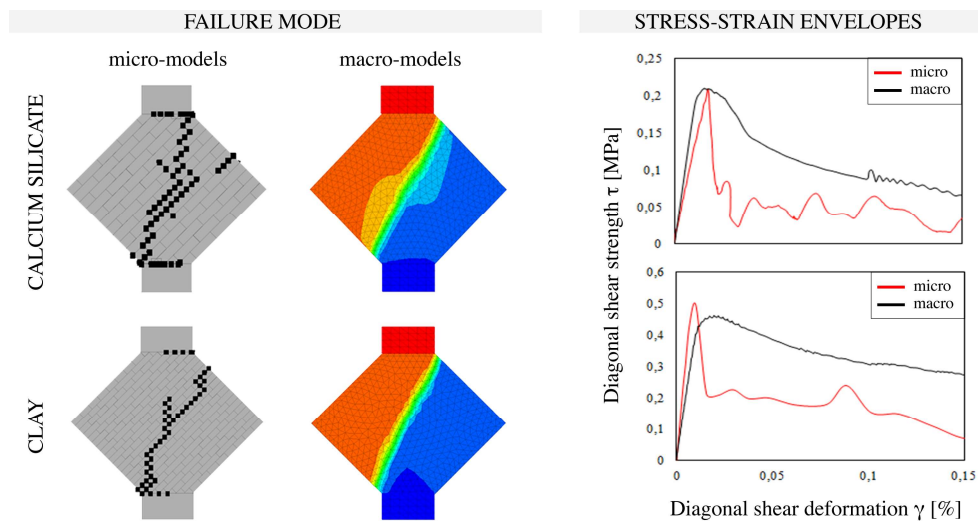


Figure 104 FE macro-block and Mohr-Coulomb strain-softening plasticity model

An acceptable agreement was found in terms of both stress-strain envelopes and deformed shapes, albeit the macro-block marginally overestimated the CS/CL residual strength. The best fit of micro-modelling results was obtained assuming $\tau_{eq} = 0.45$ MPa with $G_m = 0.35E_m$ for both CS/CL specimens. It was observed that the optimum value of τ_{eq} was about twice the CS/CL bond tensile strength f_w and it almost corresponds to the in-plane flexural strength determined experimentally by Graziotti et al. (2016) testing CL reduced-scale prototypes under in-plane four-point bending. In Table 49, the additional properties assigned to the macro-block are briefly summarised:

Table 49 CS/CL material properties assigned to the macro-block

	CS – masonry density = 1839 [kg/m ³]						CL – masonry density = 1979 [kg/m ³]					
	E_m	G_m	c	G_f^{II} [J/m ²]	μ [-]	τ_{eq}	E_m	G_m	c	G_f^{II} [J/m ²]	μ [-]	τ_{eq}
Mean [MPa]	4182	1464	0.21	250	0.42	0.45	9833	3442	0.21	300	0.42	0.45
C.o.V. [%]	33.27	-	-	-	-	-	25.42	-	-	-	-	-

Giving the encouraging results obtained, analogous values were also employed for the simulation of the cyclic behaviour of URM assemblies subjected to shear-compression presented in the subsequent sections.

8.3 Modelling the in-plane cyclic behaviour of URM piers

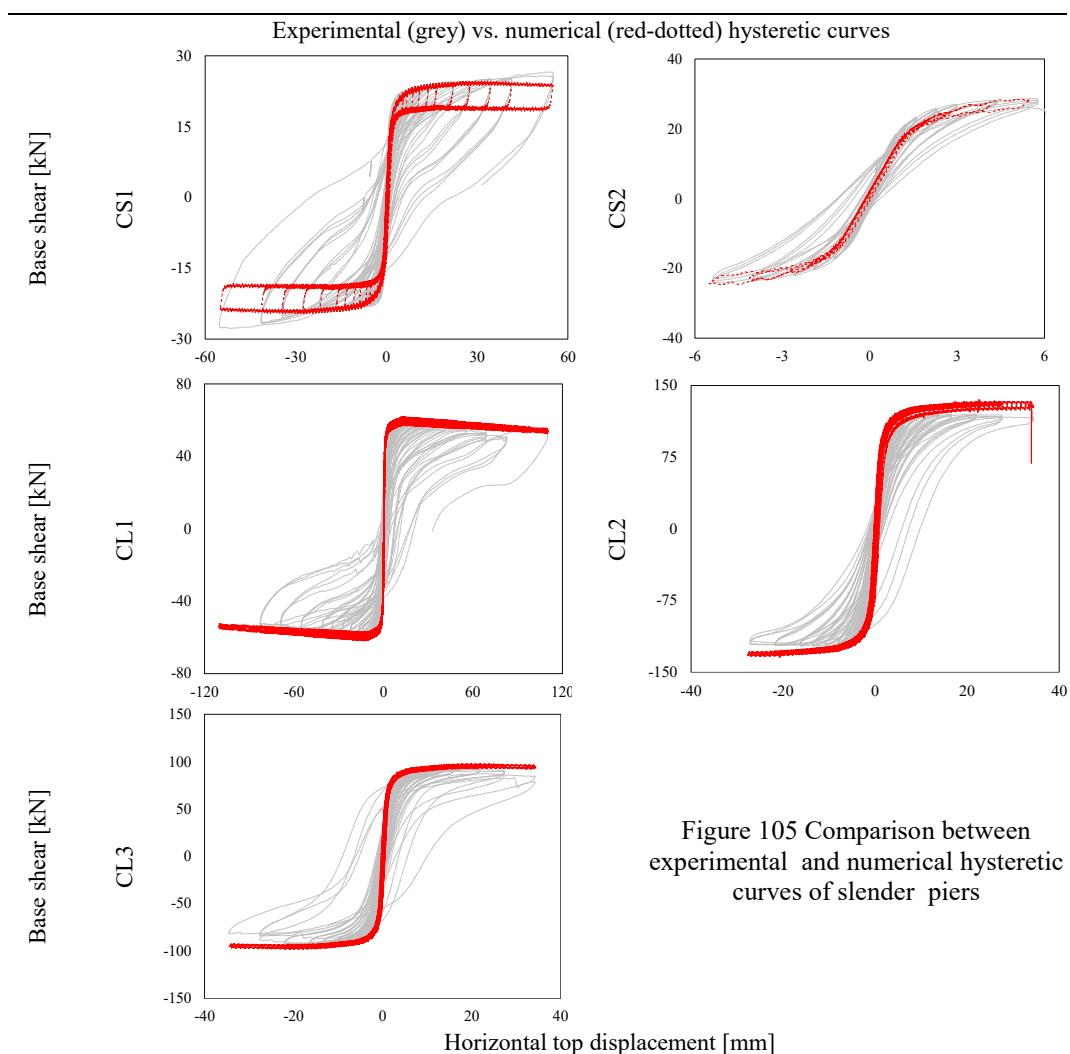
Three CS (CS1-2-3) and five CL (CL1-2-3-4-5) full-scale URM panels were subjected to quasi-static in-plane cyclic shear-compression loading with several combinations of boundary conditions, overburden and aspect ratios (see Table 50). It is noted that, since the only difference between CL4 and CL5 was the loading history (i.e. each cycle was repeated three times in CL5), the latter has not been considered in this work. The walls were founded on a reinforced concrete (RC) beam, which was clamped to the lab strong floor. The cyclic displacement histories, as well as the envisaged vertical compressions and boundary conditions, were imposed through a vertical actuator rigidly connected to the top RC beam. Interested readers are referred to the technical reports by Eucentre (i.e. Graziotti et al. 2015, 2016) for further details about loading protocols and experimental outcomes.

Wall ID	Length [m]	Height [m]	Asp. ratio [-]	Thickness [m]	Overburden [MPa]	Boundary conditions
CS1	1.1	2.75	2.50 (slender)	0.102	0.70	Fixed-Fixed
CS2	1.1	2.75	2.50 (slender)	0.102	0.52	Fixed-Fixed
CS3	4.0	2.75	0.69 (squat)	0.102	0.30	Cantilever
CL1	1.2	2.71	2.26 (slender)	0.208	0.52	Fixed-Fixed
CL2	1.2	2.71	2.26 (slender)	0.208	1.20	Fixed-Fixed
CL3	1.2	2.71	2.26 (slender)	0.208	0.86	Fixed-Fixed
CL4	2.7	2.71	1.00 (squat)	0.208	0.30	Fixed-Fixed

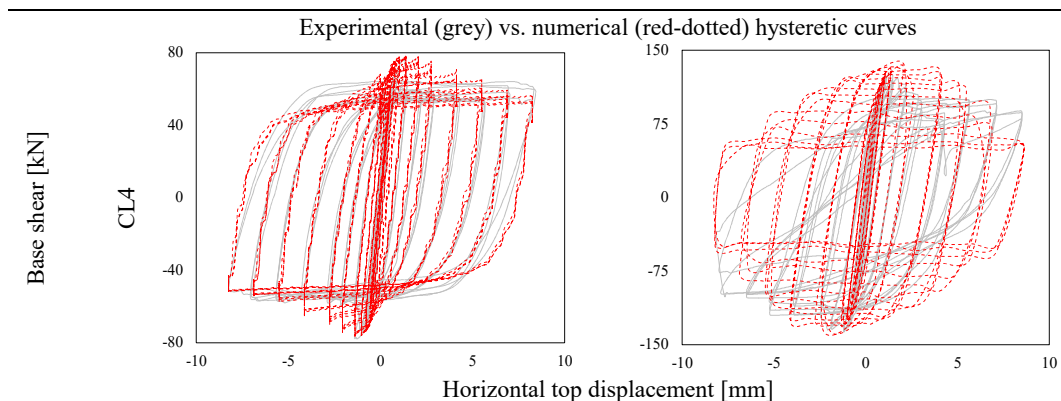
Table 50 Tested specimens: dimensions, vertical stress and boundary conditions

In Figure 105 (slender piers) and Figure 106 (squat piers), numerical and experimental force-displacement hysteretic curves are summarised, while in Figure 107 and Figure 108, plots of the equivalent plastic strains detected in the FE macro-block are included and compared against experimental crack patterns. As noted by Wilding et al. (2018), who adopted a rather similar computational strategy, equivalent plastic strains might be intended as a scalar measure of how far the current stress-strain state in the element has progressed along the assigned in-elastic uniaxial stress-strain law in compression.

The HDM model captured with varying levels of accuracy the experimental cyclic responses exhibited by the full-scale URM components. In the case of CS slender piers (i.e. CS1-CS2), a good agreement was found in terms of lateral stiffness and peak shear strength, although the experimentally-observed energy dissipation of CS1 was not properly accounted for. However, as further discussed in Graziotti et al. (2016a), during the test a peculiar crack propagation, migrating toward the centre of the panel, produced the shortening of its effective height, resulting in an unusually high energy dissipation and hardening response compared with the others specimens tested. It might be worth mentioning that similar discrepancies regarding the simulation of CS1 were also experienced by Malomo et al. (2018b), using an advanced micro-modelling approach. With reference to CL1, the model struggled to predict the progressive lateral stiffness reduction, mostly due to masonry crushing phenomena, resulting in a not-negligible underestimation of the dissipated energy. Nevertheless, both $P-\Delta$ effect and shear strength were accurately described. Similarly, the HDM model represented satisfactorily initial stiffness and lateral strength of both CL2 and CL3, even though noticeable differences in terms of energy dissipation were found.



Contrarily, the energy dissipation of CS3 was duly accounted by the model, as well as both loading/unloading stiffness and cohesion degradation, which was particularly evident.



The shear-governed cyclic response of the CL4 specimen was characterised by a significant deterioration of stiffness and in-plane strength, especially in the last loading phases. The performances of the HDM model seems to be representative of the latter phenomena, adequately approximating the force-displacement experimental envelope.

Looking at Figure 105, where the predicted damage (the warmer is the colour the higher is the related plastic strain) of slender piers (i.e. CS1-2, CL1-2-3) are shown, it can be gathered that the response of the models was mainly characterised by rocking behaviour and associated damage. Contrarily, the CL brick masonry panels underwent both flexural-shear damage during the tests, thereby explaining the observed differences in terms of hysteretic curves. For what concerns the CS walls, the model predictions can be considered rather satisfactory, given that a good correspondence between experimental cracks and strain localisations was found. It is herein recalled that in the case of CS2 the test ended prematurely, and negligible damage was detected during post-test surveys. Hence, the reduced extent of plastic strains predicted by the CS2 model is encouraging.

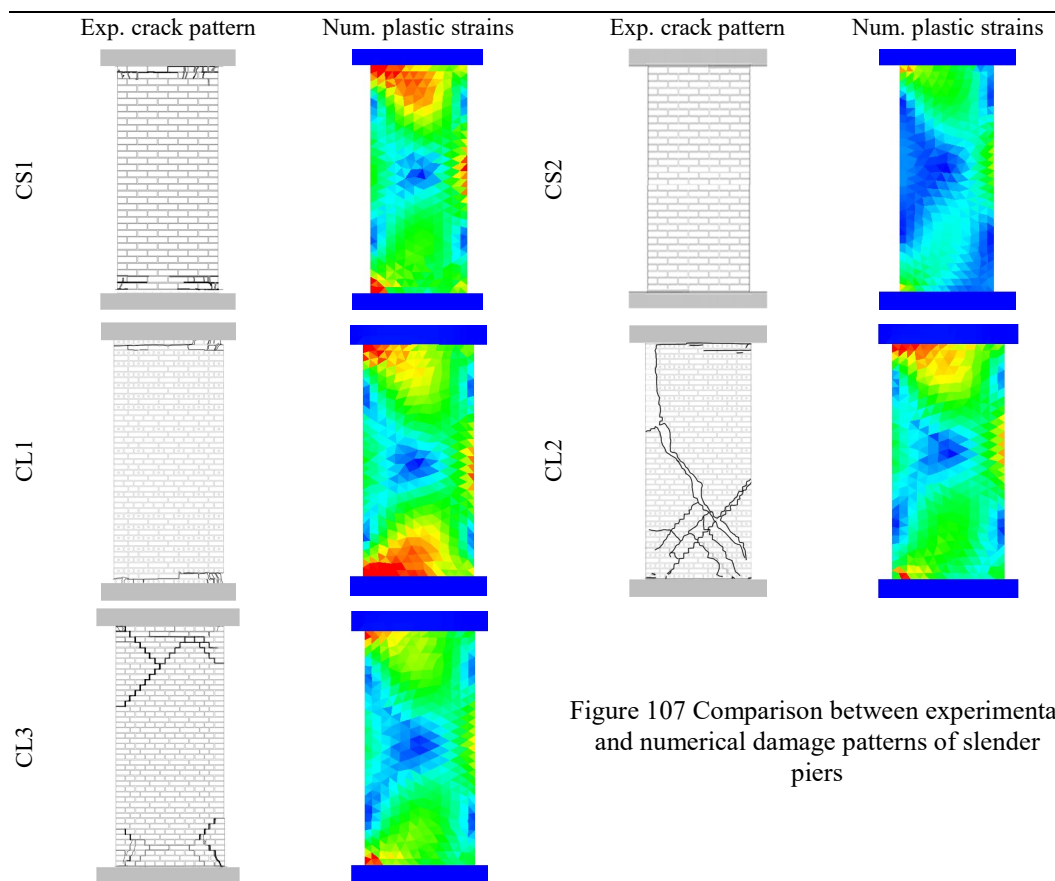


Figure 107 Comparison between experimental and numerical damage patterns of slender piers

The simulations of squat piers (i.e. CS3-CL4) appear particularly convincing. Indeed, in both cases, the diagonal shear cracks were duly represented. The predicted response of CS3 also comprised some damage on the bottom of the panel, which seems in good accordance with the experimentally-observed failure mechanism. Similarly, the crack pattern of CL4 was adequately captured by the corresponding HDM model.

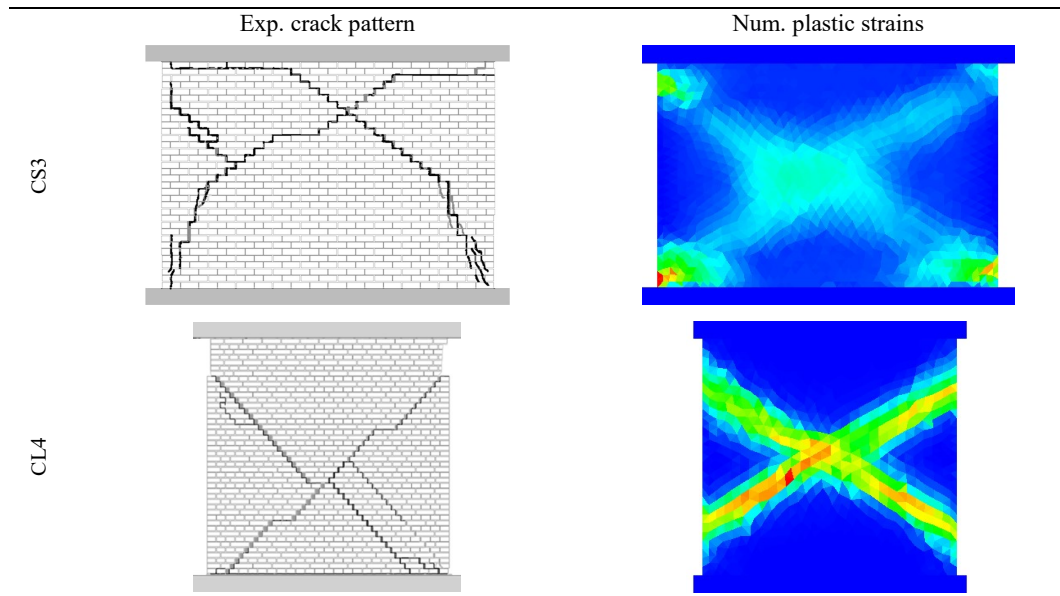


Figure 108 Comparison between experimental and numerical damage patterns of squat piers

8.4 Simulation of the cyclic lateral response of a URM façade and comparison with micro-modelling approach

In this section, the methodology presented above was extended to the simulation of a URM façade subjected to in-plane shear-compression cyclic loading. Further, with a view to assessing the adequacy of the HDM model, the results were compared to those obtained using a DE micro-modelling approach. As depicted in Figure 109, the numerical prototype consisted in an assembly of three main panels, characterised by an aspect ratio compatible with the ones on which the model was calibrated, namely 2.5 (slender pier), 1.4 and 0.7 (squat pier). In order to investigate the modelling of URM spandrels and their connecting with the macro-block, two openings were also introduced. The loading protocol, included in the same figure, resembled the one of CS3 and CL4, according to which three repetitions of the same cycles were imposed until up to a maximum displacement of 9 mm.

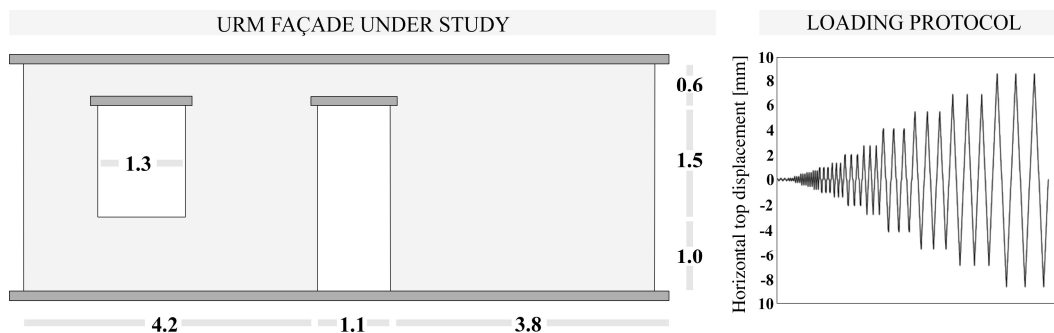


Figure 109 URM façade tested numerically and adopted loading protocol

The lintels, as well as both top and bottom beam, consisted of 100 mm-height RC elements. A rotational restraint was assigned to the top RC beam, assuring fixed-fixed boundary conditions, while the applied vertical pressure was 0.3 MPa. The masonry material properties, as well as the brick type and dimensions, were equal to those of the CS specimens reported in Table 48.

The micro-model was developed in the framework of the DEM, and calibrated on the same experimental cyclic tests, as broadly discussed in Malomo et al. (2018a). The constitutive laws assigned to both joints (i.e. Mohr-Coulomb slip model with tension cut-off) and deformable bricks (i.e. Mohr-Coulomb plasticity model) corresponded to those allotted to interface and macro-block respectively. The latter and the discrete bricks, however, were characterised by different equivalent mechanical properties. Indeed, through an adjustment of the tensile-shear properties of the discrete bricks, a compression cap was introduced, providing a faithful description of crushing mechanisms. Regardless, with a view to optimise the comparison between the two approaches, the numerical prototype was specifically designed for avoiding crushing phenomena, which, in fact, were not predominant. The two models slightly differed in terms of FE mesh: the macro-block is based on a Delaunay triangular subdivision, while the mixed discretisation proposed by Marti and Cundall (1982) was assigned to the discrete bricks. As it can be gathered by Figure 110, where both micro and macro-models are represented, the latter is composed of three main different elements:

- The macro-block/interface assemblies, each of which represents a single URM pier. Contrarily to most of the typically-employed macroelement techniques (e.g. Lagomarsino et al. 2013), no rigid nodes had to be introduced. Indeed, it was observed that best fit of micro-modelling results was obtained considering the mechanical contribution of the entire height of the wall
- URM spandrels, which provided the horizontal connection among piers. Each brick and spandrel were represented separately, according to a micro-modelling approach. The connection among bricks is based on a Mohr-Coulomb slip model, analogous to the one selected for the micro-model
- Spring interfaces connecting macro-blocks and spandrels. These zero-thickness layers were characterised by the same normal/shear stiffness properties of the other interfaces, albeit a linear-elastic constitutive law was employed aimed at avoiding spurious failure modes among the two elements

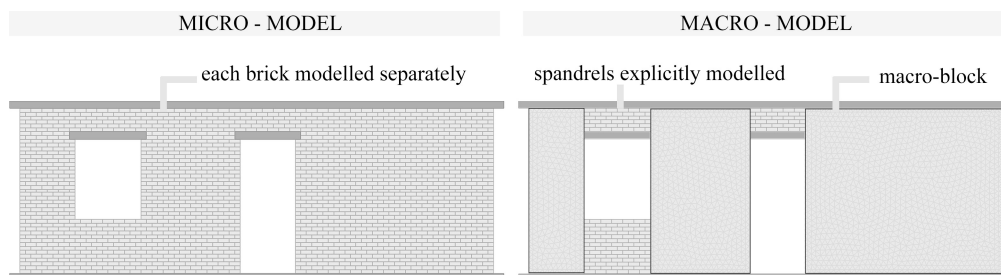


Figure 110 Screenshot of both micro and macro numerical models

In what follows, the predictions of micro and macro-models are compared in terms of hysteretic behaviour and damage propagation:

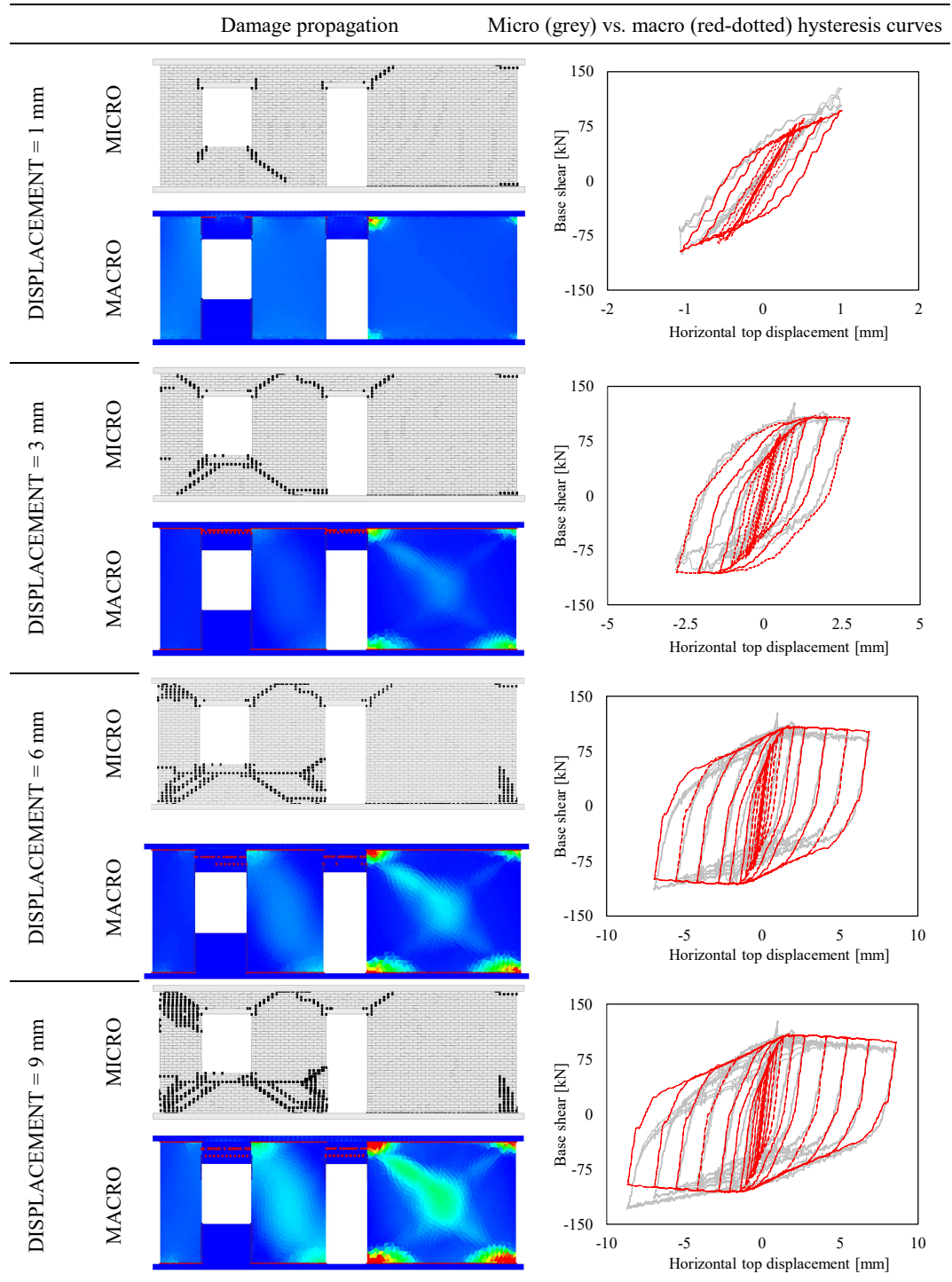


Figure 111 Comparison between micro/macro hysteretic response and damage propagation

As shown in Figure 111, during the initial loading phases (1-3 mm), the micro-model mainly suffered flexural and base-sliding cracks. Up to this point, the damage patterns seem to be in accordance with those predicted by the macro HDM assembly. Then (3-6 mm), the cyclic response of the latter was mainly governed by sliding and diagonal shear (squat pier on the right side), as well as flexural (central pier) mechanisms. Similarly, the micro-model underwent several flexural cracks, which migrated from the openings towards top/bottom RC beams, albeit no diagonal shear phenomena were predicted. During the last cycles (6-end of the test, i.e. 9 mm), both the models substantially exhibited an increase in the damage previously suffered. For what concerns the spandrels, negligible damage was detected by the micro-model, while a few horizontal cracks were shown by its macro counterpart.

Despite the abovementioned dissimilarities, a good agreement was found in terms of hysteretic curves for all the cycles. Slight differences were noted at 1 mm of lateral displacements, where the squat pier of the macro-model started exhibiting a pronounced shear response, as witnessed by the higher dissipated energy. The micro/macro predicted loading and unloading stiffnesses were comparable, as well as both peak and residual strength. Regardless, the micro-model, due to the progressive shortening of the effective height of both slender and central piers, exhibited a hardening (negative) response, resulting in an asymmetrical hysteretic curve. Understandably, the HDM model was not able to account for this phenomenon, producing symmetric force-displacement envelopes.

Whilst this modelling exercise substantially highlighted the differences in terms of accuracy with respect to the representation of predicted damage between micro and macro numerical approaches, it is worth mentioning that rather comparable peak/residual shear capacity, loading/unloading stiffness and energy dissipation were predicted. In fact, even though the strains/cracks localisation was different, the main components of the considered URM façade exhibited similar behaviours. However, it is clear that a certain degree of abstraction should be accepted when dealing with simplified models, typically employed for reducing computational cost. Regarding this point, significant differences were found, to some extent justifying the various level of details observed. Indeed, the analysis time required by the micro-model (i.e. 49 hours) was more than five times larger than the one needed by the HDM (i.e. 9 hours). It is recalled that the employed DE code is based on an explicit time integration scheme, which explains why, when performing quasi-static analyses, the computational expense referred to the macro-model is still relatively high.

8.5 Conclusions

The simulation of the global seismic performances of URM buildings still represents an open challenge. Whilst the employment of simplified methods appear suitable in case of in-plane governed responses, they usually neglect the contribution of out-of-plane modes and their potential interaction with adjacent elements. On the other hand, advanced numerical approaches often require a relatively high computational expense, limiting their applicability to the analysis of local mechanisms or to the simulation of reduced-scale prototypes. In this work, aimed at combining the efficiency of simplified methods with the capabilities of discontinuum-based numerical procedures, a new Finite-Distinct macroelement model for representing the cyclic response of laterally-loaded piers, herein named Homogenised Distinct Macro-block model (HDM), is proposed. Having been

implemented in an explicit Distinct Element code, naturally suitable for large-displacement analysis, out-of-plane modes and collapses can also be considered by modelling each unit separately. The HDM model consists in an assembly of a three-dimensional deformable Finite-Element (FE) macro-block and two zero-thickness interface spring layers, located at the top/bottom extremities of the latter, which provide connection with adjacent elements. Shear damage is accounted by the FE macro-block, to which the mass of the system is assigned, while flexural and sliding phenomena are considered by the spring layers.

With a view to assess the capabilities of interface springs in appropriately representing tensile and shear-compression mechanisms, characterisation tests on small-scale samples were reproduced. In absence of diagonal shear tests on the selected masonry typology, the calibration process of the FE macro-block was based on a micro-model previously verified by the authors. Comparisons with the in-plane cyclic performances of full-scale URM piers subjected to shear-compression, made of different masonry types (i.e. calcium silicate and clay bricks) and tested under several combinations of vertical pressures, boundary conditions and aspect ratios, have shown that the HDM models can adequately predict both peak and residual capacity, as well as loading/unloading stiffnesses and dissipated energy. Moreover, contrarily to most of the macroelements presently available in literature, the damage propagation can be reproduced explicitly, and an acceptable agreement with experimentally-observed failure modes was found.

Given the satisfactory results obtained, the methodology was extended to the modelling of the cyclic lateral response of a full-scale URM façade, and the related outcomes compared with those inferred using a micro-modelling technique. For what concerns the damage propagation, not-negligible differences, as expected, were observed. This, notwithstanding, the hysteretic force-displacement responses almost corresponded, which is reassuring. This modelling exercise pointed out both drawbacks and advantages associated with the use of simplified and advanced methods. Amongst the latter, it is worth noting that, albeit the results were comparable, in this specific case the analysis time required by the HDM model was approximately five times lesser than the one needed by its micro counterpart.

With reference to the general framework, although further improvements should be pursued in the future, the preliminary results obtained can be considered as encouraging. Possible enhancements might include a more accurate modelling of masonry crushing phenomena, as well as the extension to the simulation of in-plane/out-of-plane mechanical interaction.

Acknowledgements

The first author gratefully acknowledges the financial support provided by University of Pavia – Research and Third Mission Unit (mobility grants for doctoral candidates – n.1914/2016- 92592). Part of this work was carried out with the financial support of the ReLUIIS-DPC Project 2017-2018 PR1 ‘Masonry structures’ funded by the Italian Department of Civil Protection. The authors also acknowledge all those at both the European Centre for Training and Research in Earthquake Engineering (Eucentre, Pavia, Italy) and the University of Pavia (Pavia, Italy) that were involved in the testing campaign referred to in this paper.

References

- ASTM E 519-02. (2002). "Standard Test Method for Diagonal Tension (Shear) in Masonry Assemblages." *American Society for Testing Materials*, 5.
- Brooks, J. J., and Baker, A. (1998). "Modulus of Elasticity of Masonry." *Masonry International*, 12(2), 58–63.
- Bui, T. T., Limam, A., Sarhosis, V., and Hjjaj, M. (2017). "Discrete element modelling of the in-plane and out-of-plane behaviour of dry-joint masonry wall constructions." *Engineering Structures*, Elsevier, 136, 277–294.
- Calderoni, B., Marone, P., and Pagano, M. (1987). "Modelli per la verifica statica degli edifici in muratura in zona sismica." *III Convegno nazionale ANIDIS" L'ingegneria sismica in Italia"*.
- Calvi, G. M., Kingsley, G. R., and Magenes, G. (1996). "Testing of masonry structures for seismic assessment." *Earthquake Spectra*, 12(1), 145–162.
- Chen, S.-Y., Moon, F. L., and Yi, T. (2008). "A macroelement for the nonlinear analysis of in-plane unreinforced masonry piers." *Engineering Structures*, Elsevier, 30(8), 2242–2252.
- Ciesielski, R. (1999). "The dynamic module of elasticity of brick walls." *Proceedings of the Conference of the Committee of Civil Engineering PZITB: Lublin, Poland*.
- Cundall, P. A. (1971). "A computer model for simulating progressive large scale movements in blocky rock systems." *Proc. Symp. Rock Fracture (ISRM)*, Nancy.
- DeJong, M. J., and Vibert, C. (2012). "Seismic response of stone masonry spires: Computational and experimental modeling." *Engineering Structures*, Elsevier, 40, 566–574.
- DeLorenzis, L., DeJong, M. J., and Ochsendorf, J. A. (2007). "Failure of masonry arches under impulse base motion." *Earthquake Engineering & Structural Dynamics*, Wiley Online Library, 36(14), 2119–2136.
- Frocht, M. M. (1931). "Recent Advances in Photoelasticity - And an Investigation of the Stress Distribution in Square Blocks Subjected to Diagonal Compression." *The American society of Mechanical Engineers*, 135(APM-53-11), 135–153.
- Galvez, F., Giaretton, M., Abeling, S., Ingham, J., and Dizhur, D. (2018). "Discrete Element modelling of a two-storey unreinforced masonry scaled model." *16th European Conference on Earthquake Engineering*, Thessaloniki, Greece.
- Graziotti, F., Rossi, A., Mandirola, M., Penna, A., and Magenes, G. (2016a). "Experimental characterisation of calcium-silicate brick masonry for seismic assessment." *International Brick and Block Masonry Conference*, Padua, Italy, 1619–1628.
- Graziotti, F., Tomassetti, U., Rossi, A., Kallioras, S., Mandirola, M., Cenja, E., Penna, A., and Magenes, G. (2015). *Experimental campaign on cavity-wall systems representative of the Groningen building stock - Report n. EUC318/2015U*. Pavia, Italy.
- Graziotti, F., Tomassetti, U., Rossi, A., Marchesi, B., Kallioras, S., Mandirola, M., Fragomeli, A., Mellia, E., Peloso, S., Cuppari, F., Guerrini, G., Penna, A., and Magenes, G. (2016b). *Experimental campaign on a clay URM full-scale specimen representative of the Groningen building stock - Report n. EUC128/2016U*. Pavia, Italy.
- Haach, V. G., Vasconcelos, G., and Lourenço, P. B. (2011). "Parametrical study of masonry walls subjected to in-plane loading through numerical modeling." *Engineering Structures*, Elsevier, 33(4), 1377–1389.

- Itasca Consulting Group Inc. (2013). “3DEC. Three Dimensional Distinct Element Code.”
- Jäger, W., Irmschler, H., and Schubert, P. (2004). *Mauerwerk-Kalender 2004*. Ernst & Sohn Verlag für Architektur und technische Wissenschaften.
- Kallioras, S. (2017). “Numerical Simulation of Shaking Table Tests on a URM Cavity-Wall Building.” *Journal of the International Masonry Society*, 30(2), 39.
- Kassotakis, N., Sarhosis, V., Forgács, T., and Bagi, K. (2017). “Discrete element modelling of multi-ring brickwork masonry arches.” *Proceedings of the 13th Canadian Masonry Symposium*, Halifax, Canada.
- Kaushik, H. B., Rai, D. C., and Jain, S. K. (2007). “Stress-strain characteristics of clay brick masonry under uniaxial compression.” *Journal of materials in Civil Engineering*, American Society of Civil Engineers, 19(9), 728–739.
- Lagomarsino, S., Penna, A., Galasco, A., and Cattari, S. (2013). “TREMURI program: an equivalent frame model for the nonlinear seismic analysis of masonry buildings.” *Engineering Structures*, Elsevier, 56, 1787–1799.
- Lemos, J. V., and Campos Costa, A. (2017). “Simulation of Shake Table Tests on Out-of-Plane Masonry Buildings. Part (V): Discrete Element Approach.” *International Journal of Architectural Heritage*, Taylor & Francis, 11(1), 117–124.
- Lemos, J. V. (2007). “Discrete element modeling of masonry structures.” *International Journal of Architectural Heritage*, Taylor & Francis, 1(2), 190–213.
- Lourenço, P. B., Rots, J. G. J. G., and Blaauwendraad, J. (1995). “Two approaches for the analysis of masonry structures - micro and macro-modeling.” *Research article HERON - Delft Univ. of Technology (Delft, The Netherlands)*, 40(4), 313–340.
- Magenes, G., Bolognini, D., and Braggio, C. (2000). *Metodi semplificati per l'analisi sismica non lineare di edifici in muratura*. CNR-Gruppo Nazionale per la Difesa dai Terremoti, CNR-Gruppo nazionale per la difesa dai terremoti, Rome, Italy.
- Magenes, G., and Calvi, G. M. (1997). “In-plane seismic response of brick masonry walls.” *Earthquake engineering & structural dynamics*, 26(11), 1091–1112.
- Malomo, D., DeJong, M. J., and Penna, A. (2018a). “Distinct Element modelling of the in-plane cyclic response of URM piers subjected to shear-compression.” *to be submitted*.
- Malomo, D., Pinho, R., and Penna, A. (2018b). “Using the applied element method for modelling calcium silicate brick masonry subjected to in-plane cyclic loading.” *Earthquake Engineering and Structural Dynamics*, 47(7), 1610–1630.
- Marti, J., and Cundall, P. (1982). “Mixed discretization procedure for accurate modelling of plastic collapse.” *International Journal for Numerical and Analytical Methods in Geomechanics*, 6(1), 129–139.
- Matysek, P., and Janowski, Z. (1996). “Analysis of factors affecting the modulus of elasticity of the walls.” *Proceedings of the Conference of the Committee of Civil Engineering PZITB: Lublin, Poland*.
- Milani, G., Esquivel, Y. W., Lourenço, P. B., Riveiro, B., and Oliveira, D. V. (2013). “Characterization of the response of quasi-periodic masonry: Geometrical investigation, homogenization and application to the Guimarães castle, Portugal.” *Engineering Structures*, Elsevier, 56, 621–641.
- NPR 9998. (2017). “Assessment of structural safety of buildings in case of erection, reconstruction and disapproval - Basic rules for seismic actions: induced earthquakes.”
- Pantò, B., Cannizzaro, F., Calì, I., and Lourenço, P. B. (2017). “Numerical and experimental validation of a 3D macro-model for the in-plane and out-of-plane behavior of unreinforced masonry walls.” *International Journal of Architectural*

- Heritage*, Taylor & Francis, 11(7), 946–964.
- Papantonopoulos, C., Psycharis, I. N., Papastamatiou, D. Y., Lemos, J. V., and Mouzakis, H. P. (2002). “Numerical prediction of the earthquake response of classical columns using the distinct element method.” *Earthquake Engineering & Structural Dynamics*, Wiley Online Library, 31(9), 1699–1717.
- Penna, A., Lagomarsino, S., and Galasco, A. (2014). “A nonlinear macroelement model for the seismic analysis of masonry buildings.” *Earthquake Engineering & Structural Dynamics*, Wiley Online Library, 43(2), 159–179.
- Petry, S., and Beyer, K. (2015). “Cyclic test data of six unreinforced masonry walls with different boundary conditions.” *Earthquake Spectra*, Earthquake Engineering Research Institute, 31(4), 2459–2484.
- Van der Pluijm, R. (1993). “Shear behaviour of bed joints.” *Proceedings of the 6th North American Masonry Conference*, Philadelphia, USA.
- Quagliarini, E., Maracchini, G., and Clementi, F. (2017). “Uses and limits of the Equivalent Frame Model on existing unreinforced masonry buildings for assessing their seismic risk: A review.” *Journal of Building Engineering*, Elsevier, 10, 166–182.
- Raka, E., Spacone, E., Sepe, V., and Camata, G. (2015). “Advanced frame element for seismic analysis of masonry structures: model formulation and validation.” *Earthquake Engineering & Structural Dynamics*, Wiley Online Library, 44(14), 2489–2506.
- Salerno, G., and de Felice, G. (2009). “Continuum modeling of periodic brickwork.” *International Journal of Solids and Structures*, Pergamon, 46(5), 1251–1267.
- Tomažević, M. (1987). “Dynamic modelling of masonry buildings: storey mechanism model as a simple alternative.” *Earthquake engineering & structural dynamics*, Wiley Online Library, 15(6), 731–749.
- Turnšek, V., and Čačovič, F. (1971). “Some experimental results on the strength of brick masonry walls.” *Proc. of the 2nd International Brick Masonry Conference*, 149–156.
- U.B.C. (1991). “International Conference of Building Officials. Uniform Building Code.” *International conference of building officials, USA*, Whittier, USA.
- Vanin, F., Zaganelli, D., Penna, A., and Beyer, K. (2017). “Estimates for the stiffness, strength and drift capacity of stone masonry walls based on 123 quasi-static cyclic tests reported in the literature.” *Bulletin of Earthquake Engineering*, Springer Netherlands, 15(12), 5435–5479.
- Wilding, B. V., Dolatshahi, K. M., and Beyer, K. (2018). “Shear-compression tests of URM walls: Various setups and their influence on experimental results.” *Engineering Structures*, Elsevier, 156, 472–479.
- Yokel, F. Y., and Fattal, S. G. (1976). “Failure hypothesis for masonry shear walls.” *Journal of the Structural Division*, ASCE, 102(3), 515–532.
- Zucchini, A., and Lourenço, P. B. (2002). “A micro-mechanical model for the homogenisation of masonry.” *International Journal of Solids and Structures*, Pergamon, 39(12), 3233–3255.

CHAPTER 9

Closing remarks and future research



CHAPTER 9 Closing remarks and future research

In this Chapter, the main findings and the results achieved are briefly summarised. Moreover, the areas of future research related to the contributions herein proposed are identified and discussed. It is recalled that further comments regarding the aspects investigated in this work, as well as their potential developments, are reported at the end of each Chapter on a case-by-case basis.

9.1 Summary of main findings and primary contributions

The principal aim of this research, as broadly discussed in the body of the dissertation, is to increase the capabilities of discontinuum-based numerical micro-models in effectively and adequately predicting the local and global response of URM structures subjected to static and dynamic horizontal actions. To this end, the use of two discrete element methods, namely the Applied Element and the Distinct Element methods (hereinafter referred to as AEM and DEM respectively) has been scrutinised, optimised and calibrated through the introduction of specific modelling strategies and by comparing their performances with a wide range of experimental tests. The main findings and the objectives addressed are as follows:

- Cyclic quasi-static testing of URM components is a valuable source of information of their actual behaviour under lateral loads. The AEM effectively predicted local damage and hysteretic response of horizontally-loaded piers, albeit the springs among rigid block should be carefully calibrated. In this respect, a comprehensive methodology for optimising the numerical outcomes is proposed. Moreover, several empirical formulae for inferring mortar and brick material properties separately (usually not provided by experimental campaigns) were proposed and verified. It was found, as expected, that the models struggled to capture experimentally-observed toe-crushing mechanisms. This aspect is much more evident when considering isolated tests on components rather than complete systems, where the boundary conditions are implicitly defined by the mutual interaction among adjacent elements instead of being idealised into cantilevered and fixed-fixed conditions.
- The post-cracking dynamic response of out-of-plane-loaded components under both one-way and two-way bending conditions is particularly brittle, thereby its modelling poses several difficulties from a numerical viewpoint. It was found that the AEM models are extremely sensitive to the imposed boundary conditions, as well as to the employed value of bond tensile strength. In this connection, the tensile strength inferred through bond wrench tests led to best results. Moreover, the typically-designed shake-table test layouts are difficult to reproduce explicitly, because of the presence of pre-stressed springs (for assuring the envisaged vertical compression) and several other auxiliary elements. In this work the restraining and

the loading system has been drastically simplified combining the use of rigid bodies with pre-stressed links. After having addressed the abovementioned issues, the out-of-plane one-way and two-way dynamic response of tested URM assemblies was reproduced satisfactorily both in terms of hysteretic behaviour and crack propagation, which was particularly relevant for the case of two-way bending walls, where in-plane and out-of-plane modes are combined. Comparisons with such experimental outcomes have shown that the AEM can also adequately predict the produced debris area after a partial and full collapses.

- With reference to the AEM modelling of complete cavity-wall building URM prototypes tested dynamically, it was found that the numerical representation of constructive details was of primary importance. In these structures, metal ties, connecting calcium silicate and clay walls, are largely employed. The latter should be adequately considered numerically, since they might affect in a not-negligible manner the overall response, especially in terms of failure mode. Similarly, the presence of complex flexible diaphragms and their configurations should be represented carefully. Regardless, accounting for all these aspects explicitly was found to be unpractical, resulting in a considerable increase of computational expense. To overcome this limitation, based on both analytical formulations and experimental evidence, specific simplified methodologies were elaborated and validated, leading to a satisfactory representation of partial and full collapse phenomena exhibited by various full-scale building specimens. The modelling exercises herein proposed substantially shown that the AEM can be successfully adapted to the simulation of large-scale URM constructions.
- Analogous considerations can be made for the AEM modelling of a full-scale double wythe URM building specimen subjected to shake-table motion. As witnessed by some of the findings described in the following, numerical outcomes would suggest that the use of the Dutch-cross bond pattern, which characterised the considered structure, can be deemed as an additional source of vulnerability, further reducing lateral strength and displacement capacity. To account for this aspect, the AEM model was accurately calibrated against in-plane tests on components, resulting in an adequate representation of the experimentally-observed dynamic response. Since the test was stopped before explicit collapse, additional analyses were performed using the calibrated AEM model, which provided useful information concerning the ultimate seismic resistance of the specimen.
- The capabilities of DEM, originally conceived for solving rock mechanics problems, in reproducing numerically the quasi-static lateral response of URM piers were accurately scrutinised and assessed in this work. The DEM modelling of mortared joint URM assemblies subjected to cyclic loading was not present in current literature. Thus, with a view to address such knowledge gap, the use of DEM was optimised and enhanced, introducing several new features originally not implemented in the standard formulation, including the possibility of simulating explicitly masonry crushing phenomena. It was found that the combined employment of mass, time, and size scaling procedures consistently reduced the

required computational expense, also enabling the modelling exercised summarised in the following.

- The abovementioned findings and achievements allowed to perform a parametric analysis with a view to quantify the influence of the most commonly employed periodic and quasi-periodic brickwork bonds on the in-plane response of URM panels. This aspect is not yet addressed neither experimentally nor numerically. Thus, the effect of five bond patterns (running, Flemish, English, Dutch-cross and header bonds), two masonry types, and several combinations of boundary condition, vertical compression and aspect ratio was investigated. It was found that the running bond walls performed better than the others in terms of both shear and displacement capacity. It was observed that even during the first stages of loading, the propagation of normal stresses through the various brickworks noticeably differs from each other, strongly influencing the initial lateral response. Significant differences in terms of in-plane strength were also detected, and for equal masonry type, they tend to increase with increased axial and shear span ratio. Failure mode and displacement capacity are unavoidably related. In this respect, a critical range of the shear span ratio αv has been identified. Indeed, for $0.5 < \alpha v < 1.0$, while running and Flemish bond walls underwent top and bottom sliding, English, Dutch-cross and Header bond panels prematurely failed in diagonal shear, thereby exhibiting reduced displacement capacity. For these walls, a strong decay in resistance to earthquake is to be expected.
- Finally, aimed at combining the efficiency of simplified methods with the capabilities of discontinuum-based numerical procedures, a new Finite-Distinct macroelement model for representing the cyclic response of laterally-loaded piers is proposed and preliminary validated within an explicit DEM framework, this including the possibility of representing out-of-plane modes by modelling each brick separately. It was found that even using an empirically-based calibration procedure, a good agreement with experimental tests was found, also in terms of crack patterns, which, can be explicitly reproduced, unlike most of the other available macro-models. Comparison with calibrated DEM micro-models have shown that the extension of the proposed approach to the simulation of more complex structures (e.g. URM façades and large-scale assemblies) seems to be promising, also considering that the analysis time required by the micro-model was more than five times larger.

9.2 Future developments

The large variety of experimental tests and related modelling exercises presented in this research allowed a wide-range exploration of the contribution that the selected micro-models can make towards the numerical assessment of URM structures subjected to earthquake loading. At the same time, it also provides a further insight into ways of improving them. Thus, in addition to the investigations proposed in this endeavour, the following potential areas of continued research, amongst others, are identified:

- The constitutive laws typically implemented in discontinuum-based micro-models for representing damage at the joint level should be further enhance. Indeed, it was

observed that the tension cut-off criterion assigned to the interfaces often resulted in an underestimation of the actual post-peak capacity. This is much more evident when considering either rocking-governed behaviours of large-scale URM constructions, in which the damage caused by tensile failure has been frequently overestimated, or one-way bending out-of-plane tests on components. In this last case, since when a given spring fails in tension contact is lost, the displacement capacity has been underestimated significantly, even though for a limited number of specimens.

- The in-plane performances of URM elements are strongly influenced by loading rate. This aspect has not been fully explored experimentally yet. The use of calibrated discrete micro-models might contribute significantly towards the definition of simplified parameters for correlating the responses observed under different loading conditions (e.g. monotonic, cyclic-symmetrical, cyclic-unsymmetrical and dynamic displacement histories).
- URM structures may exhibit a large variety of collapse modes under earthquake loading depending on several factors, such as plan and elevation geometry, masonry properties and texture, diaphragm type. This aspect should be further investigated numerically, also giving its importance in practical applications of seismic risk.
- Dynamic interaction among adjacent buildings is something that has not been investigated in detail neither experimentally nor numerically. In this framework, both AEM and DEM appear suitable for performing parametric studies.
- According to several simplified methods, including the macroelement strategy, the building structure is discretised as an assembly of deformable and rigid regions, thus identifying an equivalent frame. Although this assumption is supported by damage observation and experimental evidence, it is still not clear how to define the effective height of piers and, especially in case of irregular distribution of openings, which regions should be defined as rigid. Again, discrete element methods might provide a significant contribution in this sense.
- Historical URM constructions are often characterised by the presence of various masonry typologies, and material discontinuity. For understandable reasons, there is still some lacking of consistency regarding how it can affect the global seismic response, also because only limited applications of discrete element micro-models (rather than continuum-based methods) are presently available in literature. Thus, also in view of the results herein presented, this is something that deserves attention.
- Analysis of debris areas produced by both impact loading and progressive collapse of URM structures is lately becoming a trend in the field of masonry modelling. Discrete models are naturally suitable for this purpose, and further research is surely needed for calibrating re-contact spring factors and appropriate damping coefficients.

APPENDIX I

Derivation and assemblage of stiffness matrices in the
framework of the Applied Element Method (2D)



APPENDIX I Derivation and assemblage of stiffness matrices in the framework of the Applied Element Method (2D)

With reference to a two-dimensional case, it is possible to compute directly the stiffness matrix of a couple of adjacent units, undertaking a linearized kinematic approach (Bathe and Saunders 1984), hence an alternative simplified procedure to derive the numerical interaction between units, with respect to the one proposed by Meguro and Tagel-Din (2000) was herein developed. It is herein noted that this was done only with a view to facilitate the understanding of what follows. Further improvements, including the possibility of implementing in the code such slight modifications, are currently under developments. The main dissimilarity between the two approaches lies in a different geometrical modelling of the control points (CP) location, as shown in Figure 112:

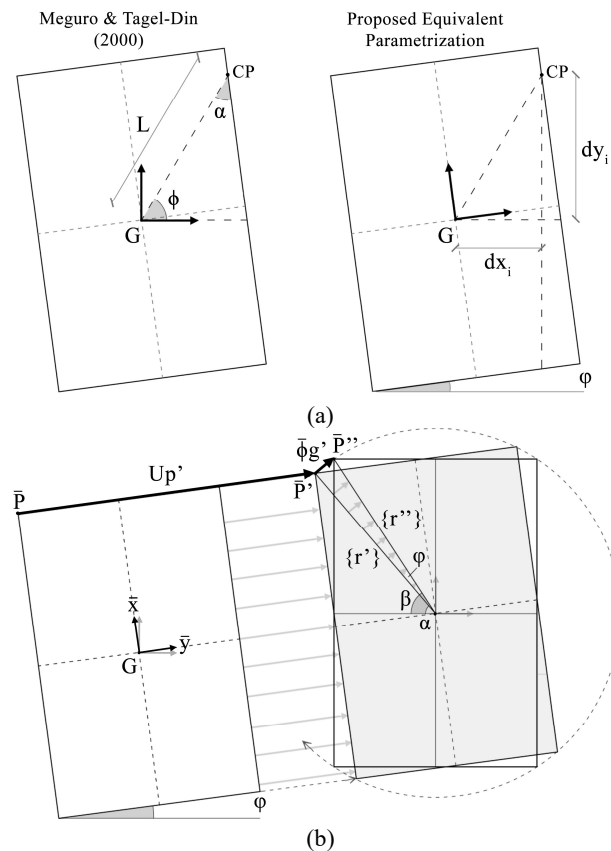


Figure 112 Geometrical interpretations of the CP location (a) and representation of the rigid displacement of a plane unit (b)

According to Meguro and Tagel-Din (2000), the employed parameters to describe CP location are: the length L , representing the distance between CP and the unit centroid G , and the trigonometric functions of α (angle between the segment from G to the longest unit side and the longest side slope with respect to the local axes) and θ (angle formed by the segment connecting G to CP). In the following, aimed at reducing the complexity of the numerical formulation, the parameterisation of an arbitrary CP was represented only by functions of φ , in addition to x_{gi}, y_{gi} (projections of the segment G -CP, with reference to the global coordinates system), describing the shortest side slope with respect to the global axes. Considering the rigid body in Figure 112(a), arranged in accordance with its local coordinate system, the displacement due to a rigid rotation $\{\bar{\phi}_g'\}$ of a vector $\{r'\}$ to $\{r''\}$ was evaluated using Eq. (3), where the matrix $\{\bar{N}\}$ describes its rotation with respect to $G\bar{X}\bar{Y}$, as reported in Eq. (4).

$$\{r'\} = \begin{Bmatrix} \bar{x}_p' \\ \bar{y}_p' \\ \mathbf{0} \end{Bmatrix} = \begin{Bmatrix} |r'| \cos(\alpha) \\ |r'| \sin(\alpha) \\ \mathbf{0} \end{Bmatrix}, \beta = (\alpha + \varphi) \quad (1)$$

$$\{r''\} = \begin{Bmatrix} \bar{x}_p'' \\ \bar{y}_p'' \\ \mathbf{0} \end{Bmatrix} = \begin{Bmatrix} |r''| \cos(\alpha + \varphi) \\ |r''| \sin(\alpha + \varphi) \\ \mathbf{0} \end{Bmatrix} = \begin{bmatrix} \cos(\varphi) & \sin(\varphi) & \mathbf{0} \\ -\sin(\varphi) & \cos(\varphi) & \mathbf{0} \\ \mathbf{0} & \mathbf{0} & \mathbf{1} \end{bmatrix} \begin{Bmatrix} \bar{x}_p' \\ \bar{y}_p' \\ \mathbf{0} \end{Bmatrix} = [N]_{3 \times 3} \{r'\}_{3 \times 1} \quad (2)$$

$$\{\bar{\phi}_g'\}_{3 \times 1} = \{\{r''\} - \{r'\}\}_{3 \times 1} = [N]_{3 \times 3} \{\{r'\} - \{r'\}\}_{3 \times 1} = [[N] - [I]]_{3 \times 3} \{r'\}_{3 \times 1} = [\bar{N}]_{3 \times 3} \{r'\}_{3 \times 1} \quad (3)$$

where

$$[\bar{N}] = \begin{bmatrix} \cos(\varphi - 1) & \sin(\varphi) & 0 \\ -\sin(\varphi) & \cos(\varphi - 1) & 0 \\ 0 & 0 & 1 \end{bmatrix} \quad (4)$$

A plane rigid body displacement $\{\bar{U}_p\}$ of a generic unit, can be easily represented as a composition of different vector components, summing rigid translations and rotations. Therefore, a vector $\{\bar{U}_p'\}$, which defines an arbitrary displacement due to pure translation from a generic point $\bar{P}(\bar{x}_p, \bar{y}_p)$ to $\bar{P}'(\bar{x}_p', \bar{y}_p')$, and a rotation contribution $[\bar{N}]\{\bar{\Delta}_{p-g}'\}$ with respect to an arbitrary pole $\bar{G}'(\bar{x}_g', \bar{y}_g')$, was defined as reported in Eq. (5).

$$\{\bar{U}_p\}_{3 \times 1} = \{\bar{U}_p'\}_{3 \times 1} + [\bar{N}_p]_{3 \times 3} \{\bar{\Delta}_{p-g}'\}_{3 \times 1}$$

or

$$\begin{Bmatrix} \bar{u}_p \\ \bar{v}_p \\ \varphi_p \end{Bmatrix} = \begin{Bmatrix} \bar{u}_p' \\ \bar{v}_p' \\ \mathbf{0} \end{Bmatrix} + \begin{bmatrix} \cos(\varphi - 1) & \sin(\varphi) & 0 \\ -\sin(\varphi) & \cos(\varphi - 1) & 0 \\ 0 & 0 & 1 \end{bmatrix} \begin{Bmatrix} \bar{x}_p' - \bar{x}_g' \\ \bar{y}_p' - \bar{y}_g' \\ \varphi_p' - \varphi_g' \end{Bmatrix} \quad (5)$$

It is noted that the Eq. (5) can be changed into Eq. (6):

$$\{\bar{U}_p\}_{3 \times 1} = [\bar{N}_p]_{3 \times 6} \{\bar{U}_p'\}_{3 \times 1}$$

or

$$\begin{Bmatrix} \bar{u}_p \\ \bar{v}_p \\ \varphi_p \end{Bmatrix} = \begin{bmatrix} 1 & 0 & \cos(\varphi - 1)\Delta\bar{x}' + \sin(\varphi)\Delta\bar{y}' \\ 0 & 1 & -\sin(\varphi)\Delta\bar{x}' + \cos(\varphi - 1)\Delta\bar{y}' \\ 0 & 0 & \varphi \end{bmatrix} \begin{Bmatrix} \bar{u}_p' \\ \bar{v}_p' \\ 1 \end{Bmatrix} \quad (6)$$

where $\{\bar{U}_p\}$ is now inferred multiplying a matrix $[\bar{N}]$ by a vector $\{\bar{U}_p'\}$. Under the assumption of small displacements and considering the assembly proposed in Figure 113, with $\bar{G}_1(\bar{x}_{g1}, \bar{y}_{g1}), \bar{G}_2(\bar{x}_{g2}, \bar{y}_{g2})$ rotation poles, the relative displacement $\delta\Delta\bar{U}_{st}$ between $\bar{S}(\bar{x}_s, \bar{y}_s)$ and $\bar{T}(\bar{x}_t, \bar{y}_t)$ can be computed employing Eq. (7):

$$\begin{aligned} \{\delta\Delta\bar{U}_{st}\}_{3 \times 1} &= [\bar{N}_t]_{3 \times 3} \{\delta\bar{U}_t\}_{3 \times 1} - [\bar{N}_s]_{3 \times 3} \{\delta\bar{U}_s\}_{3 \times 1} = [\bar{N}]_{3 \times 6} \{\delta\bar{U}\}_{6 \times 1} \\ &\text{or} \\ \begin{Bmatrix} \delta\Delta\bar{v}_{st} \\ \delta\Delta\bar{\varphi}_{st} \end{Bmatrix} &= \begin{bmatrix} 1 & 0 & (\bar{y}_t - \bar{y}_{g2}) & -1 & 0 & -(\bar{y}_s - \bar{y}_{g1}) \\ 0 & 1 & -(\bar{x}_t - \bar{x}_{g2}) & 0 & -1 & (\bar{x}_s - \bar{x}_{g1}) \\ 0 & 0 & 1 & 0 & 0 & -1 \end{bmatrix} \{\delta\bar{u}_t, \delta\bar{v}_t, \delta\bar{\varphi}_t, \delta\bar{u}_s, \delta\bar{v}_s, \delta\bar{\varphi}_s\}^T \end{aligned} \quad (7)$$

Where $[\bar{N}]$ is a matrix containing the geometrical data, whereas $\{\delta\bar{U}\}$ represents the Lagrangian coordinates.

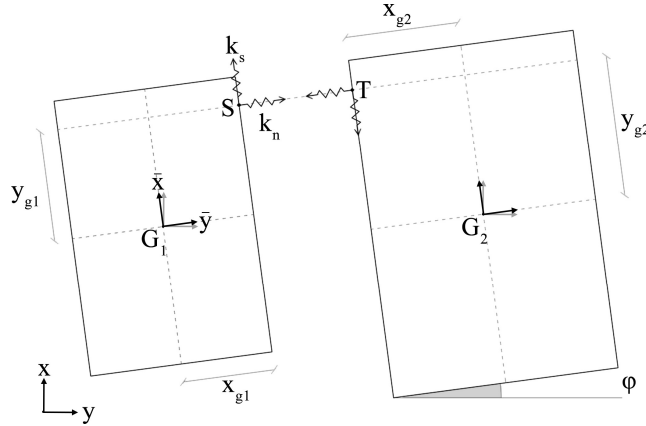


Figure 113 Assembly of rigid units connected by horizontal and shear springs

According to the Principle of Virtual Work, and given an external loads vector $\{\bar{F}_v^e\} = \{\bar{0}\}$, the relation $W_v^e = W_v^i = 0$ was established, leading to the following expressions:

$$W_v^i \stackrel{\text{def}}{=} \{\delta\Delta\bar{U}_v^i\}^T \{\bar{F}_v^i\} \quad (8) \quad \{\bar{F}_v^i\} \stackrel{\text{def}}{=} [\bar{k}] \{\delta\Delta\bar{U}_v^i\} \quad (9) \quad \{\delta\Delta\bar{U}_v^i\}^T = \{\delta\bar{U}\}^T [\bar{N}]^T \quad (10)$$

From the description of the local stiffness matrix $[\bar{k}]$ of a singular rigid body in Eq. (23), and replacing $\{\bar{F}_v^i\}$ in Eq. (8), the Eq. (12) can be obtained by means of Eq. (22) as follows:

$$[\bar{k}] = \begin{bmatrix} k_n & 0 & 0 \\ 0 & k_s & 0 \\ 0 & 0 & 0 \end{bmatrix} \quad (11)$$

$$\{\delta\bar{U}\}^T_{1 \times 6} [\bar{N}]^T_{6 \times 3} [\bar{k}]_{3 \times 3} [\bar{N}]_{3 \times 6} \{\delta\bar{U}\}_{6 \times 1} = 0 \quad (12)$$

Consequently, a local stiffness matrix $[\bar{K}]$, referred to a couple of adjacent rigid bodies, can be evaluated using Eq. (25):

$$[\bar{K}] = [\bar{N}]^T [\bar{k}] [\bar{N}] = \quad (13)$$

$$\begin{bmatrix} k_n & 0 & -k_n(\Delta\bar{y}_{sg1}) & -k_n & 0 & k_n(\Delta\bar{y}_{tg2}) \\ \cdot & k_s & k_s(\Delta\bar{x}_{sg1}) & 0 & -k_s & -k_s(\Delta\bar{x}_{tg2}) \\ \cdot & \cdot & k_n(\Delta\bar{y}_{sg1})^2 + k_s(\Delta\bar{x}_{sg1})^2 & k_n(\Delta\bar{y}_{tg1}) - k_s(\Delta\bar{x}_{tg1}) & -k_n(\Delta\bar{y}_{sg1})(\Delta\bar{y}_{tg2}) + k_s(\Delta\bar{x}_{sg1})(\Delta\bar{x}_{tg2}) \\ \cdot & \cdot & \cdot & k_n & 0 & -k_n(\Delta\bar{y}_{tg2}) \\ \cdot & \cdot & \cdot & \cdot & k_s & k_s(\Delta\bar{x}_{tg2}) \\ \cdot & \cdot & \cdot & \cdot & \cdot & k_n(\Delta\bar{y}_{tg2})^2 + k_s(\Delta\bar{x}_{tg2})^2 \end{bmatrix}$$

Considering the global coordinate system, and aiming at obtaining the corresponding global stiffness matrix $[K_g]$, a transformation matrix $[T_\varphi]$ for plane frame elements (Chandrupatla et al. 2002) was consequently introduced:

$$[T_\varphi] = \begin{bmatrix} c\varphi & s\varphi & 0 & 0 & 0 & 0 \\ -s\varphi & c\varphi & 0 & 0 & 0 & 0 \\ 0 & 0 & 1 & 0 & 0 & 0 \\ 0 & 0 & 0 & c\varphi & s\varphi & 0 \\ 0 & 0 & 0 & -s\varphi & c\varphi & 0 \\ 0 & 0 & 0 & 0 & 0 & 1 \end{bmatrix} \quad \text{with} \quad \begin{cases} c\varphi = \cos(\varphi) \\ s\varphi = \sin(\varphi) \end{cases} \quad (14)$$

The matrix $[K_g]$ was thus inferred using Eq. (15):

$$[K_g]_{6 \times 6} = [T_\varphi]_{6 \times 3}^T [\bar{K}]_{3 \times 3} [T_\varphi]_{3 \times 6} \quad (15)$$

In Eq. (16), the upper left quarter components of $[K_g]$ are presented:

$$[K_{g/4}] = \quad (16)$$

$$\begin{bmatrix} (c\varphi)^2 k_n + (s\varphi)^2 k_s & (c\varphi)(s\varphi)(k_n - k_s) & -k_n(c\varphi)(\Delta\bar{y}_{sg1}) - k_s(s\varphi)(\Delta\bar{x}_{sg1}) \\ (c\varphi)(s\varphi)(k_n - k_s) & k_s & -k_n(c\varphi)(\Delta\bar{y}_{sg1}) + k_s(s\varphi)(\Delta\bar{x}_{sg1}) \\ -k_n(c\varphi)(\Delta\bar{y}_{sg1}) - k_s(s\varphi)(\Delta\bar{x}_{sg1}) & -k_n(c\varphi)(\Delta\bar{y}_{sg1}) + k_s(s\varphi)(\Delta\bar{x}_{sg1}) & k_n(\Delta\bar{y}_{sg1})^2 + k_s(\Delta\bar{x}_{sg1})^2 \end{bmatrix}$$

Obviously, as shown in Eq. (17) and with reference to the nomenclature reported in Figure 114, $[K_{g/4}]$ is equivalent to the partial stiffness matrix $[K_{m/4}]$ reported in Meguro and Tagel-Din (2000), imposing $(\alpha + \theta) = \eta$, $\cos(\eta) = c\eta$ and $\sin(\eta) = s\eta$.

$$[K_{m/4}] = \quad (17)$$

$$\begin{bmatrix} k_n(s\eta)^2 + k_s(c\eta)^2 & (k_s - k_n)(s\eta)(c\eta) & k_s(c\eta)(L)(s\alpha) - k_n(s\eta)(L)(c\alpha) \\ (k_s - k_n)(s\eta)(c\eta) & k_n(c\eta)^2 + (s\eta)^2 & k_n(c\eta)(L)(c\alpha) - k_s(s\eta)(L)(s\alpha) \\ k_s(c\eta)(L)(s\alpha) - k_n(s\eta)(L)(c\alpha) & k_n(c\eta)(L)(c\alpha) - k_s(s\eta)(L)(s\alpha) & k_n(c^2\alpha)(L)^2 + k_s(s^2\alpha)(L)^2 \end{bmatrix}$$

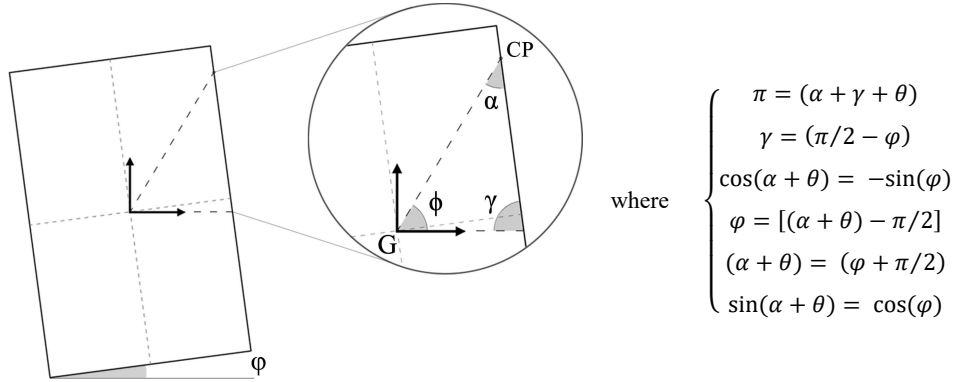


Figure 114 Definition of the angles for the parameterization of CP

Even though Eq. (17) describes the mechanical interaction between only one pair of springs, a global stiffness matrix $[K_G]$ of the whole structure can be obtained by assembling the matrices referred to each couple of units in the considered directions. Consequently, the governing equation (both in load and displacement control case) for an n -unit assembly is:

$$\{F\} = [K_G]\{\Delta\} \quad (18)$$

where a global $3n \times 3n$ stiffness matrix $[K_G]$ is multiplied by a $3n \times 1$ displacement vector $\{\Delta\}$.

Then, from each computed spring reaction, the stresses applied to δA are computed and compared with the initial material properties, according to the implemented failure criteria. Thus, from each relative displacement of the springs, the strain field can be evaluated.

